Adsorption of Cu(II) and Ni(II) Ions on Functionalized Colloidal Silica Particles Model Studies for Wastewater Treatment

Rattiya Singhon

THESE DE DOCTORAT

Présentée en vue d'obtenir le grade de
Docteur de l'Université de Franche-Comté
de l'Université de Franche-Comté

Spécialité Chimie

Adsorption of Cu(II) and Ni(II) Ions on Functionalized Colloidal Silica Particles Model Studies for Wastewater Treatment

Présentée publiquement par

Rattiya SINGHON

Le 8 avril 2014

Rapporteurs :
Marc Hebrant, Professeur des Universités, Université de Lorraine
Hamidou Haidara, Chargé de Recherches HDR CNRS, Université de Haute-Alsace

Examinateurs :
Claudine Filiatre, Professeur des Universités, Université de Franche-Comté
Sébastien Clément, Maître de Conférences, Université de Montpellier 2

Encadrants :
Michael Knorr, Professeur des Universités, Université de Franche-Comté, Directeur de thèse
Myriam Euvrard Maître de Conférences, Université de Franche-Comté, Co-encadrant

Rattiya SINGHON

Adsorption of Cu(II) and Ni(II) Ions on Chitosan-Functionalized Colloidal Silica Particles. Model Studies for Wastewater Treatment

Thesis for the degree of Doctor of Science (Chemistry)

Preface

This experimental research work for the PhD-thesis was conducted within the *Equipe Matériaux et Surfaces Structurés*, Institut UTINUM UMR CNRS 6213, Franche-Comté University in Besançon during September 2007 - December 2012.

I am highly grateful for my supervisor Professor Michael KNORR for guiding me to carry out this work and his support during my work. I would like to express my gratitude to Dr. Myriam EUVRARD for her kind and helpful guidance during the whole this work. Dr. Jérôme HUSSON for his advises, Professor Claudine Filiatre for giving me useful information sans hints, Professor Boris Lakard for helping me about Atomic Force Microscopy, Dr. Sandrine MONNEY for being my extra hands about Atomic Absorbance Spectrophotometer, Dr. Nicolas ROUGE for a good hands about scanning electron microscope, Dr. Abderrahim Khatyr for guidance about UV-Vis Spectrophotometry, and Dr. Alexandra Monnin for helping me and advices during the course of my work.

I am very grateful for all my friends at *Equipe Matériaux et Surfaces Structurés* for all support and help, the *Laboratoire de Chimie des Eaux* and the *IUT de Chimie* for their support to do my work.

Finally, I would like to thank my lovely father who is still in my heart to encourage me to come to France for study abroad even if he is now deceased. My special thanks go to my mother for all support over the times, and my younger sisters and my best friend for being a good listener and helping me whenever I needed. Furthermore, I would like to thanks Dr. Thongbai Thongmak (the best friend of my father) for language revisions.

Last but not least I am highly grateful for all friends for being in my life.

Thailand, January 2014

Rattiya SINGHON

List of Publications

I. R. SINGHON, M. EUVRARD, J. HUSSON, M. KNORR, B. LAKARD

« Adsorption of Ni(II) ions on colloidal hybrid organic-inorganic silica composites ».

Colloids and Surfaces B: Biointerfaces, 93 (2012) 1-7.

II. R. SINGHON, M. EUVRARD, J. HUSSON, M. KNORR

« Preparation of silica supported sorbent for copper removal ».

Journal of Dispersion Science and Technology, 32 (2011) 1735-1741.

List of Communications

I. Oral R. SINGHON

« Fonctionnalisation de silice colloïdale pour l'adsorption d'ions métalliques».

Journées des Ecoles Doctorales Louis Pasteur-Carnot, 5-6 mai 2011, Dijon.

II. Poster R. SINGHON, M. EUVRARD, J. HUSSON, M. KNORR

« Synthèse, caractérisation et fonctionnalités de composites silice-polysaccharide».
Journées Particules, Molécules et Surfaces, 1 avril 2011, Besançon.

III. Poster R. SINGHON

« Biopolymère supportés sur silice pour l'adsorption de micropollutants métalliques ».

Journées des Ecoles Doctorales Louis Pasteur-Carnot, 6-7 mai 2010, Besançon.

IV. Poster R. SINGHON, M. EUVRARD, J. HUSSON, M. KNORR

« Chitosane supporté sur silice colloïdale : vers de nouveaux matériaux dépolluants ».

Journée GFP (Groupe Français des Polymères), Reims, 9 septembre 2010.

V. Poster R. SINGHON

« Préparation de particules fonctionnalisées : biopolymère supporté sur silice colloïdale greffée ». Journées des Ecoles Doctorales Louis Pasteur-Carnot, 15-16 mai 2009, Dijon.

VI. Poster R. SINGHON, M. EUVRARD, J. HUSSON, M. KNORR

« Préparation de particules fonctionnalisées : biopolymère supporté sur silice colloïdale greffée ». Journée GFP (Groupe Français des Polymères), Strasbourg, 18 juin 2009.

Table of Contents

List of Tables

List of Figures

Abstract

This study is focused on the preparation of three types of silica-based composites for the capture of Cu(II) and Ni(II) ions. The first strategy consists in coating chitosan on colloidal fumed silica after acidic treatment yielding the composite **SiO_2+CS**. The second strategy can be separated into two routes: the first one involves surface grafting of silica with aminopropyltriethoxysilane to obtaining silica particles covered by amino groups (**$SiO_2(NH_2)$**). The second one involves in surface condensation of triethoxysilylbutyronitrile, followed by acidic hydrolysis of the surface-bound nitrile groups affording silica particles covered by carboxyl groups (**$SiO_2(CO_2H)$**). In the last step, chitosan has been grafted on the surface bound NH_2 or -CO_2H groups yielding the composites **$SiO_2(NH_2)$+CS** or **$SiO_2(CO_2H)$+CS**. The third strategy involves in the modified CS surface with -CO_2H groups, followed by coating onto the non-modified silica nanoparticles to obtain the composite **SiO_2+CS(CO_2H)**. The novel hybrid materials were characterized by IR spectroscopy, scanning electron microscopy, atomic force microscopy, and zeta potential measurements. Batch experiments were conducted to study the sorption performance of these composites for Cu(II) and Ni(II) removal from aqueous solution at optimum pH at 298 K. The kinetics were evaluated utilizing pseudo-first-order, pseudo-second-order, and intraparticle diffusion models. The adsorption kinetics followed the mechanism of the pseudo-second-order equation for all types of adsorbents. The adsorption isotherms were evaluated utilizing Langmuir, Freundlich, and Temkin models. The best interpretation for equilibrium data was given by Langmuir isotherm model. This study demonstrates that the adsorption capacities for Cu(II) ion is more efficient for the **SiO_2+CS** (256 mg g^{-1}) compared to **$SiO_2(NH_2)$** (75 mg g^{-1}). However, the carboxyl grafted CS-coated silica **(SiO_2+CS(CO_2H)** exhibited an excellent adsorption capacity (333 mg g^{-1}). In case of Ni(II), based on Langmuir isotherm the maximum adsorption capacity found to be 182 mg $g^{-1}$for **SiO_2+CS**, and 210 mg g^{-1} for **$SiO_2(CO_2H)$ + CS**. Using single-metal solutions, these adsorbents were found to have an affinity for metal ions in order as Cu(II) > Ni(II). The adsorption of Cu(II) ion by **SiO_2+CS** was affected by the nature of the respective anion. Application of these composite materials to remove Cu(II) and Ni(II) from aqueous solution was shown to be more efficient than the adsorption capacities of many sorbents probed by other research groups.

Keywords: functionalized silica, chitosan-coated silica, adsorption isotherms, Cu(II), Ni(II)

RESUME DE THESE

Fonctionnalisation de silices colloïdales pour l'adsorption de cations métalliques Cu(II) and Ni(II)

Elaboration de composites pour le traitement des eaux

Ce doctorat porte sur la fonctionnalisation de silices colloïdales en vue de la rétention de micropolluants métalliques dans des effluents.

Les nanoparticules et microparticules ouvrent des potentialités d'application dans de nombreux secteurs industriels (chimie, environnement, pharmacie...). Ainsi, ces travaux de recherche portent sur la synthèse et la caractérisation de matériaux composites submicroniques : il s'agit de silices colloïdales sur lesquelles sont greffés des silanes ou supportés des polysaccharides. Une des applications de ces travaux de recherche porte sur l'adsorption de métaux de transition sur ces composites en solution aqueuse.

Dans le cadre de ce doctorat, les caractéristiques des composites sont définies par leur morphologie de surface, par l'étude des groupements fonctionnels présents, par détermination de leurs surfaces spécifiques ainsi qu'en solution aqueuse par détermination de leurs diamètres hydrodynamiques et de leurs potentiels zéta. Dans un premier temps, la fonctionnalisation de la silice a permis le greffage de groupements carboxyliques et amines dont tes taux de greffage obtenus ont été respectivement de 0,47 µmol/m² et 3,86µmol/m². En présence de groupements amines, le potentiel ζ des composites est positif jusqu' à pH 9 alors qu'il est négatif dès pH 3 pour des silices non fonctionnalisées.

Dans un second temps, la silice est supportée par du chitosane dont le degré de désacétylation est de 77%. Conjointement, l'encapsulation de la silice est réalisées par du chitosane sur lequel des fonctions carboxyliques ont été greffées. La morphologie des particules est alors modifiée, leurs diamètres hydrodynamiques sont plus élevés et leurs potentiels ζ sont positifs jusqu' à pH basique.

La rétention d'ions métalliques (Cu(II) et Ni(II)) par ces composites à différents pH est ensuite étudiée. Pour chacun des cations métalliques, les capacités d'adsorption sont déterminées ainsi que les cinétiques d'adsorption. L'application de plusieurs modèles d'isotherme d'équilibre a été réalisée. Dans le cas de Cu(II), à pH 5, les meilleures capacités d'adsorption sont obtenues pour des silices supportées par du chitosane greffé : la capacité de rétention des ions Cu(II) est de 270 mg/g à pH 5. De même, c'est ce composite qui permet la meilleurs rétention des ions Ni(II) à pH 7 avec une capacité d'adsorption de 263 m/g. Concernant la cinétique, le modèle de réaction de surface du pseudo-second ordre s'applique bien aux résultats expérimentaux.

General Introduction

Part 1 Background Information

1.1 Environnemental Pollution

Pollution is the introduction of contaminants into a natural environment, which causes harmful effects to the ecosystem, including living organism and last but not least to humans. Pollution can take a physical form, such as noise, heat (thermal pollution), or light and other electromagnetic radiations (electrical pollution from cell phone antennas etc.). However, in the majority of cases, the term "pollution" is associated with chemical pollution. Pollutants can be released into the environment by several ways. There are different types of pollutions of our biosphere* like air pollution, land pollution and water pollution. As a consequence of the steady growth of the world population, unfortunately combined with a non-ecological, even irresponsible consummation of energy and raw materials, the most important and still increasing contribution to pollution stems from anthropogenic sources. Moreover, naturally sources may cause pollution such as volcanic eruptions, forest fires, etc. Air pollution is the accumulation of any hazardous substances into the atmosphere, that danger to human life and other living organism [1, 2]. Air pollution is caused by the release of air pollutants (SO_2, NO_x, CO, NH_3, O_3, volatile organic compounds, etc.) at a rate faster as than they can be accommodated by the environment (removed from the atmosphere) [3]. Some sources of air pollution are power plants, aerosol sprays, combustion of plants, nuclear weapons, smoke from engines and factories, etc. An important urban compound is sulfur dioxide combined with from the use of fossil fuels in heat and power production. Moreover, the growing traffic gave the nitrogen oxides and volatile organic compounds [4-6]. Land pollution is the pollution of earth's surface, releases from household, industries, and agriculture activities. The sources of land pollutions are human sewages, oil refineries, construction debris, mining, etc. Thermal pollution and the global temperature rise are considered as principal sources causing the climate change [7]. The warming of the Earth's surface and lower atmosphere is to be the result of the greenhouse effect, mostly due to human-produced increases in atmospheric greenhouse gases.

*The biosphere is the part of the earth where life is; it includes the surface, the oceans, rivers and the lower atmosphere.

Agricultural soils can constitute a source of the principal greenhouse gases: nitrous oxide (N_2O), methane, and carbon dioxide [8, 9]. In the context of this PhD work, we focus exclusively on water pollution and decontamination, what will be discussed in detail below.

Water pollution

The water pollution constitutes one of the most important environmental problems of our blue planet, the origin of this pollution being due to anthropic activity. Inorganic nitrogen pollution seems to be one of water problem found around the world [10]. Three major environmental harmful consequences due to inorganic nitrogen are water acidification, cultural eutrophication (toxic algae), and direct toxicity of inorganic nitrogen compounds [11]. Ammonium (NH_4^+), nitrite (NO_2^-), and nitrate (NO_3^-) are the most common ionic reactive forms of dissolved inorganic nitrogen in aquatic ecosystems [12]. The distribution of nitrate indicates that serious nitrate concentration (10-50 mg NO_3^-/L) occur in areas with important agricultural activities. Elevated nitrate concentrations are found in Northern China, Northern India, and the North-western regions of the U.S.A., and contribute also to the overproduction of toxic algae in the "Bretagne" region of France [13-16]. Apart from the elevated level of nitrogen-based salts, there are also reports describing the problems caused by high phosphate concentration in rivers in China and Thailand, which drains from agricultural activities [17, 18]. Another global problem is the widespread geographic contamination of water sources by heavy metal ions. In the case of Thailand, the water pollution due to high level of metal ions and other contaminants combined with the low quality of water sources for drinking water production is widespread in many regions of Thailand. This problem will be explained more in detail in the following section.

The particular case of water pollution in Thailand

The water pollution in Thailand will certainly tend to get worse in the future unless proper measures will be undertaken. The contaminated and often untreated wastewater stemming from household, agricultural, and industrial activities are the main cause of the water pollution. Thailand exports agricultural products for example rice, cassava, etc [19]. To increase the productivity, large quantities of pesticides and fertilizers are used, that are distributed in both ground and surface water. The contaminated wastewater released from the industry is one of factors contributing to the water pollution problem in Thailand. For example, large amounts of waste products are drained from rubber industry [20], and palm oil mills [21].

Thailand consists of 25 river basins. Major rivers, which are particularly exposed to pollutants discharged from household, industrial, and agricultural activities are the *Lower Chao Praya*, *Tha Chin*, *Mae Klong* and *Songkhla Lake* [22-24]. The largest source of groundwater is located in the Lower Central Plain, particularly in the Bangkok Metropolitan Region and surrounding provinces [25]. In the middle part of Thailand, numerous researches have been done to investigate the water quality. A high level of toxic metals is found in the *Chao Praya* river estuary [24]. Furthermore, the Gulf of Thailand (Inner Gulf), a major marine resource in term of fisheries, aquaculture, coral, oil and mineral resource, also suffers problems due to water pollution [26-28]. In the North of Thailand, nitrate and fluoride ions originating from fertilizers are found in groundwater as well as in the *Mae Ping* river which is the most important alternative surface water source for the *Chiang Mai* province [29] . In the south of Thailand, there is a serious long time problem due to high concentration of heavy metal ions as well as arsenic. These toxic compounds are found in both contaminated surface water and ground water in the *Ron Phibun* district of the *Nakhon Si Thammarat* province. People in this mining industry area had and still have problems because of a long-time consumption of surface and ground water [30-32].

Unfortunately, water pollution in Thailand is continuing, a serious environmental problem caused by the funding limitations in cities, operation costs, lack of operational experience, the absence of a high-efficient waste-water treatment station before releasing to environment and the growing population. In my opinion, for example recycling of waste products from seafood industry could be considered as promising ecological and also economically interesting solution to reduce the consequences of this national problem. For this reason, the University of Phayao, where I'm employed in the teaching stuff, is financially supporting this research project concerning the water pollution in my home country.

1.1.1 Pollutants in water and wastewater

There are many types of pollutants in water, which can be divided as radioactive materials, sediments, pathogens and parasites (viruses, bacteria, etc.), organic compounds (gasoline, oil, solvents, pesticides, phenols, phthalates, polychlorinated biphenyls (PCBs), detergents, organic matter, etc.), and inorganic compounds (nitrate, fluoride, chromium, copper, lead, etc.). These pollutants reduce the quality of life and may eventually cause even death. Focusing on inorganic pollutants, especially problematic metallic ions from discharge of industrial wastewater, let's cite cadmium, mercury, copper, nickel, lead, chromium, and arsenic, etc. Many metallic ions are known to be toxic and carcinogenic to humans because

they can accumulate in living organisms, causing several disorders and diseases. One well-documented example is lead poisoning, also called saturnism [33]. Lead interferes with a variety of body processes and is toxic to many organs and tissues, including the reproductive systems. It interferes also with the development of the nervous system and is therefore particularly toxic to children, causing potentially permanent learning and behavior disorders. Another example is natural arsenic contamination (Arsenicosis**),** which is a cause for concern in many countries of the world including Argentina, Bangladesh, Chile, China, India, Mexico, Taiwan and the south of Thailand [34-37]. People who have drunken arsenic-contaminated water (The WHO's guideline value for arsenic in drinking water is 0.01 mg / l) over a long period are suffering a skin problem called "black foot disease".* Furthermore, skin cancer, cancers of the bladder, kidney and lung may be the consequence of an Arsenicosis [38].

*Blackfoot disease (BFD) is a peripheral vascular disease. The symptoms of BFD start with spotted discoloration on the skin of the extremities, especially the feet.

1.1.2 The chemical equilibrium of metallic ions in water, their toxicity and specification

In an aquatic environment, a given metal exist in a chemical equilibrium between free metal ions, dissolved inorganic coordination complexes and metals associated with colloidal particles, etc. For example, copper ions can be complexed with dissolved organic matter [39], clay mineral, iron, and manganese in aqueous media.

The toxicity of metal ions depends first of all the concentration (see table 1) and the chemical form of a given metal. Chemical speciation of metal ions form can exist in different oxidation states depending on type of metal ions and environmental conditions. Speciation of metallic ions is very important for example nickel. Nickel is found in several oxidation states (from 0 to + 4), the Ni(II) ion being the most prevalent form of nickel in aquatic sources. Ni(II) ions found in aqueous solution (neutral pH) are hydrated as hexa-aquo complex : $[Ni(H_2O)_6]^{2+}$ [40]. Chronic nickel poisoning can affect several organs including the respiratory systems, skin, and kidney. In neutral aqueous solution, Cu(II) salts such as copper sulfate dissolve to give the paramagnetic aqua complex $[Cu(H_2O)_6]^{2+}$, which has octahedral molecular geometry. For $Cu(NO_3)_2$ (stoichiometric amounts in solution : 10 mg/L of copper and 19.5 mg/L of nitrate), the distribution at basic pH, but less than 10, the dominant species is $[Cu_2(OH)_2]^{2-}$. When the pH is above 10, anionic forms of copper hydroxides are $[Cu(OH)_3]^-$ and $[Cu(OH)_4]^{2-}$. The precipitation of copper hydroxide $[Cu(OH)_2]$ starts at around pH 8 [41]. Bioaccumulation is the process by which organisms (including humans) can take up contaminants more rapidly than their bodies can eliminate them. Some metal ions, such as

copper, which are an essential nutrient in low concentration (copper proteins have diverse roles in biological electron transport and oxygen transportation), become toxic at an elevated level. Some harmful effects to human due to a sustained high copper level are cardiac enlargement, and arteries with smooth muscle degeneration. It has also been reported that copper can cause cell damage [42a]. The maximum tolerated values for some selected metal ions in drinking water in France are listed in Table 1 [42b].

Table 1 Some maximum values for drinking water in EU

Metals	Maximum concentration	Unit
Arsenic	10	μg/L
Cadmium	5	μg/L
Copper	2	mg/L
Nickel	20	μg/L
Lead	10	μg/L
Mercury (total)	1	μg/L

1.2 Metal-containing Wastewater Treatment Techniques

In contrast to the most part of organic matter, metal ions are not biodegradable. Therefore, they accumulate their amounts along the food chain. For this reason, it is very important to remove metals from contaminated water. Various methods are used for removal of metals from water and wastewater. Some conventional techniques that have been used to treat industrial wastewater include ion exchange, filtration, chemical precipitation, flotation, and adsorption (see Fig. 1).

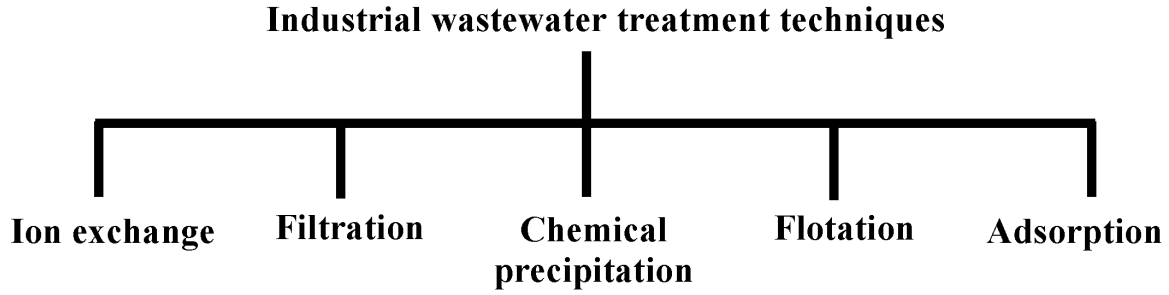

Fig. 1 Summarization of techniques used in industrial wastewater treatment

1.2.1 Conventional Techniques

1.2.1.1 Ion exchange

The ion exchange technique is currently used for the removal of heavy metal from contaminated water [43,44]. Ion exchange resins consist of insoluble polymeric matrices containing a functional group. The principle of this technique is the exchanging a counter ion of the exchanger resin with an ion in aqueous solution. Ion exchange can be classified in two types of resin; cationic exchange resin, and anionic exchange resin (Fig. 2). The exchange reaction of a strong cationic exchange resin ($R\text{-}SO_3^-H^+$ for instance) with a metal ion (M^{n+}) is shown in the following equation (where R represents an organic polymer support):

$$n(R\text{-}SO_3^-H^+) + M^{n+} \longrightarrow R\text{-}SO_3\text{-}M^{n+} + H^+$$

Most typical ion-exchange resins are based on cross-linked polystyrene. For example, Sangeetha *et al*. investigated recently the trapping of heavy metals using a quaternized anionic membrane, prepared by chloromethylation of the tri-block polymer Polystyrene-ethylene-butylene and subsequent quaternization in the presence of NEt_3. This study revealed that the polymer membrane showed high efficiency in adsorption for Cr(VI) ions rather than for removal of Cu(II) and Ni(II) ions [45].

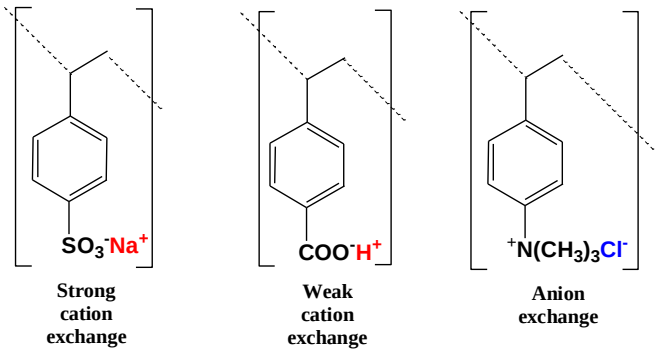

Fig. 2 Polystyrene cation and anion exchange resins

Advantages of this technique are metal selectivity, and high regeneration of the adsorbent materials. However, a serious drawback of ion-exchange resins is the production a large volumes of strong acids as consequence of the release of H^+, causing environmental problems due to acidification.

1.2.1.2 Filtration techniques

Alternatively, filtration techniques including reverse osmosis (RO) [46], nanofiltration [47], and ultrafiltration are used to remove pollutants from water.

Reverse osmosis (RO)

RO is a widespread membrane separation process used to remove metals from wastewater (Fig. 3) [48]. A common membrane material employed in RO is for example cellulose acetate, which is used for the separation of metallic ions. The RO process in the presence of the disodium salt of ethylene diamine tetraacetic acid as chelating agent for Cu(II) and Ni(II) removal have been carried out by Madoarres *et al*. Using the membrane RE2012-100, the authors of this study succeeded to increase the metal ion removal up to 99%. This high rejection percentage was explained by an increase of the coordination sphere around Cu(II) and Ni(II) by chelatation of the added agent EDTA around the metal ions and thereby blocking the solute to pass through the pores of the membrane used [49].

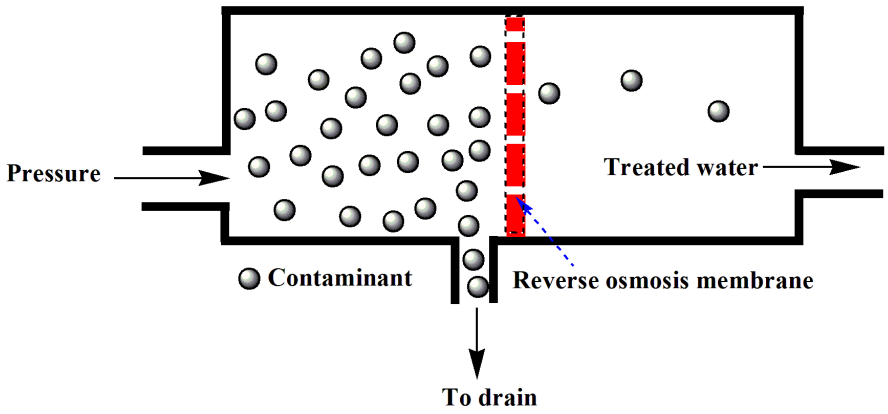

Fig. 3 Illustration of the reverse osmosis membrane process

Nanofiltration (NF)

NF is one another membrane filtration process, which is considered to be intermediate between ultrafiltration and reverse osmosis in terms of operating conditions. The nominal pore size of the membrane is typically about 1 nanometer. NF processes operate at pressures between 50 and 150 psi*, which is much lower than in RO (200 to 1000 psi), but higher than in UF (10 to 70 psi). For example, H. Saitua *et al* developed a Nanofiltration pilot plan to evaluate the efficiency and mechanism of arsenic removal from naturally contaminated groundwater [47]. A commercial NF-300 membrane (TFC polyamide), enclosed in an OSMO 19E-HR 500-ECN membrane housing, was used for this study. This negatively charged membrane with 1.5 m^2 active surface shows high rejection over 95% for arsenate ($HAsO_4^{2-}$) and quantitative rejection of SO_4^{2-} from naturally contaminated groundwater. This NF device was also used to reject divalent cations such as Ca(II) and Mg(II).

* 1 psi approximately equals 6,894.757 Pa

Ultrafiltration (UF)

The UF technique represents a variety of membrane filtration in which hydrostatic pressure forces a liquid against a semipermeable membrane. This separation technique allows the passage of water and low molecular weight molecules through the membrane, while macromolecules and suspended solids (basis of pore size 5-20 nm, and molecular weight of the compounds in the range of 1000-100,000 Da) cannot be permeated. The traditional UF shows therefore low efficiency for the removal of small contaminants from water.

However, the use of water-soluble metal-binding polymers in combination with UF is a hybrid approach to combine selectively and to recover also heavy metals. In the complexation-UF process cationic forms of heavy metals are first complexed by a macromolecular ligand in order to increase their molecular weight with a size larger than the pores of the selected membrane that can be retained whereas permeate water is then purified from the heavy metals (Fig. 4). In a recent study of Barakat and Schmidt, the polymer-enhanced ultrafiltration process has been investigated for removal of heavy metals such as Cu(II), Ni(II), and Cr(III) from synthetic wastewater solutions, using carboxy methyl cellulose as a water-soluble polymer and a polyethersulfone membrane with a 10000 Da cut-off. Maximum capacity of metals removal was obtained at pH ≤ 7 [50].

Another emerging modification is the Micellar-enhanced ultrafiltration (MEUF). Its advantage is to combine the high selectivity of RO and the high flux and the low-energy requirements involved in UF processes. The high removal efficiency can be rationalized by the effective trapping of solutes by the micelles. This separation technique is based on the addition of surfactants to the solution to be filtered. When surfactants are present in aqueous solutions above a certain concentration, i.e., the critical micelle concentration, aggregates are formed that may entrap a solute existing in the solution. The increased hydrodynamic size* of the solutes enables their rejection by polymeric UF membranes. The micellar solution is then passed through a UF membrane having pore sizes small enough to reject the micelles containing the attracted metal ions. The permeate side will consequently contain very low concentrations of unbound metal ions. MEUF has for example been used by De la Rubia *et al.* to eliminate of Cd(II), Cu(II), Ni(II), Pb(II), and Zn(II) from synthetic waste water. Sodium dodecyl sulfate (SDS) and linear alkylbenzene sulfonate (LAS) were use as anionic surfactant. This MEUF technique gave a high removal percentage (90%) for Cd(II), Cu(II), Pb(II), and Zn(II), except for Ni(II) [51].

In general, filtration technology may attain high efficiency for removing heavy metal ions, but limitations in its use are (i) the high operating cost, (ii) the problem of membrane fouling [52], and (iii) low permeate flux [53].

* The hydrodynamic size (or radius) is the effective radius of an ion in a solution measured by assuming that it is a body moving through the solution and resisted by the solution's viscosity. If the solvent is water, the hydrodynamic radius includes all the H_2O molecules attracted to the ion. As a result, it is possible for a small ion to have a larger hydrodynamic radius than a large ion – if it is surrounded by more solvent molecules.

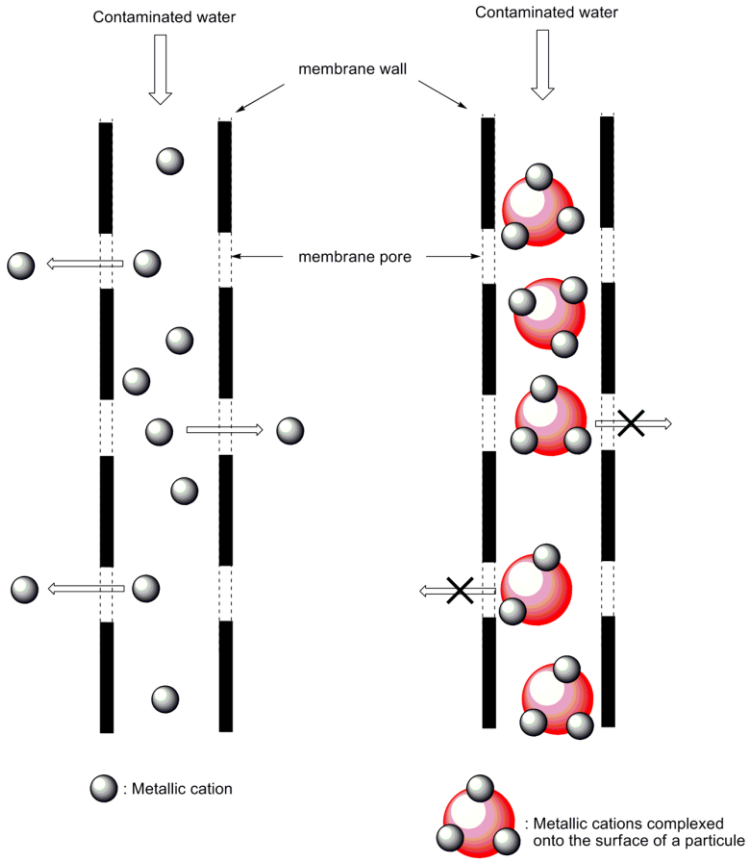

Fig. 4 Schematic representation of the principle of polymer-enhanced filtration

1.2.1.3 Chemical precipitation

The chemical precipitation [54] is widely used in the industrial sector to remove heavy metals because it is easy to operate. Metal precipitation from water consists in the conversion of soluble metal to an insoluble solid phase that can be precipitated. The precipitate then can be removed by filtration or clarification processes. Typically, the metal precipitate is in hydroxide form. Lime (CaO) is known to act as collector for the precipitation of Cu(II) in form of copper(II) hydroxides from aqueous solution [55]. The most important factor for precipitation is the control of the pH of the solution. The combination between Electro-

Fenton* treatment and chemical precipitation was used to remove Zn(II) from rayon industry wastewater [56]. About 99% of Zn(II) was removed in the range of pH 9-10 using lime as precipitant. Chemical precipitation of heavy metals from acid mine drainage was also achieved using the 1,3-benzenediamidoethanethiol dianion (BDET, known commercially as MetX), which selectively and irreversibly binds soft heavy metals from aqueous solution. In a study of Atwood *et al*., BDET was found to remove >90% of several problematic metals from acid mine drainage samples taken from abandoned coal mines [57]. The concentrations of metals such as iron may be reduced at pH 4.5 from 194 ppm to below 0.009 ppm. The major advantage of utilizing the low-cost organosulphur complexation ligand within the mines lays in the reduction of metal waste formed during current treatment methods. However, chemical precipitation requires in general a large amount of precipitants for removing metals. The water treatment often requires pH adjustment, and toxic sludge is generated from the process.

* The classical Fenton's reagent involves using ferrous sulfate and hydrogen peroxide as reagents to oxidize organic compounds, where the Fe(II) ion plays an active role in generating the strongly oxidizing radicals •OH radicals actually responsible for attacking the organic molecules. A modification of the classical Fenton process by electrochemical dissolution of Fe, supplying the Fe(II) ion to the reactions, is called electro-Fenton method.

1.2.1.4 Flotation

Flotation is employed to separate a liquid or a solid from a liquid phase using bubble attachment [58]. The colloid flotation process used for the precipitation of metal ions is based on imparting ionic metal species present in wastewater a hydrophobic character. The initially hydrophilic metal ions are converted to hydrophobic by interaction with a surfactant (surface active agent, also called “collector” in this context). Both stages, sorption and flotation, can operate in the same treatment device. When air bubbles are introduced in the second stage into a flotation cell, metal ion - surfactant assemblies are removed by the action of air bubbles (foaming phase) because of the favored interactions between the exposed hydrocarbon chains and the air bubbles (see Fig. 5). Anionic sodium dodecyl sulfate (SDS) and cationic hexadecyltrimethyl ammonium bromide (HTAB) were used as surfactants for precipitation of Cu(II), Zn(II), Cr(III), and Ag(I) from waste waters at low pH (74% removal). Under basic pH condition, even a 90% removal could be achieved [41].

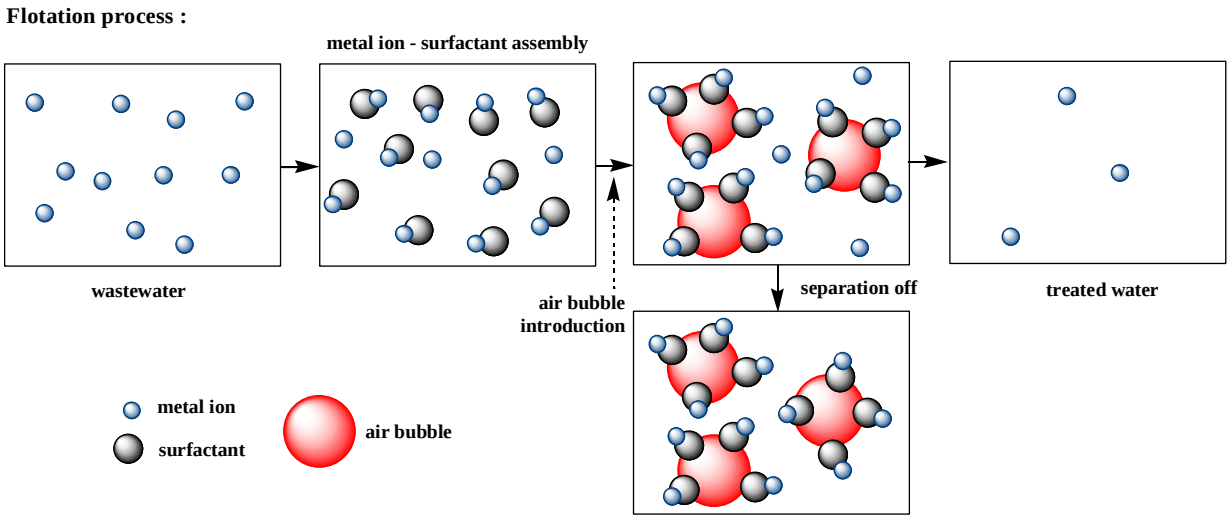

Fig. 5 Schematic representation of the sorptive flotation technique

1.2.1.5 Adsorption

Adsorption, a physico-chemical treatment process, is found to be an effective and economic method for removing heavy metals from aquatic system [59]. The adsorption process offers both ease in design and operation. Metal ions can be removed by adsorption on adsorbent materials. The principal materials used for adsorption of pollutants are activated carbon, zeolites, clay, etc.

Activated carbon (AC)

AC is an efficient adsorbent widely used for removal organic and inorganic pollutants from water because its high porosity and the enormous surface area per unit mass (300-1500 $m^2.g^{-1}$) [60-62]. AC is an efficient sorbent for Cr(III) (98%), Cr(VI), Pb(II) (98%), Cd(II) (92%), Hg(II) (80%) retention from wastewater [63-67]. AC can be divided in three types based on size and shapes: Powder Activated Carbon (PAC), Granular Activated Carbon (GAC), and Activated Carbon Fibers (ACF). For example, GAC was used as a packed bed in column for removal of Pb(II) [68]. ACF was prepared from the fibers of jute and coconut. Chemical activation by phosphoric acid is the most suitable process to produce fibrous activated carbon. The thus obtained materials have high porosity (S_{BET} up to 1500 m^2 g^{-1}). This ACF exhibits maximum adsorption capacities for phenol (181 mg/g) [69]. Modified activated coconut shell carbon was used to adsorb heavy metal from water. Coconut shell carbon was modified with chitosan and/or phosphoric acid. The chitosan-coated and acid-treated coconut shell carbon shows good results for Zn(II) ion removal from synthetic

industrial wastewater. Particle sizes of 1.0 nm and 1.25 nm exhibit the highest removal percentage [70]. However, drawbacks in the use of AC are the high costs (commercial activated carbon is more expensive compared to other adsorbents such as zeolites and plant products), and the fact that AC can in general not be regenerated and recycled after utilization (note that some types can be regenerated using acidic aqueous solution) [68].

Zeolites

These microporous materials consist of a mineral framework of tetrahedral aluminosilicates linked together by oxygen atoms. Zeolites have large pores (Fig. 6) and channels within their three-dimensional network and are commonly used as commercial adsorbents [71a].

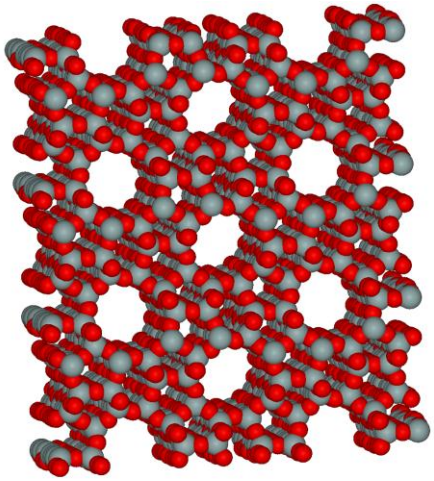

Fig. 6 The microporous molecular structure of the zeolite ZSM-5 [71b]

They show high effectiveness for the capture of metal ions such as Cu(II), Ni(II), Zn(II), Cd(II), Pb(II), and Cr(II). This is due to the fact that the Al(III) ion is small enough to occupy the position in the center of the tetrahedron of four oxygen atoms, and the isomorphous replacement of Si^{4+} by Al^{3+} produces a negative charge in the lattice. The net negative charge is balanced by the exchangeable monovalent cations Na^{+} and K^{+}. These cations are in solutions exchangeable with the above-cited heavy metal cations [72]. The naturally occurring mineral clinoptilolite is the most abundant zeolite in nature. It has been shown to have a high selectivity for certain heavy metals (Pb(II), Cd(II), Zn(II), and Cu(II)). Various types of zeolites are prepared from coal fly ash (CFA) as well as from a SiO_2-Al_2O_3 system. For example, Na-X, Na-A, zeolite-13X (Na-13X), zeolite Na-P1 (Na-P1), zeolite Y (Na-Y), sodalite, hydroxy-sodalite, phillipsite, K-chabazite, and Analcime were prepared using the sodium hydroxide fusion process and using different NaOH concentration. For

example, zeolite X (38.7% SiO_2 and 20.9% Al_2O_3) was used to remove Ni(II), Cd(II), Cu(II) and Pb(II) in bi-, tri- and tetra-metallic component systems using a batch method [73]. The zeolites A and X, prepared from kaolin, were used to remove divalent metal ions (Cd, Cu, Pb, Zn and Ni) from synthetic solutions. The optimum adsorption, using 0.8 g of each zeolite, reached to equilibrium after 30 min for Cd, Cu, Zn and Ni. But, the contact time reached to equilibrium up to 60 min for nickel adsorption [74]. A natural Bulgarian zeolite with a SiO_2 content of 68.7 wt% is reported to exhibit a copper removal of 89.3% at pH 5. Another study has demonstrated that also Y zeolite ion-exchangers containing the series Cs^+, Rb^+, Na^+ and Li^+ as alkali metal ions may retain copper and nickel ions, the exchange efficiency for copper being superior than the retention of Ni(II) under competitive conditions [75-78]. An important advantage of zeolites compared to activated carbon is the relative low price, but a limitation is their reactivity and slow degradation upon contact with an acidic aqueous environment.

Clay

Clay is another naturally occurring aluminosilicates. Basic types of clay are montmorillonite, kaolinite, and micas. Acid-modified clay presents porous structures, which offer the possibility to use them as sorbent to capture metal ions [79]. In a study of Vengris *et al.*, a clay stemming from a deposit in North Lithuania was activated by treatment with 20% HCl to increase porosity. This activated clay was used for removal of Cu(II), Ni(II), and Zn(II) from wastewater [80]. In another study, the surface of a montmorillonite-illite-type clay has been activated by an aqueous solution of H_2SO_4 to create new pores by replacing some cations (Al^{3+}, Ca^{2+}) by H^+ [81]. Although clay can like zeolites be considered as low-cost adsorbent, an inconvenient is the need of high temperature in the calcination process some times applied to improve its mechanical resistance and to eliminate some impurities [82].

1.2.2 Emerging new techniques

Despite the established techniques presented above, there is a need for new innovative and low-cost effective techniques for removing of metals from wastewater, in particular for countries in Asia and Africa. Biosorption is one of the promising technologies (emerging technique) for removing metals from water. Using biosorbents, their various advantages are low cost as biomaterials (considered as low-cost if it is requires little processing), their environment friendly features such as biodegradability and biocompatibility, easy availability (biomass), and minimization of chemical volume usage. Biosorbents can be obtained from

industrial waste materials (activated sludge biomass). In the past, our laboratory has participated in a study to use low-cost chemically modified starch-enriched flour stemming from paper industry to adsorb organic dyes [83].

Some biosorbents, like chitosan, alginate, plant products, etc., have also been used to capture metals in aqueous solution. Moreover, it appears very promising to develop further the use of biomaterials as biosorbent because of their effectiness and versatility to bind metal ions (the functional group on their structure can act as active site). The adsorption capacities of a given adsorbents depends on the characteristics of the adsorbent for each water pollutants and its concentration in water. Biosorbents bear functional groups on their backbone structure, which confers them the propensity to bind readily various metal ions [84]. Rice straw was used for removal of Cu(II), Zn(II), Cd(II) and Hg(II) ions from industrial wastewater [85]. Adsorption process reached the equilibrium before 1.5 h. Adsorption of metal ions on rice straw decreases in the order Cd(II) > Cu(II) > Zn(II) > Hg(II). Maximum adsorption values, at pH 5.0 at room temperature, were 0.128, 0.132, 0.133 and 0.110 $mmol.g^{-1}$ for Cu(II), Zn(II), Cd(II) and Hg(II), respectively. The adsorption capacity for removal of Pb(II) and Cd(II) on *Carica papaya seeds*, were 1667 mg/g and 1000 mg/g, respectively [86]. Cr(II) was removed using modified *Phanerochaete chrysosporium* (a fungal biomass). Modified *macrofungus Pleurotus platypus* (fruit bodies of Oyster mushrooms) was used for Cd(II) removal from industrial wastewater. The removal percentage was up to 68%, when the flow rate system was 5 mL/min. This packed bed column can be regenerate for three times recycles [87]. Numerous articles demonstrate that chitosan is a good biosorbent combining low-cost and high efficiency for the removal of heavy metal ions [88, 89]. Chitosan offers also other advantages such as being a high abundant and renewable resource, friendly to environment (biocompatibility, biodegradability) and last but not least ease of chemical modification. In this context, the use of this polysaccharide-biosorbent for the removal of Cu(II) and Ni(II) ions constitutes an import part of this PhD thesis and will be discussed in the following chapters.

In parallel to the use of biopolymers as adsorbents, another novel generation of adsorbents is emerging. The progress in the preparation and characterization of nanoparticles has also stimulated the utilization of these materials (magnetic nanoparticles such $MnFe_2O_4$, ferrite nanoparticles, carbon nanotube supported ceria, alumina−silica nanoparticles, TiO_2, ZrO_2, Fe_3O_4,..) for the removal of both inorganic an organic pollutants. The state of the art concerning water treatment by adsorption on nanoparticles has been reviewed in 2012 [90].

Even hybrid materials combining biosorbent and inorganic nanoparticles are known. One example are monodisperse chitosan-bound magnetic Fe_3O_4 nanoparticles (13.5 nm), which have been probed for the removal of Cu(II) [91].

Part 2 Aims of this Research Study

To realize my research project, this work has been supported by funding of a PhD grant allowing to start a cooperation between the University of Phayao and the group "Matériaux et Surfaces Structurés" within the Université de Franche-Comté on the preparation of novel low-cost and environmentally friendly composite materials. One goal was to prospective the possibility to use an industrial waste products for water treatment.

The objective of this research project focuses on the preparation of novel materials using silica-based particles as supporting polyelectrolyte. Silica was chosen as a supporting material because of its large surface area, low costs, high mass exchange characteristics, non-swelling and excellent mechanical resistance. Its surface can easily be modified by many reagents to improve the adsorption properties. In this research project, there are two strategies developed for the preparation of silica-based nano-composites to enhance the adsorption capacity for metal ions removal. The first one consists in coating silica particles with the biopolymer CS, the second one is functionalization of silica with surface-bound amine and/or carboxyl groups. Prior functionalization, silica was activated with acid solution to obtain more reactive silanol groups on its surface and subsequently the activated silica surface was then coated with chitosan and/or silanized with amino and/or carboxyl groups.

The manuscript is divided into four sections:

The first chapter focuses on silica particles. After a general information about nanoparticles and SiO_2, the surface chemistry of silica and its properties as colloidal silica particles in aqueous solution are represented. The silica surface was activated by treatment with acid solution in order to augment the number of surface silanol groups. The activated silica powders were characterized by various techniques such as FT-IR to detect the silanol groups on the silica surface; scanning electron microscope and atomic force microscopy were used to study the image of the composites, and the specific surface was determined using the

BET method. The behavior of silica in aqueous solution was studied by pH and conductivity measurements, zeta potential and hydrodynamic size measurements.

The second chapter describes the functionalization of silica-particles by amine and/or carboxyl groups under reflux conditions. These composites bear amine and/or carboxyl groups that can bind divalent metal ions. The functionalized composites were characterized by FT-IR to characterize the functional groups grafted on the silica surface, as well by the other techniques mentioned for chapter 1.

The third chapter deals on the biopolymer chitosan (CS) including the production process of CS, its intrinsic properties and advantages, the physicochemical properties, and the deacetylation degree (%DD) of CS. In order to obtain the adsorption capacity, functionalized CS with various organic reagents was evaluated. In this work, also the synthesis of carboxylic modified CS was undertaken. As in the precedent chapter, the prepared composite was characterized by FT-IR spectroscopy. To functionalize the silica surface by organic molecules, biopolymer used for coating the silica nano-materials to enhance its adsorption properties for metal ions removal. CS was chosen to functionalize the silica surface because the principal amino groups on its structure, which makes CS a promising biosorbent with excellent capacity to entrap heavy metal ions. The obtained materials were characterized by different techniques. Their properties in aqueous solution was measurement such as the stability in aqueous solution using pH, conductivity, zeta potential, and hydrodynamic particles size.

In the last chapter, the potential of the novel prepared composites for wastewater treatment is investigated. There are many pollutants found in water, but for this thesis we focused on divalent transition metal cations as model pollutant and Cu(II) and Ni(II) cations have been chosen. The composites evaluated as adsorbent for the capture of Cu(II) and Ni(II) are amine-functionalized silica, CS-coated silica, carboxyl-grafted silica, and carboxyl-grafted silica coated with CS. The most suitable pH for adsorption of these metal ions was determined and the effect of contact time for adsorption was probed. To study the adsorption isotherms, Langmuir, Freundlich, Temkin, BET, and Dubinin-Radushkevich models were applied. The adsorption kinetics were also studied by pseudo-first-order, pseudo-second-order, and intraparticle diffusion models. The plan of this research project is summarized in Fig. 7 to provide an outlook concerning the organization and structuration of this work.

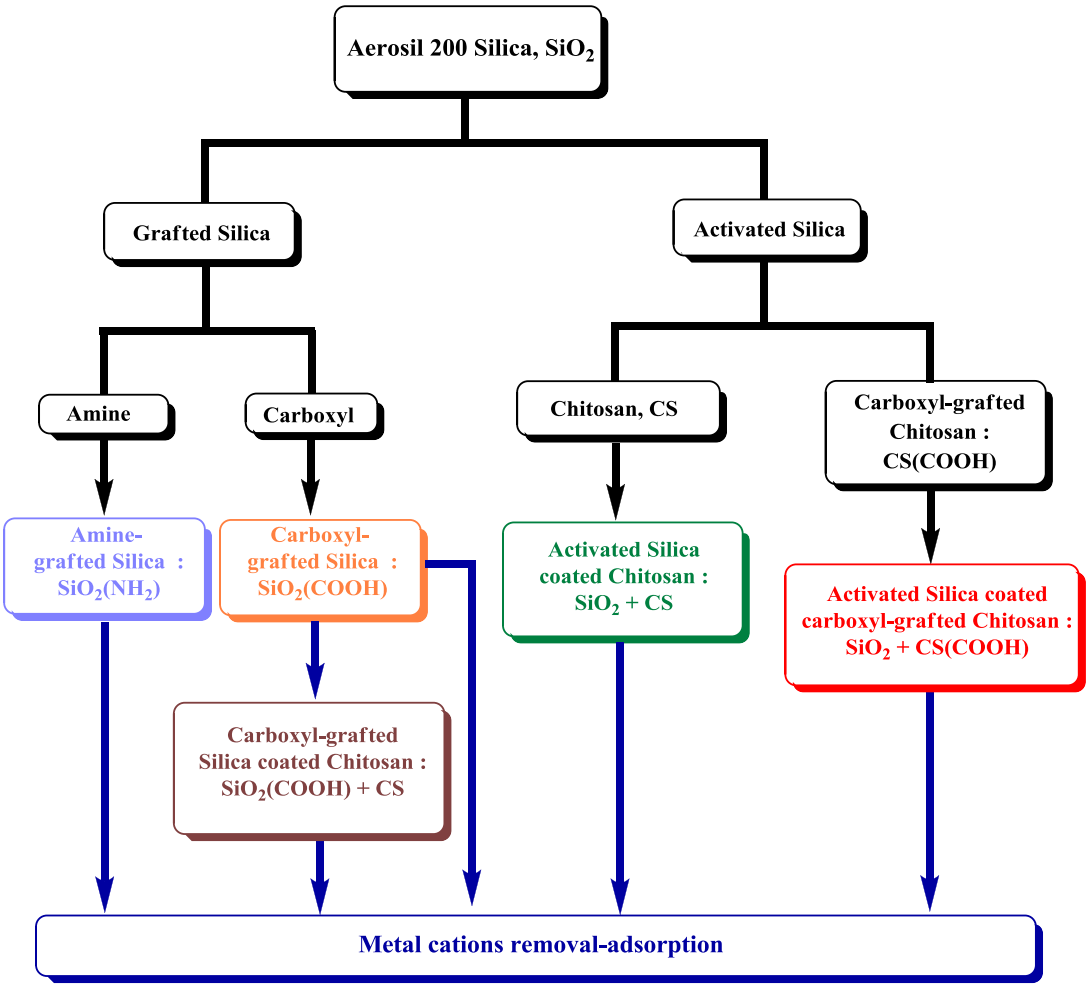

Fig. 7 Overview of the structuration of this PhD thesis

References

1. A. Dvorsk, G. Lammel, and I. Holoubek, *Recent trends of persistent organic pollutants in air in central Europe - Air monitoring in combination with air mass trajectory statistics as a tool to study the effectivity of regional chemical policy*, Atmos. Environ., 43 (2009) 1280-1287.
2. W. Yang, and S.T. Omaye, *Air pollutants, oxidative stress and human health*, Mutat. Res.-Gen. Tox. En., 674 (2009) 45-54.
3. P. Kongtip, W. Thongsuk, W. Yoosook, and S. Chantanakul, *Health effects of metropolitan traffic-related air pollutants on street vendors*, Atmos. Environ., 40 (2006) 7138-7145.
4. J. Fenger, *Air pollution in the last 50 years - From local to global*, Atmos. Environ., 43 (2009) 13-22.
5. R.W. Allen, O. Amram, A.J. Wheeler, and M. Brauer, *The transferability of NO and NO_2 land use regression models between cities and pollutants*, Atmos. Environ., 45 (2011) 369-378.
6. A. Guenther, C. Geron, T. Pierce, B. Lamb, P. Harley, and R. Fall, *Natural emissions of non-methane volatile organic compounds, carbon monoxide, and oxides of nitrogen from North America*, Atmos. Environ., 34 (2000) 2205-2230.

7. R. Brereton, S. Bennett, and I. Mansergh, *Enhanced greenhouse climate change and its potential effect on selected fauna of south-eastern Australia: A trend analysis*, Biol. Conserv., 72 (1995) 339-354.
8. B. Nordell, *Thermal pollution causes global warming*, Global Planet. Change, 38 (2003) 305-312.
9. E.G. Gregorich, P. Rochette, A.J. VandenBygaart, and D.A. Angers, *Greenhouse gas contributions of agricultural soils and potential mitigation practices in Eastern Canada*, Soil Till. Res., 83 (2005) 53-72.
10. S.-W. Nie, W.-S. Gao, Y.-Q. Chen, P. Sui, and A.E. Eneji, *Review of Current Status and Research Approaches to Nitrogen Pollution in Farmlands*, Agr. Sci. China, 8 (2009) 843-849.
11. J.A. Camargo, and A. Alonso, *Ecological and toxicological effects of inorganic nitrogen pollution in aquatic ecosystems: A global assessment*, Environ. Int., 32 (2006) 831-849.
12. S. Fields, *Global Nitrogen: Cycling out of Control*, Environ. Health Perspect., 112 (2004) 556-563.
13. B. He, S. Kanae, T. Oki, Y. Hirabayashi, Y. Yamashiki, and K. Takara, *Assessment of global nitrogen pollution in rivers using an integrated biogeochemical modeling framework*, Water Res., 45 (2011) 2573-2586.
18. P. Reopanichkul, R.W. Carter, S. Worachananant, and C.J. Crossland, *Wastewater discharge degrades coastal waters and reef communities in southern Thailand*, Mar. Environ. Res., 69 (2010) 287-296.
19. A. Azizullah, M.N. Khattak, P. Richter, and D.P. Häder, *Water pollution in Pakistan and its impact on public health-A review*, Environ. Int., 37 (2011) 479-497.
20. X. Xia, X. Chen, R. Liu, and H. Liu, *Heavy metals in urban soils with various types of land use in Beijing, China*, J. Hazard. Mater., 186 (2011) 2043-2050.
21. E.D. Ongley, Z. Xiaolan, and Y. Tao, *Current status of agricultural and rural non-point source Pollution assessment in China*, Environ. Pollut., 158 (2010) 1159-1168.
22. Y.-X. Xie, Z.-Q. Xiong, G.-X. Xing, G.-Q. Sun, and Z.-L. Zhu, *Assessment of Nitrogen Pollutant Sources in Surface Waters of Taihu Lake Region*, Pedosphere, 17 (2007) 200-208.
23. H.C. Co, and R. Boosarawongse, *Forecasting Thailand's rice export: Statistical techniques vs. artificial neural networks*, Comput. Indus. Eng., 53 (2007) 610-627.
24. A. Kumlanghan, P.A Kanatharana, P. Asawatreratanakul, B. Mattiasson, and P. Thavarungkul, *Microbial BOD sensor for monitoring treatment of wastewater from a rubber latex industry*, Enzyme Microb. Technol., 42 (2008) 483-491.
25. S. Prasertsan, and P. Prasertsan, *Biomass residues from palm oil mills in Thailand: An overview on quantity and potential usage*, Biomass Bioenergy, 11 (1996) 387-395.
26. A.A. Bordalo, W. Nilsumranchit, and K. Chalermwat, *Water quality and uses of the Bangpakong River (Eastern Thailand)*, Water Res., 35 (2001) 3635-3642.
27. T. Poolpak, P. Pokethitiyook, M. Kruatrachue, U. Arjarasirikoon, and N. Thanwaniwat, *Residue analysis of organochlorine pesticides in the Mae Klong river of Central Thailand*, J. Hazard. Mater., 156 (2008) 230-239.
28. T.K. Dalai, K. Nishimura, and Y. Nozaki, *Geochemistry of molybdenum in the Chao Phraya River estuary, Thailand: Role of suboxic diagenesis and porewater transport*, Chem. Geol., 218 (2005) 189-202.

29. K. Kruawal, F. Sacher, A. Werner, J. Müller, and T.P. Knepper, *Chemical water quality in Thailand and its impacts on the drinking water production in Thailand*, Sci. Total Environ., 340 (2005) 57-70.

30. V. Cheevaporn, and P. Menasveta, *Water pollution and habitat degradation in the Gulf of Thailand*, Mar. Pollut. Bull., 47 (2003) 43-51.

31. P. Censi, S.E. Spoto, F. Saiano, M. Sprovieri, S. Mazzola, G. Nardone, S.I. Di Geronimo, R. Punturo, and D. Ottonello, *Heavy metals in coastal water systems. A case study from the northwestern Gulf of Thailand*, Chemosphere, 64 (2006) 1167-1176.

32. A.W. Lothongkum, S. Suren, S. Chaturabul, N. Thamphiphit, and U. Pancharoen, *Simultaneous removal of arsenic and mercury from natural-gas-co-produced water from the Gulf of Thailand using synergistic extractant via HFSLM*, J. Membr. Sci., 369 (2011) 350-358.

33. P. Asnachinda, *Hydrogeochemistry of the Chiang Mai Basin, northernThailand*, J. Asian Earth Sci., 15 (1997) 317-326.

34. S. Nakwanit, P. Visoottiviseth, S. Khokiattiwong, and W. Sangchoom, *Management of arsenic-accumulated waste from constructed wetland treatment of mountain tap-water*, J. Hazard. Mater., 185 (2011) 1081-1085.

35. W. Chintakovid, P. Visoottiviseth, S. Khokiattiwong, and S. Lauengsuchonkul, *Potential of the hybrid marigolds for arsenic phytoremediation and income generation of remediators in Ron Phibun District, Thailand*, Chemosphere, 70 (2008) 1532-1537.

36. P. Visoottiviseth, K. Francesconi, and W. Sridokchan, *The potential of Thai indigenous plant species for the phytoremediation of arsenic contaminated land*, Environ. Pollut., 118 (2002) 453-461.

33. M.-B. Gilberto, A.Z.-C. Miguel, C.O. Adolfo, S.-C.R. Pedro, and S.-C.V. Pedro, *Lead concentrations in the blood of children from pottery-making families exposed to lead salts in a Mexican village*, Bull. Pan. Am. Health Organ., 17 (l983) 35-41.

34. J.L. Barringer, A. Mumford, L.Y. Young, P.A. Reilly, J.L. Bonin, and R. Rosman, *Pathways for arsenic from sediments to groundwater to streams: Biogeochemical processes in the Inner Coastal Plain, New Jersey, USA*, Water Res., 44 (2010) 5532-5544.

35. C.F. Harvey, K.N. Ashfaque, W. Yu, A.B.M. Badruzzaman, M.A. Ali, P.M. Oates, H.A. Michael, R.B. Neumann, R. Beckie, S.Islam, and M.F. Ahmed, *Groundwater dynamics and arsenic contamination in Bangladesh*, Chem. Geol., 228 (2006) 112-136.

36. C. Patinha, E.F. da Silva, and E.C. Fonseca, *Mobilisation of arsenic at the Talhadas old mining area-Central Portugal*, J. Geochem. Explor., 84 (2004) 167-180.

37. J.C. Ng, J. Wang, and A. Shraim, *A global health problem caused by arsenic from natural sources*, Chemosphere, 52 (2003) 1353-1359.

38. S. Tapio, and B. Grosche, *Arsenic in the aetiology of cancer*, Mutat. Res.-Rev. Mutat., 612 (2006) 215-246.

39. M. Witt, and T. Jickells, *Copper complexation in marine and terrestrial rain water*, Atmos. Environ., 39 (2005) 7657-7666.

40. E. Denkhaus, and K. Salnikow, *Nickel essentiality, toxicity, and carcinogenicity*, Crit. Rev. Oncol. Hemat., 42 (2002) 35-56.

41. H. Polat, and D. Erdogan, *Heavy metal removal from waste waters by ion flotation*, J. Hazard. Mater., 148 (2007) 267-273.

42. (a) N. Arnal, M.J.T. de Alaniz, and C.A. Marra, *Carnosine and neocuproine as neutralizing agents for copper overload-induced damages in cultured human cells*, Chem. Biol. Interact., 192 (2011) 257-263. (b) http://www.dwi.gov.uk

43. I.H. Lee, Y.-C. Kuan, and J.-M. Chern, *Equilibrium and kinetics of heavy metal ion exchange*, J. Chin. Inst. Chem. Eng., 38 (2007) 71-84.

44. A. Dabrowski, Z. Hubicki, P. Podkościelny, and E. Robens, *Selective removal of the heavy metal ions from waters and industrial wastewaters by ion-exchange method*, Chemosphere, 56 (2004) 91-106.

45. R. Vinodh, R. Padmavathi, and D. Sangeetha, *Separation of heavy metals from water samples using anion exchange polymers by adsorption process*, Desalination, 267 (2011) 267-276.

46. L. Malaeb, and G.M. Ayoub, *Reverse osmosis technology for water treatment: State of the art review*, Desalination, 267 (2011) 1-8.

47. H. Saitua, R.L. Gil, and A.P. Padilla, *Experimental investigation on arsenic removal with a nanofiltration pilot plant from naturally contaminated groundwater*, Desalination, 274 (2011) 1-6.

48. V.V. Goncharuk, D.D. Kucheruk, V.M. Kochkodan, and V.P. Badekha, *Removal of organic substances from aqueous solutions by reagent enhanced reverse osmosis*, Desalination, 143 (2002) 45-51.

49. M. Mohsen-Nia, P. Montazeri, and H. Modarress, *Removal of Cu^{2+} and Ni^{2+} from wastewater with a chelating agent and reverse osmosis processes*, Desalination, 217 (2007) 276-281.

50. M.A. Barakat, and E. Schmidt, *Polymer-enhanced ultrafiltration process for heavy metals removal from industrial wastewater*, Desalination, 256 (2010) 90-93.

51. E. Samper, M. Rodriuguez, M.A. De la Rubia, and D. Prats, *Removal of metal ions at low concentration by micellar-enhanced ultrafiltration (MEUF) using sodium dodecyl sulfate (SDS) and linear alkylbenzene sulfonate (LAS)*, Sep. Purif. Technol., 65 (2009) 337-342.

52. M. Palencia, B.L. Rivas, and E. Pereira, *Metal ion recovery by polymer-enhanced ultrafiltration using poly(vinyl sulfonic acid): Fouling description and membrane-metal ion interaction*, J. Membr. Sci., 345 (2009) 191-200.

53. A. Caetano, M.N. De Pinho, E. Drioli, and H. Muntau, *Membrane technology: Applications to industrial wastewater treatment*, Kluwer Academic Publishers, (1995) 65.

54. M. Mohapatra, K. Rout, P. Singh, S. Anand, S. Layek, H.C. Verma, and B.K. Mishra, *Fluoride adsorption studies on mixed-phase nano iron oxides prepared by surfactant mediation-precipitation technique*, J. Hazard. Materi., 186 (2011) 1751-1757.

55. K.A. Baltpurvins, R.C. Burns, and G.A. Lawrance, *Heavy metals in wastewater: Modelling the hydroxide precipitation of copper(II) from wastewater using lime as the precipitant*, Waste Manage., 16 (1996) 717-725.

56. P. Ghosh, A.N. Samanta, and S. Ray, *Reduction of COD and removal of Zn^{2+} from rayon industry wastewater by combined electro-Fenton treatment and chemical precipitation*, Desalination, 266 (2011) 213-217.

57. M.M. Matlock, B.S. Howerton, and D.A. Atwood, *Chemical precipitation of heavy metals from acid mine drainage*, Water Res., 36 (2002) 4757-4764.

58. A.I Zouboulis, K.A Matis, N.K Lazaridis, and P.N Golyshin, *The use of biosurfactants in flotation: application for the removal of metal ions*, Miner. Eng., 16 (2003) 1231-1236.

59. A. Bhatnagar, and M. Sillanpää, *Utilization of agro-industrial and municipal waste materials as potential adsorbents for water treatment-A review*, Chem. Eng. J., 157 (2010) 277-296.

60. H. Modin, K.M. Persson, A. Andersson, and M. van Praagh, *Removal of metals from landfill leachate by sorption to activated carbon, bone meal and iron fines*, J. Hazard. Mater., 189 (2011) 749-754.

61. C. Faur-Brasquet, K. Kadirvelu, and P. Le Cloirec, *Removal of metal ions from aqueous solution by adsorption onto activated carbon cloths: adsorption competition with organic matter*, Carbon, 40 (2002) 2387-2392.

62. Y. Suzuki, K. Mochidzuki, Y. Takeuchi, Y. Yagishita, T. Fukuda, H. Amakusa, and H. Abe, *Biological activated carbon treatment of effluent water from wastewater treatment processes of plating industries*, Sep. Technol., 6 (1996) 147-153.

63. K. Muthukumaran, and S. Beulah, *Removal of Chromium (VI) from wastewater using chemically activated Syzygium jambolanum nut carbon by batch studies*, Procedia Environ. Sci., 4 (2011) 266-280.

64. N.F. Fahim, B.N. Barsoum, A.E. Eid, and M.S. Khalil, *Removal of chromium(III) from tannery wastewater using activated carbon from sugar industrial waste*, J. Hazard. Mater., 136 (2006) 303-309.

65. J. Acharya, J.N. Sahu, C.R. Mohanty, and B.C. Meikap, *Studies on the removal of Pb(II) from wastewater by activated carbon developed from Tamarind wood activated with sulphuric acid*, J. Hazard. Mater., 153 (2008) 221-228.

66. A.F. Tajar, T. Kaghazchi, and M. Soleimani, *Adsorption of cadmium from aqueous solutions on sulfurized activated carbon prepared from nut shells*, J. Hazard. Mater., 165 (2009) 1159-1164.

67. F.-S. Zhang, J.O. Nriagu, and H. Itoh, *Mercury removal from water using activated carbons derived from organic sewage sludge*, Water Res., 39 (2005) 389-395.

68. C.P. Dwivedi, J.N. Sahu, C.R. Mohanty, B.R. Mohan, and B.C. Meikap, *Column performance of granular activated carbon packed bed for Pb(II) removal*, J. Hazard. Mater., 156 (2008) 596-603.

69. N.H. Phan, S. Rio, C. Faur, L. Le Coq, P. Le Cloirec, and T.H. Nguyen, *Production of fibrous activated carbons from natural cellulose (jute, coconut) fibers for water treatment applications*, Carbon, 44 (2006) 2569-2577.

70. O.S. Amuda, A.A. Giwa, and I.A. Bello, *Removal of heavy metal from industrial wastewater using modified activated coconut shell carbon*, Biochem. Eng. J., 36 (2007) 174-181.

71. (a) Y. Sugi, H. Maekawa, Y. Hasegawa, A. Ito, R. Asai, D. Yamamoto, K. Komura, Y. Kubota, J.H. Kim, and G. Seo, *The alkylation of biphenyl over three-dimensional large pore zeolites: The influence of zeolite structure and alkylating agent on the selectivity for 4,4'-dialkylbiphenyl*, Catal. Today, 131 (2008) 413-422. (b) http://en.wikipedia.org/wiki/Zeolite.

72. F. RamoaRibeiro, F. Alvarez, C. Henriques, F. Lemos, J.M. Lopes, and M.F. Ribeiro, *Structure-activity relationship in zeolites*, J. Mol. Catal. A: Chem., 96 (1995) 245-270.

73. V.K. Jha, M. Nagae, M. Matsuda, and M. Miyake , *Zeolite formation from coal fly ash and heavy metal ion removal characteristics of thus-obtained Zeolite X in multi-metal systems*, J. Environ. Manage., 90 (2009) 2507-2514.

74. T.S. Jamil, H.S. Ibrahim, I.H. Abd El-Maksoud, and S.T. El-Wakeel, *Application of zeolite prepared from Egyptian kaolin for removal of heavy metals: I. Optimum conditions*, Desalination. 258 (2010) 34-40.

75. E. Erdem, N. Karapinar, and R. Donat, *The removal of heavy metal cations by natural zeolites*, J. Colloid Interface Sci., 280 (2004) 309-314.

76. F. Ruggieri, V. Marín, D. Gimeno, J.L. Fernandez-Turiel, M. García-Valles, and L. Gutierrez, *Application of zeolitic volcanic rocks for arsenic removal from water*, Eng. Geol., 101 (2008) 245-250.

77. M.I. Panayotova, *Kinetics and thermodynamics of copper ions removal from wastewater by use of zeolite*, Waste Management, 21 (2001) 671-676.

78. M.A. Keane, *The removal of copper and nickel from aqueous solution using Y zeolite ion exchangers*, Colloids Surf., A, 138 (1998) 11-20.

79. S. Sato, K. Yoshihara, K. Moriyama, M. Machida, and H. Tatsumoto, *Influence of activated carbon surface acidity on adsorption of heavy metal ions and aromatics from aqueous solution*, Appl. Surf. Sci., 253 (2007) 8554-8559.

80. T. Vengris, R. Binkiene, and A. Sveikauskaite, *Nickel, copper and zinc removal from waste water by a modified clay sorbent*, Appl. Clay Sci., 18 (2001) 183-190.

81. J.U.K. Oubagaranadin, Z.V.P. Murthy, and V.P. Mallapur, *Removal of Cu(II) and Zn(II) from industrial wastewater by acid-activated montmorillonite-illite type of clay*, C. R. Chim., 13 (2010) 1359-1363.

82. M.G. Vieira, A.F. Neto, M.L. Gimenes, and M.G. da Silva, *Sorption kinetics and equilibrium for the removal of nickel ions from aqueous phase on calcined Bofe bentonite clay*, J. Hazard. Mater., 177 (2010) 362-371.

83. F. Delval, G. Crini, J. Vebrel, M. Knorr, E. Conte, and G. Sauvin, *Starch-modified filters used for the removal of dyes from waste water*, Macromol. Symp. 203 (2003) 165-171.

84. L. Fuks, D. Filipiuk, and M. Majdan, *Transition metal complexes with alginate biosorbent*, J. Mol. Struct., 792 (2006) 104-109.

85. C.G. Rocha, D.A.M. Zaia, R.V. da Silva Alfaya, and A.A. da Silva Alfaya , *Use of rice straw as biosorbent for removal of Cu(II), Zn(II), Cd(II) and Hg(II) ions in industrial effluents*, J. Hazard. Mater., 166 (2009) 383-388.

86. U.A. Gilbert, I.U. Emmanuel, A.A. Adebanjo, and G.A. Olalere, *Biosorptive removal of Pb^{2+} and Cd^{2+} onto novel biosorbent: Defatted Carica papaya seeds*, Biomass Bioenergy. 35 (2011) 2517-2525.

87. R. Vimala, D. Charumathi, and N. Das, *Packed bed column studies on Cd(II) removal from industrial wastewater by macrofungus Pleurotus platypus*, Desalination, 275 (2011) 291-296.

88. W.S. Wan Ngah, L.C. Teong, and M.A.K.M. Hanafiah, *Adsorption of dyes and heavy metal ions by chitosan composites: A review*, Carbohydr. Polym., 83 (2011) 1446-1456.

89. S. Babel, and T.A. Kurniawan, *Low-cost adsorbents for heavy metals uptake from contaminated wa a review*, J. Hazard. Mater., 97 (2003) 219-243.

90. I. Ali, *New Generation Adsorbents for Water Treatment*, Chem. Rev. 112 (2012) 5073-5091.

91. Y.-C. Chang, and D.-H. Chen, *Preparation and adsorption properties of monodisperse chitosan-bound Fe3O4 magnetic nanoparticles for removal of Cu(II) ions*, J. Coll. Interface Sci. 283 (2005) 446-451.

Chapter 1

Properties and Chemical Reactivity of Silica, SiO_2

Introduction

1.1 Nanomaterials

The use of nanoparticles as adsorbents has been mentioned in section 1.2.2 of the preceding chapter. A brief general definition of the term "nanomaterials" seems therefore appropriate. Nanomaterials can be defined as functional objects where one or more components are seized in the nanoscale (1-100 nm), as shown in Fig. 8. Their shape and morphology can be made visible using techniques like Scanning Electron Microscopy or Atomic Force Microscopy, etc. They are fabricated from metals, polymers, ceramics, glasses or molecular precursors using the so-called *top-down* or *bottom-up* strategies.*

- The *top-down* approach often uses the traditional workshop or microfabrication methods where externally-controlled tools are used to cut, mill, and shape materials into the desired shape and order.

- *Bottom-up* approaches, in contrast, use the chemical properties of single molecules to cause single-molecule components to (a) self-organize or self-assemble into some useful conformation, or (b) rely on positional assembly. These approaches utilize the concepts of molecular self-assembly and/or molecular recognition, which also used in our laboratory to self-assemble for example luminescent 1D molecular wires (see below).

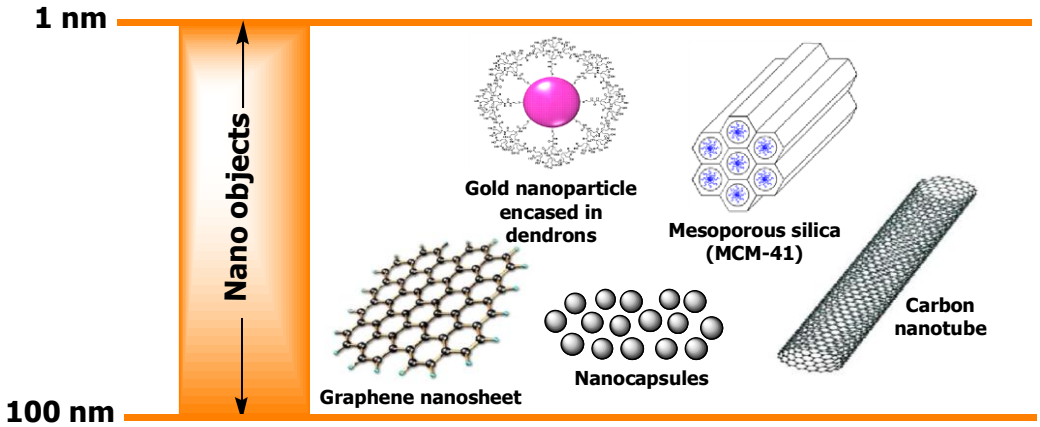

Fig. 8 The particle nano-scale

*The famous quotation "*There's Plenty of Room at the Bottom*" stems from the Nobel Prize winner and pioneer of nanotechnology, Richard Feynman, who quoted this phrase in 1959.

One of the different possibilities to classify nanomaterials or nanostructures is a classification according their dimensionality. As shown in Fig. 9, dimensional classifications are zero-dimensional (0-D): the nanostructure has all dimensions in the nanometer scale (nanoparticles), one-dimensional (1-D): one dimension of the nanostructure is outside the nanometer scale (nanorods, nanotubes, nanowires), two-dimensional (2-D): two dimensions of the nanostructure are outside the nanometer scale (thin film multilayers), and three-dimensional (3-D): three dimension of the nanostructure are outside the nanometer scale (bulk materials), respectively [1].

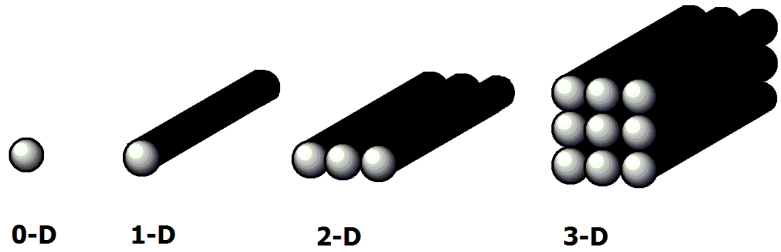

Fig. 9 Dimensionality of nanomaterial

According to a targeted application, different shapes of nanomaterials can be tailor-made fabricated. For example, cobalt-iron cyanide hollow cubes with interesting magnetic properties have been assembled by hydrothermal synthesis in the presence of poly(vinyl)pyrrolidone [2]. Amine-terminated functionalized silica nanospheres have been developed as biosensors for glucose detection [3] or gold nanoparticle embedded silicon nanowires were used as biosensor to enhance the sensitivity for label-free DNA detection [4]. In the domain of heterogeneous catalysis, cage-like nanostructured NiO-silica composite particle have been designed and probed as catalysts for the oxidation of organic pollutants [5].

Since the discovery of fullerenes and related carbon-based nanomaterials [6], the chemistry and physics of carbon nanotubes (CNT), which can be considered as a monodimensional variation, has known a tremendous growth. Some selected applications include their use in devices for fuel cell (hydrogen storage) or solar cell [7-10]. The concept to use single-walled carbon nanotubes coated with MgH_2 for hydrogen storage has been investigated both from a theoretical point of view and experimentally [11]. The use of CNT as sensors and actuators has recently been reviewed [12]. Also at the Université of Franche-Comté, some research groups work on applications of CNT in pharmaceutical sciences or on their experimental development and theoretical modeling as chemosensors [13]. In this context, single-walled carbon nanotubes and the interaction energy in the presence of amino acids inside and outside the CNT have been studied. It was found that outside adsorption provides a better detection

performance than inside adsorption. Theoretical calculations suggest the possibility to use carbon nanotubes as nanocapsules to transport molecule without chemical modification [14, 15]. Graphene, a 2-D form of carbon-based nanomaterial is currently a very hot topic after awarding the physics Nobel Prize in 2010 to two Russian researchers (K. Novoselov and A. Geim) for their import contribution on the preparation and understanding of this promising carbon allotrope. For example, graphene has proven is usefulness as biosensor for the detection of glucose, hemoglobin, or cholesterol, etc [16]. Bilayer graphene sheets (BLGS) are currently receiving increasing attention because of their unique vibrational properties and large stiffness. These properties of BLGS make them suitable candidates for manufacturing nanosensors; electromechanical resonators, and nanodevices [17].

Inorganic nano-multilayers of composition CrAlN/AlON have been obtained by sputtering techniques using under N_2 atmosphere Cr-Al alloys and Al_2O_3 as precursors. The mixed metal-nitride-oxide layers were probed as hard protective coatings because of their high hardness, good wear and high corrosion/oxidation resistance at elevated temperatures (900 $^{\circ}$C) [18]. Organometallic molecular rods like the depicted nano-sized ferrocenyl compound have been engineered using classical organic synthesis with the aim to use them as conducting materials for molecular electronics (Fig.10).

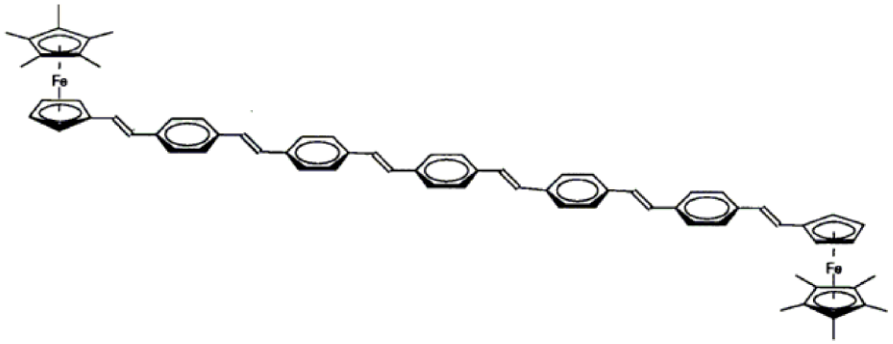

Fig. 10 Example of a molecular nanowire, the separation between the two ferrocenyl extremities being about 4 nm [19].

The famous spherical fullerenes obtained by soot extraction with toluene can now be prepared even in multi-gram scale. This opened the possibility for molecular chemists to further functionalize these fascinating objects by attaching covalently organic groups or metal complexes on the surface of these C_{60}-C_{84} objects [20, 21]. Other nano-sized spherical objects obtained using the toolbox of molecular chemistry is the so-called dendrimers. These star-shaped molecules formed by successive chemical assembly of several layers (called generations) found applications for drug delivery, catalysis and as sensors [22]. Finally, also

the synthesis of metallic nanoparticles can be achieved by controlled decomposition of molecular precursor complexes. Several techniques were used for the characterization of the obtained nanoparticles (approximately 2.5 nm) that organize into spherical or elongated superstructures of 45 nm made of small individual nanoparticles [23]. Some typical structural motifs and shapes of current nanomaterials are represented in Fig. 11.

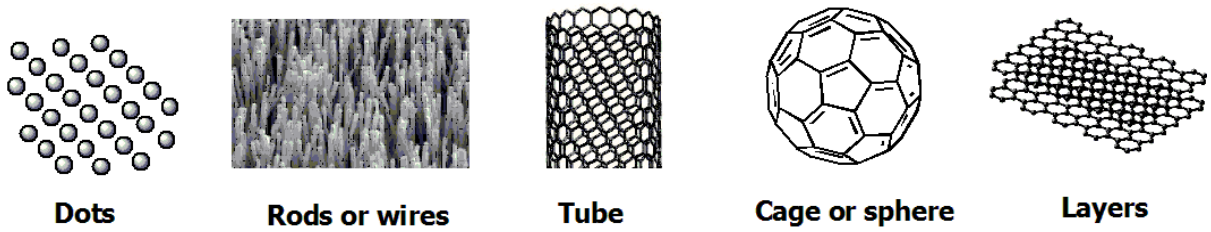

Fig. 11 Illustration of the shape of some nanomaterial in form of dots, rods, tubes, cages and layers.

1.2 Quantum effect

The special nature of nanoclusters (particles of any kind with a size too small to exhibit characteristic bulk properties), is due to a quantum confinement of electrons which leads to a change of relevant properties of a nano-sized material compared to a bulk material. G. Schmid and co-workers propose an explication of the transition from a bulk material to a nano-sized material as depicted in Fig. 12 [24].

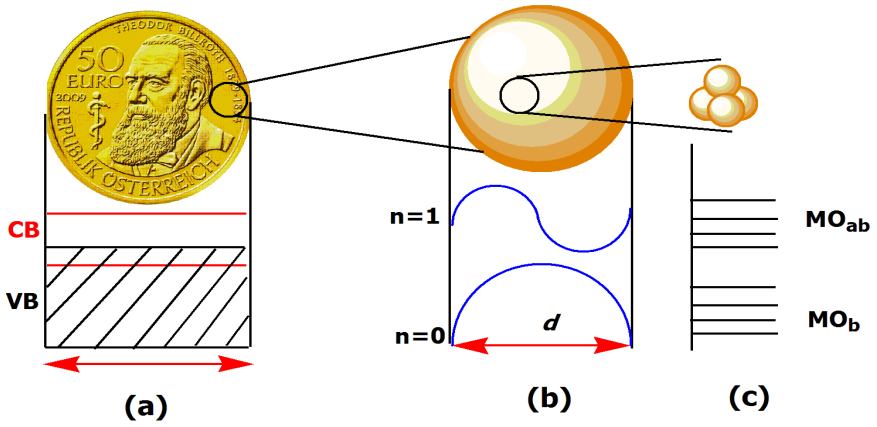

Fig. 12 The transition of a bulk metal via a nanocluster to a molecule

The electronic situation of metal atoms represented in Fig. 12**a** can be described a quasi-delocalized electronic state of overlapping valence (VB) and conductivity bands (CB). The situation of particles where the diameter (*d*) corresponds to $\lambda/2$ (λ = de Broglie wavelength) in the ground state is shown in Fig. 12**b**. Fig. 12**c** shows bonding (MO_b) and

antibonding (MO_{ab}) molecular orbitals of localized bonds between few atoms in a molecular cluster [24].

As already stated, nanoscale dimensions confer nano-objcets special properties compared to bulk objects of the same materials due to quantum confinement effects. For example, the size of the particles has an influence on the wavelength of their absorbance and light emission. The size quantization effect in a series of a given material of various nanosizes may give cause different colours. For example, ZnS-capped CdSe semiconductor nanoparticles (quantum dots) with a diameter of 2 nm give rise to a blue-shifted emission, but having a diameter of 6 nm, they emit with a red-shift (see Fig. 13). The size is inversely related to the band gap energy (dictating the fluorescence emission) of the nanoparticles [25, 26]. The same quantum confinement effect is observed for the photoluminescence (PL) of silicon quantum dots. The PL maximum is shifted to higher energy when decreasing the size of silicon quantum dots (Si QD). The average diameter of Si QD embedded in silicon nitride films showing PL peak energies of 1.7, 2.25, 2.5, and 2.77 eV was 4.9, 3.7, 3.2, and 2.9 nm, respectively. This phenomenon can be rationalized by an increase of the band gap energy when decreasing the size of Si QD [27]. The PL appearance in porous silicon is also attributed to quantum confinement effects [28].

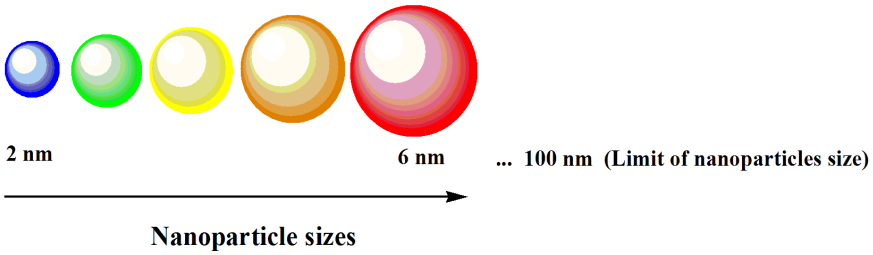

Fig. 13 The size quantization effect of optical property of nanoparticles

The preparation and application of nanomaterials makes also part of the research activity of our Institute UTINAM, where this acronym stand for **U**nivers**, T**ransport**, I**nterfaces**, N**anostructures**, A**tmosphère et environnement, **M**olécules. The "**N**anostructures part" of this acronym includes research on silica nanostructures and silica nanoparticles, carbon nanotubes, gold nanoparticles, molecular rods etc. For example, deposition of thin silica films on silicon wafer (100 nm diameter) using the sol-gel method was studied. To investigate the initial stages of sol-gel thin film formation, effects of sol parameters on the deposition and aggregation of silica nanoparticles were analysed [29]. The behaviour of a single ammonia molecule encapsulated in C_{60} fullerene nano-cage has also been studied to

understand how the fullerene modifies the spectral signature of a NH_3 molecule in vibration-inversion mode called umbrella. This work shows that simulation of the spectra of ammonia can be used to probe the temperature of the surrounding media in which fullerene is observed [30]. Our team has investigated the electrodeposition of latex particles (50 nm diameter) on functionalized polythiophene films obtained by electropolymerisation. Three-dimensional structures of the polythiophene derivatives could be evidenced by AFM. This deposition on the film offers promising possibilities for surface functionalization and selective latex particles adhesion [31]. The retention of Cu(II) and Ni(II) complexes chelated with polyaminocarboxylates in the presence of polyethyleneimine (PEI) or chitosan, assisted by ultrafiltration, was also investigated in our laboratory. Metal retention with PEI of 98% in the pH range of 4-9 was obtained [32]. Adsorption of the polymer poly(vinylimidazole) onto an Aerosil 200 silica surface at pH 3, 5, and 7 was studied in our group. It has been shown that the adsorption decreases with increasing the pH of the solution and with increasing in NaCl concentration, demonstrating that the amount of the adsorbed polymer strongly depends on pH and ionic strength. The uptake of basic imidazole by acidic silica is strongly due to electrostatic interaction [33]. Moreover, the coagulation of monodispersed silica (around 15 nm diameter) in the presence of Ca(II) ions was studied. The adsorption is pH dependent. It was found that, one Ca(II) ion adsorbed releases one H^+ from the silica surface. During the coagulation, shrinkage of the silica nanoparticles to 6 nm occurred giving an aggregation of strongly linked particles, as evidenced by X-ray scattering technique [34]. Another paper of our group deals on the behaviour of silica nanoparticles suspended in aqueous solution, which aggregates after addition of Al_{13}. Then osmotic stress was applied to the system in order to extract water and to obtain a smaller particles volume. It was found that the system shows different aggregation behaviours under acidic (pH 5) and basic (pH 9) conditions. In the latter case, the reaction was much faster than under acidic condition and the dispersion contained both aggregated and non-aggregated particles, depending on the concentration of Al_{13} [35].

These are just some few selected examples to give an overview about the properties and applications of various nanomaterials, which may help to overcome some intrinsic limitations of bulk materials. Since our research group has acquired some experience in the past on the preparation and physicochemical properties of silica, we have chosen to use silica-based nanomaterials and composites in this present PhD work for the retention of pollutants from model wastewater solution. To facilitate the understanding for this choice, some information on the physical and chemical properties of SiO_2 are presented. Furthermore,

synthesis and characterization techniques for this versatile inorganic compound are detailed in the following section.

1.3 Silicon (Si) and silicon oxide (SiO)

In Earth's crust, silicon is the second most abundant element with oxygen, and constitutes 27.7% of mass of the crust. Elemental silicon plays an import role in solid-state physics as well as constituent in inorganic and organic silicon chemistry [36, 37]. The reactivity of silicon depends on the particle size. Silicon nanoparticles (SiNPs) are silicon nanomaterials with crystalline structure with an average size around 1 to 10 nm. They are also referred to silicon nanodots, silicon quantum dots, nanocrystalline silicon, and silicon nanoclusters. Silicon nanowires (SiNWs) are 1D silicon crystalline nanomaterials with cross-sectional diameter of less than about 100 nm and are used in electronic devices. Silicon nanoribbons or silicon nanomembranes are 2D silicon crystalline nanomaterials with a thickness < 100 nm. Porous silicon is generated by etching crystalline silicon wafers in aqueous solution containing HF; electrochemical etching, anodization under galvanostatic conditions. Porous silicon is also produced by light-simulated etching of crystalline silicon in HF without electrodes or electrochemical etching [37]. Silicon in form of silicon thin film is fabricated by Vapor Deposition and thermal processing and employed in photocopy systems, X-ray detectors and photovoltaic solar cells. Silicon nanocrystallites embedded in a silicon oxide matrix shows electrical interesting and optoelectronic properties [36- 38].

In the universe, the reaction of silicon with O_2 mainly leads to gaseous SiO and small amounts of SiO_2. Gaseous SiO is obtained from the condensation of Si and O_2 at high-temperature between 1250-1400 ^{o}C as shown in equation (1) [36].

$$Si(g) + 1/2\ O_2(g) \rightleftharpoons SiO(g) \qquad (1)$$

However, solid SiO does not exist naturally on Earth. Solid SiO was first prepared in 1995 by Potter by reduction of SiO_2 with C, Si or SiC [36]. SiO is always present whenever silica or silicates are reduced at high temperatures such as in carbothermal reduction of SiO_2 to produce silicon carbide SiC. In this context, silicon or SiO_x particles is also related to solid SiO. It is used as a vapour-deposition material in the fabrication of SiO_x thin film for optical or electronic applications [38, 39].

1.4 Silica (SiO_2)

Silica, also known as silicon dioxide, is the second, thermodynamically more stable oxide, commonly found in nature. Sand and quartz are the two most common forms of SiO_2. The tetrahedral $[SiO_4]^{4-}$ building blocks can be joined together by two or four oxygen corners. The tetrahedral coordination of the oxygen ions around the silicon atom is shown in Fig. 14.

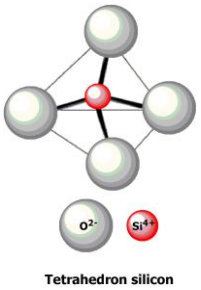

Fig. 14 The tetrahedral coordination skeleton of the Si atom surrounded by 4 oxygen atoms, found for example in amorphous silica (Adaped from A. M. Coclite, 2010 [40])

As already mentioned in the introduction, another naturally occurring inorganic material incorporating three-dimensional frameworks of tetrahedral SiO_4 and AlO_4 units are zeolites, having the composition $M_{x/n}[(AlO_2)x(SiO_2)y]$. zH_2O, where M is an extra-framework alkali or alkaline earth cations (Li^+, Na^+, K^+, Ca^{2+}, Sr^{2+},…) [41, 42]. Natural zeolite, clinoptilolite (Fig. 6) is one of the most common found in sedimentary rocks, the formula is $(Na, K)_6Si_{30}A_{l6}O_{72} \cdot nH_2O$ [43]. There are about 800 different zeolites, which can be classified by 119 different zeolite structure types [42]. The zeolite ZSM-5 has been used as heterogeneous catalyst for direct NO*x* decomposition [44], the utility of these porous compounds as adsorbents has already been outlined in the General Introduction.

Synthetic silica is known to exist in both in form of microparticles and nanoparticles. After chemical modification, the latter may be subdivided as shown in Fig. 15. For example, colloidal nanocomposite particles of polymer-silica composites with different silica content represent different morphologies determined by transmission electron microscopy (TEM), or small angle X-ray scattering (SAXS), X-ray photoelectron spectroscopy (XPS), etc. Polypyrrole-silica nanocomposite can adopt a raspberry morphology (Fig. 15**a**) [45], but exist also in a variation possessing a SiO_2 core coated with a polypyrrole-shell allowing to use them as capsules (Fig.15**c**) [46]. Another core-shell structure in which the silica core is surrounded by a layer of alkylammonium ions together with solvent was elaborated by synthesis of SiO_2 nanoparticles from hydrolysis and condensation of $Si(OEt)_4$ in aqueous tetrahydrofuran solution in the presence of different long-chained primary amines [46, 47].

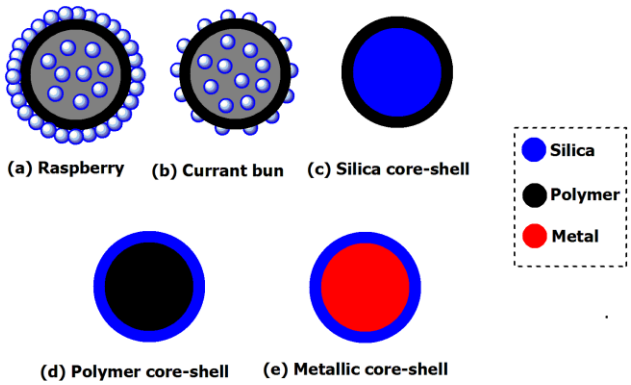

Fig. 15 Morphologies of colloidal polymer-silica nanocomposites

Poly(4-vinylpyridine)-silica nanocomposites (150-170 nm) containing 34-38 wt% of silica content have a so-called « currant-bun » morphology (Fig. 15**b**). Poly(methylmethacrylate) (PMMA)-silica nanocomposites (180 nm & 600 nm containing 15 to 60 wt% of SiO_2), have a silica core coated by a PMMA-shell (Fig. 15**c**), and polystyrene-silica nanoparticles with a mean diameter between 330-460 nm containing 13 to 26 wt% SiO_2 exhibit a polymer core coated by silica-shell (see Fig. 15**d**). Coating of Rhodium nanoparticles (obtained by reduction of Rh(III) with hydrazine) with silica is also represented as shown Fig. 15**e**. This metallic core-silica shell architecture was obtained by subsequent hydrolysis of tetraethyl orthosilicate [48]. A report of cubic-shaped skeletal silica nanoparticles using a cubic template (calcium carbonate with calcite crystal structure) whose surface is coated by dehydroabietic acid (DAA). The DAA adsorbed calcite were suspended in two different media (EtOH and diglyme), subsequently sol-gel process in the presence of TEOS lead to core-shell nanoparticles formation. The thin silica shell is obtained after removal of the calcite core by dilute acid etching. Two different types were identified by SEM (Fig. 16): The cubic skeletal one prepared in EtOH, and the hollow one prepared in dyglyme [49].

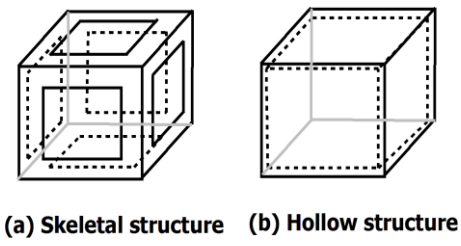

Fig. 16 Silica nanoparticles prepared in two different media 1) ethanol and 2) diglyme showing skeletal (a) and hollow structures (b).

Applications of silica include the use as solid phase extraction cartridges (for extracting polar analytes such as epinephrine, and metanephrine from urine samples) [50],

drug delivery devices (porous silica) [51], chemosensors [1,8-naphthalimide functionalized mesoporous silica (SBA-15)] [52], food ingredient separation [mesoporous silica (MCM-41), see Fig. 17] [53], metal ion collector from aqueous solution [sorption of Pb(II) and Cd(II)] [54], etc. Nanoporous silica was used as adsorbent for the removal of anionic dyes [55]. Silica-coated gold nanoparticles have been used as a radiotracer in industrial process [56]. For the removal of anions (F^-, Cl^-, Br^-, I^-, HSO_4^-), mesoporous silica was functionalized by a covalently bound naphthalene-based receptor using the sol-gel process [57a]. In addition, mesoporous silica nanoparticles have been used in the field of cancer therapy [57b].

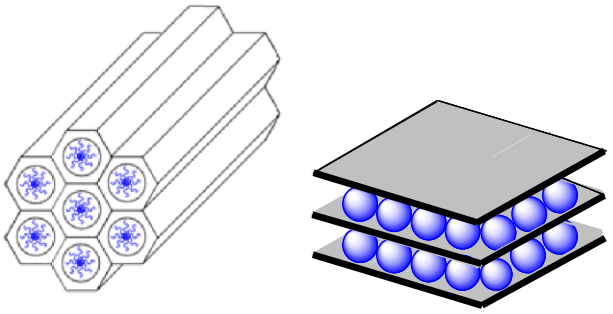

(a) MCM-41
(2D hexaginal, space group *p6mm*)

(b) MCM-50
(lamellar, space group *p2*)

Fig. 17 Structures of mesoporous silicas (adapted from F. Hoffmann, 2006)

1.4.1 Types of silica

Silica can be divided into two forms: crystalline silica and amorphous silica (see Fig. 18). Crystalline silica exists in forms such as quartz, cristobalite, and tridymite, which are an important constituent of a many minerals and gemstones, both in pure form or mixed with related oxides. Amorphous silica can be classed into three types: vitreous silica [58], silica M (obtained from amorphous or crystalline silica irradiated with fast neutrons) [59] and microamorphous silica. Vitreous silica (fumed silica or pyrogenic silica) is obtained by reduction of high purity quartz with coke in electric arc furnaces in production of silicon and ferrosilicon alloy. Microamorphous silicas can be divided into three classes: (i) microscopic sheets (ribbon or fiber), (ii) common amorphous forms (spherical particles of SiO_2 < 1000 Å in diameter, the surface consist of anhydrous SiO_2 and SiOH groups), and (iii) hydrated amorphous silica.

1.4.2 Advantages of amorphous silica

This research work is focused on amorphous silica nanomaterials, because they offer several important properties making them a unique support for introducing functional components [60-64].

1. Amorphous silica nanoparticles exhibit high porosity, providing space required for attaching functional groups or entities.
2. The effective porosity of silica nanomaterials allow grafted molecules inside their matrix to keep original their inherent properties of original molecules and may even add novel ones (e. g. optical and magnetic properties).
3. Silica nanomaterials are non-toxic and biocompatible, a very important requirement for any development in medical and pharmaceutical sciences. Colloidal silica is also used as a wine, beer, and juice-fining agent. Note however that inhaling finely divided crystalline silica dust in very small quantities over time can lead to silicosis, bronchitis, or cancer, as the dust becomes lodged in the lungs and continuously irritates them, reducing lung capacities.
4. Silica exhibits a high surface area and is a non-swelling material. The surface chemistry of silica facilitates the chemical modification of silica-based nanomaterials.
5. Silica possesses an excellent high thermal resistance.
6. Last but not least, silica can be considered as a low-cost material, which is accessible in large quantities.

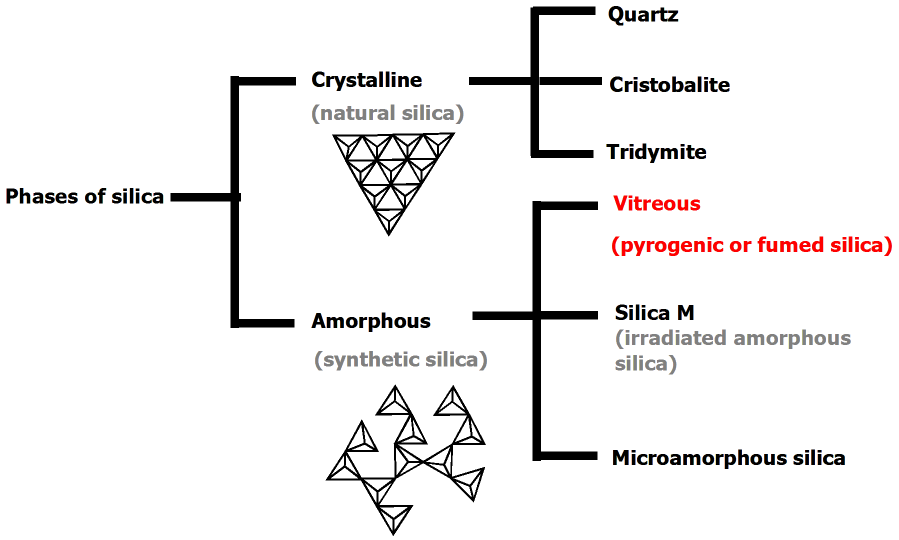

Fig. 18 The two main types of silica and their corresponding sub-classes

In amorphous silica, the bulk structure is determined by random packing of $[SiO_4]^{4-}$ units. The density ρ of amorphous silica (2.20 g/cm^{-3}) is lower than that of crystalline silica,

which ranges between 2.21 to 3.01 g/cm^{-3} [59]. The bond length of the slightly polarized covalent Si-O bond between the electropositive element Si and the electronegative Oxygen atom is 155 pm, as established by X-ray, electron-, and neutron diffraction [65].

1.4.3 Synthesis of silica

Several strategies have been developed for the synthesis of silica materials in the form of sols, gels, and powders in function of the desired applications. Synthetic amorphous silica can be obtained by wet preparation in a solvent or via a thermal synthetic route (Fig. 19). Both wet and thermal ways will be described in the next topic. For this work, we have chosen pyrogenic silica (Aerosil 200) as silica-based nanomaterial for surface modification because of its advantageous properties just described before.

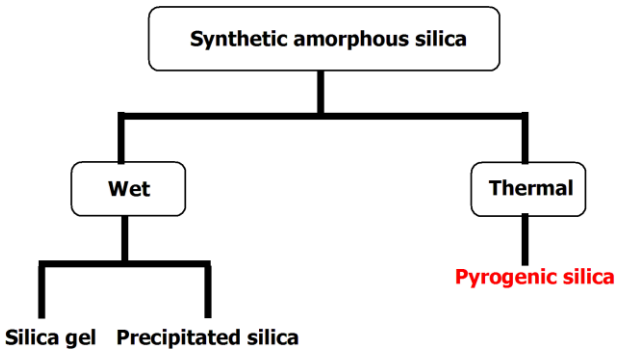

Fig. 19 Two preparative routes for the synthesis of amorphous silica

1.4.3.1 Sol-gel silica

Sol or gel silica results from the sol-gel process; a versatile method used for preparation of silica gels and precipitated silica (see Fig. 20). This process produces silica in an aqueous solution (wet process), its surface chemical properties are different from those of high temperature silica.

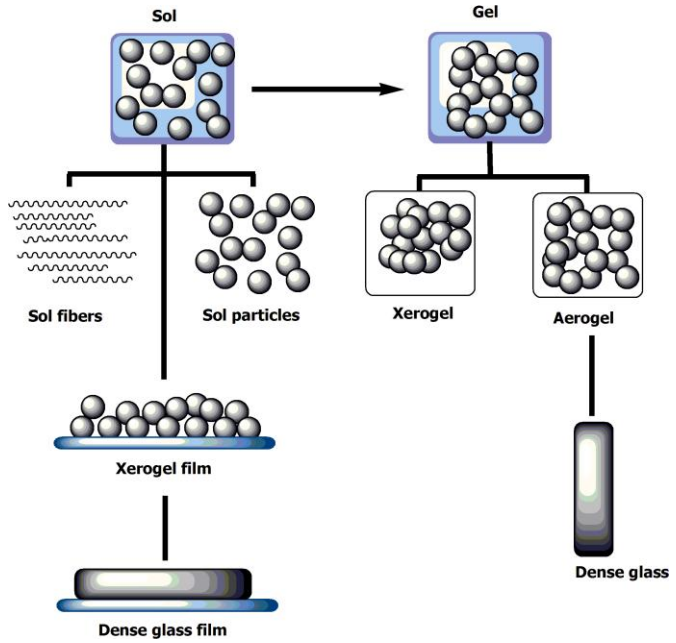

Fig. 20 The sol-gel process

Silica nanoparticles are formed by various methods. In the Stöber method [66], silica nanoparticles are produced by a sequence of hydrolysis and condensation processes of alkoxysilanes. The overall equations can be written as:

Stöber process:

$$(RO)_3Si\text{-}OR + H_2O \rightleftharpoons (RO)_3Si\text{-}OH + ROH \qquad \text{hydrolysis} \qquad (2)$$

$$\left.\begin{array}{l}(RO)_3Si\text{-}OR + ROSi(RO)_3 \rightleftharpoons (RO)_3Si\text{-}O\text{-}Si(RO)_3 + ROH \\ (RO)_3Si\text{-}OR + HOSi(RO)_3 \rightleftharpoons (RO)_3Si\text{-}O\text{-}Si(RO)_3 + ROH\end{array}\right\} \text{condensation} \quad (3)$$

The Stöber process is a variation of the sol-gel method for the generation of colloidal monodispersed silica nanoparticles. The particle size can be tuned by changing the process parameters. A key parameter affecting the size of primary silanol species [$(RO)_3Si\text{-}OH$] derived from the TEOS monomer when fixing the concentration of tetraethylorthosilicate (TEOS or $Si(OEt)_4$) is the nature of solvent. For example, when fixing the concentration of TEOS (0.5 M) and using 0.01-0.1 M NH_3 and 1.1-4.4 M H_2O, it was found that in ethanol as solvent the size of the primary particle is larger (around 8 nm) than for those generated in methanol (around 4 nm). The difference in primary size is probably caused by a higher supersaturation ratio of [$(OR)_3Si\text{-}OH$] in methanol than in ethanol [67]. Also bioencapsulated forms have been prepared using the sol-gel process and been used in the medical sector [68]. The sol-gel covalent crosslinking process was also used for the preparation of cellulose/silica hybrid biomaterials [69].

Aerogel silica

Sol-gel technology is also used to preparation of aerogel silica [70]. An aerogel is a gel in which the liquid phase has been replaced by a gaseous phase in such a way as to avoid the shrinkage, which would be happen if the gel had been directly from a liquid. Note that SiO_2-aerogels are manufactured materials with the lowest bulk density of any known porous solids of only 0.1 $g.cm^{-3}$.

Xerogel silica

This porous form is also prepared by the sol-gel method based on hydrolysis and polycondensation of TEOS but in an acid medium. The ratio of water / TEOS typically used is 4:1. The formation of the species ≡Si-$OOCCH_3$ and $CH_3COOC_2H_5$ in TEOS / ethanol systems was proposed (in the presence of acetic acid), several reaction steps are shown as follows

$$\equiv Si\text{-}OC_2H_5 + CH_3COOH \longrightarrow \equiv Si\text{-}OOCCH_3 + C_2H_5OH \quad (4)$$

$$CH_3COOH + C_2H_5OH \longrightarrow CH_3COOC_2H_5 + H_2O \quad (5)$$

$$\equiv Si\text{-}OOCCH_3 + C_2H_5OH \longrightarrow \equiv SiOH + CH_3COOC_2H_5 \quad (6)$$

$$\equiv Si\text{-}OC_2H_5 + \equiv Si\text{-}OOCH_3 \longrightarrow \equiv Si\text{-}O\text{-}Si\equiv + CH_3COOC_2H_5 \quad (7)$$

The highest surface area value attained was 850 $m^2\ g^{-1}$ for samples submitted to a gelling temperature of 20 °C [71].

1.4.3.2 Pyrogenic silica

Fumed silica is produced in a flame process (thermal process) using hydrogen, oxygen (air) and silicon tetrachloride ($SiCl_4$) as raw materials according to equations 8 and 9 [65a].

$$2\ H_2 + O_2 \longrightarrow H_2O \quad (8)$$

$$SiCl_4 + 2\ H_2O \longrightarrow SiO_2 + 4\ HCl \quad (9)$$

The by-product HCl is recycled to produce silicontetrachloride and hydrogen from silicon metal according eq.10:

$$Si + 4\ HCl \longrightarrow SiCl_4 + 2\ H_2 \quad (10)$$

Fumed silica is also produced by oxidization of metallic silicon according eq. 11:

$$Si + O_2 \longrightarrow SiO_2 \quad (11)$$

All synthetic amorphous silicas are white powders. Their densities vary around 50 g/L to 600 g/L. First are produced primary particles (2-20 nm), which can grow together to form agglomerates, which are connected by van der Waals and hydrogen bonding. Agglomerates

exhibit particles sizes around several hundred μm in powder or up to 3000 μm in microgranular form [65b]. Characterization of the specific surface, often determined by the BET method, is one of the most important parameter in reinforcement, rheological behaviour, and adsorption applications. Fumed silica exhibits specific surfaces in the range between 10 m^2/g to 400 m^2/g.

1.4.4 Surface of silica

The surface of silica is mainly composed of siloxane groups (Si–O–Si) in the inward region and silanol groups (Si–OH) distributed on the surface. The latter can be classified in three types as isolated (single) silanol, geminal (double) silanol, and vicinal silanol (see Fig. 21). The silanol groups on silica surface readily react with many reagents. The chemically modification via attachment of functional groups will be described in Chapter 2.

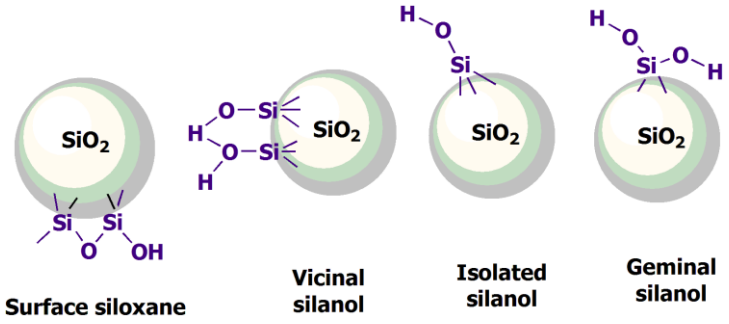

Fig. 21 Different types of silanols and siloxane-bridges on a SiO_2 surface (modified from ref. [72])

Many of the adsorption, adhesion, chemical and catalytic properties of silica depend on chemistry and geometry of their surface, therefore the surface chemistry is a topic of intensive studies and has been reviewed by Zhuravlev [72]. The content of residual SiOH groups was measured at high temperature. Above 400-450 ^oC, more hydroxyl groups are removed, retaining large siloxane areas. The physical adsorbed water was removed at 115 ^oC and the bound water was present as hydroxyl groups layer on the surface. According to literature, silanol groups are not only found on the surface, but may also occur inside of the silica skeleton and very fine ultramicropores (diameter < 1 nm) [72].

Interface of silica in aqueous medium

At the silica-water interface, two types of surface groups can be found as singly coordinated SiOH groups and doubly coordinated Si_2O surface groups. In solution, only singly coordinated SiOH groups undergo protonation and deprotonation, while doubly

coordinated Si-O-Si surface groups are unreactive vis-à-vis protons because of the high electropositive repulsion of two Si^{4+} ions.

Using the Brönsted acid/base properties, two protonation reactions can occur on the silica surface:

$$-SiO^- + H_s^+ \rightleftharpoons -Si\text{-}OH \qquad K_{1.1} \qquad (12)$$

$$-SiOH + H_s^+ \rightleftharpoons -SiOH_2^+ \qquad K_{1.2} \qquad (13)$$

where $K_{1.1}$ and $K_{1.2}$ are the first protonation and second protonation constants for singly coordinated SiOH groups [73].

Hydrophilicity and hydrophobicity

The silica surface contains both hydrophilic and hydrophobic patches. Silanol groups impart hydrophilicity, while siloxane groups confer hydrophobicity [74]. The silanols can be protonated or deprotonated depending on the pH environment. At pH 7, silanols are negatively charges because they are deprotonated (the silica surface becomes negative due to the formation of siloxides $Si\text{-}O^-$). Laser Doppler electrophoresis (LDE) is a technique used to measure the zeta potential value of dispersion particles in aqueous solution. In the case of silica, the zeta potential is a function of surface charge of the silica particles in aqueous solution. Therefore, zeta potential values can predict the stability of the material in the liquid phase. This technique will be discussed in the experimental part.

Surface charging

Silica particles in aqueous solution exhibit a surface charge due to dissolution of surface species and interfacial ion-exchange. The surface charge of silica is assumed to originate from the deprotonation of silanol groups (eq. 14) [75].

$$SiOH \rightleftharpoons SiO^- + H^+ \qquad Ka = 10^{-5.7} \qquad (14)$$

The site densities of both surface groups (τ_{SiOH} and τ_{SiO}) respect to the mass-action law:

$$\frac{\tau_{(SiO^-)}\alpha_H}{\tau_{SiO}} = K_{exp}(\beta_e \psi_0) \qquad (15)$$

where K is the intrinsic equilibrium constant (with $pK = -\log K$), α_H is the activity of the protons (with $pH = -\log \alpha_H$), φ_0 the surface potential, e the elementary charge, and β the inverse thermal energy [76]. The main cause for the surface charge generation is the dissociation of the silanol groups. In aqueous solution, the silica surface forms -Si(OH), $-Si(OH)_2$, $-Si(OH)_3$ at the interface [77].

The charge plays a crucial role in the adsorption of matter and in particle and/or cell adhesion. The surface charge of silica can be determined using X-ray photoelectron spectroscopy [78]. Surface charging behavior of silica in water has been studied. From literature, amorphous silica shows point of zero charge (pzc) at around pH 3 depending on source of silica [73, 77]. Moreover, the surface charge in function of pH is due to the ionic strength (I)*. Fig. 22 shows the correlation of the surface charge (σ_o) density and the pH determined by potentiometric titration with various concentration of $NaNO_3$. Ionic strength is affected to the surface charge of the sol suspended in that solution. In high ionic strength (I = 1 M/I) solution represents the higher surface charge density than low ionic strength (I = 0.002 M/I) [77].

* The ionic strength of a solution is a function of the concentration and of the charge of all ions present in that solution.

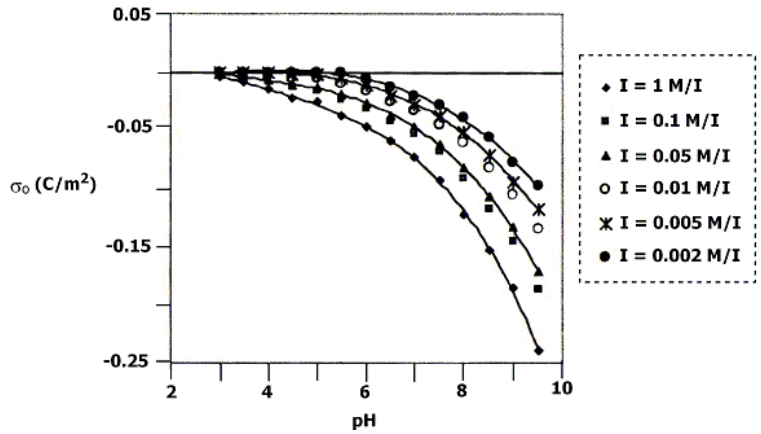

Fig. 22 The surface charge of silica as function of pH in presence of different $NaNO_3$ (Mol/L) concentrations (source: E. Papirer, 2000)

A survey of the literature reveals that the silanol number per nm^2 is quite variable and can vary from 2-8 depending on the type of silica, temperature and characterization technique (^{29}Si NMR, BET, TGA,..). For fumed silica it is about 2 nm^{-2}, whereas for fully hydroxylated surface of sols, gel, or precipitated silica (each surface Si atom has -OH groups), the silanol number is around 5 or larger. The silanol number is also affected by the age of a sample. For example, after one year of storing an Aerosil 200 sample, its silanol number had changed from 1.8 to 2.6 [77a]. The silanol number of Aerosil 200 has also been determined by adsorption of CO molecules and found to be between 1.2 and 2.1 [77a]. The silanol number of Aerosil 200 determined by thermogravimetric analysis (TGA) was found to be 4.4 nm^2 (at 100 ^oC) and 1.0 nm^2 at higher temperature (550 ^oC) [78a]. According to Cabot and Foissy, the total surface SiOH density of Aerosil 200 is about 5 nm^{-2} [33]. A similar silanol number

(4.55 SiOH nm^{-2}) has been calculated theoretically [78b]. This topic has been treated more in detail in a review article from Mishra *et al*. [77b].

1.4.5 Chemistry and reactivity of silica

The solution chemistry of silica will be discussed in following sections dealing on the solubility and polymerization of silica. The surface chemistry of silica involving the chemical reactivity and transformation of surface-bound silanol groups will be treated in Chapter 2.

The solubility of silica

a) ***In HF solution***

The Si-O bond is from a thermodynamic point of view a very stable bond. The bond dissociation energy necessary to cleave a Si-O-Si bond is about 136 kcal mol^{-1}. Nevertheless, the Si-F bond is still stronger. For that reason gaseous hydrofluoric acid (HF) converts silica to silicon tetrafluoride according eq. (16). As explained, this transformation is not due to the acidity of hydrofluoric acid, but to formation of a Si-F bond, whose bond dissociation energy has been determined to be 167 kcal mol^{-1}.

$$4\ HF(g) + SiO_2(s) \longrightarrow SiF_4(g) + H_2O(l) \qquad (16)$$

In aqueous solution, reaction with HF yields hexafluorosilicic acid, in which the silicon atom of the octahedral hexafluorosilicate anion is coordinated by six fluoride ligands (17) [79].

$$6\ HF + SiO_2 \longrightarrow H_2SiF_6 + 2\ H_2O \qquad (17)$$

This reactivity has been exploited by Xu and Asher to prepare hollow particles [80]. In a first stage, monodisperse silica particles with a diameter of 300 nm were prepared by the Stöber process, and modified by dispersion polymerization to envelop a polystyrene shell around the silica core particles. In a second stage, the silica core was removed by action of HF to give capsules.

b) Dissolution in hot concentrated alkaline

Silica is also soluble in hot concentrated alkaline or in fused hydroxide to give sodium metasilicate Na_2SiO_3 as shown in eq. (18). This water-soluble salt is also formed upon reaction with Na_2O [81].

$$SiO_2 + 2\ NaOH \longrightarrow Na_2SiO_3 + H_2O \qquad (18)$$

c) Dissolution in presence of aromatic vicinal diols

It is also literate-known that silica can be dissolved by complexation by aromatic vicinal diols $Ar(OH)_2$ in basic aqueous solution. For instance, upon addition of catechol to colloidal silica in 8-15 M aqueous NH_4OH solution colourless crystals of an octahedral hypervalent silicon complex are formed, whose molecular structure is depicted in Fig. 23. The driving force for this complexation is the thermodynamically favourable chelate effect due to formation of five-membered cycles.

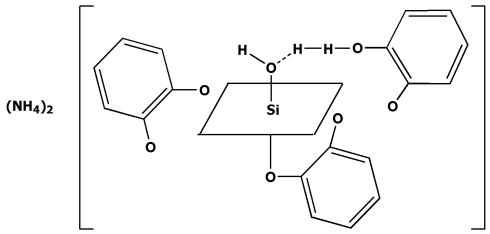

Fig. 23 Molecular structure of the octahedral $Si(cat)_3^{2-}$ anion [82]

d) Dissolution in water

Small amounts of silica can be solubilized in water. Monosilicic acid, a soluble form of silica, contains only one silicon atom and is generally formulated as $Si(OH)_4$. The dissolution of silica by chemical reaction with water is shown in eq. 19 and 20.

$$SiO_2 + 2\,H_2O \rightleftharpoons Si(OH)_4 \qquad (19)$$

$$(SiO_2)_2 + 2\,H_2O \underset{\text{dehydration}}{\overset{\text{hydration}}{\rightleftharpoons}} (SiO_2)_{x-1} + Si(OH)_4 \qquad (20)$$

The solubility of silica is dependent on many factors such as the state of silica (crystalline or amorphous form), pH of the solution, temperature, and presence of other ions.

Solubility of amorphous silica

Amorphous silica has a uniform solubility in neutral pH region. The dissolved species is almost monomer (pH range from 3 to 6). The rate of dissolution increases with increasing pH. From pH 9 to pH 10.7, there is an increase in the solubility of amorphous silica as shown in Fig. 24. In this range, amorphous silica is in solubility equilibrium with neutral monomer as well as silicate ions (equation 21 and 22) [59].

$$(SiO_2)x + 2H_2O \rightleftharpoons Si(OH)_4 + (SiO_2)_{x-1} \quad (21)$$

$$Si(OH)_4 + OH^- \rightleftharpoons Si(OH)_5^- \text{ or } (HSiO_3^- + H_2O) \quad (22)$$

At pH above 10.7, all the solid phase of amorphous silica is dissolved to form soluble silicate. Note that porous vitreous silica can also be soluble in nitric acid solution at pH 3.

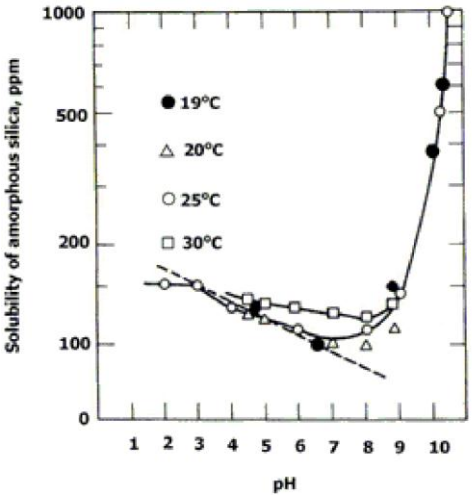

Fig. 24 Solubility of amorphous silica at various pH (source: R.K. Iler, 1979)

The effect of impurities (Al^{3+}, Ca^{2+}, Mg^{2+}, SO_4^{2-}, and F^-) on a silica surface reduces the solubility. For example, the dissolution rate of silica decreases when only one aluminium atom adsorbed on silica surface as anionic aluminosilicate per 2 nm^2 [77]. Impurities present on the surface of pyrogenic silica (Aerosil) are Al, Fe, Ti, and Cl [73].

Polycondensation of silicic acid

The polycondensation of silicic acid is a reaction leading to an increase in molecular weight of silica. It involves the successive polycondensation of monosilicic acid as shown in reaction 23 [83].

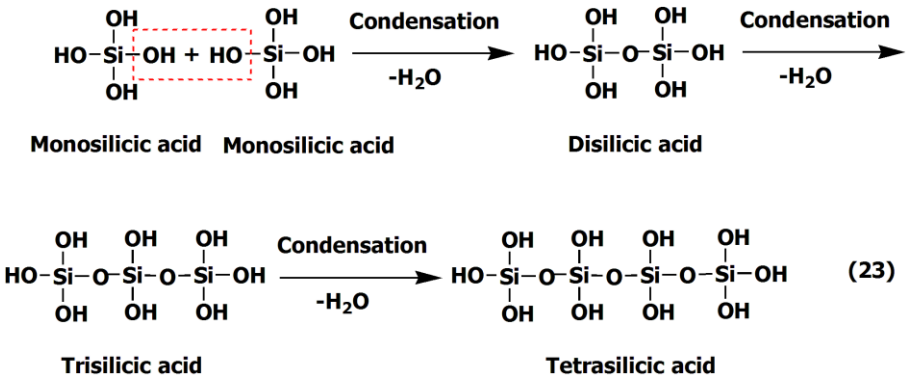

(23)

Three steps of polycondensation are recognized as:

i) Polycondensation of molecular species to form particles.

ii) The growth of particles.

iii) The particles are linked together into branched chains, then become networks, and finally extending throughout the liquid medium to generate a gel.

The isoelectric point (pzc) of silica is around pH 2. Therefore, below pH 2 the catalyst is a proton, which forms an active cationic complex by protonation of a silanol. Above pH 2, the OH^- ion is the catalyst generating active anionic silica species. The self-condensation of the monomer to form various structures like chain (1D), ribbon (1D), layers (2D), and finally, the condensation of the layers generates a 3D network is shown in Fig. 25.

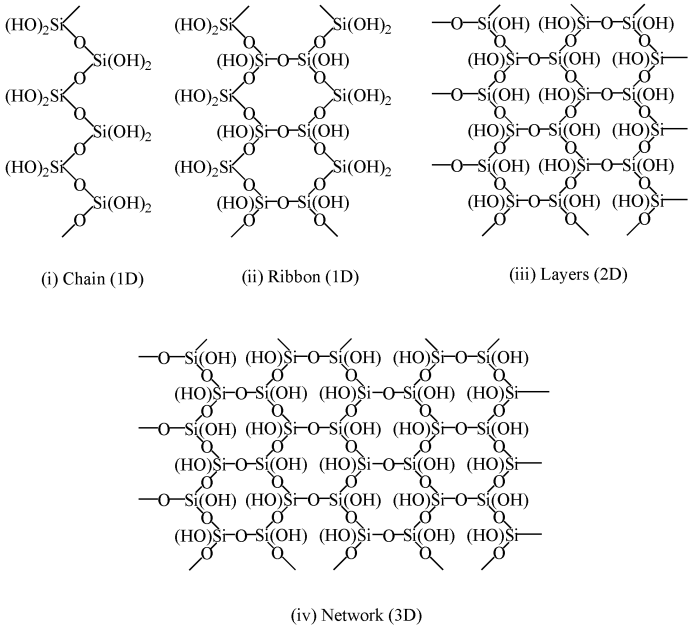

Fig. 25 Polycondensation of silicic acid to form of chains (i), ribbons (ii), layers (iii), and networks (iv) [83].

The polymerization of silicic acid [$Si(OH)_4$] is strongly pH dependent. In a strongly alkaline solution, monosilicic acid does not polymerize. Polymerization of silica in H_2O/K_2O solution was studied [84]. When silica concentration increased, it promotes silica polymerization, and that increasing in the K_2O/SiO_2 ratio. An increasing pressure may also cause depolymerization of aqueous silica.

1.4.6 Colloidal silica

Colloidal silica is a suspension of SiO_2 particles with diameters in the 1-1.000 nm range [85]. The colloidal silica particles are used in many applications such as binder, nanoparticle-based fluorescent bioassays, sensors, etc. The stability of colloidal silica is an important parameter to understand the aggregation properties in aqueous suspensions.

Aggregation of particles

Aggregation occurs when colloidal particles are bonded together in liquid phase. The colloidal particles are linked together in many ways, hence the aggregation includes gelling (i), coagulation (ii), and flocculation (iii) as shown in Fig. 26.

Silica gels: the particles are linked together via branched chains that fill the whole volume of thesol. Factors controlling gel characteristics are the size of original silica particles, amount of silica particles in solution, the pH, salt, temperature, etc.

Coagulation: the silica particles come together into relatively closed-packed clumps (more concentrated than in original sol). It is proposed that coagulation of silica in the presence of alkaline cations is caused by interparticle hydroxo-bridging [86].

Flocculation: the silica particles are linked together by bridges of flocculating agent. Flocculation of dispersion silica by polyvinyl alcohol (PVA) depends on type of silica and pH of the solution [87a]. Maximum adsorption of PVA by flocculation occurs at point of zero charge of the oxide. When increasing the pH, the adsorption and flocculation decreases.

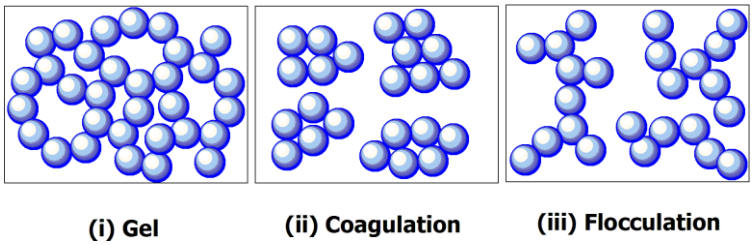

Fig. 26 Three different types of particles aggregation

Results and Discussion

For this research work, fumed hydrophilic silica, commercialized by EVONIK as Aerosil 200, was studied. The average primary particle size of this material is about 12 nm. It is known that Aerosil silica particles are aggregated even when dispersed mechanically in water [87b].

Therefore, pretreatment of the Aerosil silica with acid solution may change the properties of the silica surfaces [87c,d]. That is why two types of silica were studied:

Untreated native Aerosil 200 denoted as **SiO_2**

Aerosil treated by an acid (see experimental part), which is denoted as **Activated Silica**.

Several techniques have been used in this work to characterize native Aerosil 200 and/or functionalized silica materials such as FT-IR, SEM, AFM, BET, and EDS. The properties of the silica particles in the aqueous solution are investigated by measuring the zeta potential, hydrodynamic size, pH, and conductivity.

1.5 Characterization of Silica Powders in the Solid State

1.5.1 Fourier Transform Infrared spectroscopy (FT-IR)

FT-IR is among the most useful techniques to identify either organic or inorganic species [88]. It can be used to quantify some components of an unknown mixture in form of solids, liquids, and gasses. In FT-IR, the data are collected and then converted from an interference pattern to a spectrum. By interpreting the infrared absorption spectrum, the chemical bonds in a molecule can be determined. FT-IR spectra of pure compounds are generally unique and they are like a molecular "fingerprint". For most common materials, the spectrum of an unknown substance can be identified by comparing it with a library of a known compounds. Characteristic absorptions of silica in the 4000 cm^{-1} to 1300 cm^{-1} region are gathered in Table 1.1 [89].

Table 1.1 The IR spectrum bands of OH groups on a silica surface

Type of OH group	**Peak (cm^{-1})**
Free hydroxyl groups	3745 - 3750
Vicinal	3650 - 3660
Adjacent pairs of SiOH groups with H-bonded to each other	3540 - 3550
H_2O adsorbed on the above	3400 - 3500

In the present work, both native **SiO_2** and activated Aerosil 200 were characterized by FT-IR. The silicas were mixed with dry KBr and spectra were recorded with a resolution of 4 cm^{-1}. The FT-IR spectrum of the neat **SiO_2** displays a number of characteristic bands at 3411 cm^{-1}, 1093 cm^{-1} (vs) and 804 cm^{-1} (m) (Fig. 27). These peaks are assigned to silanol groups (-SiOH) with H_2O adsorbed, stretching vibration of -Si-O-Si- (siloxane backbone), and Si-O bond rocking, respectively [90]. The spectrum of Activated silica displays a sharp band at

3504 cm^{-1} is assigned to the -OH stretching vibration band due to physisorbed water and hydrogen-bonded silanol groups [91]. The -Si-O-Si- absorption at 1093 cm^{-1} and the Si-O stretching of silanol groups at 804 cm^{-1} have been shifted 1089 cm^{-1} and 817 cm^{-1} in the case of Activated silica. The vibration occurring at 453 cm^{-1} in **SiO_2** confirms the -Si-O-Si- functional group also appearing in Activated silica, but it has been shifted to 486 cm^{-1}.

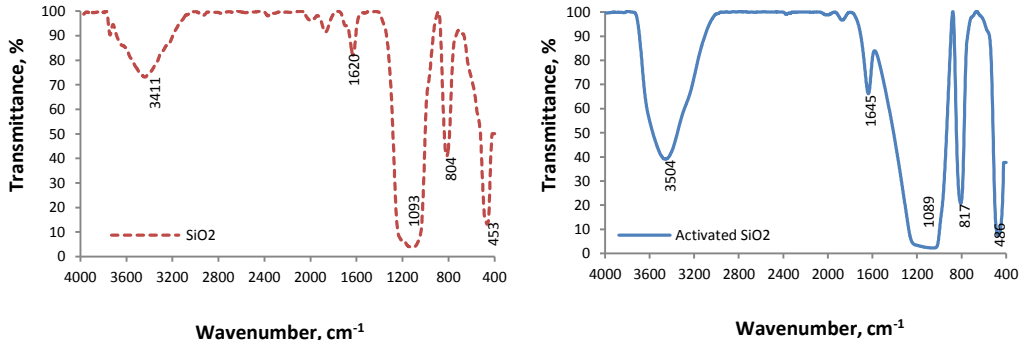

(a) (b)

Fig. 27 The FT-IR spectra of native Aerosil 200 (a), and Activated Aerosil 200

1.5.2 Energy Dispersive Spectroscopy (EDS)

EDS is based on the detection of X-rays produced by a sample placed in an electron beam [92]. The sample is excited by the electron beam subsequently to produce X-rays to discharge the excess energy. The X-rays energy is a characteristic for each element. The element percentage presents in our samples was analyzed by the EDS technique and the results for each element found are given in Table 1.2. The EDS analysis gave the percentage by number of atoms (wt %) of each of the elements identified. The analysis of Aerosil 200 shows a large peak of silicon (64.6 % atomic). Another strong one is the oxygen peak (34.68% atomic). Small amounts of hydrogen are also detected (0.33%). Other small peaks (residual impurity elements) are due to chlorine (0.2% atomic) and potassium (0.2%).

Table 1.2 Elemental percentage of native Aerosil 200

Technique	Elemental Analysis, (Atomic %)
Si	64.6
O	34.7
Cl	0.2
K	0.2

1.5.3 Scanning Electron Microscopy (SEM)

SEM is used to visualize a surface texture of materials with high resolution (less than 2 nm) [93]. It can be used for determining particle size, shape as well as chemical

composition and distribution from the characteristic X-ray signal. In SEM, the electron beam scans across the specimen surface point by point (Fig. 28). The signal collected from each point is used to construct an image on the display, with the cathode ray tube beam and the column beam following a synchronized scanning pattern. This means the displayed image is the variation in detected signal intensity as the column beam is scanned across the sample.

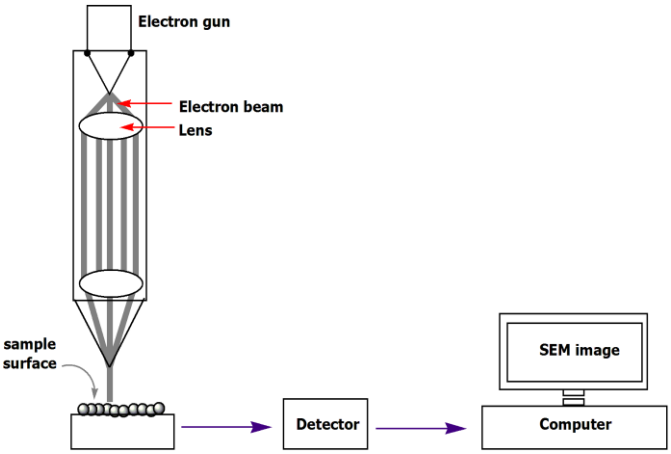

Fig. 28 Principle of SEM [94]

The morphology of our materials was studied by SEM. The SEM used is a typical SEM tungsten cathode with a resolution of 3.5 nm (at a voltage of 30 KV). All samples were metallized by sputtering with gold (about 5 nm) before examination. The SEM of the outer surface morphology of native silica is shown in Fig. 29**a** the image represents a rough and irregular geometry as well as the SEM image of Activated silica treated with acidic aqueous solution (Fig. 29**b**).

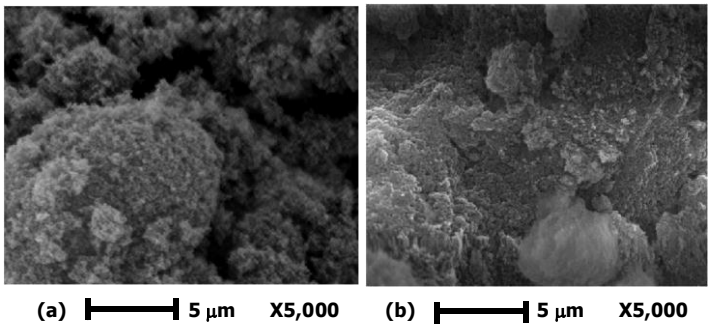

Fig. 29 Characterization of native Aerosil (a) and Activated Aerosil (b) by SEM

1.5.4 Atomic Force Microscopy (AFM)

The AFM technique is a powerful technique to characterize the residual scratches, indentations of a given surface. AFM is an accurate and versatile technique for measuring surface morphology of a material at the nano-scale. A very fine sensor tip, mounted at the end of a small deflecting cantilever, is in contact with the sample surface to be investigated (see Fig. 30).

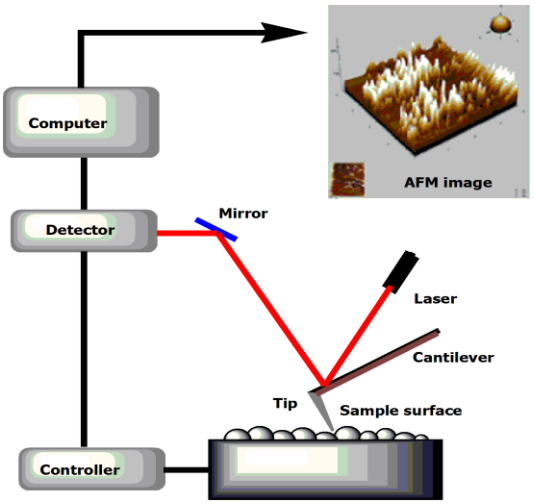

Fig. 30 The principle of AFM technique (Modified from Y. L. Lyubchenko, 2011[95a])

The deflection of a cantilever holding the tip is monitored by a detector. The sensor tip is moved across the surface of sample in numerous line scans, which produces a three-dimensional image of the surface with ultra-high resolution.

A droplet of the sample (colloidal SiO_2 suspension) was deposited onto a thin glass substrate. To dry the sample before scanning, the sample was kept in a desiccator for a week. The surface morphology of native Aerosil 200 was characterized by AFM in the contact mode using an aluminum coated silicon tip. The cantilever was 450 µm long and its stiffness was about 0.27 $N.m^{-1}$. The AFM image was obtained by scanning a 4 µm x 4 µm surface area, revealing the presence of colloidal nodules on the glass substrates, having an average height of 50 nm. The surface of the particles is quite rough and irregular (Fig. 31).

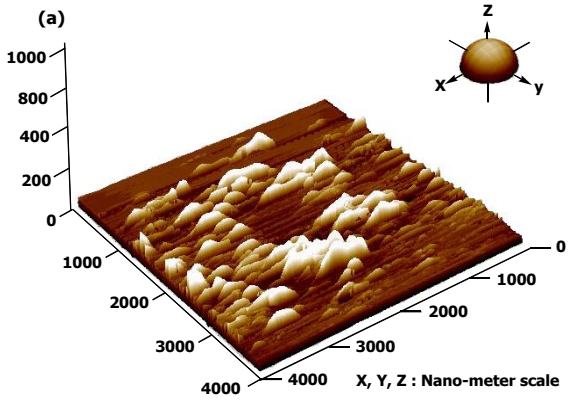

Fig. 31 The AFM image of native silica

Aggregation of silica particles occurred when native Aerosil 200 particles were dispersed in DI water, the interaction between the silanol groups on the surface of the silica particles with water happened via hydrogen bonding [72]. This result corresponds to the report of J.

Eisenlauer and E. Killmann [87b]. This report confirmed our work that the primary silica particles are fused together to form aggregates as shown in Fig. 32.

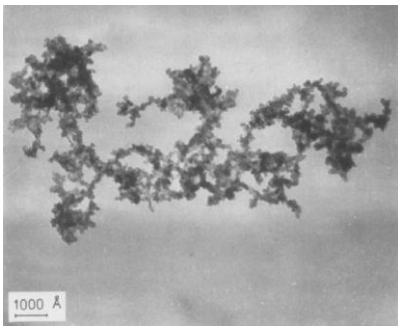

Fig. 32 The TEM image of aggregated Aerosil 200 particles (original magnification x 40,000; final magnification x 80,000) [87b].

1.5.5 BET specific surface

The BET technique informs about the physical adsorption of gas molecules on a solid surface [96]. It is an important analysis technique for the measurement of the specific surface area of a material. The BET theory was developed in 1938 by Stephen Brunauer, Paul Hugh Emmett, and Edward Teller [97]. The theory is an extension of the Langmuir theory, dedicated to monolayer molecular adsorption, to multilayer adsorption. The resulting BET equation is expressed by

$$\frac{1}{\upsilon[(P_0 / P) - 1]} = \frac{c - 1}{\upsilon_m c[(P_0 / P) + 1]} + \frac{1}{\upsilon_m c} \qquad (24)$$

P and P_0 are the equilibrium and the saturation pressure of adsorbates at the adsorption temperature, υ is the adsorbed gas quantity (in volume units), and υ_m is the monolayer adsorbed gas quantity. And c is the BET constant, which is expressed by

$$c = \exp(E_1 - E_L / RT) \qquad (25)$$

E_1 is the heat of adsorption for the first layer, and E_L is the one for the second and higher layers and is equal to the heat of liquefaction. According the supplier EVONIK, the specific surface area of native Aerosil 200 is indicated to be 200 ± 25 m^2/g. For this thesis, the BET values of **SiO_2** and Activated Aerosil 200 were independently checked. The specific surface areas were determined to be 182 and 184 m^2/g, respectively. These results (somewhat lower than the supplier data) indicate there is no significant difference between (three repeated measurements) and Activated Aerosil 200 (see Table.1.3.).

Table 1.3 BET specific surfaces of native **SiO_2** and activated **SiO_2**

Sample	**BET, m^2/g**
Untreated silica, **SiO_2**	182 ± 4
Activated SiO_2	184 ± 4

1.6 Behavior and Characterization of Aerosil 200 in Aqueous Solution

1.6.1 pH measurements

Different types of activated silica

We chose a 0.5% silica content to prepare colloidal silica for pH and conductivity studies. The pH value of native **SiO_2** and activated silica were measured during 0.5 to 72 h interval. As expected, the pH of Activated SiO_2 is inferior to that of untreated SiO_2 (Fig. 33). This can be ascribed by partial protonation of the silica surface after acid treatment and small amounts of residual acid traces (see eq. 26). All pH values of colloidal silica remained quite stable during 3 days of monitoring.

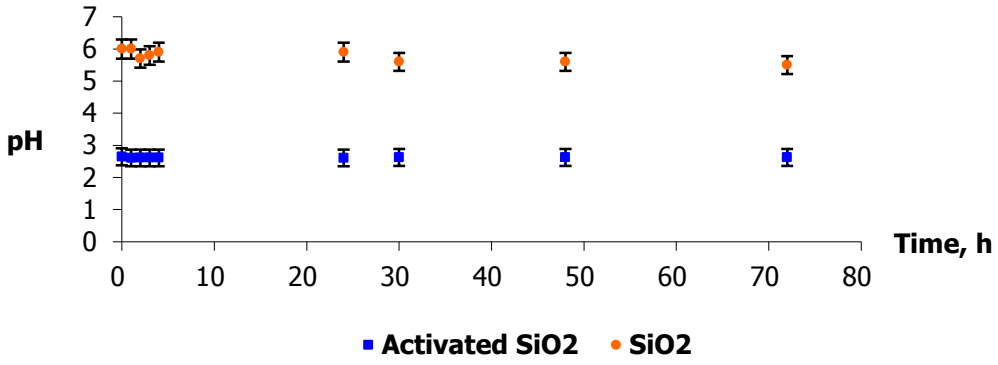

Fig. 33 Evolution of the pH of 0.5% colloidal untreated **SiO_2** and activated **SiO_2**

1.6.2 Conductivity

To determine the conductivity data of all colloidal silica suspension, 0.5% solutions were prepared in the same manner as used for pH measurement. The conductivity of both two types of colloidal silica was measured during a 0.5 to 75 h interval. Within the first 4 h, the conductivity of native Aerosil particles (suspended in aqueous solution) strongly increases because of the formation of protonated and deprotonated silanol groups at the interface of silica with the aqueous medium (see eq. 12 and 13) [74]. The conductivity continuously increases until 75 h with the value of about 7.4 ± 0.8 µS/cm (Fig. 34**a**). For activated SiO_2, the conductivity is quite stable and the average value is around 100 µS/cm (Fig. 34**b**). The activated silica suspension exhibits a ten times stronger conductivity than native Aerosil. This may be due to some residual hydrochloric acid molecules disturbing the surface as shown in equation (26) [77].

$$\equiv Si\text{-}OH + HCl \longrightarrow \equiv SiOH_2^+Cl^- \qquad (26)$$

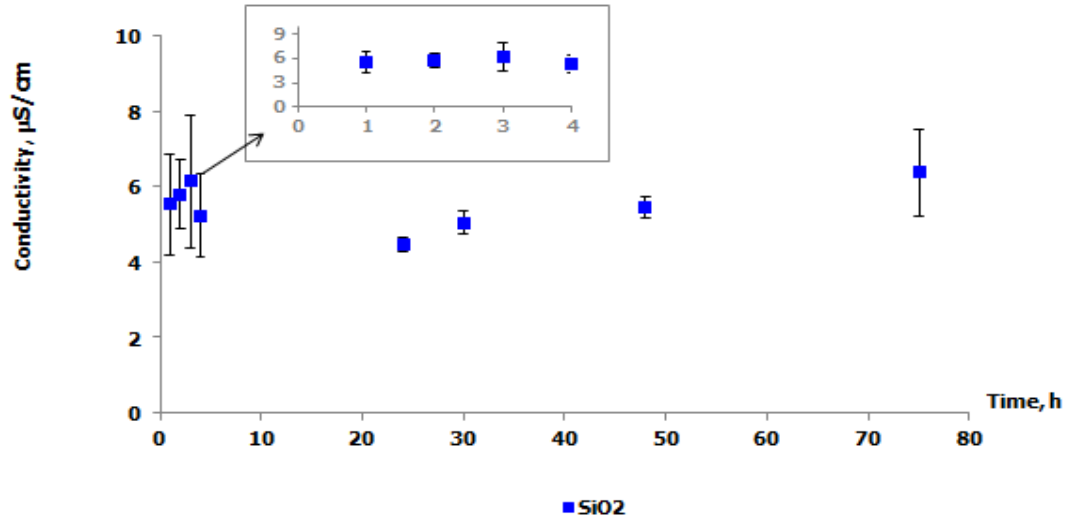

Fig. 34a Evolution of the conductivity of 0.5% colloidal **SiO_2** over 3 days

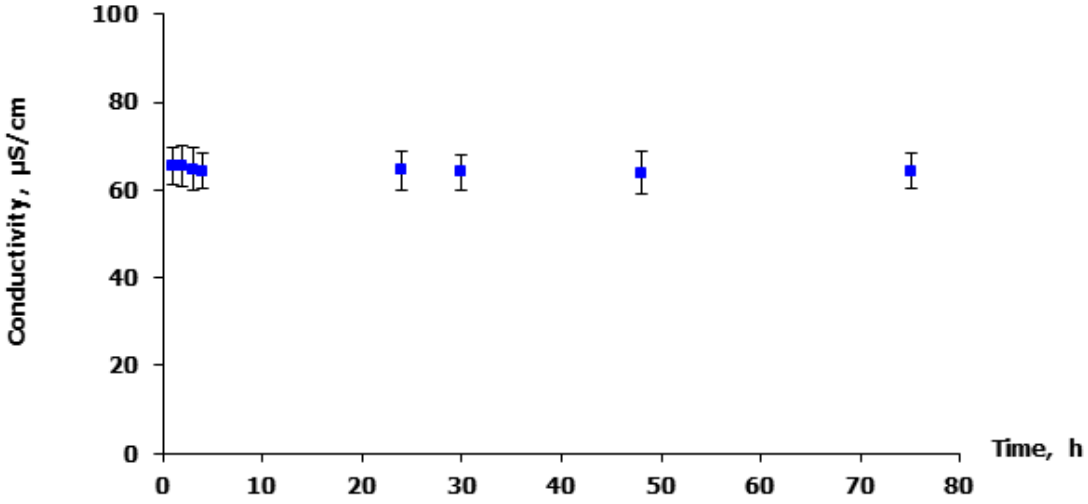

Fig. 34b Evolution of the conductivity of 0.5% colloidal **Activated SiO_2** over 3 days

1.6.3 Zeta potential measurement

The particles in suspension display a zeta potential. In solution, the presence of a net charge on a particle affects the distribution of ions surrounding the particle, resulting in an increase in the concentration of counter-ions. The region over which this influence extends is called “electrical double layer”. This double layer is thought to comprise two separate regions (Fig. 35): The inner region (Stern layer) consists of strongly bound ions, whilst the outer region (diffuse layer) consists of loosely associated ions. The zeta potential is the electrical potential at the slipping plane. Zeta potential measurement by Laser Doppler electrophoresis (LDE) is used to assess the charge stability of a disperse system. A voltage is applied across a pair of electrodes at either end of a cell containing the particle dispersion. Charged particles

are attracted to the oppositely charged electrode. Their velocity is measured and expressed in unit field strength as their electrophoretic mobility (U_E). LDE measures small frequency shifts (Δf) in the scattered light that arise owing to the movement of particles in an applied electric field [98]. The frequency shift is equal to

$$\Delta f = \frac{2\upsilon \sin(\theta/2)}{\lambda} \qquad (27)$$

where υ is the particle velocity, λ is the laser wavelength, and θ is the scattering angle. The measured U_E is converted into zeta potential (ζ) through the Henry's equation [99].

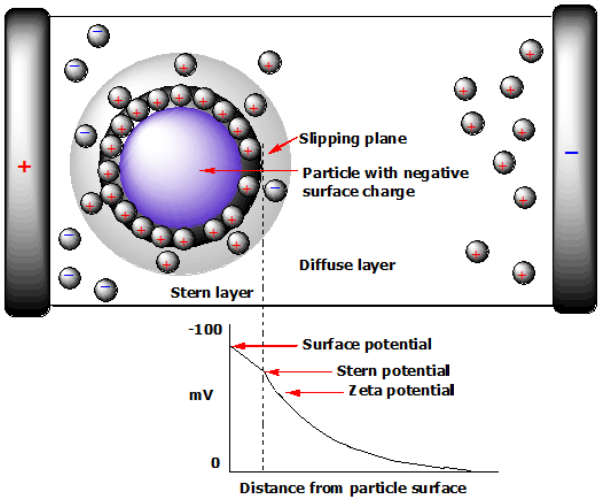

Fig. 35 Schematic representation of the zeta potential measurement using LDE

The effect of pH on the zeta potential value of the sorbent was study using a Zetasizer instrument (Nano-Zs, Malvern Ltd., UK). These values are plotted against different pH at 25 ^{o}C as shown in Fig. 36. Zeta potential values of the untreated silica and activated silica are near zero at pH 2. At pH > 2, the zeta potential decreases accordingly [100], since the concentration of the negative charges on the silica surface increases [101].

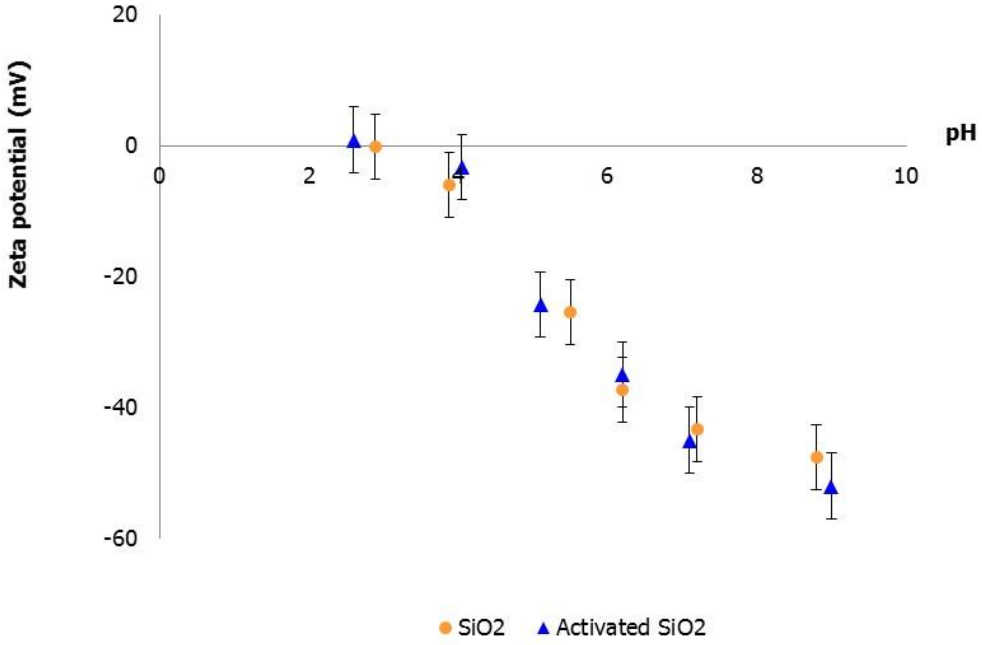

Fig. 36 The zeta potential value of untreated $\mathbf{SiO_2}$ and activated $\mathbf{SiO_2}$, respectively

As describes in the section "*Surface charging"*, the silica suspended in different solution represents different zeta potentials in comparison to silica in pure water [100]. In our case, the zeta potentials of both native and Activated Aerosil follows in function of the pH the same trend. There is no significant difference between the two recorded curves (three repeated measurements), but nevertheless the conductivity was somewhat higher for activated silica. This may imply that just few siloxanes units on the silica surface have been activated. Note that the content of silanol groups after acid treatment has not been determined.

1.6.4 Hydrodynamic size measurements

Dynamic light scattering (DLS) is used to determine the size and size distribution of particles emulsions and molecules dispersed or dissolved in a liquid [102]. It measures the Brownian motion corresponding to the size of particles. The intensity of the scattered light fluctuates at a rate that is dependent on the size of the particles (smaller particles move more rapidly). Analysis of these intensity fluctuations yields the velocity of the Brownian motion and hence the particle size using the Stokes-Einstein relationship as

$$d(H) = \frac{kT}{3\pi\eta D} \qquad (30)$$

Where $d(H)$ is hydrodynamic diameter, D is translational diffusion coefficient, k is Boltzmann's constant, T is absolute temperature, and η is viscosity. The diameter obtained by

DSL technique (Fig. 37), called “hydrodynamic diameter”, refers how a particle diffuses within a fluid. The hydrodynamic diameter is the diameter of a sphere that has the same translational diffusion coefficient as the particle. The DLS is performed by measuring the rate at which the intensity of the scattered light fluctuates when detected using a suitable optical arrangement.

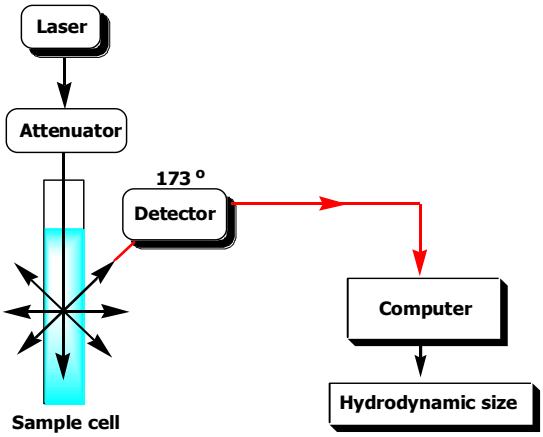

Fig. 37 The Dynamic Light Scattering technique

As already mentioned, Aerosil 200 is composed of spherical primary particles which a diameter of around 12 nm, which are highly aggregated in the dry state. These particles remain highly aggregated even when dispersed under sonication (1 h) in water with average hydrodynamic particle sizes of 300 nm [103]. The hydrodynamic sizes (in volume percentage) of neat **SiO_2** and activated **SiO_2** were measured for this work using a Zetasizer instrument. As shown in Table 1.4, the average hydrodynamic size of neat **SiO_2** was 328 ± 25 nm and found to be 140 ± 10 nm for activated **SiO_2**

Table 1.4 The hydrodynamic sizes of native **SiO_2** and Activated **SiO_2**

No	Sample	Z-Ave	Volume percentage		
			Peak 1	Peak 2	Peak 3
1	Aerosil 200 silica	305 nm	89.9	8.9	1.3
2		323 nm	100	-	-
3		356 nm	94	6	-
Average		328 ±25 nm			
1	Activated silica	147 nm	100	-	-
2		133 nm	100	-	-
Average		140 ± 10 nm			

Moreover, Table 1.4 shows that the mean hydrodynamic sizes of the particles after acidic treatment were more homogeneous and smaller than that of untreated silica. This can be

explained by repulsion between some residual H^+ ions on the surface of the **Activated SiO_2** particles.

Conclusion

The surface of Aerosil 200 nanoparticles was chemical activated with hydrochloric acid solution to obtain more silanol groups on their surface. The untreated silica and the activated silica particles were characterized by FT-IR spectroscopy. The spectrum of activated silica displays the characteristic sharp bands at 3458 cm^{-1} of the -OH groups due to physisorbed water and hydrogen-bonded silanol groups. There is no significant difference of BET specific surface value between untreated silica and activated silica. Stability of the composites in aqueous solution was studied by measuring values of pH, and conductivity. The obtained result displays that the pH values are quite stable at the period time studied (72 h). The effect of time to measure did not significant on the pH studied. These composites show stability properties in aqueous solution. The conductivity value of untreated silica suspension after 75 h is about 7.4 ± 0.8 μS/cm. After silica was activated by acid aqueous solution, the conductivity is quite stable and the average value is around 969 ± 8 μS/cm. Zeta potential value of untreated silica and activated silica are nearly zero at pH 2. When pH increase more than 2, zeta potential values decrease accordingly, resulting from the increase of the concentration of the negative charges on the silica surface. For that result, at pH > 2, the negative charges silica could capture metal cations in aqueous solution. The basic information of untreated silica and activated silica in nano-size are obtained. In order to develop the adsorption properties, silica nanoparticles will be chemically surface modified by introduction of organic functional groups (Chapter 2).

Experimental part

Materials and Apparatus

Hydrophilic fumed Aerosil 200 silica (neat silica **SiO_2)** was purchased from EVONIK industries, Japan. All reagents are analytical grade. The water used in all experiments was obtained from Millipore filtration units (18.2 MΩ cm). Fourier Transform IR spectra were recorded using a VERTEX 70 Spectrometer equipped with a DTGS detector (BRUKER). The morphology of the composites was studied by Scanning Electron Microscopy (JSM 5600, JEOL, Germany) and Atomic Force Microscopy (PicoSPM, Molecular Imaging, USA). BET analyses have been performed the by the *Welience* service at the University of Burgundy. Conductivity data were measured using a conductivity meter from Mettler-Toledo, Switzerland. Zeta potentials were obtained by means of a Zetasizer NanoZ (Malvern Instruments). The suspensions were prepared by suspending the particles in DI water, and adjusting the pH using 0.1 M HCl or NaOH. After sonication of the samples during 30 minutes, the zeta potentials were determined and pH was measured. The device was calibrated with a standard suspension, whose ζ value was 68±6.8 mV, so the deviation is about ± 10%. During the experiments, three ζ measurements were performed, then the average and standard deviation were calculated. Elemental analyses have been carried out by UMR 7565 CNRS Université Henri Poincaré Faculté des Sciences, Boulevard des Aiguillettes Case 79, BP 70279, VANDOEUVRE les NANCY.

Preparation of activated silica

Activated silica (**Activated SiO_2**) was prepared in the following manner: 5 g of Aerosil 200 silica particles were suspended in 100 ml of 1.1 M of hydrochloric acid aqueous solution to obtain activated silica. After agitation during 24 hours (50 rpm/min), the activated silica was washed with DI water. Then the sample was centrifuged and the supernatant removed; then 200 mL of DI was added to the activated silica and the suspension was again centrifuged. This operation was repeated several times (10 times) until the pH of the supernatant remained stable (~ pH 3, measured by a pH meter) and the conductivity was found to be around 914 μS/cm. Then the activated silica was dried at 100 ^{o}C and kept in desiccator until used.

References

1. C. N. R. Rao, and A. K. Cheetham, *Science and technology of nanomaterials: current status and future prospects*, J. Mater. Chem., 11 (2001) 2887-2894.
2. C. Zhai, N. Du, H. Zhang, and D. Yang, *Cobalt-iron cyanide hollow cubes: Three-dimensional self-assembly and magnetic properties*, J. Alloys Compd., 509 (2011) 8382–8386.
3. W. Li, R. Yuan, and Y. Chai, *Amine-terminated organosilica nanosphere functionalized prussian blue for the electrochemical detection of glucose*, Talanta, 82 (2010) 367-371.
4. S.-W. Ryu, C.-H. Kim, J.-W. Han, C.-J. Kim, C. Jung, H.G. Park, and Y.-K. Choi, *Gold nanoparticle embedded silicon nanowire biosensor for applications of label-free DNA detection*, Biosens. Bioelectron., 25 (2010) 2182-2185.
5. S.A. El-Safty, Y. Kiyozumi, T. Hanaoka, and F. Mizukami, *Heterogeneous catalytic activity of NiO-silica composites designated with cubic Pm^3n cage nanostructures*, Appl. Catal., B, 82 (2008) 169-179.
6. C. André, R. Aljhani, T. Gharbi, and Y.C. Guillaume, *Incorporation of carbon nanotubes in a silica HPLC column to enhance the chromatographic separation of peptides: Theoretical and practical aspects*, J. Sep. Sci., 34 (2011) 1221-1227.
7. K.-T. Jeng, N.-Y. Hsu, and C.-C. Chien, *Synthesis and evaluation of carbon nanotube-supported RuSe catalyst for direct methanol fuel cell cathode*, Int. J. Hydrogen Energy, 36 (2011) 3997-4006.
8. Y.-C. Chiang, and J.-R. Ciou, *Effects of surface chemical states of carbon nanotubes supported Pt nanoparticles on performance of proton exchange membrane fuel cells*, Int. J. Hydrogen Energy, 36 (2011) 6826-6831.
9. M.O. Danilov, and A.V. Melezhyk, *Carbon nanotubes modified with catalyst*, J. Power Sources, 163 (2006) 376-381.
10. H. Chu, L. Wei, R. Cui, J. Wang, and Y. Li , *Carbon nanotubes combined with inorganic nanomaterials: Preparations and applications*, Coor. Chem. Rev., 254 (2010) 1117-1134.
11. R. K. Pandyan, S. Seenithurai, and M. Mahendran, *Hydrogen storage in MgH_2 coated single walled carbon nanotubes*, Int. J. Hydrogen Energy, 36 (2011) 3007-3015.
12. C. Li, E.T. Thostenson, and T.-W. Chou, *Sensors and actuators based on carbon nanotubes and their composites: A review*, Compos. Sci. Technol., 68 (2008) 1227-1249.
13. D. Vardanega, F. Picaud, and C. Girardet**,** *Chiral interaction in double-wall carbon nanotubes: simple rules deduced from a large sampling of tubes*, J. Chem. Phys. 132 (2010) 124704-12470410.
14. D. Vardanega, F. Picaud, *Detection of amino acids encapsulation and adsorption with dielectric carbon nanotube*, J. Biotechnol., 144 (2009) 96-101.
15. F. Picaud, G. Herlem, and C. Girardet, *Control of carbon nanotube handedness using a supramolecular chiral surface* , J. Chem. Phys., 135 (2011) 154703-154706.
16. T. Kuila, S. Bose, P. Khanra, A.K. Mishra, N.H. Kim, and J.H. Lee, *Recent advances in graphene-based biosensors*, Biosens Bioelectron., 26 (2011) 4637-4648.
17. Y. Chandra, R. Chowdhury, F. Scarpa, S. Adhikaricor, *Vibrational characteristics of bilayer graphene sheets*, Thin Solid Films, 519 (2011) 6026-6032.

18. K. Zheng, P. Liu, W. Li, F. Ma, X. Liu, and X. Chen, *Investigation on microstructure and properties of CrAlN/AlON nanomultilayers*, Appl. Surf. Sci., 257 (2011) 9583-9586.
19. J.-P. Launay, *Long Distance Intervalence Electron Transfer*, Chem. Soc. Rev., 30 (2001) 386-397.
20. R. Kessinger, J. Crassous, A. Herrmann, M. Rüttimann, L. Echegoyen, F. Diederich, *Preparation of Enantiomerically Pure C76 with a General Electrochemical Method for the Removal of Di(alkoxycarbonyl)methano Bridges from Methanofullerenes: The Retro-Bingel Reaction*, Angew. Chem. Int. Edit., 37 (1998) 1768-1965.
21. J.E. Cortés-Figueroa, *An Experiment for the Inorganic Chemistry Laboratory The Sunlight-Induced Photosynthesis of (η2-C60)M(CO)5 Complexes (M = Mo, W)*, J. Chem. Educ., 80 (2003) 799-800.
22. D. Astruc, E. Boisselier, and C. Ornelas, *Dendrimers Designed for Functions: From Physical, Photophysical, and Supramolecular Properties to Applications in Sensing, Catalysis, Molecular Electronics, and Nanomedicine, Chem. Rev.*, 110 (2010) 1857-1959.
23. M. Tristany, M. Moreno-Manas, R. Pleixats, B. Chaudret, K. Philippot, Y. Guari, V. Matsura, and P. Lecante, *Self-assembled platinum nanoparticles into heavily fluorinated templates: Reactive gas effect on the morphology*, New J. Chem. 33 (2009) 1529-1534.
24. G. Schmid, M. Baeumle, M. Geerkens, I. Heim, C. Osemann, T. Sawitowski, *Current and future applications of nanoclusters*, Chem. Soc. Rev. 28 (1999) 179-185.
25. S. W. Haggata, D. J. Cole-hamilton, and J.R. Fryer, *Control of average size and size distribution in as-grown nanoparticle polymer composites of MSe (M=Cd or Zn)*, J. Mater. Chem., 7 (1997) 1969-1975.
26. M. Sharma, A.B. Sharma, N. Mishra, and R.K. Pandey, *Investigation of size dependent structural and optical properties of thin films of CdSe quantum dots*, Mater. Res. Bull., 46 (2011) 453-459.
27. T.-W. Kim, C.-H. Cho, B.-H. Kim, and S.-J. Park, *Quantum confinement effect in crystalline silicon quantum dots in silicon nitride grown using SiH_4 and NH_3*, Appl. Phys. Lett., 88, (2006) 1231021-1231023.
28. P. Kumar, *Effect of Silicon Crystal Size on Photoluminescence Appearance in Porous Silicon*, ISRN Nanotechnol, 2011 (2011) 1-6.
29. H. Guleryuz, I. Kaus, C. Filiàtre, T. Grande, and M.-A. Einarsrud, *Deposition of silica thin films formed by sol-gel method*, J. Sol-Gel Sci. Technol., 54 (2010) 249-257.
30. A. Lakhlifi, P.R. Dahoo, *Enhanced localization of tunneling of the NH_3 umbrella mode in nano-cage fullerene*, Chem. Phys., 386 (2011) 73-80.
31. C. Belot, C. Filiatre, L. Guyard, A. Foissy, and M. Knorr, *Electrosynthesis of structured derivated polythiophenes: Application to electrodeposition of latex particles on these substrates*, Electrochem. Commun., 7 (2005) 1439-1444.
32. D. Zamariotto, B. Lakard, P. Fievet, N. Fatin-Rouge, *Retention of Cu(II)– and Ni(II)–polyaminocarboxylate complexes by ultrafiltration assisted with polyamines*, Desalination., 258 (2010) 87-92.
33. B. Cabot, A. Dertani, and A. Foissy, *Adsorption of poly(vinylimidazoles) onto silica surfaces*, Colloids Surf., A, 139 (1998) 287-297.
34. R. Zerrouk, A. Foissy, R. Mercier, Y. Chevallier, and J.-C. Morawski, *Study of Ca^{2+}-induced silica coagulation by small angle scattering*, J. Colloid Interface Sci., 139 (1990) 20-29.

35. C. Parneix, J. Persello, R. Schweins, and B. Cabane, How do colloidal aggregates yield to compressive stress?, Langmuir, 25 (2009) 4692-4707.
36. P. Jutzi, and U. Schubert, *Silicon Chemistry : From the atom to extended systems*, WiLEY-VCH, (2003) p.21.
37. H. Okamoto, Y. Sugiyama, and H. Nakano, *Systhesis and modification of silicon nanosheets and other silicon nanomaterials*, Chem. Eur. J. 17 (2011) 9864-9887.
38. J. Sritharathikhun, A. Moollakorn, S. Kittisontirak, and A. Limmanee, *High quality hydrogenated amorphous silicon oxide film and its application in thin film silicon solar cells*, Curr. Appl. Phys., 11 (2011) 517-520.
39. A. Lambertz, T. Grundler, and F. Finger, *Hydrogenated amorphous silicon oxide containing a microcrystalline silicon phase and usage as an intermediate reflector in thin-film silicon solar cells*, J. Appl. Phys. 109 (2011) 1131091-11310910.
40. A. M. Coclite, A. Milella, F. Palumbo, R. d'Agostino, *On the relationship between the structure and the barrier performance of plasma deposited silicon dioxide-like films*, Surf. Coat. Technol., 204 (2010) 4012-4017.
41. E. Erdem, N. Karapinar, and R. Donat, *The removal of heavy metal cations by natural zeolites*, J. Colloid Interface Sci., 280 (2004) 309-314.
42. H. Ghobarkar, O. Schaf, U. Guth, *Zeolites - from kitchen to space*, Prog. Solid State Chem., 27 (1999) 29-73.
43. S. Navalon, M. Alvaro, and H. Garcia, *Heterogeneous Fenton catalysts based on clays, silicas and zeolites*, Appl. Catal., B, 99 (2010) 1-26.
44. M.A. Keane, *The removal of copper and nickel from aqueous solution using Y zeolite ion-exchangers*, Colloidals Surf., A, 138 (1998) 11-20.
45. J.A. Balmer, A. Schmid, and S.P. Armes, *Colloidal nanocomposite particles: quo vadis?*, J. Mater. Chem., 18 (2008) 5722-5730.
46. L. Hao, C. Zhu, C. Chen, P. Kang, Y. Hu, W. Fan, and Z. Chen, *Fabrication of silica core-conductive polymer polypyrrole shell composite particles and polypyrrole capsule on monodispersed silica templates*, Synth. Met., 139 (2003) 391-396.
47. N. El Hawi, C. Nayral, F. Delpech, Y. Coppel, A. Cornejo, A. Castel, and B. Chaudret, *Silica Nanoparticles Grown and Stabilized in Organic Nonalcoholic Media*, Langmuir, 25 (2009) 7540-7446.
48. M. Kishida, T. Tago, T. Hatsuta, and K. Wakabayashi, *Preparation of silica-coated Rhodium nanoparticles using water-in-oil microemulsion*, Chem. Lett., (2000) 1108-1109.
49. C. Takai, M. Fuji and K. Fujimoto, *Skeletal Silica Nanoparticles Prepared by Control of Reaction Polarity*, Chem. Lett., 40 (2011) 1346-1348.
50. T. Nema, E.C. Chan, P.C. Ho, *Application of silica-based monolith as solid phase extraction cartridge for extracting polar compounds from urine*, Talanta. 82 (2010) 488-494.
51. Z.-G. Shi, Q.-Z. Guo, Y.-T. Liu, Y.-X. Xiao, and L. Xu, *Drug delivery devices based on macroporous silica spheres*, Mater. Chem. Phys., 126 (2011) 826-831.

52. Q. Meng, X. Zhang, C. He, P. Zhou, W. Su, and C. Duan, *A hybrid mesoporous material functionalized by 1,8-naphthalimide-base receptor and the application as chemosensor and absorbent for Hg^{2+} in water*, Talanta, 84 (2011) 53-59.

53. R. Brady, B. Woonton, M.L. Gee, A.J. O'Connor, *Hierarchical mesoporous silica materials for separation of functional food ingredients-A review*, Innovat. Food Sci. Emerg. Tech., 9 (2008) 243-248.

54. X. Liang, Yi. Xu, G. Sun, L. Wang, Y. Sun, and X. Qin, *Preparation, characterization of thiol-functionalized silica and application for sorption of Pb^{2+} and Cd^{2+}*, Colloids Surf., A, 349 (2009) 61-68.

55. M. Anbia, S.A. Hariri, S.N. Ashrafizadeh, *Adsorptive removal of anionic dyes by modified nanoporous silica SBA-3*, Appl. Surf. Sci., 256 (2010) 3228-3233.

56. S.H. Jung, K.I. Kim, J.H. Ryu, S.H. Choi, J.B. Kim, J.H. Moon, J.H. Jin, *Preparation of radioactive core-shell type 198Au@SiO_2 nanoparticles as a radiotracer for industrial process applications*, Appl. Radiat. Isot., 68 (2010) 1025-1029.

57. (a) S. M. Seo, E.J. Cho, S.J. Lee, K.C. Nam, S.-H. Park, and J.H. Jung, *A mesoporous silica functionalized by a covalently bound naphthalene-based receptor for selective optical detection of fluoride ion in water*, Microporous Mesoporous Mater., 114 (2008) 448-454. (b) Y. Kuthati, P.J. Sung, C.F. Weng, C.Y. Mou, and C.H. Lee, *Functionalization of mesoporous silica nanoparticles for targeting, biocompatibility, combined cancer therapies and theragnosis*, J. Nanosci. Nanotechnol., 13 (2013) 2399-2430.

58. R. Brüning, and D. Cottrell, *X-ray and neutron scattering observations of structural relaxation of vitreous silica*, J. Non-Cryst. Solids, 325 (2003) 6-15.

59. R.K. ILER, *The chemistry of silica. Solubility, polymerization, colloidal and surface properties, and biochemistry*, JOHN WILEY & SONS, New York, (1979) p. 47, 328.

60. Y. Jin, A. Li, S.G. Hazelton, S. Liang, C.L. John, P.D. Selid, D.T. Pierce, J. X. Zhao, *Amorphous silica nanohybrids: Synthesis, properties and applications*, Coordin. Chem. Rev., 253 (2009) 2998-3014.

61. P.S. Singh, *High surface area nanoporous amorphous silica prepared by dodecanol assisted silica formate sol-gel approach*, J. Colloid Interface Sci., 325 (2008) 207-214.

62. P. He, D. Jia, M. Wang, and Y. Zhou, *Improvement of high-temperature mechanical properties of heat treated C_f /geopolymer composites by Sol-SiO_2 impregnation*, J. Eur. Ceram. Soc., 30 (2010) 3053-3061.

63. M. Jafarzadeh, I.A. Rahman, and C.S. Sipaut, Optical properties of amorphous organo-modified silica nanoparticles produced via co-condensation method, Ceram. Int., 36 (2010) 333-338.

64. Y.F. Tao, W.G. Lin, L. Gao, J. Yang, Y. Zhou, J.Y. Yang, F. Wei, Y. Wang, and J.H. Zhu, *Low-cost and effective phenol and basic dyes trapper derived from the porous silica coated with hydrotalcite gel*, J. Colloid Interface Sci., 358 (2011) 554-561.

65. (a) H.E. Bergna, and W.O. Roberts, *Colloidal silica. Fundamentals and applications*, Taylor & Francis, (2006) p. 11, 528. (b) H. Madani, A. Bagheri, T. Parhizkar, A. Raisghasemi, and A. Ramezanianpoor, http//www.claisse.info/Proceedings.htm.

66. F. Branda, B. Silvestri, G. Luciani, and A. Costantini, *The effect of mixing alkoxides on the Stöber particles size*, Colloids Surf., A, 299 (2007) 252-255.

67. D.L Green, J.S Lin, Y.-F. Lam, M.Z.-C Hu, D.W. Schaefer, and M.T Harris, *Size, volume fraction, and nucleation of Stöber silica nanoparticles*, J. Colloid Interface Sci., 266 (2003) 346-358.

68. W.E. Müller, S. Engel, X. Wang, S.E. Wolf, W. Tremel, N.L. Thakur, A. Krasko, M. Divekar, and H.C. Schröder, *Bioencapsulation of living bacteria (Escherichia coli) with poly(silicate) after transformation with silicatein-alpha gene*, Biomaterials., 29 (2008) 771-779.
69. A. Hou , Y. Shi, and Y. Yu, *Preparation of the cellulose/silica hybrid containing cationic group by sol–gel crosslinking process and its dyeing properties*, Carbohydr. Polym., 77 (2009) 201-205.
70. H. Liu, W. Sha, A.T. Cooper, and M. Fan, *Preparation and characterization of a novel silica aerogel as adsorbent for toxic organic compounds*, Colloids Surf., A, 347 (2009) 38-44.
71. L.T. Arenas, C.W. Simm, Y. Gushikem, S.L. P. Dias, C.C. Moro, T.M.H. Costa, E.V. Benvenutti, *Synthesis of silica xerogels with high surface area using acetic acid as catalyst*, J. Braz. Chem. Soc., 18 (2007) 886-890.
72. L.T. Zhuravlev, *The surface chemistry of amorphous silica. Zhuravlev model*, Colloids Surf., A, 173 (2000) 1-38.
73. A. Foissy, and J. Persello, *The surface properties of silicas: surface group ionization on silicas*, JOHN WILEY & SONS, New York, (1998) p. 367-368.
74. P.B. Wagh, S.V. Ingale, *Comparison of some physico-chemical properties of hydrophilic and hydrophobic silica aerogels*, Ceram. Int., 28 (2002) 43-50.
75. P.M. Dove, and C.M. Craven, *Surface charge density on silica in alkali and alkaline earth chloride electrolyte solution*, Geochim. Cosmochim. Acta, 69 (2005) 4963-4970.
76. M. Kobayashi, F. Juillerat, P. Galletto, P. Bowen, and M. Borkovec, *Aggregation and Charging of Colloidal Silica Particles: Effect of Particle Size*, Langmuir, 21 (2005) 5761-5769.
77. (a) E. Papirer, *Adsorption on silica surfaces*, Marcel Dekker, Inc. New York, 90 (2003) p. 317, 442, 708. (b) P.K. Pal, S. Patel, B. KK. Mishra, *Chemical modification of silica surface by immobilization of functional groups for extractive concentration of metal ions*, Talanta, 62 (2004) 1005-1028.
78. (a) Inorganic Materials for Catalyst Innovation; AEROSIL, AEROXIDE and SIPERNAT, Metal Oxides and Silica Based Materials Industry Information, 1-20, (b) J.B. Peri and A.L. Hensley, Jr., *The Surface Structure of Silica Gel*, J. Phys. Chem. 72 (1968), 2926-2933. (b) J.B. Peri and A.L. Hensley, Jr., *The Surface Structure of Silica Gel*, J. Phys. Chem. 72 (1968), 2926-2933.
79. A.F. Holleman, E. Wiberg, *Inorganic Chemistry*, San Diego: Academic Press, ISBN 0-12-352651-5, (2001).
80. X. Xu, and S.A. Asher, *Synthesis and utilization of monodisperse hollow polymeric particles in photonic crystals*, J. Am. Chem. Soc., 126 (2004) 7940-7945.
81. N.N. Greenwood, A. Earnshaw, *Chemistry of the Elements*. Oxford: Pergamon, ISBN 0-08-022057-6, (1984) p. 393-399.
82. D.W. Barnum, *Reaction of catechol with colloidal silica and silicic acid in aqueous ammonia*, Inorg. Chem., 11 (1972) 1424-1429.
83. J. Livage, Les procédés sol-gel, L'Act. Chim. (R), 10 (1997) 4-10.
84. J.D. Hunt, A. Kavner, E.A. Schauble, D. Snyder, and C.E. Manning, *Polymerization of aqueous silica in H_2O-K_2O solutions at 25-200 °C and 1 bar to 20 kbar*, Chem. Geol., 283 (2011) 161-170.
85. Y. Huang, J.E. Pemberton**,** *Fabrication of colloidal arrays by self-assembly of sub-100 nm silica particles*, Colloids Surf., A, 377 (2011) 76-86.

86. J. Depasse, *Coagulation of Colloidal Silica by Alkaline Cations: Surface Dehydration or Interparticle Bridging?*, J. Colloid Interface Sci., 194 (1997) 260-262.

87. (a) C.A.M. Baltar, J.F. Oliveira**,** *Flocculation of colloidal silica with polyacrylamide and the effect of dodecylamine and aluminium chloride pre-conditioning*, Mineral. Eng., 11 (1998) 463-467. (b) J. Eisenlauer, and E. Killmann, *Stability of colloidal silica (aerosil) hydrosols. I Preparation and characterization of silica (aerosil) hydrosols*, J. Colloid Interface Sci., 74 (1980) 108-119. (c) Y. Zhang, H. Yang, K. Zhou, and Z. Ping, *Synthesis of an affinity adsorbent based on silica gel and its application in endotoxin removal*, React. Funct. Polym., 67 (2007) 728-736, (d) A. Goswami, and A.K. Singh, *Silica gel functionalized with recetophenine: synthesis of a new chelating matrix and its application as metal ion collector for their flame atomic absorption spectrometric determination*, Anal. Chim Acta, 454 (2002) 229-240.

88. G. Dhoot, R. Auras, M. Rubino, K. Dolan, and H. Soto-Valdez, *Determination of eugenol diffusion through LLDPE using FTIR-ATR flow cell and HPLC techniques*, Polym. 50 (2009) 1470-1482.

89. (a) A.M. Efimov, and V.G. Pogareva, *IR absorption spectra of vitreous silica and silicate glasses: The nature of bands in the 1300 to 5000 cm^{-1} region*, Chem. Geol., 229 (2006) 198-217.
(b) B. A. Morrow, and A. J. McFarlan, *Surface Vibrational Modes of Silanol Groups on Silica*, J. Phys. Chem., 96 (1992) 1345-1400.

90. A.M. Donia , A.A. Atia, W.A. Al-amrani, and A.M. El-Nahas, *Effect of structural properties of acid dyes on their adsorption behaviour from aqueous solutions by amine modified silica*, J. Hazard. Mater., 161 (2009) 1544-1550.

91. C. Bartholome, E. Beyou, E. Bourgeat-Lami, P. Chaumont, N. Zydowicz, *Nitroxide-mediated polymerization of styrene initiated from the surface of fumed silica. Comparison of two synthetic routes*, Polym. 46 (2005) 8502-8510.

92. Q. Luo, and P. Eh. Hovsepian, *Transmission electron microscopy and energy dispersive X-ray spectroscopy on the worn surface of nano-structured TiAlN/VN multilayer coating*, Thin Solid Films., 497 (2006) 203-209.

93. D. Lubda, W. Lindner, M. Quaglia, C.D.F.V. Hohenesche, and K.K. Unger, *Comprehensive pore structure characterization of silica monoliths with controlled mesopore size and macropore size by nitrogen sorption, mercury porosimetry, transmission electron microscopy and inverse size exclusion chromatography*, J. Chromatogr. A, 1083 (2005) 14-22.

94. A.M. Donald, *Environmental scanning electron microscopy for the study of 'wet' systems*, Curr. Opin. Colloid Interface Sci., 3 (1998) 143-147.

95. Y.L. Lyubchenko, *Preparation of DNA and nucleoprotein samples for AFM imaging*, Micron, 42 (2011) 196-206.

96. E.E. Bodor, J. Skalny, S. Brunauer, J. Hagymassy Jr., and M. Yudenfreund, *Pore structures of hydrated calcium silicates and portland cements by nitrogen adsorption*, J. Colloid Interface Sci., 34 (1970, 560-570.

97. S. Brunauer, P. H. Emmett, and E. Teller, *Adsorption of Gases in Multimolecular Layers*, J. Am. Chem. Soc., 60 (1938) 309-319.

98. A. Antunes, F.V. Gozzo, M. Nakamura, A.M. Safatle, S.L. Morelhão, H.E. Toma, and P.S. Barros, *Analysis of the healthy rabbit lens surface using MAC Mode atomic force microscopy*, Micron, 38 (2007) 286-90.

99. R. Tantra, P. Schulze, and P. Quincey, *Effect of nanoparticle concentration on zeta-potential measurement results and reproducibility*, Particuology, 8 (2010) 279-285.

100. S. Bai, S. Urabe, Y. Okaue, and T. Yokoyama, *Acceleration effect of sulfate ion on the dissolution of amorphous silica*, J. Colloid Interface Sci., 331 (2009) 551-554.

101. L. Peng, W. Qisui, L. Xi, and Z. Chaocan, *Zeta-potentials and enthalpy changes in the process of electrostatic self-assembly of cations on silica surface*, Powder Technol., 193 (2009) 46-49.

102. D.G. Dalgleish, and F.R. Hallett, *Dynamic light scattering: applications to food systems*, Food Res. Int., 28 (1995) 181-193.

103. G. Lee, S. Murray, and H. Rupprecht, *The dispersion of hydrophilic and hydrophobic flame-hydrokysed silicas in short-chained alkanols*, Colloid. Polym. Sci. 265 (1987) 535-541

Chapter 2

Surface-Functionalization of Silica

Introduction

As outlined in the preceding chapter, Silica is known as a good supporting material because of its large surface area, high mass exchange characteristics, non-swelling, and excellent mechanical resistance. Moreover, the presence of surface-bound silanol groups permits easily a chemical modification of this inorganic polymer by introduction of new functional groups. This kind of surface modification provides a unique opportunity to modulate the interface properties of a solid support, retaining in many cases its physical properties like porosity and mesoscopic order. For example, it was shown mesoporous silica SBA-15 can be grown in the presence of Pt nanoparticles (2.9 nm diameter) preserving the mesoscopic order, the final pore lattice parameter in SBA-15 rising around 10% [1]. A functionalized silica material should have a sufficient chemical stability under experimental conditions and when used as sorbent, a high adsorption capacity combined with a sufficient selectivity. Silica surfaces can be modified by physical or chemical treatment as summarized in Fig. 38.

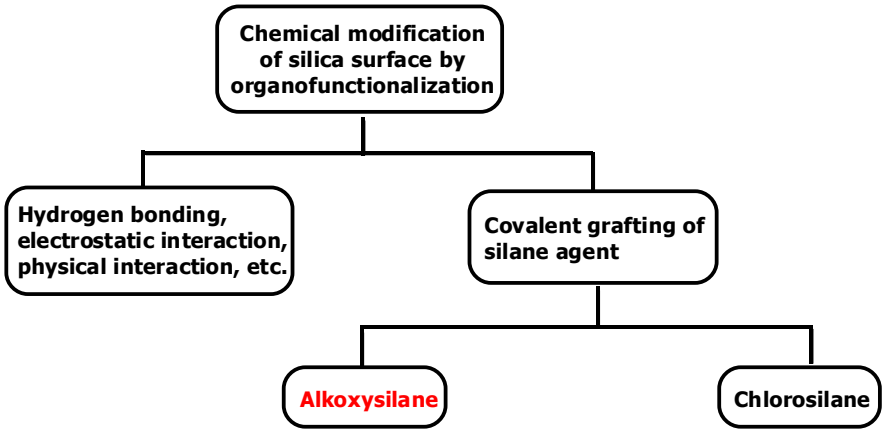

Fig. 38 Overview of chemical modifications of silica surfaces

(i) The physical treatment includes thermal and hydrothermal processes leading to changes of the density of silanol and siloxane concentration on the silica surface. For example, Zhuravlev and Potapov reported a diminution of silanol groups on the silica surface (4.9 Si-OH /nm^2 to 2 Si-OH/nm^2) when the temperature was raised from 190 ^{o}C to 400 ^{o}C [2].

(ii) Chemical treatment leads to a change in the chemical characteristic of the surface of silica. This chemical modification can be achieved by attachment of functional groups, which can be introduced using two main approaches:

- The first one implies interaction of organic molecules to silica via hydrogen bonding, electrostatic interaction, etc. For example, the surface-grafted organometallic catalyst $Ru(NCMe)_3(sulphos)](OSO_2CF_3)/SiO_2$ and/or $(Ru(II)/SiO_2$ was obtained by immobilization of $[Ru(NCMe)_3(sulphos)](OSO_2CF_3)$ and/or (Ru(II)-sulphos) on silica [3,4]. The binding modes of both complexes involve a hydrogen bonding between silanol groups of the silica surface and SO_3^- groups from both the sulphos ligand $[^-O_3S(C_6H_4)CH_2C(CH_2PPh_2)_3$ and the $CF_3SO_3^-$ anion (trifluoromethanesulfonate) as depicted in Fig. 39. A comparative study of the hydrogenation of various heterocycles by either these silica-immobilized Ru(II) complexes or Ru(0) nanoparticles deposited on the same support has been performed.

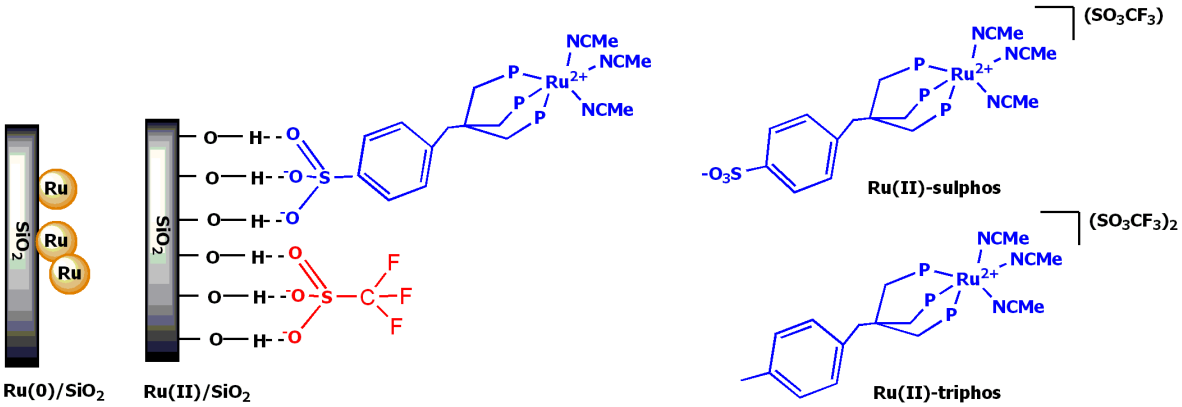

Fig. 39 Immobilization of Ru(0) nanoparticles and a Ru(II) catalyst on mesoporous silica

Concerning the adsorption of the organic polymers poly(vinylimidazole) and quaternized poly(vinylimidazole) on the silica surface, our laboratory has established that the electrostatic forces between these cationic polyelectrolytes and the silica surface depend both on pH and ionic strength [5,6]. In our laboratory, Foissy has also studied the adsorption of $ZnSO_4$ on a silica surface in function of the pH. It was found that Zn(II) adsorption starts around pH 4 and the principal surface species is the bidentate complex $(SiO)_2Zn$ up to pH 9. Furthermore, some monodentate ($SiOZn^+$) species are formed at around pH 6, and formation of SiZnOH starts at pH 9 [7a]. A sorption modelling approach has also been applied for the uptake of Cu(II) ions by silica. This study revealed that the simple assumption of formation of SiO^-CuOH^+ species does not match in a satisfying manner with the experimental and modelling results. Instead, additionally sorption of the dimeric copper species $Cu_2(OH)_2^{2+}$ must be taken in consideration [7b].

Another inorganic example is the preparation of Aerosil 200 supported dodecatungstic heteropolyacid ($H_3PW_{12}O_{40}$) obtained by impregnation in water. Spectroscopic studies (IR, Raman, XPS and solid-state ^1H MAS NMR) show that three protons in $H_3PW_{12}O_{40}$ react with silanol groups by an acid-base mechanism. The impregnation process leads to formation of $[\equiv SiOH_2]_3\ PW_{12}O_{40}$ surface species. These species remain stable until 300 ^oC [8]. Lanthanum sulfonate was immobilized on mesoporous silica (SBA-15) through ionic interaction and probed as catalyst in allylation reaction of carbonyl compounds with tetraallyltin and Diels-Alder cycloaddition of 3-acryloyl-1, 3-oxazolidin-2-one with cyclopentadiene (Fig. 40) [9].

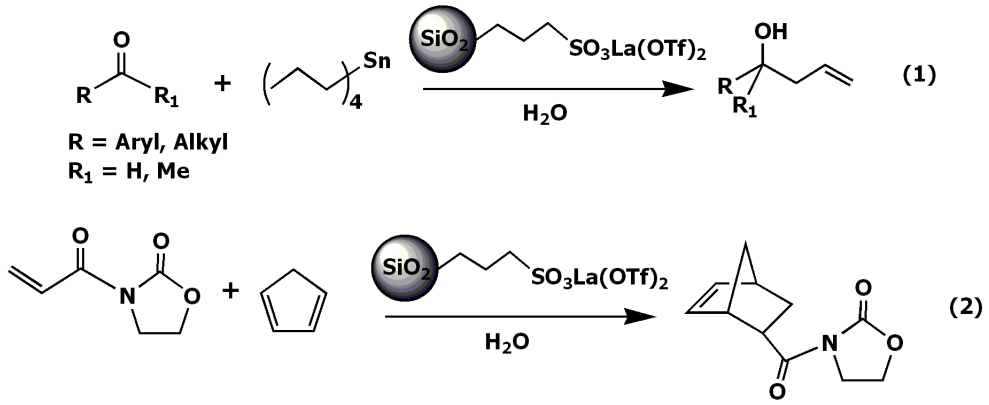

Fig. 40 Silica-immobilized La(III) as catalysts for organic transformations

- The second approach is strong interaction via covalent bonding. For example, the modification of silica surfaces by aluminium alkyls constitutes a versatile method to covalent surface functionalization. The group of Bassett has recently modified a silica support with aluminum alkyl [Al(*i*Bu)$_3$/Et$_2$O)] by impregnation [10a]. The reaction, which implies an unusual protonolysis-alkyl transfer between the organometallic reagent and the acidic silanol groups is shown in Fig. 41.

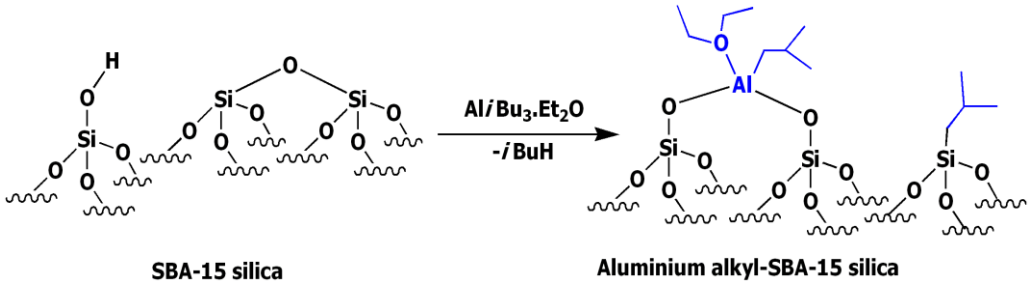

Fig. 41 Surface modification by aluminum alkyl impregnation on SBA-15 silica

The group of Caseri has also achieved the modification of Aerosil 200 by reaction with trialkoxymethanes, triphenoxymethane, acetals, ketals, orthoesters and orthocarbonates [10b,c]. However, undoubtedly the most common method is the use of chlorosilane and

alkoxysilane agents bearing organic substituents. For this work, this organo-functionalization by modifier agents appeared promising because the condensation of such silane compounds onto the surface of silica occurs under mild conditions and is easy to realize even in a multigram-scale. Other advantages are the relative low costs of the silane agent and the strong bonding between the substrate and the surface. Moreover, by a proper choice of the functional end-groups of the $Si(CH_2)_nX$ chain, an effective binding site for the capture of metal ions can be generated. The chemical modification of the silica surface utilizing coupling agent is discussed in detail in following section.

Results and Discussion

Grafting of Organosilane Agents on a Silica Surface - State of the Art

The most convenient way to alter a silica surface through chemical modification via covalent grafting is the immobilization of the organic functional group onto the SiO_2 surface. This derivatization of the silica surface involves covalent coupling of the silane agent with silanol groups of the silica surface. The general formula of a silane agent can be represented as $F_nSiX_{(4-n)}$ (n = 1, 2, 3), where **F** contains organic functional groups, and **X** represents a hydrolysable group such as alkoxy -OR or halide [11]. An example of condensation of a chlorosilane in order to use it as a coupling agent in the preparation of a silica-supported carbene-Cu(II) composite, which can be used as a catalyst. First, the chlorosilane agent was grafted onto the surface of silica as represented in Fig. 42. In a second step, the SiO_2-grafted silane was further *N*-alkylated with various imidazoles [12]. However, one inconvenient of this method is the extrusion of hydrogen chloride liberated during the initial condensation reaction.

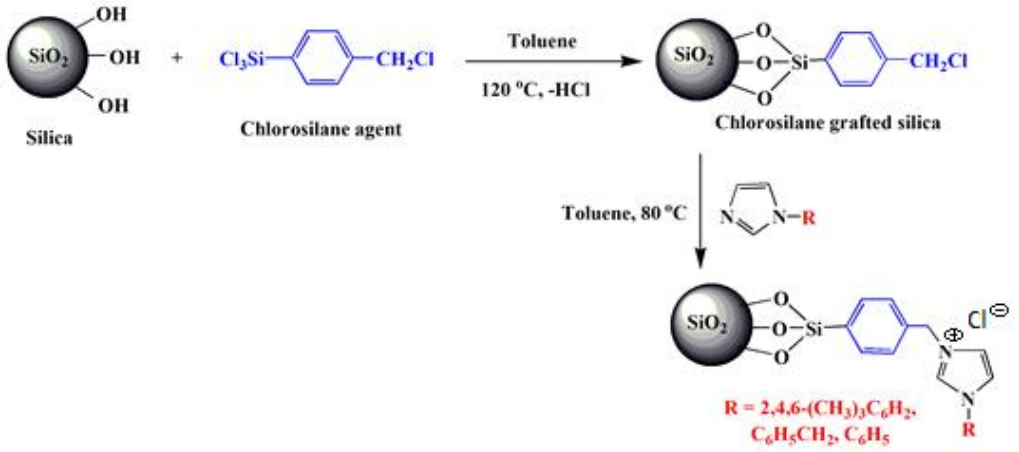

Fig. 42 Treatment of a SiO_2 surface with trichloro(4-(chloromethyl)phenyl)silane and post-functionalization by *N*-alkylation. The subsequent Cu-complexation sequence is not shown.

In the case of alkoxysilanes, the most common alkoxy groups are -OMe and -OEt, which produce less harmful methanol and ethanol as elimination-products. Therefore, the alkoxysilane route is generally preferred over the chlorosilane condensation. Some representative alkoxysilane coupling agents, which have been used to incorporate onto silica surfaces, are summarized in Table 2.1.

Table 2.1 Some alkoxysilane coupling agents used for modification of silica surfaces

Name	Abbreviation	Structure
3-Chloropropyltrimethoxysilane	CPMS	$(MeO)_3Si$–Cl
3-Mercaptopropyltrimethoxysilane	MPS	$(MeO)_3Si$–SH
3-Methacryloxylpropyltrimethoxysilane	MPTMS	$(MeO)_3Si$–O–C(=O)–C(CH_3)=CH_2
Aminopropyltrimethoxysilane	APTMS	$(MeO)_3Si$–NH_2
Aminopropyltriethoxysilane	APTES	$(EtO)_3Si$–NH_2
Cyanopropyltriethoxysilane	CPTES	$(EtO)_3Si$–CN

These organosilanes play the role of coupling agent or precursor [13]. Advantages of organosilanes-grafted silica are apart from the strong binding on the silica surface are the possibility to post-functionalize the amino, halide, thiol and nitrile endgroups F. The typical schematic elaboration of alkoxysilane-functionalized silica particles is represented in Fig. 43.

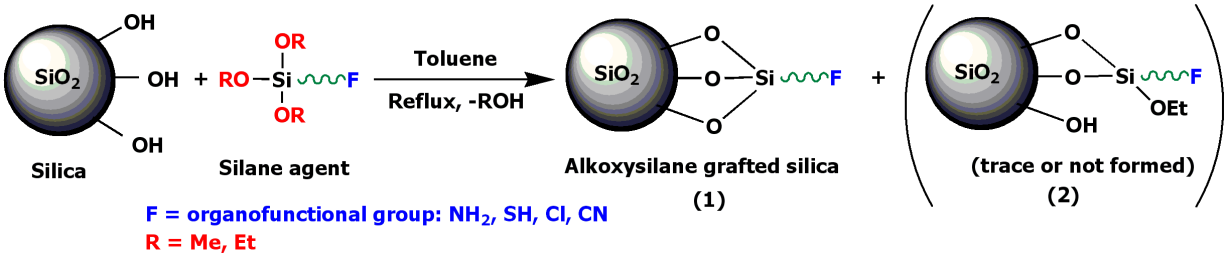

Fig. 43 Schematic representation of covalent grafting of an alkoxysilane onto a silica surface

Nowadays, an impressive and rapidly growing number of articles deal on the condensation of alkoxysilanes on SiO_2. Therefore just a very limited number of recent examples is presented below:

Timofte and Woodward used solid-state ^{13}C NMR to characterize a $(EtO)_3Si(CH_2)_3NH_2$-functionalized SiO_2 (**1**) [14]. The spectra show sharp resonances at 5.2, 22.7, and 39.9 ppm for the methylene chain. The observation of additional weak signals at 12.1 and 53.9 ppm attributed to OEt groups indicates the co-existence of small amount of species (**2**) due to incomplete condensation (Fig. 44). In order to elaborate a sorbent for the extraction of uranium(VI) ions, the CPMS agent was grafted on activated silica gel. Subsequent post-functionalization of the CPMS-grafted silica **SiO-CPMS** with sulfasalazine (SSZ) yielded silica **SiO-CPMS-SSZ**, which in turn can interact with uranyl ions [15].

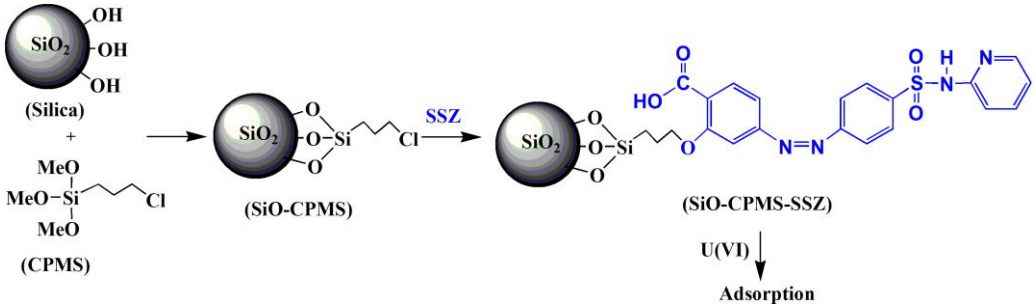

Fig. 44 Synthesis of CPMS-grafted silica gel with sulfasalazine (SSZ)

Fig. 45 shows an example of functionalization of silica utilizing **MPS** as coupling agent. MPS was grafted on silica gel to obtain the MPS-grafted silica (**MPS-silica**). The monomer *N*-didodecylglutamidemaleimide (DGMI) was copolymerized with octadecyl acrylate (ODA) from MPS-grafted silica to form alternating copolymer-grafted silica (poly(ODA-*alt*-DGMI)-grafted silica). The reaction scheme for the synthesis of poly(ODA-*alt*-DGMI)-grafted silica is shown in Fig. 46 [16].

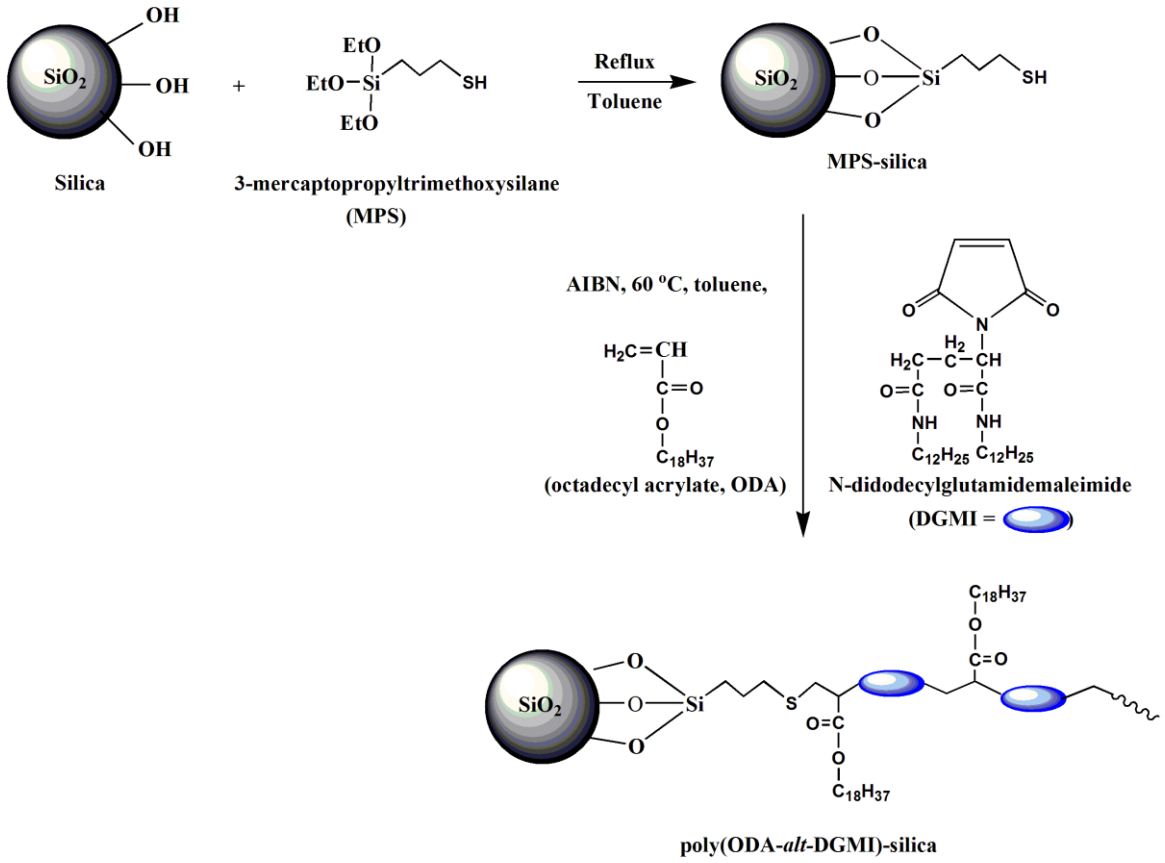

Fig. 45 Synthesis of MPS-grafted silica with *N*-didodecylglutamidemaleimide and octadecyl acrylate

Exploiting the high affinity of the soft Hg(II) ions toward thiol groups, MPS-treated mesoporous silica has also been used by the group of Walcurius to study the absorption of mercury nitrate [17]. Mercury(II) coordination to MPS-treated mesoporous silica at varying pH is shown in Fig. 46.

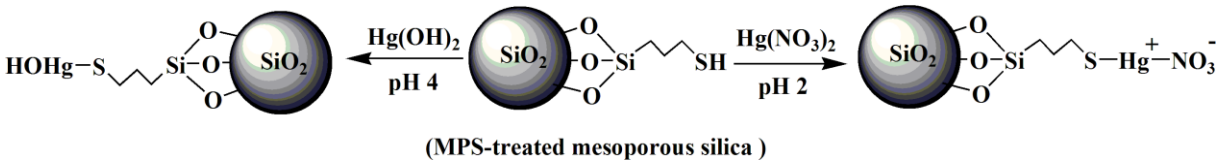

Fig. 46 Formation of charged and neutral Hg(II) complexes resulting from adsorption of Hg(II) on MPS-functionalized silica at various pH

The coupling agent MPTMS was used to silanize the surface of Aerosil 200 in toluene as shown in Fig. 47. In this process, the MPTMS was first hydrolysed and condensed, and then reacted with the silica. The ^{29}Si NMR spectra of the MPTMS-grafted silica reveal that

MPTMS molecules were grafted by one or two siloxane bonds, giving rise to resonance at -49 and -58 ppm [18].

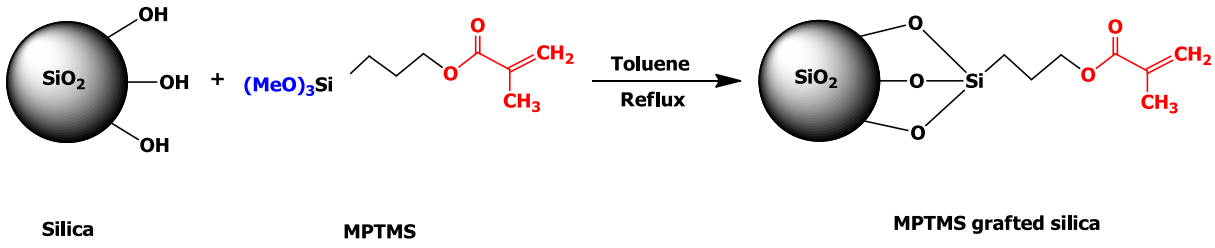

Fig. 47 Synthesis of MPTMS-functionalized silica (Aerosil A200 V)

To resume, alkoxysilane agents are coupling agents allowing a facile modification of inorganic supports under relative mild conditions. Functional groups at the end-chain of the grafted silica have strong affinity to bind inorganic or organic molecules [14-22]. The covalent bonding of the grafted silica materials can also enhances the long-term stability of the silica in acidic medium [23]. A wide range of alkoxysilane reagents is nowadays commercially available by various suppliers. The sum of all these advantages explains the "success story" of these agents giving rise to an import number of articles dealing on their use for surface-silanization and sol-gel chemistry.

For this work, both aminopropyltriethoxysilane and cyanopropyltriethoxysilane have been chosen to prepare SiO_2 particle bearing amino- and/or carboxyl groups on the surface. It is well-established that due to the presence of a electron pair (non-bonding doublet) on the nitrogen atom of silica surface bound amino group and the negative charges of carboxyl groups these groups may act as donor sites allowing complexation of metal cation ions i.e. Cu(II), Ni(II), Hg(II), V(I), etc. in aqueous solution [24-26]. Silanization of the surface of the SiO_2 particles used in this work with APTES and/or CPTES was therefore expected to enhance the selectivity and capacity for metal adsorption [27]. Although a lot of work has been published concerning the silanization of various silica surfaces, we are just aware of one work on the functionalization of Aerosil 200 microparticles with APTES or CPTES [28]. Therefore, these two strategies are presented herein in detail to evaluate the impact of the intrinsic characteristics of Aerosil 200 (size effect, specific surface area and morphology, surface charge and z-potential …). First is presented the preparation and characterization of APTES-functionalized Aerosil 200. Then the chemical modification of our silica particles with CPTES is described.

2.1. Functionalization of Silica with APTES and APTMS

The covalent coupling between silica and alkoxysilanes often employs APTES **(3)**, which possesses three -O-CH_2-CH_3 groups and a propyl chain terminated with an amino group. Silanization of silica with APTES is accomplished by refluxing silica with APTES in dry toluene to allow a homogenous diffusion of the silane and coverage of the silica surface [29]. The condensation process of surface silanol groups with the ethoxy groups of APTES liberates ethanol (Fig. 48).

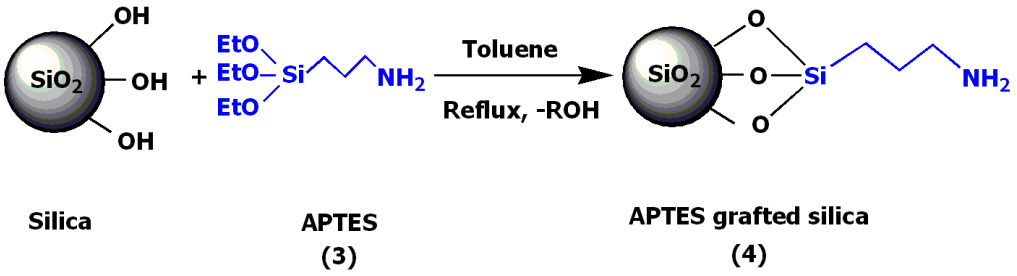

Fig. 48 Surface modification of silica by grafting with APTES

In parallel to our work, this procedure has been used by P. Punyacharoennon and his team to condense APTES on the surface of Aerosil 200 [28a]. After initial reaction in toluene, a methanol : water mixture was added. It was found that the amino group content of APTES-grafted silica increased with an increase of the amount of water (methanol : water ratios 4 : 1 and 2 : 1 were used) and the reaction time (72 hours). The resulting material has then been used for post-functionalization to elaborate a composite covered with a hyperbranched polyamidoamine polymer layer. Very recently, Aerosil 200 has also been silanized with APTMS. Quantification of the silanization indicated the presence of 3-4 reactive NH_2 groups per nm^2 of Aerosil, which was then treated with a series of acid anhydrides to yield more stable amidoalkyl and imidoalkyl silica [28b]. Some other selected examples of silanization reactions using different types of alkoxysilating agent bearing amino groups and their grafting on silica (porous silica obtained via sol-gel process and/or nonporous silica) are presented below.

For example, mesoporous SBA-15 silica was functionalized with different types of three organic sources (3-aminopropyltrimethoxysilane (APTMS), [1-(2-aminoethyl)-3-aminopropyl] trimethoxysilane, and [1-(3-(trimethoxysilyl)-propyl] - diethylenetriamine) by grafting processes. It was found that the resulting amine-functionalized silicas exhibit high amino group contents (up to 1.8 mmol g^{-1}), the amino content depending on the different chain length of initial alkoxysilating agents [24a]. For another mesoporous silica silanized

with 3-aminopropyltrimethoxysilane the grafted APTMS amount was determined by TGA to be 1.4 molecules of APTMS per nm^2, corresponding to 1.6 mmol g^{-1} [24b]. Note that is known that the grafting density can depend on the concentration of APTES used [24b].

Noteworthy is also the observation that (evidenced my microcalorimetry and FT-IR) this NH_2-grafted silica reacts chemically with CO_2 to form carbamate and carbamic acid species, whereas neat silica only interacts with CO_2 by physisorption [24c].

Amino-modified ordered mesoporous silica (APS-MCM-41) was also evaluated. In a first step, MCM-41* silica was prepared by stirring tetraethoxysilane (TEOS) with cetyltrimethylammonium bromide (CTAB) exploiting the interaction between the positive charge (CTA^+) of CTAB and the negative charge ($\equiv SiO^-$) of silica. In a second step, the calcined MCM-41 was further reacted with APTES to produce the APTES-grafted silica as shown Fig. 49. This material has then been evaluated as nano-sorbent for the removal of chlorophenols from aqueous media [30].

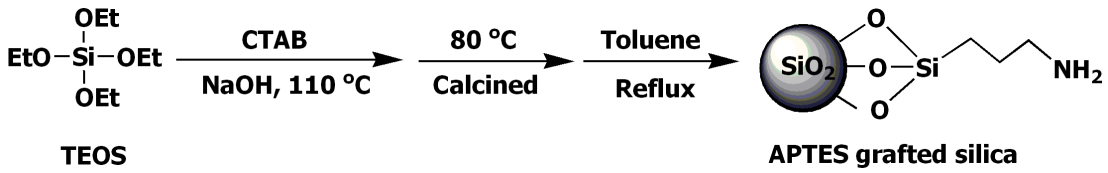

Fig. 49 Synthesis of amino-modified ordered mesoporous silica

*MCM-41 is a member of family of mesoporous silicate materials with a pore size in the broad range of 13-100 Å, whose network is formed by an array of parallel hexagonal channels of about 3.5 nm.

Figure 50 summarizes some other reactions. The preparation of the dioctadecyl L-glutamide-derived lipid-grafted porous silica particles (**5**) includes coupling of *N, N'*-didodecyl-L-glutamide with APTMS-silica particle in THF using diethylphosphorocyanide as a condensing agent [31]. The histidine-grafted composite **(6)** was obtained in a two-step sequence: Condensation of APTES-SiO_2 with glutaraldehyde yielded first an imine, which was than reacted with histidine [32]. Ammonium-functionalized silica was obtained by acidification of amine-grafted silica with hydrochloric acid solution. This protonation converts the amino groups to positively charged ammonium moieties **(7)** [33]. NH_2-grafted silica has also been reacted with succinic anhydride in toluene to provide the carboxyl-functionalized silica **(8)** linked through an amide group [34]. An organometallic surface modification has been achieved by reaction of ferrocene aldehyde with APTES-grafted silica (imine condensation) to give the interesting hybrid material **(9)**. Survey of internal surface of

a pellet of this material by electron microscopy coupled to Fe-EDX back-scatter techniques revealed that the ferrocenyl sites were on average evenly distributed across the entire sample [14].

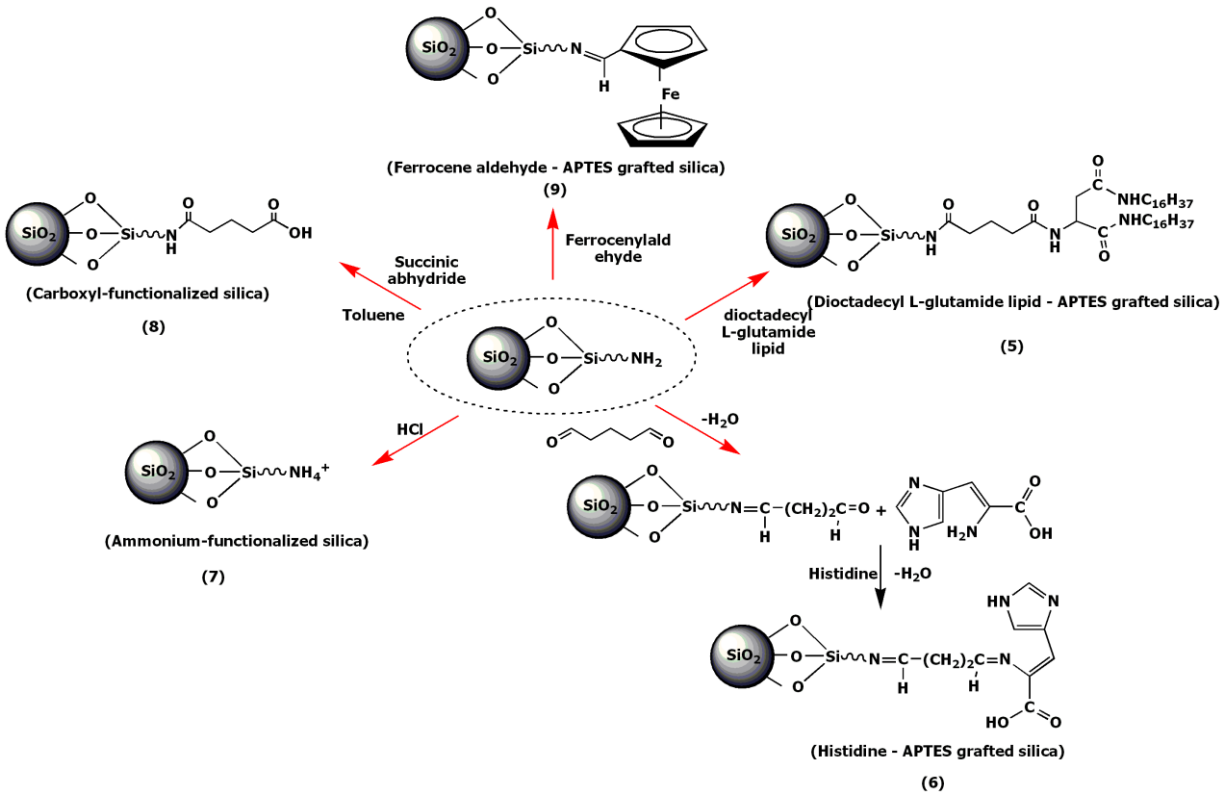

Fig. 50 Preparation of composites by reaction of APTES-grafted silica with various organic and organometallic reagents

In this work, the APTES-grafted Aerosil 200 was prepared according to the procedure represented in Fig. 48. The amine grafted silica material **$SiO_2(NH_2)$** was then characterized by FT-IR spectroscopy in order to confirm the presence of amino groups on the silica surface. The quantity of amino-groups contained on the surface was also measured by the Kjeldahl method and Elemental analysis. Characterization of the **$SiO_2(NH_2)$** composites was also done by BET surface area measurements, SEM, and AFM. Furthermore, the physicochemical characteristics in aqueous solution such as pH, conductivity, zeta potential, and hydrodynamic particles size have been investigated and are discussed.

2.1.1. The IR spectrum of functionalized Aerosil particles

Three major bands, namely the -OH stretching vibration band due to physisorbed water (hydrogen-bonded to silanol groups) [35], stretching vibration of -Si-O-Si- (siloxane backbone), and bulk mode of **SiO_2** at 3411 cm^{-1}, 1093 cm^{-1} (vs) and 804 cm^{-1} (m),

respectively are found in amine-functionalized silica as shown in Fig. 51. The appearance of a weak band at 2972 cm^{-1} and 1654 cm^{-1} is assigned to the stretching vibration of CH_2 groups and primary amine (N-H) bending from APTES molecules, respectively [22, 29, 36]. This gives an indication of the success of modification of silica particle. In comparison with literature, for APTES-grafted Aerosil 200 the new absorption band at 2932 cm^{-1} and 1640 cm^{-1} are assigned to C-H stretching (correspond with the absorption characteristics of APTES spectrum) and H-O-H bending vibration (corresponding to adsorbed water) [24b]. Moreover, in our **$SiO_2(NH_2)$** spectrum the band at around 1597 is not found this may be due to low concentration of APS molecules. The band at 3411 cm^{-1} is shifted to higher wave number (3479 cm^{-1}) due to the interaction between the hydroxyl groups on silica with the amine groups of the APTES reagent [28b].

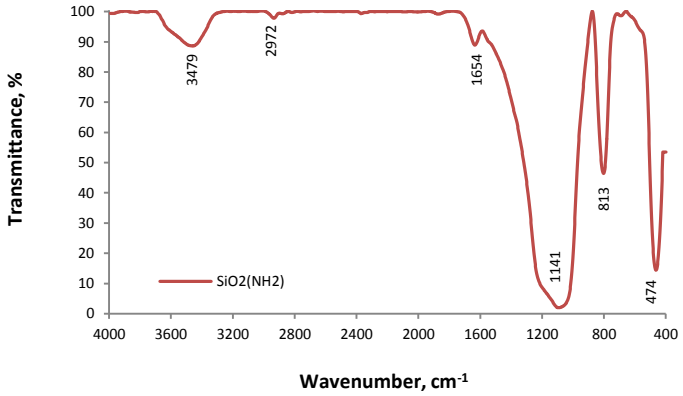

Fig. 51 The FT-IR spectrum of **$SiO_2(NH_2)$**

2.1.2 Determination of the N-content by Elemental analysis and by the Kjeldahl method

The amino content of two types of grafted silica was determined by Elemental analysis and the Kjeldahl method (Table 2.2) [37]. The carbon, hydrogen, and nitrogen content obtained from Elemental analysis was found to be 2.41%, 0.51%, and 0.76%, respectively**.** The Kjeldahl method consists in three analysis steps : digestion, distillation, and titration. The nitrogen content obtained from the Kjeldahl method is about 0.82 % for **$SiO_2(NH_2)$**.

Elemental analysis allows the calculation of the covering of our APTES-grafted silica. A nitrogen percentage of 0.76% was calculated for **$SiO_2(NH_2)$** corresponding to 4.75×10^{-4} mol of amine functions ($-NH_2$) per gram of silica (after a reaction time of 12 h). For comparison, the amino content of APTES-grafted Aerosil 200 was found to be 5.46×10^{-3} mol per gram of silica after a reaction time of 72 hours using a methanol to water 2 : 1 ratio according the protocol described in ref. 28a. This important discrepancy between our protocol and that of ref. 28a requires undoubtedly a re-examination.

Table 2.2 Elemental analysis of **$SiO_2(NH_2)$**

Sample	Elemental analysis (%, w/w)			Kjeldahl method (%, w/w)
$SiO_2(NH_2)$	C	H	N	N
	2.41	0.51	0.76	0.82 ± 0.02
SiO_2	Elemental Analysis, (Atomic %)*			
	Si	O	Cl	K
	64.6	34.7	0.2	0.2

*****EDS analysis gave the percentage by number of atoms (wt %) of each of the elements identified

2.1.3 BET specific surface

The BET specific surface area of the **$SiO_2(NH_2)$** was investigated and determined to about 131± 4 m^2/g. This BET value of the **$SiO_2(NH_2)$** composite is reduced compared to that of native silica (182 ± 4 m^2/g) as shown in Table 2.3. This can be explained by an aggregation of the functionalized silica particles. Therefore, the BET value of the amine-grafted silica is lower than neat silica [38]. Our result is in agreement with BET data from literature, the BET value decreases with an increase of the surface density of amino groups [39].

Table 2.3 The BET specific surface value of grafted silica with amine groups

No.	Sample	BET, m^2/g
1	**SiO_2**	182 ± 4
2	**$SiO_2(NH_2)$**	131 ± 4

To obtain more information about the grafting density (loading) [13], the BET value was used to calculate the amine grafting density or surface coverage, Γ (μ mol m^{-2}), as follows (equation 1):

$$\Gamma = fc\ 10^6 / [(M_c\ nc - fc\ M_{group})\ S_{BET}]$$

fc is the mass fraction of carbon in the sample, M_c is the molecular weight of carbon, nc is the number of carbon atoms within the grafted ligand, M_{group} is the molecular weight of the grafted ligands; it means the difference between the molecular weight of the ungrafted reagent and that of the leaving group and S is the specific surface of the silica ($m^2.g^{-1}$).

The grafting density of **$SiO_2(NH_2)$** calculated from the carbon content is 3.86 μmol m^{-2}, corresponding to 2.32 APTS groups/nm^2. A similar calculation using the nitrogen percentage resulted in a grafting density of 3.12 μmol m^{-2}, so the results show a slight discrepancy. M. Lazghab *et al.* reported that the grafting density of APTES onto silica with a higher porosity of 480 $m^2.g^{-1}$ (MP silica 63-200, Echochrom) was 2.88 μmol.m^{-2}, equivalent

to 1.79 APTS groups/nm^2 [13]. It can be concluded that the chosen procedure for the preparation of amine-grafted silica seems to be a suitable one for chemically modification of a silica surface containing both geminated and isolated silanol functions [40].

2.1.4 Determination of the effective specific surface

Exact knowledge of the specific surface area of silica is essential to express concentration of reactive surface species. We have attempted to obtain information concening the specific surface of activated silica and amine-grafted silica employing the CTAB adsorption technique [41a]. Table 2.4 shows that the specific surface of **$SiO_2(NH_2)$** decreased to just one third compared to that of non-grafted silica. The same trend has been noticed for the mesoporous silica cited in ref. 24b and 24c. In the first case, the BET surface area drops from 910 to 336 m^2/g after silanization with APTES, in the latter case, the BET surface area drops from 672 to 409 m^2/g after silanization with APTMS. However the values obtained by the CTAB adsorption technique appear much too low, since the BET surface of Aerosil 200 should be about 200 m^2/g as shown in Table 1.3. It therefore seems that the CTAB adsorption technique is not appropriate to give reliable results in the case of Aerosil 200. Perhaps the experimental procedure needs to be modified to afford more realistic values. Note that the surfactant CTAB is also known to adsorb as bi- or multilayer on silica surfaces [41b].

Table 2.4 Effective specific surface value of silica and amine-grafted silica materials

Material	Specific surface by CTAB, m^2/g
SiO_2	36.1 ± 2
$SiO_2(NH_2)$	10.4 ± 1

2.1.5 Examination of the surface morphology of $SiO_2(NH_2)$ by SEM and AFM

The SEM image of the amine functionalized silica composite is shown in Fig. 52. In these images, the amine-functionalized silica composites show a more uniform texture and a more homogeneous surface compared to native Aerosil 200 (Fig. 29a, Chapter 1).

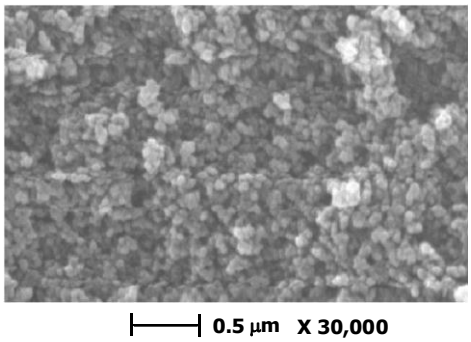

Fig. 52 The surface morphology of grafted silica with amine groups: **$SiO_2(NH_2)$**

AFM was also used as characterization technique. A droplet of the sample of the suspended amino-grafted silica composite was deposited onto a thin glass substrate. To dry the sample before scanning, the sample was kept in a desiccator for one week. The AFM morphology of the **$SiO_2(NH_2)$** composite obtained by scanning a 8 µm x 8 µm surface area (Fig. 53) reveals the presence of colloidal nodules, having an average height of 500 nm. It is evident from the AFM image of amine-grafted silica that the surface is quite regular and smooth, in accordance with the SEM results.

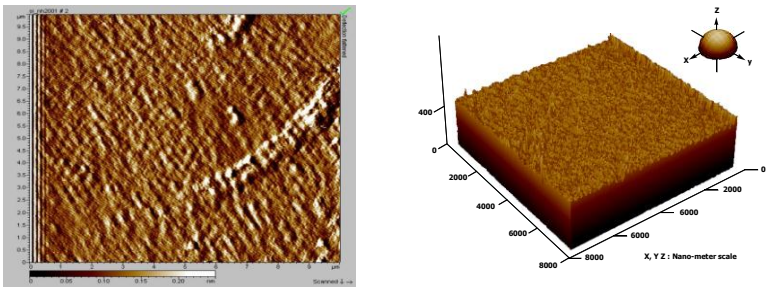

(a) (b)

Fig. 53 The AFM images (2-D (a) and 3-D (b)) of the **$SiO_2(NH_2)$** material

To conclude, both SEM and AFM present a more regular, smoother, and homogeneous surface texture of the amine-grafted silica compared to that of neat silica (Fig. 31).

2.1.6 pH and conductivity

From pH and conductivity measurements, the average pH value of the amino-grafted silica suspension composite was determined to be about pH 9.6 when adding 0.5% of the composite to DI water. **$SiO_2(NH_2)$** suspension shows a stable pH at least for 3 days. The chemical stability of silica in aqueous solution is pH-dependent and decreases significantly in alkaline solutions. The solubilization of APTES-grafted silica is very low at pH 1 and much higher at pH 5.7 [23]. Our composite intended for the adsorption of metal ions conserves its stability in acidic medium and it will therefore be utilized as an adsorbent for the removal of metallic ion at pH 3-5 (Chapter 4). The conductivity of the **$SiO_2(NH_2)$** suspension was quite stable and determined to be about 50 ±10 µS/cm. As deduced from pH and conductivity measurements, the amino-functionalized silica sols exhibits stability in aqueous solution for at least three days of study.

2.1.7 Zeta potential

The chemical modification of Aerosil 200 by grafting with APTES changes the surface properties. Since in DI water (pH 5.6), the silanol groups on the surface of native silica exhibit a negative zeta potential of -19.6 mV due to the ionization of the surface

hydroxyl groups. After silanization with APTES, the surface was expected to show a basic character. It is also documented in the literature that after surface modification the zeta potential of the amine-grafted silica nanoparticles (139.4 nm) changes to a less negative zeta potential (-10.1 mV) compared with unmodified silica (-35.3 mV) [20].

The effect of pH on the zeta potential at 25 ^{o}C was studied. It was found that the effect of pH causes the zeta potential of **$SiO_2(NH_2)$** to be positive between pH 2 and pH 8. However, **$SiO_2(NH_2)$** shows a low zeta potential value of about 3.8 mV at pH ~ 9. After functionalization, the zeta potential of the grafted silica was changed compared to native **SiO_2** as shown in Fig. 54. From the curve, the point of zero charge (pzc) of the amine-grafted silica was around pH 9. Therefore, at pH 2 - 8, the zeta potential was positive with a value between 41.7 mV to 20.2 mV for **$SiO_2(NH_2)$**. At those pH ranges, the functional amine groups on the silica surface are probably protonated (at least partially), so positively charged (NH_3^+) species occur [23]. And under more alkaline conditions, an increase of the OH^- concentration in the solution will reduce the density of positive charges. In consequence, the zeta potential diminishes further, reaching the point of zero charge at ~ pH 9.

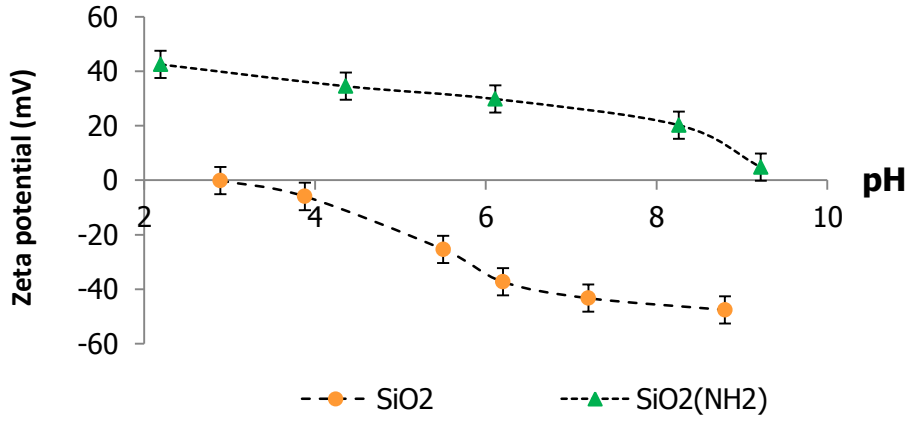

Fig. 54 The zeta potentials of **SiO_2**, and **$SiO_2(NH_2)$** in function of the pH

As a reminder, the conductivity is an electrical current in a solution, which depends on the ionic strength of the solution. The more the conductivity (high ionic strength) is high, the more the double layer becomes compressed. Indirectly, the conductivity has an influence on the zeta potential value. The amine-grafted silica suspension exhibits a higher conductivity than the unmodified **SiO_2**. From zeta potential measurement, at pH 2-5 the amine-grafted silica exhibits a higher zeta potential value than **SiO_2** protonation of the amino groups to give positively charged NH_3^+ species. Our results are similar to those of an earlier study of Foissy and Persello [42]. In this study, a graph is represented showing a plot between surface charge

density (σ_o) versus pH for ultra-pure silica precipitated from pyrogenic Aerosil solutions (NaCl electrolyte). The curve shows that at pH > 2 the surface charge density of silica raises due to an increase of the ionic strength [42].

2.1.8 Hydrodynamic size measurement

During the preparation, the amine-grafted silica was dried at 100 ^{o}C before being used. We suppose when dispersing the dried particles in aqueous solution by ultrasonication for 1 hour, hydrogen bonding between the amino groups on the surface of the modified silica and water occurs. The hydrodynamic size of the hydrated amine-grafted silica was found to be more than 1 μm (Fig. 55). Their sizes are in the micrometer range, caused by the apparition of an aggregation of the amine-grafted silica particles in aqueous solution (~ pH 8), which are more aggregated than native silica (mean size ≈ 270 nm). In consequence, the particles become larger in aqueous solution. The hydrodynamic size value of the APTES-grafted silica (>1 μm) is consistent with a study of P. Punyacharoennon *et al.* [28]. They found that the APTES-grafted Aerosil 200 forms micron-sized nanoclusters in suspension. Our finding is also consistent with the results of Y. An *et al.* who noticed an aggregation of SiO_2-NH_2 nanoparticles at pH 7-8 due to the change of surface charge after surface modification [20].

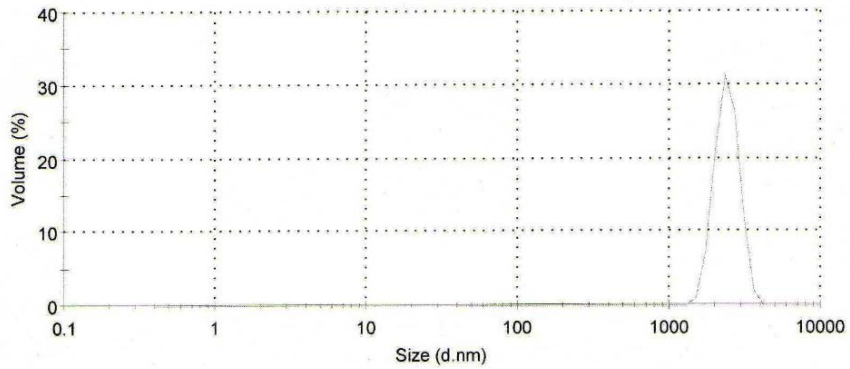

Fig. 55 Size distribution in volume of **$SiO_2(NH_2)$**

2.2 Functionalization of Silica with Carboxyl Groups

To introduce a carboxyl group on a silica surface, the alkoxysilane agent CPTES has been used for silanization of the silica surface [43]. CPTES consists of three ethoxy groups and a cyanide group at the end-chain as shown in Fig. 57. Silanization of silica with CPTES can be accomplished by reflux in dry toluene allowing the diffusion of the CPTES precursor to be condensed onto the surface of silica. The CN-grafted silica (intermediate composite) can

be afterward hydrolysed to -CO_2H groups by strong acids like sulphuric acid. The procedure of the synthesis of the carboxyl-grafted silica is represented in Fig. 56.

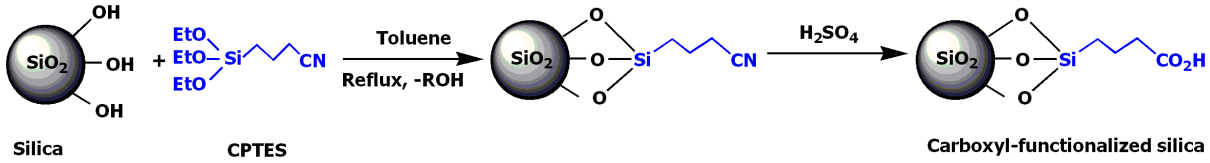

Fig. 56 Two-step surface modification of silica via grafting with cyano groups

For example, K.M. Ponvel *et al.* have used CPTES as cross-linker in order to obtain carboxyl-grafted mesoporous silica via a co-condensation route [44]. First, a mesoporous silica support was prepared and then CPTES was immobilized, and in a last stage hydrolysed by a strong acid to obtain a carboxyl-grafted silica. The latter was further modified by incorporation of magnetic nanoparticles inside of this carboxyl-grafted mesoporous silica material.

Another report describes the elaboration of carboxyl-functionalized SBA-15 silica utilizing CPTES as agent. CPTES was first added to HCl solution containing pluronic P123 ($EO_{20}PO_{70}EO_{20}$, triblock copolymer) and KCl. Then TEOS was added to the stirred mixture. After aging and drying, the final product was obtained by hydrolysis with sulphuric acid [45]. Carboxyl-grafted silica was further reacted with hexamethyldisilazane to obtain bifunctional groups of trimethylsilyl-carboxyl modified SBA-15 **(10)**, shown in Fig. 57 [46].

Recently, Y. Fang *et al.* have condensed the CPTES agent onto an Aerosil 300 surface and then hydrolysed the CN-grafted silica in sulphuric acid. In order to utilize this material as electrolyte, this carboxyl-grafted composite was further mixed with the two ionic liquids 1-hexyl-1-3-methylimidazolium iodide and 1-allyl-3-methylimidazolium iodide and two additives of N-methylbenzoimidazole and guanidinium thiocyanate. This mixture was then spread on a TiO_2 electrode. The carboxyl-grafted silica emerged in the ionic electrolyte was found to exhibit an improved charge transfer reaction at the TiO_2 electrode (Fig. 57) [47].

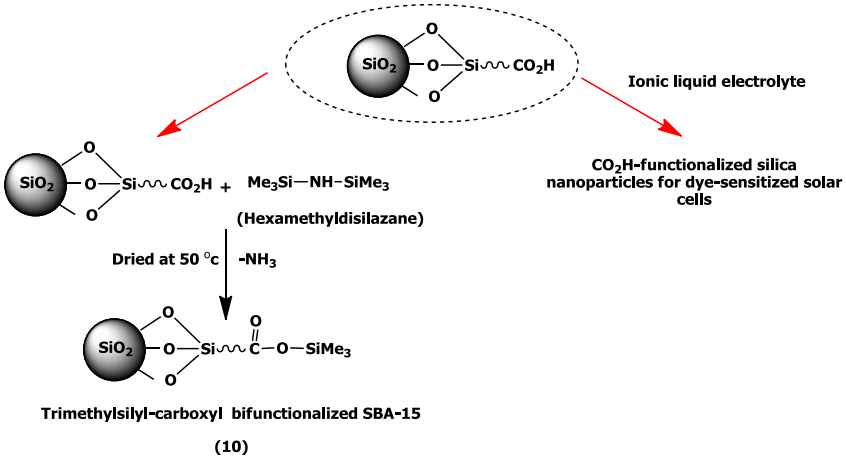

Fig. 57 Selected applications of carboxyl-functionalized silica

In this present work, Aerosil 200 nanoparticles were functionalized with CPTES to obtain particles loaded with carboxyl groups on the silica surface. The aforementioned two-step sequence was carried out according to a procedure described in the literature (Fig. 56) [44]. The first step implies immobilization the silica surface with CPTES by reflux in dry toluene. The resulting -CN grafted silica was the acid-hydrolysed to yield the -CO_2H groups by treatment with H_2SO_4. The silica composite **$SiO_2(CO_2H)$** covered with carboxyl groups was characterized in the same manner as **$SiO_2(NH_2)$** including Elemental analysis, FT-IR, BET specific surface, SEM, and AFM, respectively. The particle suspension in DI water was analysed by measuring the pH, conductivity, the zeta potential, and the hydrodynamic size.

2.2.1. Elemental analysis

After chemical modification, the elemental content of carbon, hydrogen and nitrogen has been determined. Results of the elemental analysis are shown in Table 2.5. The carbon percentage of **$SiO_2(CO_2H)$** was 0.41%, corresponding to a grafting density of 0.47 μmol.m^2. The carbon content of the carboxyl-modified silica was used to calculate the grafting density utilizing equation (1).

From literature, for a silica gel having a BET surface area of 320 m^2/g calculated from TGA, the organic loading (-CO_2H) was found to be 0.95 ± 0.05 mmol/g [48].

Table 2.5 The elemental percentage of **$SiO_2(CO_2H)$**

Sample	Elemental analysis (%, w/w)		
	C	H	N
$SiO_2(CO_2H)$	0.41	0.45	< detection limit

2.2.2 The FT-IR spectra of silica particles grafted with nitrile and carboxyl groups

The nitrile-containing material exhibits a band at 2266 cm^{-1} assigned to the C≡N stretching vibration as shown in Fig. 58**a**. After hydrolysis of the -CN groups to -CO_2H groups, three characteristic bands from silica particle such as the -OH stretching vibration band corresponding to physisorbed water and hydrogen-bonded silanol groups, stretching vibration of -Si-O-Si- (siloxane backbone), and bulk mode of **SiO_2** at 3490 cm^{-1}, 1014 cm^{-1} (vs) and 825 cm^{-1} (m), were detected in the IR spectrum of **$SiO_2(CO_2H)$** (Fig. 58**b**). The occurrence of a weak band at 1711 cm^{-1} due to the C=O stretching vibration and disappearance of the absorption band of the nitrile group at 2266 cm^{-1} confirms the successfully conversion to silica particles loaded with carboxylic groups [44].

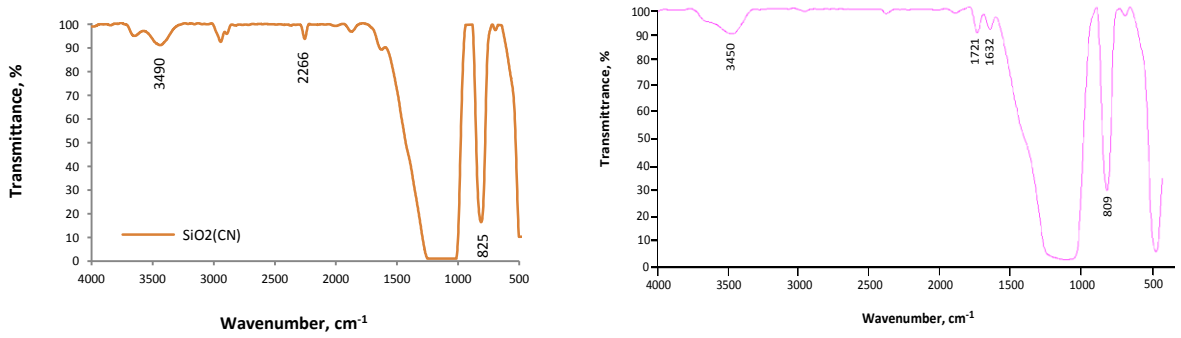

(a) (b)

Fig. 58 The FT-IR spectra of cyanide-grafted silica (a), and carboxyl-grafted silica (b)

2.2.3 BET specific surface

The BET specific surface area of the carboxyl-grafted silica composite was also investigated. This BET value of **$SiO_2(CO_2H)$** is lowered from 182 m^2/g to about 118 m^2/g compared to native **SiO_2** as shown in Table 2.6 [49, 24b]. This confirms a successful surface modification of the silica nanoparticles. Our result is consistent with the data reported by K.Y. Ho *et al*. where the BET specific surface area of carboxyl-grafted ordered mesoporous silica decreases to 757 m^2/g compared to unmodified silica (1071 m^2/g) [49].

Table 2.6 The BET specific surface value of carboxyl-grafted silica particles

Sample	BET, m^2/g
SiO_2	182 ± 4
$SiO_2(CO_2H)$	118 ± 2

Elemental analysis and BET value of native silica and grafted silica allow the calculation of the carboxyl groups grafting density. It was found that the grafting density of carboxyl groups containing on the silica surface calculated from equation (1) is 0.47 μmol.m^{-2} corresponding to the 0.28 groups/nm^2.

Note that grafting density of carboxyl groups on SB15 silica (obtained by co-condensation of TEOS and CTES, followed by hydrolysis of nitrile groups) was reported to be in the range between 0.60 groups/nm^2 and 2.10 groups/nm^2 (depending on the concentration of TEOS) [50]. However, the grafting density remains constant with further increases in the silane reagent concentration because of the limited amount of silanol (SiOH) groups available on the surface of silica [24d].

2.2.4 Determination of the effective specific surface of $SiO_2(CO_2H)$

We have also attempted to determine the specific surface of **$SiO_2(CO_2H)$** using the CTAB adsorption technique. Table 2.7 shows that the specific surface of **$SiO_2(CO_2H)$** is reduced to only one third compared to that of non-grafted silica. It was found that the specific surface value of **$SiO_2(CO_2H)$** is close to the specific surface of the **$SiO_2(NH_2)$** (10.4 ± 1 m^2/g). However, again the values obtained by this method appear much too low, as already discussed in section **2.1.4**.

Table 2.7 Effective specific surface of native silica and carboxyl-grafted silica particles

Material	Specific surface by CTAB, m^2/g
SiO_2	36.1 ± 2
$SiO_2(CO_2H)$	10.0 ± 6

2.2.5 Surface morphology of $SiO_2(CO_2H)$ by SEM, and AFM

The surface of the carboxyl grafted silica composite was characterized by SEM and AFM. The SEM images of **$SiO_2(CO_2H)$** silica as well as that of **SiO_2** are shown in Fig. 59. The surface morphology of **$SiO_2(CO_2H)$** was more uniform and more regular (Fig. 59**b**) when compared with that of **SiO_2** (Fig. 59**a**).

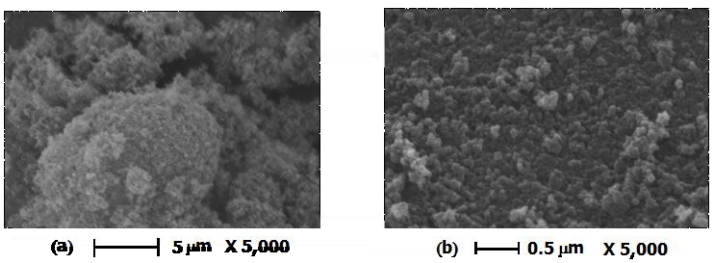

Fig. 59 Surface morphology of **SiO_2** (a), and **$SiO_2(CO_2H)$** (b), respectively

In order to use AFM for characterization, a droplet of sample (colloidal $SiO_2(CO_2H)$ suspension) was deposited onto a thin glass substrate. To dry the sample before scanning, the sample was kept in a desiccator for a week. The AFM image, obtained by scanning a 4 μm x 4 μm surface area, revealed the presence of colloidal nodules on the glass substrates, having an average height of 50 nm. The AFM image of carboxyl-grafted silica also shows a more regular surface (Fig. 60) after grafting on silica.

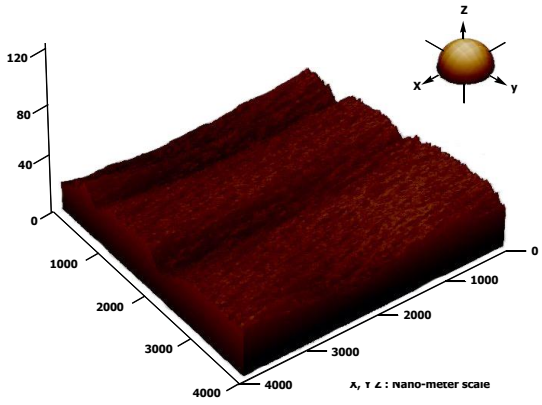

Fig. 60 The AFM image of the **$SiO_2(CO_2H)$** particles

2.2.6 pH and conductivity

The pH value of suspended colloidal carboxyl-grafted silica is quite stable over a time period with the average pH being about 4.5 [49]. According to conductivity measurements, the carboxyl-grafted silica suspension has a conductivity of 4 μS/cm, which remained stable at least for 48 h. Note that the conductivity value of carboxyl-grafted silica (~ 4 μS/cm), depending on the ionic strength of the solution, was quite similar with that of native silica (~7 μS/cm).

2.2.7 Zeta potential

A study on the influence of pH to zeta potential of the **$SiO_2(CO_2H)$** material at 25 ^oC was performed, and the zeta potential values are presented in Fig. 61. Previously, the SiO_2 has a negative zeta potential of -19.6 mV (pH 5.6) due to the ionization of the surface hydroxyl groups. The results show that the **$SiO_2(CO_2H)$** displays a negative zeta potential of about -38.6 mV (pH 4.5) superior to that of neat silica. Since the pK_a of carboxylic acid is around 4.8, it follows that there are more negative charges on the grafted silica than that of untreated silica [51]. Y. An *et al.* reported that SiO_2-CO_2H exhibits a negative zeta potential (-42.2 mV) in aqueous solution (pH of the solution was not reported in ref. [20]). This modified silica has

more negative zeta potential compared with untreated silica (-35.3 mV) due to the change of surface charge of the silica particles after modification [20].

The effect of pH on the zeta potential was studied in the pH range from 2-9. At pH ≤ 2, the carboxyl-functionalized silica shows a positive zeta potential of 7.0 mV. This can be explained by protonation of carboxyl groups to positively charged $-CO_2H^+$ species [51, 52]. At higher pH, the carboxyl-functionalized silica represents negative zeta potential of -58.8 mV, -56.9 mV, and -61.9 mV at pH 5, 7, and 9, respectively. The negative charge zeta potential of the carboxyl-modified silica was higher than the **SiO_2** due to deprotonation of the carboxyl groups grafted on the silica surface:

$$SiO_2\text{-}CO_2H + H_2O \rightleftharpoons SiO_2\text{-}CO_2^- + H_3O^+$$

Under more alkaline condition, the OH^- concentration increases, thus the negative charges on the grafted silica surface due to formation of anionic carboxylate groups increases further.

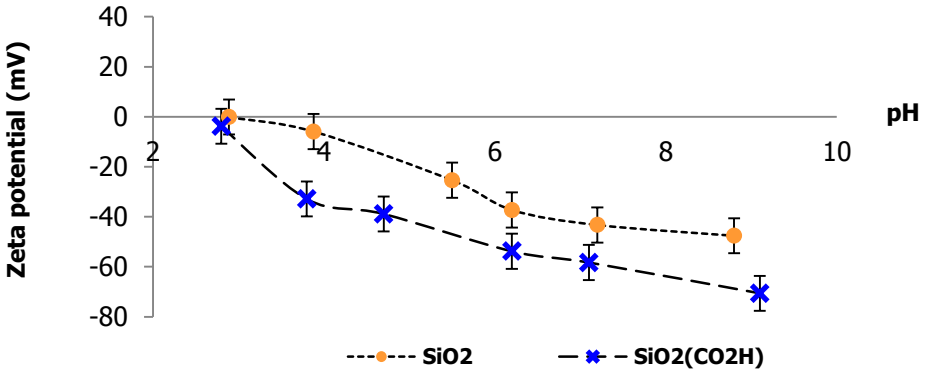

Fig. 61 The zeta potential of grafted silica with carboxyl groups

2.2.8 Hydrodynamic size measurement

The carboxyl-grafted material was dried at 100 ^oC before use. After dispersion of the dried particles in aqueous solution under sonication for 1 hour, the hydrogen bonds between water and surface charge of the modified silica takes place and so the particle size becomes more important. The hydrodynamic size of the carboxyl-functionalized silica composite is shown in Table. 2.8. Compared to native silica, the hydrodynamic size of the carboxyl-grafted Aerosil was lower (172 ± 20 nm) than that of **SiO_2** (328 ± 25 nm). This might be caused by the fact that repulsion between negative charges on each carboxyl-functionalized silica particle occurs. Note, that in contrast to our findings, no noticeable change between the diameter of non-functionalized silica particles (~139 nm) obtained by the Stöber method and that of derived **$SiO_2(CO_2H)$** nanoparticles (~135 nm) could be evidenced by TEM micrographs [20].

Table 2.8 The mean hydrodynamic size of carboxyl grafted silica particle

No.	Materials	Average particle size, nm
1	**SiO_2**	328 ± 25
2	**$SiO_2(CO_2H)$**	172 ± 20

Conclusion

The amine-functionalized silica composite **$SiO_2(NH_2)$** and carboxyl-functionalized silica composite **$SiO_2(CO_2H)$** were successfully prepared under mild conditions via covalent bonding. Three types of grafted silica composites were characterized by FT-IR to confirm the presence of the functional groups of amine and/or carboxyl groups after functionalization process. Surface morphology of the materials was characterized using SEM and AFM techniques. Both SEM and AFM images of **$SiO_2(NH_2)$** and **$SiO_2(CO_2H)$** display a more regular, smoother, and homogeneous surface texture than that of neat silica. The BET specific surfaces of all grafted silica composites decreased compared to untreated silica (328 ± 25 nm) according to functional groups on the surface of silica. The nitrogen content on the silica surface were measured utilizing the Kjeldalh method and found to be 0.82 ± 0.02 % for **$SiO_2(NH_2)$**. Elemental analysis is also used to determine C, H and N content of both amine- and carboxyl-functionalized silica. For **$SiO_2(NH_2)$**, the N-content was found to be 0.76%. This value corresponds to a concentration of amine groups containing on silica surfaces of 4.75×10^{-4} mol/g. For **$SiO_2(CO_2H)$**, the C-content from Elemental analysis was 0.41%, corresponding to a carboxyl groups concentration on the silica surfaces of 0.85×10^{-4} mol/g. The BET value of all grafted silica materials decreases compared to unmodified silica, this is due to an increase of aggregation. Both Elemental analysis and BET led to calculation of grafting density utilizing the Berendsen equation. The grafting densities, calculated from carbon-content, are 4.03 μmol m^{-2} and 0.47 μmol m^{-2} for **$SiO_2(NH_2)$** and **$SiO_2(CO_2H)$**, respectively. The grafting density, calculated from the N-content (%), was 3.86 μmol m^{-2} or 1.94 APTES groups/nm^2. In this work, the grafting density was higher than reported in the literature: 1.7 μmol m^{-2} or 1.79 APTES groups/nm^2 [12]. In case of the **$SiO_2(CO_2H)$** composite, the grafting density was found to be 1.20 CO_2H groups/nm^2. The silanization processes used in this present work afford a good grafting density for both anime- and /or carboxyl-modified silica. Measuring the zeta potential and hydrodynamic particles size provided information on the characteristics of these composites in aqueous solution. The

stability of the composite was studied by pH and conductivity measurements. These modified silica particles exhibit sufficient stability in aqueous solution during a 3 days period. The potential of these two types of grafted silica composites for the capture of divalent metal cations in aqueous solution will be evaluated and discussed in Chapter 4.

Experimental part

Materials and apparatus

3-Aminopropyltriethoxysilane (APTES), and 4-(triethoxysilyl)-butyronitrile (CPTES), 98%, were purchased from Aldrich. *N*-cetyl-*N, N, N*-trimethyl-ammoniumbromide (CTAB) was purchased from Merck, Germany. All reagents are analytical grade. The carboxyl group content on the grafted silica composite was quantified by combustion elemental analysis (UMR 7565 CNRS Université Henri Poincaré Faculté des Sciences, Boulevard des Aiguillettes Case 79, BP 70279, VANDOEUVRE les NANCY). The nitrogen content of APTES-grafted silica particle was determined by the SERAC (UFC) using the Kjeldahl method by means of a TurboTherm (Gerhardt, Germany) apparatus. The experimental procedures for pH and conductivity measurements were similar to those described in chapter I.

2.3 Preparation of the grafted silica

2.3.1 Functionalization of silica surface with APTES

Synthesis of **$SiO_2(NH_2)$**] was carried out according to the procedure represented in Fig.2.11 [25]. 10 g of silica particles were suspended in 300 ml solution of APTES in dry toluene (10% v/v). The mixture was refluxed with stirring for 12 hours. The slurry was filtered and the remaining APTES was washed out successively with toluene, ethanol and diethyl ether, respectively. The product was then dried at 70 ^{o}C for 8 hours.

2.3.2 Functionalization of silica surface with carboxyl groups

The synthesis of **$SiO_2(CO_2H)$** was carried out according ref. [49]. There are two steps for the preparation of **$SiO_2(CO_2H)$**. A CN-containing organic layer was first grafted onto Aerosil 200 silica by reflux of 2.5 g silica in 250 ml of dry toluene containing 0.1 mol of CPTES at 108 ^{o}C for 18 hours. After evaporation of the solvent, the cyanide-functionalized

silica **SiO_2(CN)** was dried at 100 ^oC for 24 hours. The CN group was then hydrolyzed to carboxylic acid by refluxing with 50% sulfuric acid at 135 ^oC for 3 hours. The grafted silica was collected, then washed and dried to obtain **$SiO_2(CO_2H)$** material. The schematic synthesis of the hydrophobic fumed silica nanoparticles with carboxyl groups is shown in Fig. 56.

2.4 Determination of the effective specific surface by adsorption of CTAB

A sample was prepared by suspending 0.5 g of silica particles in 100 ml of DI water and 20 ml of CTAB (3 g/L) was added to the sample solution, which was then allowed to stand for 24 h. After adsorption of the CTAB solution on the surface of the sample, the initial CTAB solution and supernatant of mixture of sample and CTAB were quantified for total organic carbon concentration by TOC analysis using a carbon analyzer (Shimadzu, TOC-5050).

References

1. Y. Borodko, J.W. Ager III, G. Edward Marti, H. Song, K. Niesz, and G.A. Somorjai, *Structure Sensitivity of Vibrational Spectra of Mesoporous Silica SBA-15 and Pt/SBA-15*, J. Phys. Chem. B, 109 (2005) 17386-17390.
2. L.T. Zhuravlev and V.V. Potapov, *Density of silanol groups on the surface of silica precipitated from a hydrothermal solution*, Russ. J. Phys. Chem. A, 80 (2006) 1272-1282.
3. J. Horn, F. Michalek, C.C. Tzshucke, and W. Bannwarth, *Non-covalently solid-phase bound catalysts for organic synthesis*, Top. Curr. Chem., 242 (2004) 43-75.
4. C. Bianchini, V.D. Santo, A. Meli, S. Moneti, M. Moreno, W. Oberhauser, R. Psaro, L. Sordelli, and F. Vizza, *A comparison between silica-immobilized ruthenium(II) single sites and silica-supported ruthenium nanoparticles in the catalytic hydrogenation of model hetero- and polyaromatics contained in raw oil materials*, J. Catal., 213 (2003) 47-62.
5. B. Cabot, A. Deratani, and A. Foissy, *Adsorption of poly(vinylimidazoles) on silica surfaces*, Colloids Surf. A, 139 (1998) 287-297.
6. B. Popping, A. Deratani, B. Sebille, N. Desbois, J.M. Lamarche, and A. Foissy, *The effect of electrical charge on the adsorption of a weak cationic polyelectrolyte onto silica*, silicon carbide and calcium fluoride, Colloids Surf., 64 (1992) 125-133.
7. (a) T.N.T. Phan, N. Louvard, S.-A. Bachiri, J. Persello, and A. Foissy, *Adsorption of zinc on colloidal silica, triple layer modelization and aggregation data*, Colloids Surf. A, 244 (2004) 131-140; (b) K. Subramaniam, V. Vithayaveroj, S. Yiacoumi, C. Tsouris, *Copper uptake by silica and iron oxide under high surface coverage conditions: surface charge and sorption equilibrium modeling*, J. Coll. Interf. Sci., 268, (2003), 12-22.

8. N. Legagneux, J.-M. Basset, A. Thomas, F. Lefebvre, A. Goguet, J. Sa, and C. Hardacre, *Characterization of silica-supported dodecatungstic heteropolyacids as a function of their dehydroxylation temperature*, Dalton. Trans., 12 (2009) 2235-2240.

9. S. Minakata, and M. Komatsu, *Organic reaction on silica in water*, Chem. Rev., 109 (2009) 711-724.

10. (a) J. Pelletier , J. Espinas, N. Vu , S. Norsic, A. Baudouin, L. Delevoye, J. Trébosc, E. Le Roux, C. Santini, J.-M. Basset, R.M. Gauvin, and M. Taoufik, *A well-defined silica-supported aluminium alkyl through an unprecedented, consecutive two-step protonolysis-alkyl transfer mechanism*, Chem. Commun.**,** 47 (2011) 2979-2981; (b) B. R. Guidotti, W. R. Caseri, U. W. Suter, *Modification of SiO_2 Surfaces by Reaction with Trialkoxymethanes and Triphenoxymethane*, Langmuir, 12 (1996), 4391-4394. (c) B. R. Guidotti, E. Herzog, F. Bangerter, W. R. Caseri, U. W. Suter, *Modification of SiO_2Surfaces by Reaction with Acetals, Ketals, Orthoesters, and Orthocarbonates*, J. Coll. Interface Sci., 191 (1997), 209-215.

11. H. Zou, S. Wu, and J. Shen, Polymer/silica nanocomposites: Preparation, characterization, properties, and applications, Chem. Rev., 108 (2008) 3893-3957.

12. P. Liu, J. Yang, P. Li, and L. Wang, *An efficient and recyclable silica-supported carbene-Cu(II) catalyst for the oxidative coupling reaction of terminal alkynes with H-phosphonates under base-free reaction conditions*, Appl. Organometal. Chem., 25 (2011) 830-835.

13. M. Lazghab, K. Saleh, and P. Guigon, *Functionalisation of porous silica powders in a fluidised-bed reactor with glycidoxypropyltrimethoxysilane (GPTMS) and aminopropyltriethoxysilane (APTES)*, Chem. Eng. Res., 88 (2010) 686-692.

14. R.S. Timofte, S. Woodward, *Preparation of silane-grafted pellets: silica bound reagents in a very convenient form*, Tetrahed. Lett., 45 (2004) 39-42.

15. S. Sadeghi, and E. Sheikhzadeh, *Solid phase extraction using silica gel functionalized with sulfasalazine for preconcentration of uranium(VI) ions from water samples*, Microchim Acta, 163 (2008) 133-320.

16. A.K. Mallik, H. Qiu, M. Takafuji, and H. Ihara, *Selectivity enhancement for the separation of tocopherols and steroids by integration of highly ordered weak interaction sites along the polymer main chain*, Anal. Bioanal. Chem., 404 (2012) 229-238.

17. C. Delacote, F.O.M. Gaslain, B. Lebeau, and A. Walcarius, Factors affecting the reactivity of thiol-functionalized mesoporous silica adsorbents toward mercury(II), Talanta, 79 (2009) 877-886.

18. E. Bourgeat-Lami, Ph. Espiard, and A. Guyot, *Poly(ethyl acrylate) latexes encapsulating nanoparticles of silica : 1. Functionaization and dispersion of silica*, Polymer, 36 (1995) 4385-4389.

19. J. Kecht, A. Schlossbauer, and T. Bein, *Selective functionalization of the outer and inner surface in mesoporous silica nanoparticles*, Chem. Mat., 20 (2008) 7207-7214.

20. Y. An, M. Chen, Q. Xue, and W. Liu, *Preparation and self-assembly of carboxlic acid-functionalized silica*, J. Coll. Interf. Sci., 311 (2007) 507-513

21. (a) H.W. Lee, H.J. Cho, J.-H. Yim, J.M. Kim, J.-K. Jeon, J.M. Sohn, K.-S. Yoo, S.-S. Kim, and Y.-K. Park, *Removal of Cu(II)-ion over amine-functionalized mesoporous silica materials*, J. Industrial and Eng. Chem., 17 (2011) 504-509; (b) M. Hebrant, M. Rose-Helene, J.-P. Joly, A. Walcarius, *Kinetics of the complexation of Ni^{2+} ions by 5-phenyl-azo-8-hydroxyquinoline grafted on colloidal silica particles*, Colloids Surf. **A**, 380, (2011), 261-269; (c) M. Hebrant, M. Rose-Helene, A. Walcarius, *Metal ion*

removal by ultrafiltration of colloidal suspensions of organically modified silica, Colloids Surf. **A**, 417, (2013), 65-72.

22. A.M. Burke, J.P. Hanrahan, D.A. Healy, J.R. Sodeau, J.D. Holmes, M.A. Morris, *Large pore bi-functionalised mesoporous silica for metal ion pollution treatment*, J. Hazard. Mat., 164 (2009) 229-234.
23. M. Etienne, and A. Walcarius, *Analytical investigation of the chemical reactivity and stability of aminopropyl-grafted silica in aqueous medium*, Talanta, 59 (2003) 1173-1188.
24. (a) A. Erdem, T. Shahwan, A. Cagir, and A.E. Eroglu, *Synthesis of aminopropyl triethoxysilane-functionalized silica and its application in speciation studies of vanadium(IV) and vanadium(V)*, Chem. Eng. J., 174 (2011) 76-85. (c) C. Knöfel, C. Martin, V. Hornebecq, and P.L. Llewellyn, *Study of Carbon Dioxide Adsorption on Mesoporous Aminopropylsilane-Functionalized Silica and Titania Combining Microcalorimetry and in Situ Infrared Spectroscopy*, J. Phys. Chem. C, 174 (2009) 21726-21734. (b) S. Hamoudi, A. El-Nemr, and K. Belkacemi, *Adsorptive removal of dihydrogenphosphate ion from aqueous solutions using mono, di- and tri-ammonium-functionalized SBA-15*, J. Coll. Interf. Sci., 343 (2010) 615-621. (d) J.Lin, J.A. Siddiqui, and R.M. Ottenbrite, *Surface modificationof inorganic oxide particles with silane coupling agent and organic dyes*, Polym. Adv. Technol, 12 (2001) 285-292.
25. A. Goswami, A.K. Singh, *Silica gel functionalized with resacetophenone: synthesis of a new chelating matrix and its application as metal ion collector for their flame atomic absorption spectrometric determination*, Anal. Chim. Acta., 454 (2002) 229-240.
26. J. Aguado, J.M. Arsuaga, A. Arencibia, M. Lindo, and V. Gascón, *Aqueous heavy metals removal by adsorption on amine-functionalized mesoporous silica*, J. Hazard. Mat., 163 (2009) 213-221.
27. S. Oh, T. Kang, H. Kim, J. Moon, S. Hong, and J. Yi, *Preparation of novel ceramic membranes modified by mesoporous silica with 3-aminopropyltriethoxysilane (APTES) and its application to* Cu^{2+} *separation in the aqueous phase*, J. Membr. Sci., 301 (2007) 118-125.
28. (a) P. Punyacharoennon, S. Charuchinda, and K. Srikulkit, *Grafting and Phosphonic acid functionalization of hyperbranched polyamidoamine polymer onto ultrafine silica*, J. Appl. Polym. Sci., 110 (2008) 3336-3347. (b) S. Ghosh, S. K. Goswami and L. J. Mathias, *Surface modification of nano-silica with amides and imides for use in polyester nanocomposites, J. Mat. Chem A*, 1 (2013) 6073-6080.
29. A.O. Yazaydın, and R.W. Thompson, *Molecular simulation of water adsorption in silicalite: Effect of silanol groups and different cations*, Microporous Mesoporous Mat., 123 (2009) 169-176.
30. M. Anbia, and M. Lashgari, *Synthesis of amino-modified ordered mesoporous silica as a new nano sorbent for the removal of chlorophenols from aqueous media*, Chem. Eng. J., 150 (2009) 555-560.
31. M. Takafuji, M.M. Rahman, H.R. Ansarian, M. Derakhshan, T. Sakurai, and H. Ihara, *Dioctadecyl L-glutamide-derived lipid-grafted silica as a novel organic stationary phase for RP-HPLC*, J. Chromatogr. A., 1074 (2005) 223-228.
32. Y. Zhang, H. Yang, K. Zhou, and Z. Ping, *Synthesis of an affinity adsorbent based on silica gel and its application in endotoxin removal*, React. Funct. Polym., 67 (2007) 728-736.
33. S. Hamoudi, A. El-Nemr, and K. Belkacemi, *Adsorption removal of dihydrogenphosphate ion from aqueous solutions using mono, di- and tri-ammonium-functionalized SBA-15*, J. Coll. Interf. Sci., 343 (2010) 615-621.

34. A. Suwalski, H. Dabboue, A. Delalande, S.F. Bensamoun, F. Canon, P. midoux, G. Saillant, D. Klatzmann, J.-P. Salvetat, and C. Pichon, *Accelerated Achilles tendon healing by PDGF gene delivery with mesoporous silica nanoparticles*, Biomaterials, 31 (2010) 5237-5245.

35. A.M. Donia, A.A. Atia, W.A. Al-amrani, and A.M. El-Nahas, *Effect of structural properties of acid dyes on their adsorption behavior from aqueous solution by amine modified silica*, J. Hazard. Mat., 161 (2009) 1544-1550.

36. C. Bartholome, E. Beyou, E. Bourgeat-Lami, P. Chaumont, and N. Zydowicz, *Nitroxide-mediated polymerization of styrene initiated from the surface of fumed silica*. *Comparison of two synthetic routes*, Polymer, 46 (2005) 8502-8510.

37. A. Marcó, R. Rubio, R. Compañó, and I. Casals, *Comparison of the Kjeldahl method and a combustion method for total nitrogen determination in animal feed*, Talanta, 57 (2002) 1019-1026.

38. J.C. Hicks, R. Dabestani, A.C. Buchanan III, C.W. Jones, *Assessing site-isolation of amine groups on aminopropyl-functionalized SBA-15 silica materials via spectroscopic and reactivity probes*, Inorg. Chim. Acta, 361 (2008) 3024-3032.

39. V. Manu, H.M. Mody, H.C. Bajaj, and R.V. Jasra, *Adsorption of Cu^{2+} on Amino Functionalized Silica Gel with Different Loading*, Ind. Eng. Chem. Res., 48 **(2009)** 8954-8960.

40. E. Bourgeat-Lami, Ph. Espiard, and A. Guyot, *Poly(ethyl acrylate) latexes encapsulating nanoparticles of silica : 1. Functionalzation and dispersion of silica*, Polymer, 36 (1995) 4385-4389.

41. (a) ASTM D 3765, Annual Book of ASTM Standards, 9.01 (1990) 614, (b) K. Balasundaram, *Synthesis and characterization of core/shell silica nanoparticles for chemical mechanical planarization of low-k dielectric and copper wafers*, (2010) 1-48.

42. A. Foissy and J. Persello, *The surface properties of silicas*, John Wiley & Sons, 1998, 390.

43. Y.-C. Pan, H.-Y. Wu, L.-P. Lee, G.-L. Jheng, G.T.K. Fey, and H.-M. Kao, *Cyanide-and carboxylate-functionalized cubic mesoporous silicas SBA-1: Synthesis, characterization and reactivity of organic functional groups*, Microporous Mesoporous Mat., 123 (2009) 78-90.

44. K.M. Ponvel, Y.-H. Kim, and C.-H. Lee, *Incorporation of nano-sized magnetite particles into mesoporous materials via -COOH groups*, Mat. Chem. Phys., 122 (2010) 397-401.

45. W. Wu, Q. Gao, Y. Xu, D. Wu, Y. Sun, W. Shen, and F. Deng, *Controlled drug release from bifunctionalized mesoporous silica*, J. Solid State Chem., 181 (2008) 2837-2844.

46. W. Xu, Q. Gao, Y. Xu, D. Wu, Y. Sun, W. Shen, and F. Deng, *Controlled drug release from bifunctionalized mesoporous silica*, J. Solid State Chem., 181 (2008) 2837-2844.

47. Y. Fang, J. Zhang, X. Zhou, Y. Lin, and S. Fang, *"Soggy sand" electrolyte based on COOH-functionalized silica nanoparticles for dye-sensitized solar cells*, Electrochem. Commun., 16 (2012) 10-13.

48. P. Stathi, and Y. Deligiannakis, *Humic acid-inspired hybrid materials as heavy metal absorbents*, J. Coll. Interf. Sci., 351 (2010) 239-247.

49. K.Y. Ho, G. McKay, and K.L. Yeung, *Selective adsorbents from ordered mesoporous silica*, Langmuir, 19 (2003) 3019-3024.

50. S. Shen, P.S. Chow, S. Kim, K. Zhu, and R.B.H. Tan, *Synthesis of carboxyl-modified rod-like SBA-15 by rapid co-condensation*, J. Coll. Interf. Sci., 321 (2008) 365-372.

51. M.D. Liptak, and G.C. Shields, *Accurate pKa calculations for carboxylic acids using complete basis set and Gaussian-n models combined with CPCM continuum solvation methods*, J. Am. Chem. Soc. 123 (2001) 7314-7319.

52. R.J. Kanicky and D.O. Shah, *Effect of Degree, Type, and Position of Unsaturation on the pKa of Long-Chain Fatty Acids*, J. Coll. Interf. Sci., 256 (2002) 201-207.

Chapter 3

Chitosan, Modified Chitosan and Chitosan-Coated Silica Surfaces

Introduction

A silica surface modified with a biopolymer is interesting since suitable functional groups on a biopolymer backbone confer them the propensity to capture pollutants like phenol, dyes, metal ions in aqueous solution [1]. Biopolymers such as gelatin, alginate, cellulose, collagen, and chitosan (CS) have been deposited by several groups onto the surface of silica nanoparticles. Some examples of biopolymer-functionalized silica surfaces for targeted applications are represented. For example, a hydrophobic silica surface obtained by silanization with methyltrimethoxysilane has been reacted with gelatin to give a hybrid material providing high ductility, low elastic modulus, and high mechanical strength [2]. Silica (precipitated type) was also modified with alginic acid to prepare hydrogel films. These films were tested in the presence of glycerol as membrane coating, affording an improved protection vis-à-vis hydrophobic loss of osmotic distillation PTFE membrane (pore diameter: 0.1 μm) compared to a non-treated PTFE membrane [3]. Fumed silica interacting with epoxidized natural rubber via hydrogen bonds was produced by a mechanical mixing and analyzed by FT-IR. It was shown that the fumed silica content affects the mechanical properties of the composite, which is of importance for the resistance of tyres in rubber industry [4]. The bayberry tannin (BT) - grafted silica beads was used as support for the synthesis of Pd(0) catalysts. The BT acts as stabilizer to prevent the aggregation of Pd(0) particles and as an antioxidant for keeping the Pd(0) particles from oxidation. The Pd(0) nanoparticles stabilized by BT-grafted silica beads exhibit a highly active and reusable in liquid-hydrogenation of unsaturated organic compounds [5]. In order to study its infrared emissivity, a hybrid collagen/silica composite was prepared in aqueous suspension by deposition of collagen onto the surfaces of SiO_2 spheres at pH 5. Structural features and thermal properties were measured with FTIR, SEM, TEM, and TGA-DTA. The results showed that self-aggregation of collagen macromolecules takes place during the adsorption of collagen on the SiO_2 surface and that the biopolymer is attached through electrostatic forces and hydrogen bonding [6].

Another natural biopolymer becoming increasingly important is CS thanks to its advantageous properties especially being a low-cost material, a renewable resource, widely abundant, environmental friendly (biocompatibility, biodegradability), and last but not least its ease of chemical modification. Moreover, CS is commonly used as a sorbent for removal of metal ions from water because of the presence of potentially complexing amino groups and hydroxyl groups. These aspects have been the topic of several review articles [7].

The chemical modification of CS constitutes another promising method for the preparation of new materials. It enables one to introduce special properties thus enlarging the scope of potential applications for this biopolymer. For example, one inconvenience and limitation of CS for some applications is its poor solubility in neutral and alkaline solutions. This limited solubility in aqueous solution can be overcome by carboxylmethylation rendering the derivative N-carboxylmethylchitosan soluble in a wide range of pH [8]. Some examples of the modification of CS to obtain the carboxymethylchitosan derivatives are discussed in the topic of Chemical modification of CS.

With the objective to combine the intrinsic propensity of the natural biopolymer for pollutant uptake with those of silica particles as support, we attempted to elaborate new adsorbent materials consisting of a chitosan shell coated on a silica nanoparticle core. The chitosan shell was chemically modified to improve adsorption capacity for complexation of divalent metal ions. As support, Aerosil 200 particles (activated by acidic treatment or chemically modified as described in Chapters 1 and 2), have been chosen. After giving some helpful background information on the constitution, chemistry and properties of CS, the elaboration of three new organo-mineral silica based-composites (CS-coated silica, CS-coated carboxyl grafted silica, and carboxyl modified CS-coated silica) is described in this chapter.

3.1 Constitution, Chemistry and Properties of Chitosan

Origin, Structure and Production of Chitosan

Chitin is the second most abundant natural amino polysaccharide after cellulose. Chitin is found in the skeleton of crustacean, insects, and some fungi, etc. As shown in Fig. 62, CS is structurally very related to the polysaccharide cellulose, an OH function being by a acetylated amino-group. CS itself is the *N*-deacetylated derivative of chitin.

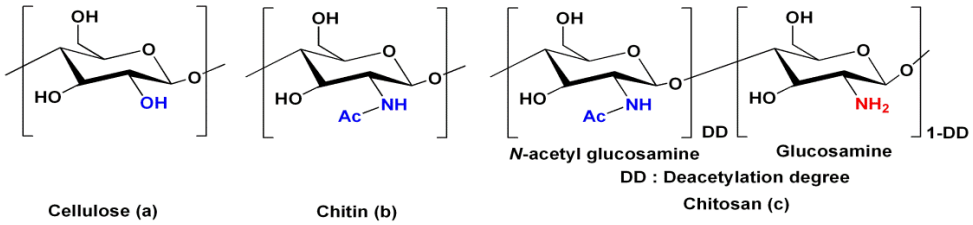

Fig. 62 Structural motives of three natural biopolymers: cellulose (a), chitin (b), and chitosan (c)

CS or poly[β-(1-4)-linked-2-amino-2-deoxy-*d*-glucose, can be considered as a randomly composed copolymer assembled by glucosamine and *N*-acetyl glucosamine units. CS constitutes a major component of arthropod and crustacean shells of lobsters, crabs, shrimps, and cuttlefish [9, 10]. Crustacean shells consist of 30-40% proteins, 30-50% calcium carbonate, and 20-30% chitin and pigments such as carotenoids [11]. These proportions vary with species and seasons. CS is obtained from a chemical purification process involving 4 steps (Fig. 63):

- (i) Demineralization step: the sample shell is demineralized with HCl and then washed to neutral pH, rinsed and filtered.
- (ii) Deproteinization step: this is accomplished by reacting the sample with NaOH.
- (iii) Deacetylation step: the solid product is added to sodium hydroxide leading to the deacetylation of chitin to CS and involves the removal of acetyl groups from the molecular chain of chitin, leaving behind a complete amino group [12].
- (iv) Decoloration step: the product is washed and dried under UV light from the sun (oxidative degradation of carbon-carbon double bonds present in astaxanthin) [13].

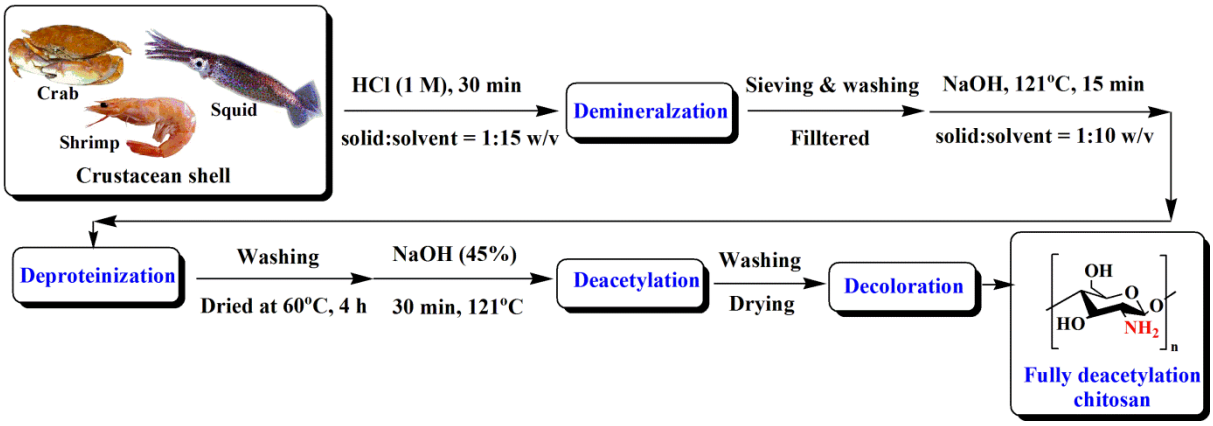

Fig. 63 Production process of CS [13]

CS powder (70-80% degree of deacetylation (DD)) exhibits a degree of crystallinity of 30-50% as determined by X-ray diffraction and IR spectroscopy [14], affected by the *N*-acetyl glucosamine unit. The percentage of this residual unit depends on the original source and the

treatment during production and can be determined by a variety of spectroscopic methods for structural analysis presented in a recent review article [15].

Behavior of CS in Solution

CS is almost insoluble in water at neutral pH and in organic solvents. The solubility of CS depends on the % DD, pH and the percentage of protonation of the free amino groups. CS can be solubilized in diluted acidic solution (acetic acid, formic acid, etc.) [10,16] and exhibits in acidic solution cationic polyelectrolyte properties because of the protonation of -NH_2 groups as shown in Fig. 64 [17]. The degree of protonation of CS depends on the pK_a (acid dissociation constant) of the acid used to dissolve CS [18]. In case of strong mineral acids (i.e. sulfuric acid, hydrochloric acid, nitric acid) dissociating completely in water, the protonation of the amino group is shown in Fig. 65. Studies by A. Domard have evidenced that interactions between CS and carboxylic acids (weak acids) are electrostatic ones between -NH_3^+ and -COO^- functions [19].

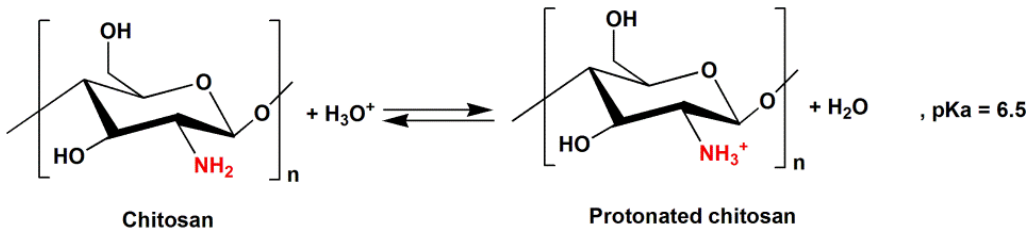

Fig. 64 Protonation of fully deacetylated CS in acidic aqueous solution

3.2 Chemical Modification of CS

A lot of research deals with the chemical modification of CS in order to improve its adsorption properties and selectivity. This chemical modification can be realized without change/degradation of the fundamental skeleton of CS. In order to widen the application of CS, many attempts have been made to optimize its properties by crosslinking [20, 21], layer coating [22-24], depositing [25-27], grafting, and functionalizing [28-34]. Note however that chemical modification utilizing crosslinking agents may decrease the metal uptake efficiency and sorption capacities [35].

An important amount of CS derivatives has been obtained by grafting new functional groups onto the CS backbone. Some reasons for chemical modification by grafting new functional groups to CS are listed as follows:

(1) to increase the density of sorption sites,

(2) to change the pH range for metal sorption, and

(3) to change the sorption sites and/or the sorption mechanism in order to increase the sorption selectivity.

State of the Art

The active sites of CS (-NH_2 and -OH groups) show an effectiveness to interact with metal ions like Cu(II), Co(II), Ni(II), Cr(VI), and Au(III), etc [36-42], but are also able to bind anionic pollutants such as As(III) arsenite and As(V) arsenate [43]. Due to its non-toxicity, biodegradability, and antibacterial and antiviral properties, CS is employed as base material in medical and pharmaceutical applications [44]. In addition, CS can be formulated in various forms such as powder, gels, and films, etc depending on the desired use. For example, CS has been used as bone tissue, since it promote cell growth and mineral rich matrix deposition by osteoblasts* cells in culture [45, 46]. CS can be moulded into porous structures to allow osteoconduction* [47]. CS has been known, with high potential, as a carrier for various active agents [48-52]. In the case of gene delivery, CS as natural cationic polysaccharide can interact with the negatively charged DNA (introduced into the target cells to get transcribed and genetic information) and form polyelectrolyte complexes. This provides a better-protected DNA from nuclease degradation leading to better transfection efficiency [53].

*Osteoblasts are large cells which are responsible for the synthesis and mineralization of bone during both initial bone formation and later bone remodeling. Osteoconduction means that bone grows on a surface.

A selection of some reagents which have linked with CS such as acrylamide, *N,N'*-biisomaleimide, *N,N'*-biisophthalimide, *N,N'*-phthalimidomaleimide, and polyamidoamine (PAMAM) is shown in Table 3.1.

Table 3.1 Structures of some reagents for functionalization of CS to uptake the adsorption of copper or nickel ions, and to enhance the solubility in aqueous solutions

Reagents	Structure
Acrylamide	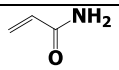 (1)
N,N'-biisomaleimide	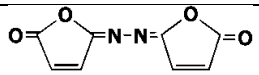 (2)
N,N'-biisophthalimide	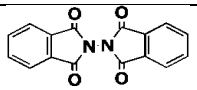 (3)
N,N'-phthalimidomaleimide	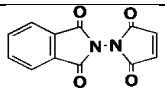 (4)
Mercaptoacetic acid	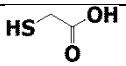 (5)
Ethylenediaminetetraacetic acid (EDTA)	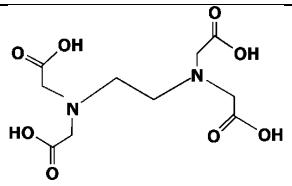 (6)
Diethylenetriaminepentaacetic acid (DTPA)	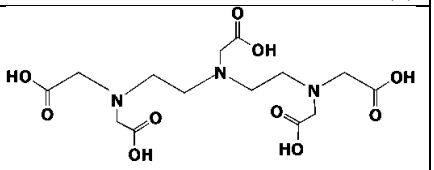 (7)

Carboxymethylchitosan

A further chemical modification of CS, which has received much attention in recent decades, is the so-called carboxymethylation. Apart from low toxicity, antibacterial activities, etc. [54-56] functionalization via carboxymethylation renders CS more hydrophilic thus dramatically increasing the solubility of CS at neutral and alkaline pH value, whereas CS itself is only soluble at pH < 6. This solubility of carboxyl-modified CS involves H-bonding between water and the polar COO^- or carboxyl groups of the modified CS [57]. Moreover, these carboxymethylated CS derivatives own the ability for capturing metal ions, which can be even superior to that of CS [37].

Depending on the reaction conditions, the site for carboxymethylation can be controlled allowing the targeted synthesis of several derivatives including *N*-carboxymethyl

CS, *O*-carboxymethyl CS, *N*, *N*-carboxymethyl CS, and *N*, *O*-carboxymethyl CS, shown in Fig. 65. Some methods for preparation of carboxymethylchitosan derivatives are described below.

(i) The first method is the preparation of the *O*-carboxymethylchitosan sodium salt. CS is first activated in alkaline solution (42 wt% NaOH) at 0 ^{o}C for 48 h. Then the pH is adjusted to 8 with HCl. The solid product is then collected, washed with methanol and dried at 40 ^{o}C [58].

(ii) The second method is the preparation of the *N*, *O*-carboxymethylchitosan. CS is suspended in a solvent (1:4 (v/v) water/isopropanol) and then alkalization is carried out using 50% NaOH at 40-70 ^{o}C for 1 h. Chloroacetic acid ($ClCH_2CO_2H$) in isopropanol is then added to the reaction mixture. The reaction is stopped by adding 70% ethanol. The pH is adjusted to neutrality with acetic acid. The solid product is rinsed with 70-90% ethanol (to desalt) and dried at 60 ^{o}C. At high alkaline concentrations (NaOH 50%), alkylation with $ClCH_2CO_2$ gives both *N*- and *O*-alkyl CS derivatives at the C2 (NH_2 groups) and C6 (OH groups) [59].

(iii) The third one is the preparation of *N*-carboxymethylchitosan. It consists of the reacting the free amino groups of CS with glyoxylic acid to produce a soluble aldimine and then reduction of the aldimine product with sodium cyanoborohydride ($NaBH_4$). The formation of *N*-carboxylmethyl CS mechanism is shown in Fig. 65 [60].

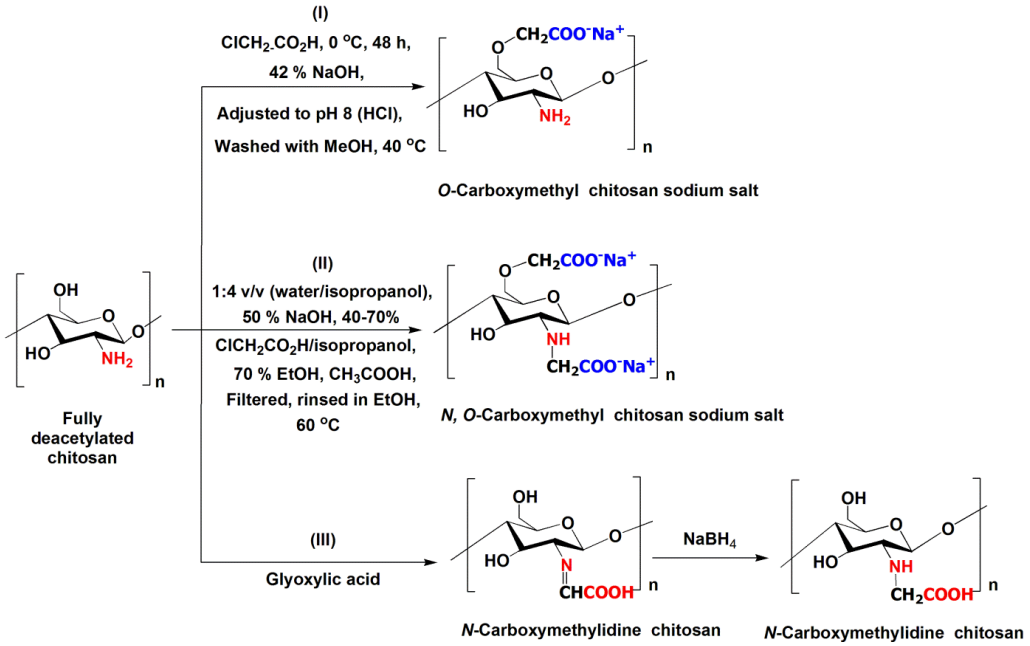

Fig. 65 Synthesis of carboxymethyl CS (according to Ref. [56-58])

For this work, a *N*,*O*-carboxymethyl-modified CS composite was synthesized using monochloroacetic acid according to a modified procedure described in the literature and shown in Fig. 66 [61]. This carboxyl-grafted CS was then further reacted with the silica particles as described below.

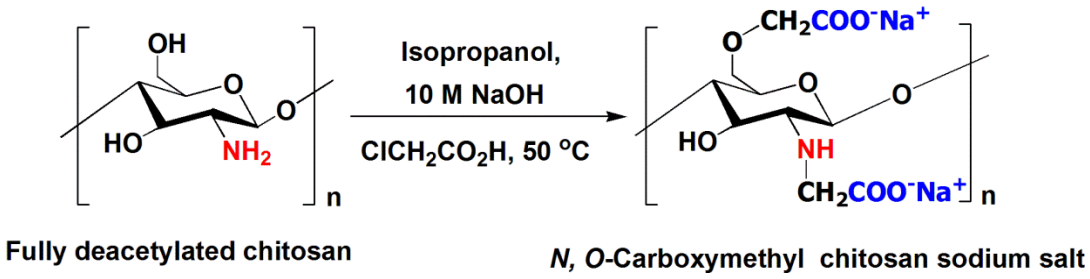

Fig. 66 Schematic modification of CS by grafting with carboxyl groups

3.3 The CS-coated Silica Surface

The study of organic-inorganic hybrid materials is an interesting subject because the latter combine both organic and inorganic properties. Biopolymers would enhance adsorption capacities, the selectivity of metal ions, and the flexibility of hybrid materials. On the other hand, silica could be used to balance some of the disadvantage of biopolymers such as lower chemical resistance, thermal resistance, stability, and mechanical performance. Therefore Silica-CS hybrid materials can be employed to combine the advantages. The hybrid materials can be fabricated as beads, membranes, films, etc. However, in this work, the silica particles used were fumed silica (Aerosil 200, Degussa) whose surface was modified by the introduction of the CS biopolymer. The hybrid material was fabricated as colloidal particles in order to be handled easily and to get more surface sites for capturing metal ions. Herein, some different forms of materials and preparation procedures of the hybrid materials were represented. The hybrid composites, based on the silica particles, were first treated with acid solution or modified before grafting the CS macromolecules. In contrast, CS could be modified with reagents like polyethylene glycol (PEG) to obtain a porous material. Then, the modified CS was attached to the silica particles.

To give an idea and overview about silica-CS hybrid composite materials including their preparation, some selected examples used for water treatment are presented. Q.H. Shi *et al.* activated silica beads (97 nm) with hydrochloric acid and interacted them with CS dissolved in 1% acetic acid. Finally, the CS-coated silica beads were treated with glutaraldehyde. In this cross-linking process, glutaraldehyde reacts with the amino groups of

CS molecules to improve the stability of the CS film (Fig. 67) [62]. Another procedure for the preparation of glutaraldehyde-modified CS coated silica particles involves treatment of SiO_2 particles (150 nm) with dodecyl sulphonic acid sodium salt in NaCl solution. A CS solution is then added into the former solution to adsorb CS onto the silica particles. Finally, the CS-coated silica is cross-linked with glutaraldehyde (Glut) [63]. To study the adsorption of anionic dyes on a silica/chitosan hybrid material, the group of A. R. Cestari first silanized silica gel (70-230 mesh) with 3-aminopropyltrimethoxysilane (APTMOS) and than reacted it with glutaraldehyde to give Glut-SiO_2. The latter was finally cross-linked with CS at room temperature (Fig. 67) [64].

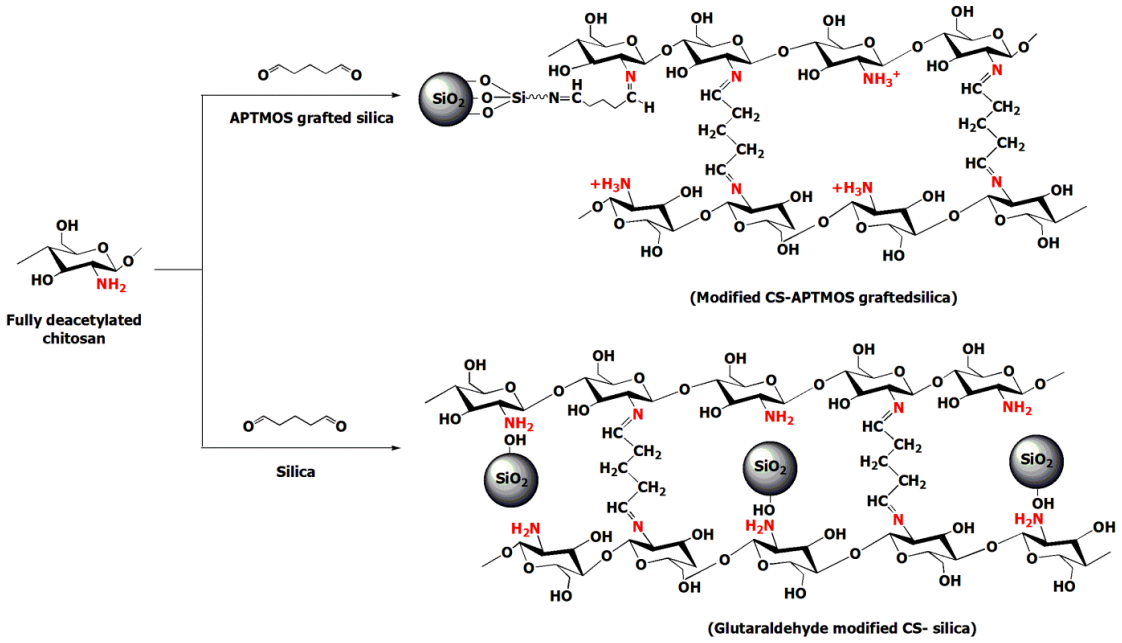

Fig. 67 Schematic preparation of silica-CS hybrid materials

Porous CS-SiO_2 hybrid microspheres with various microstructures have been obtained by A. El Kadib and M. Bousmina depending on the mould used: hydrogel (CS microspheres dispersed in water), alcogels (CS gel dispersed in ethanol) and dried aerogels [65]. Drying under supercritical CO_2 conditions led to an aerogel with high surface. The specific surface area of porous CS-SiO_2 hybrid microspheres was found to be 56 and 73 m^2/g for the core-shell and the homogeneous material-type, respectively. In case of sol-gel process, the specific surface of microspheres found to be 149 m^2/g. Note, that no size reduction of the CS-SiO_2 microspheres has been observed during CO_2 removal. Fig. 68 resumes the different routes for the preparation of CS-SiO_2 microspheres**.**

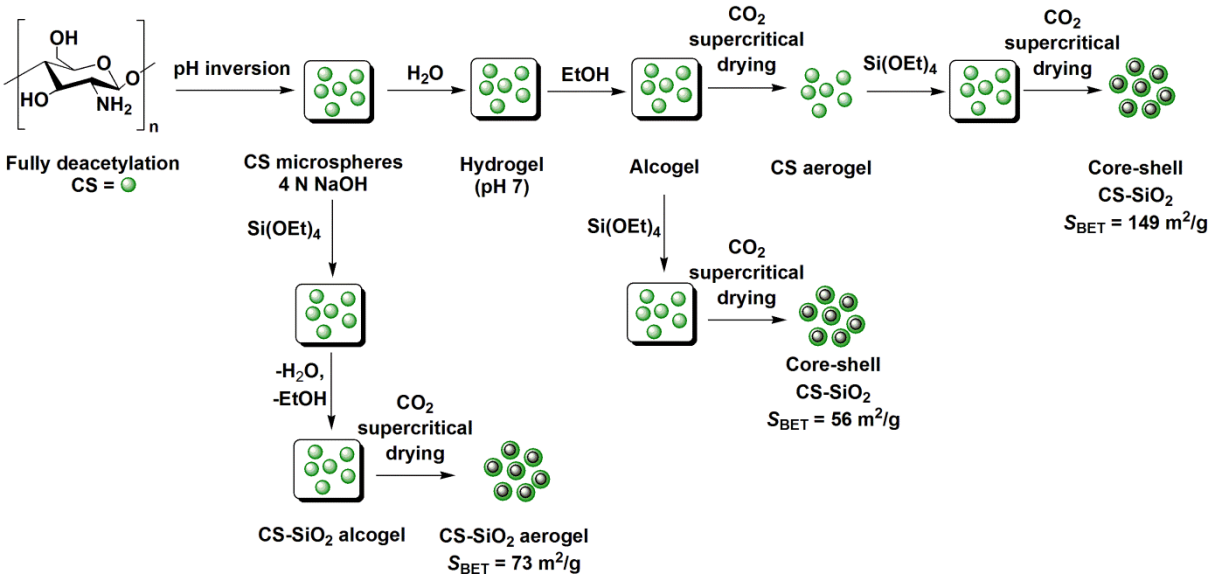

Fig. 68 Three routes for preparation of CS-SiO_2 microspheres (according to ref. [65])

A macroporous CS-coated silica gel (100-200 mesh size) has been evaluated for the immobilization of trypsin. The surface pores of the bead were generated by PEG molecular imprinting and cross-linking steps. The modified CS was then reacted with silica gel to give a macroporous CS-coated silica, which was finally cross-linked with epichlorhydrin to increase the stability of the coated chitosan layer. In this case, the poor resistance of silica at basic conditions is enhanced since the silica surface is coated with CS [66].

In the following biomedical example, an elegant electrophoretic deposition (EPD) method has been developed for the fabrication of nanocomposite silica–chitosan coatings. The EPD has been performed from suspensions of silica and hydroxyapatite ($Ca_{10}(PO_4)_6(OH)_2$ with a chemical composition similar to that of bone tissue in ethanol-water mixture containing CS. The suspensions were ultrasonicated to obtain a homogeneous dispersion of the nanoparticles. CS provides an effectively electrostatic stabilization of the ceramic particles and its positive charge allows the cathodic electrodeposition of the particles. Moreover, CS acts as an effective binder that provides adhesion of the particles to the substrate surface and prevents cracking [67].

In this work, several CS-coated silica hybrid composites were prepared by mixing CS solution and colloidal silica at room temperature to elaborate novel performing sorbents for the retention of divalent cations form aqueous solution.

Results and Discussion

3.4 Physicochemical Properties of the CS Samples

The degree of deacetylation (%DD of CS), the molecular weight distribution, viscosity, and the behavior in aqueous solution and/or in solvents are important quality criteria, especially for an application such as wastewater treatment. Therefore the %DD and other propensities of the CS samples have been analyzed to allow a reliable interpretation of the results. Three types of commercial CS were used in this work. The molecular weight of CS is one of the important factors affecting its physicochemical properties and a key variable in the adsorption process because it influences the solubility of the polymer and the viscosity in the solution. The molecular weight presented as weight average molecular weight (M_W) of the three types of CS was 52.9 kDa for **CS Yuhuan** (CS from Yuhuan Ocean Biochemical, China), 150 kDa for **CS LMW** (CS from Aldrich, U.S.A), and 390 kDa for **CS Marine** (from Marine Chemical, India) (Table 3.2). The M_W of CS depends on the original source and the degree of deacetylation of CS. Notabely a CS with low M_W and high DD should have a high capacity for metal ion removal. The exact value of %DD was determined as described in the following topic.

To prepare CS solutions, the CS samples were dissolved in 1% acetic acid. The following observation was made thereby: the solubilization of **CS Marine** (Mw = ~390 kDa) took more time than that of **CS Yuhuan** (Mw = ~52 kDa). This may be due to the higher M_W of the former type of CS than that of the latter type. Consequently, the latter type of CS exhibited a lower solution viscosity than **CS Marine**. This result is consistent with the report of H. Queen (2006). She reported that the highest molecular weight (600 kDa) produced more viscous solutions than that of middle molecular weight (400 kDa) and lowest molecular weight (150 kDa) [68]. Note that the viscosity of the three types of chitosan solutions has not been measured. However, Table 3.2 shows the wide range of viscosity data of CS LWM and CS Yuhuan.

The **CS Yuhuan** gave a yellow solution after dissolution in acetic acid. This coloration is due to the origin of this biopolymer.

Table 3.2 Three types of commercial CS used in this work

Name	**CS LMW**	**CS Yuhuan**	**CS Marine**
Company	Aldrich, U.S.A	Yuhuan Ocean Biochemical, China	Marine chemical, India
DD, %	75-85	~85	~70
M_W, kDa	~150	~52	~390
Viscosity, mPa.s*	20-300	~50-800**	-
Appearance	White powder	Yellow light powder	White powder

*mPa s = Millipascal Second. **The viscosity is determined at 20.0℃ with 1%chitosan in 1% acetic acid.

Degree of Deacetylation (%DD) of CS

The %DD influences numerous characteristics of CS including crystallinity, degradation, solubility, charge density, compactness of matrices and hydrophobic properties, etc [11, 67]. Of course, also the nitrogen content is correlated with the %DD and constitutes an important parameter especially for metal ion uptake applications, since a high %DD implies a higher number of free amine groups available for binding with metal ions. Therefore is seemed to be important to obtain an accurate value %DD of our CS samples and two independent techniques have been used:

(i) Infrared spectroscopy offers several advantages such as being nondestructive and fast, since there is no special need for the preparation of the samples before recording the ATR-IR spectra. Furthermore, the high precision of the determination of the %DD is consistent with elemental analysis as shown below. The degree of deacetylation was determined by recording the absorbance at 1655 cm^{-1} and at 3450 cm^{-1} (Sabin and Block, 1997) [69].

$$DD\ (\%) = 97.67 - [26.486 \times (A_{1655}/A_{3450})] \qquad (1)$$

where A_{1655} is the absorbance at 1655 cm^{-1} of amide I band as a measure of N-acetyl group content, (C=O band in amine group), A_{3450} is the absorbance at 3450 cm^{-1} of the hydroxyl band of CS. The %DD of two types of CS was calculated using equation (1).

According to the report of Sabnis and co-workers, the values of 97.67 and 24.486 are slope and c values, respectively. They were determined from standard curve plotted between DD% (using chitosans with known degree of deacetylation determined by titrimetry) and absorbance ratio (A_{1655}/A_{3450}) (see more detail in ref. [69]).

The degree of deacetylation thus determined via the FT-IR method is shown in Table 3.3 and was found to be around 73, 75, and 77 for **CS Marine**, **CS Yuhuan**, and **CS LMW**, respectively. The maximum value of % DD was ranked in order as follows: CS LMW (77%DD) > CS Yuhuan (75%) > CS Marine (73%).

Table 3.3 Absorbance of CS from IR spectroscopy

Type of CS	Absorbance		%DD
	1655, cm^{-1}	3450, cm^{-1}	
CS Marine	0.09	0.10	73
CS Yuhuan	0.15	0.17	75
CS LMW	0.14	0.18	77

(ii) As second independent method, elemental analysis has been chosen for the determination of %DD of CS. The determination of the amount of carbon and nitrogen of CS allows to calculation the %DD using equation 2 [70].

$$DD\ (\%) = \left[1 - \frac{(C/N - 5.145)}{(6.816 - 5.145)}\right] X\ 100 \quad (2)$$

where C/N is the percent ratio of carbon or nitrogen in a CS macromolecule. They may vary from 5.145 for completely *N*-deacetylated chitosan ($C_6H_{11}O_4N$ as repeating unit) to 6.861 for the fully *N*-acetylated polymer ($C_8H_{13}O_5N$ as repeating unit). The amount of carbon and nitrogen is shown in Table 3.4, the degree of deacetylation was then calculated utilizing equation 2. The %DD of **CS MW** was found to be 77 %.

Table 3.4 Percent content of C and N of CS by Elemental analysis

Type of CS	Element		%DD
	%C	%N	
CS LMW	40.39	7.31	77

Note that fully deacetylated CS has an amino concentration of about 6.21 mmol/g [71]. This amino concentration helps to calculate the amino amount contained in CS. From IR spectroscopy data, the amino amount of **CS LMW** was found to be 4.22 mmol/g. From elemental analysis, it was found to be 4.78 mmol/g. In comparison, the %DD of **CS LMW** determined from the two independent methods (77 %DD by IR spectroscopy and 77%DD by elemental analysis) was close to each other. In other words, the %DD value of CS determined by IR matches well with that determined by elemental analysis.

In comparison with the literature, the nitrogen amount of CS is found to be 7.325% (%DD ~ 76) [72]. This value was close to that of our chitosan (**CS LMW)** where the nitrogen amount was 7.31% (77%DD determined by elemental analysis).

3.5 Characterization

3.5.1 Preparation of Carboxymethyl-modified CS

The synthesis of a *N,O*-carboxymethylchitosan polymer by reaction of CS with monochloroacetic acid in isopropyl alcohol via alkylation reaction providing carboxymethylchitosan material **CS(CO_2H)** is shown in Fig. 66 [61]. The solubility of **CS(CO_2H)** was probed by the preparation of a 0.4% **CS(CO_2H)** solution in DI water. After one night of stirring, it was found that the **CS(CO_2H)** dissolved entirely in DI water, the pH value being 9.3. To confirm an appearance of the COO^- functional group, the **CS(CO_2H)** was characterized by FT-IR spectroscopy as shown in Fig. 71c.

3.5.2 Preparation of CS-coated Silica Hybrid Composites

With the goal to prepare novel adsorbent for metal cation removal, three types of modified CS-coated silica particles have been prepared as summarized in Fig. 69. Preparative details concerning the synthesis of the six new silica-based composites are described in the Experimental Part:

(I) **SiO_2+CS LMW**, **SiO_2+CS Yuhuan**, and **SiO_2+CS Marine**,

(II) **$SiO_2(NH_2)$+CS LMW**, **$SiO_2(CO_2H)$+CS LMW,**

(III) **SiO_2+CS(CO_2H)**.

To prepare the first family, Activated silica particles were directly coated with CS (**CS LMW**, **CS Yuhuan**, and **CS Marine**) providing the three CS-coated silica materials **SiO_2+CS LMW**, **SiO_2+CS Yuhuan**, and **SiO_2+CS Marine**. The interaction between CS and the surface occurs probably through hydrogen-bonding between silanols groups and the primary amine groups of CS. But partial deprotonation of the acidic Si-OH groups by the basic NH_2-functions cannot be ruled out. In this case, electrostatic interactions of the type $-NH_3^+\cdots{}^-O$-Si are expected. Note that recently supramolecular structures of CS on the surfaces of fumed silica have been evidenced by mass spectrometry, combined with thermorgravimetric and UV-Vis and IR studies [73].

The second family comprising the **$SiO_2(NH_2)$+CS LMW** composite was prepared by functionalizing Aerosil 200 particles via covalent bonding using APTES (see Chapter 2). The amine-grafted silica was then coated with CS at room temperature to obtain **$SiO_2(NH_2)$+CS LMW**. The other variant **$SiO_2(CO_2H)$+CS LMW** was obtained in a two-step sequence. In the first step, 4-(triethoxysilyl)-butyronitrile (CPTES) was condensed on the silica surface,

followed by acidic hydrolysis of the surface bound nitrile groups to obtain the carboxyl groups terminated silica particles. In the second step, CS was deposited on the carboxyl-grafted silica core. The interaction between CS and the carboxyl group could involve CS-NH_2···HOOC-SiO_2 hydrogen bridges or be electrostatic in nature through $–NH_3^+ \cdots {}^-O_2C$-interactions. Alternatively, a covalent linking through amide groups by condensation between -NH_2 and -COOH groups can be taken in consideration. However, this hypothesis is less likely, since formation of an amide requires in general more severe reaction conditions. Furthermore, no evidence for the formation of amide groups was obtained by FT-IR spectroscopy.

To obtain the third type, namely **SiO_2+CS(CO_2H)**, Aerosil 200 particles were coated with carboxymethylated CS. Again, the interaction between this CS derivative and the silica surface occurs most probably through hydrogen bonding between carboxylate groups and Si-OH groups according to the FT-IR spectra.

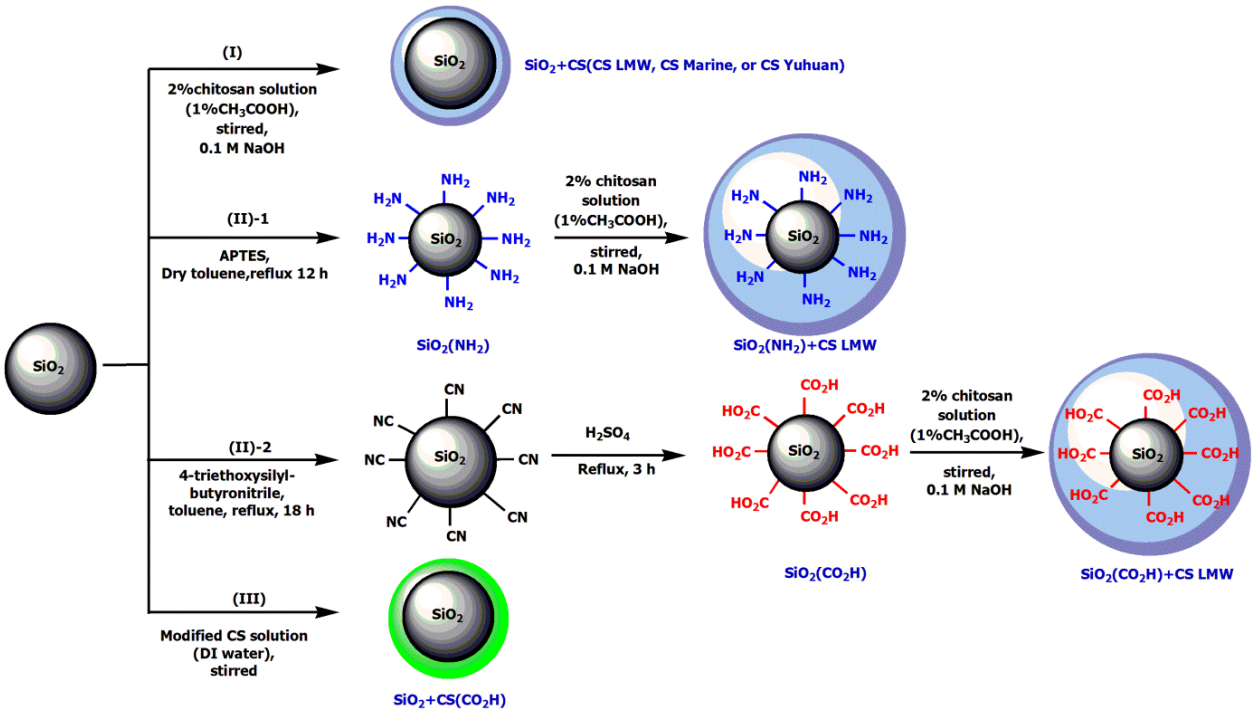

Fig. 69 Preparation of CS-coated silica particles

Color code: blue = non-modified CS, green = carboxymethyl-modified CS

3.5.3 Characterization of the Composites by Elemental Analysis

The C, H, N-contents of composites **SiO_2+CS LMW** and **SiO_2(CO_2H)+CS LMW** were determined by elemental analysis. The results are shown in Table 3.5 and allow the calculation of the percentage (%) of present NH_2-functions. A nitrogen percentage of CS

LMW coated-silica (**SiO_2+CS LMW)** was 6.31%, corresponding to 4.51×10^{-3} mol of amine functions (-NH_2) per gram of material. The other hybrid composite, **$SiO_2(CO_2H)$+CS LMW**, contained 5.89 % of nitrogen corresponding to 4.21×10^{-3} mol of amine functions (-NH_2) per gram of material. In case of **$SiO_2(NH_2)$+CS LMW**, a somewhat higher nitrogen percentage of 6.05% was obtained consistent with the presence of amino groups both in **$SiO_2(NH_2)$** and in **CS LMW**. Consequently, amine functions (-NH_2) in CS LMW could not be directly calculated.

In the literature, the CS amount containing glutaraldehyde crosslinked with silica gel was found to be 8.5 mg/g of wet bead [62].

Table 3.5 Elemental analysis of the silica particles

Material	Percent (%wt)			N, mmol/g
	C	H	N	
SiO_2	< detection limit	0.33	< detection limit	-
SiO_2+CS LMW	34.88	5.71	6.31	4.51
$SiO_2(CO_2H)$+CS LMW	33.49	5.64	5.89	4.21
$SiO_2(NH_2)$+CS LMW	34.75	5.54	6.05	-

3.5.4 Determination of the BET Specific Surface

The BET specific surface (S_{BET}) of the new silica composites was also determined. As one may expect, the specific surface of the particles decreased significantly after the modification of silica nanoparticles (see Table 3.6). The S_{BET} value of the CS-coated silicas was less than 10 $m^2.g^{-1}$. An obstruction and blocking of the adsorption sites might occur after surface-coating of the silica nanoparticles with a CS layer to explain this important lowering of the S_{BET}. This finding suggested that the surface of silica nanoparticles be functionalized with the carboxyl group or they could be covered entirely by a CS layer. The specific surface decreased according to the physical or chemical modification.

We are aware of a recent study where the S_{BET} value of the silica xerogel hybrid materials containing CS was measured in function of the CS content [74]. This study revealed that the specific surface area is considerably reduced when increasing the amount of CS. The neat xerogel exhibits a S_{BET} of 620 $m^2.g^{-1}$, whereas the hybrid containing 30% of CS has a S_{BET} value of 150 $m^2.g^{-1}$. When increasing the CS percentage to 50%. The S_{BET} value drops to less than 20 $m^2.g^{-1}$. So our findings are in line with the latter study.

Table 3.6 The BET specific surface area (S_{BET}) of neat silica and biopolymer-coated silica

S_{BET}, m^2/g	**SiO_2**	**SiO_2+CS LMW**	**SiO_2+CS Marine**	**$SiO_2(CO_2H)$+CS LMW**
	182 ± 4	5 ± 1	1.6 ± 1	5 ± 1

3.5.5 FT-IR Spectroscopy

As can be seen in Fig. 70**a-c**, the FT-IR spectra of **CS LMW**, **CS Marine**, and **CS Yuhuan** are similar and displayed a characteristic -OH stretching vibration at 3450 cm^{-1}, which overlaps the -NH stretching vibration for amines resonating. The C-H stretching vibration is observable at 2923 cm^{-1}. At 1650 cm^{-1} are found the C=O stretching vibration for amide I. Other partially overlapping absorptions at 1560 cm^{-1} are due to the -N-H bending of the amine group. Other absorptions can be assigned to amide II at 1379 cm^{-1} for -CH symmetric bending vibration in -CHOH-, at 1022 cm^{-1} for the -CO stretching vibration in -COH [9]. Based on literature data, the most frequently identified bonds which correspond to a given wave number (cm^{-1}) in IR spectra are presented in table 3.7 [7]. These data are close to those of our CS spectra (Table 3.8).

Table 3.7 IR spectra of CS and their position assignment

Wave number, cm^{-1}	Position assignment
3450, 3500	OH group (at C3 and C6)
3360	broad band derived from OH and NH groups overlay each other
2920, 2880	CH_2 groups related to the symmetric and asymmetric bonds in a saccharide ring
1660	oscillation of C=O in amino groups
1630	protonated amino groups
1590, 1560	NH_2 amino groups and oscillation of NH group in amide group, respectively
1420	oscillations of OH and CH groups
1380	-CH bond, C-CH_3 deformations in amide groups
1150, 1040	-C-O-C in glycosidic bonds
850, 840	CH_3COH groups

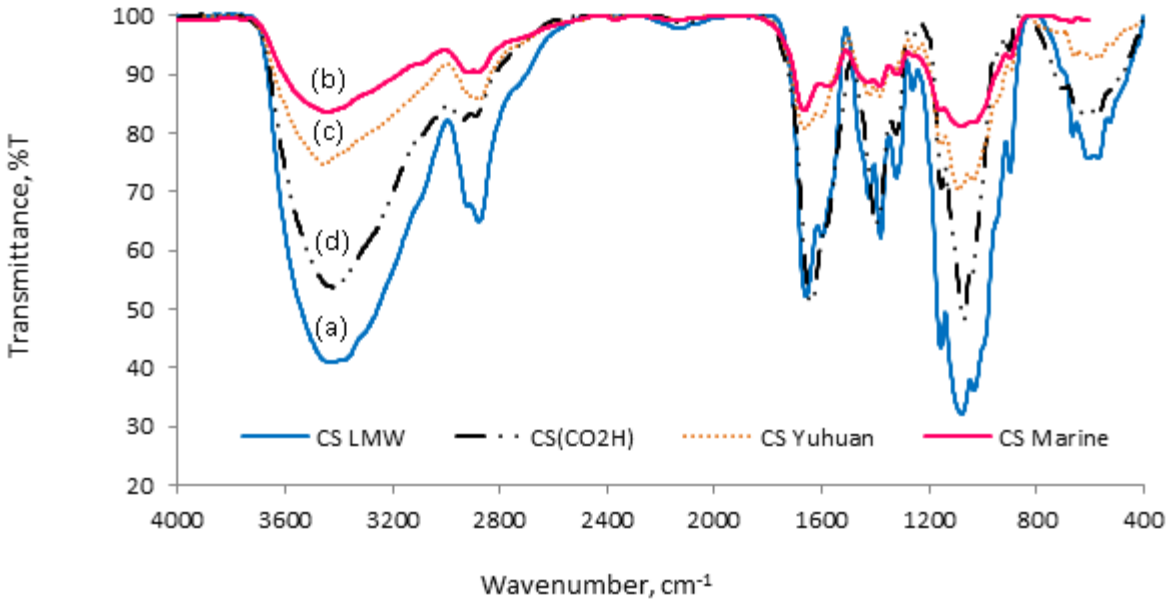

Fig. 70 FT-IR of **CS LMW** (a), **CS Marine** (b), **CS Yuhuan** (c), and **CS(CO_2H)** (d), respectively

Table 3.8 IR analysis of pure CS

Position assignment	Frequency, cm^{-1}		
	CS LMW	**CS Marine**	**CS Yuhuan**
C-OH stretching vibration	1078	1022	1024
N-H bending for amine II	1595	1560	1598
C=O stretching vibration for amide I	1658	1650	1664
C-H stretching vibration	2896	2871	2873
O-H, and N-H stretching vibration	3450	3450	3450

The characteristic absorption bands of **CS(CO_2H)** are shown in Fig. 71 (curve d) and in Table 3.9. The two bands at 1627 cm^{-1} and 1429 cm^{-1} are the characteristic absorption bands of the COO^- carboxylate group due to an asymmetric vibration and symmetric vibration according to the literature [61]. Note that after deprotonation of a -CO_2H group which resonates at about 1730 cm^{-1}, the resulting -COONa group absorption shift to lower wavenumber at around 1627 cm^{-1}. We got no evidence for the presence of -CO_2H groups in our sample. The amide II band present in **CS LMW** at 1595 cm^{-1} disappeared after carboxymethylation indicating the binding of the carboxyl group to the amino group of CS. [75, 76]. The band at 3450 cm^{-1} was shifted to 3471 cm^{-1} after carboxymethylation [38, 77].

Table 3.9 IR analysis of the different types of CS-coated silica hybrid materials

Functional groups	Frequency, cm^{-1}			
	SiO_2 +CS LMW	**$SiO_2(CO_2H)$ +CS LMW**	**$SiO_2(NH_2)$ +CS LMW**	**SiO_2 +CS(CO_2H)**
Siloxane (from silica)	1101	1081	1107	1109
-COO^- symmetric vibration (carboxylic acid)	-	-	-	1440
-COO^- asymmetric vibration (carboxylic acid)	-	-	-	1650
Carbonyl (residual amide in CS)	1656	1658	1679	-
Alkyl stretching vibration	2879	2877	2918	2933
-OH (silanols from silica or hydroxyl groups onto CS)	3448	3448	3485	3471

In the case of CS-coated silica, intense siloxane stretching bands around 1080-1100 cm^{-1} dominate the spectra (Fig. 71-72). The bands related to alkyl chains are detected at 2879 cm^{-1} in **SiO_2+CS LMW (**Fig. 71**a**), at 2922 cm^{-1} in **SiO_2+CS Yuhuan (**Fig. 71**b**), at 2929 cm^{-1} in **SiO_2+CS Marine (**Fig. 71**c**), at 2918 cm^{-1} in **$SiO_2(NH_2)$+CS LMW (**Fig. 72a), at 2877 cm^{-1} in **$SiO_2(CO_2H)$+CS LMW (**Fig. 72**b**), and at 2933 cm^{-1} in **SiO_2+CS(CO_2H) (**Fig. 72**c**). The residual amide bonds of the deposited CS give rise to the C=O stretching bands in the range between 1650-1679 cm^{-1}. Finally, the large band observed around 3450 cm^{-1} is attributed to both silanol groups on the surface of silica and hydroxyl groups presented on CS [73, 78-80]. In line with our data, J.H. Chen *et al.* found for a CS-silica hybrid membrane obtained by cross-linking of CS with 3-aminopropyl-triethoxysilane a broad band at around 3358 cm^{-1} corresponding to O-H stretching vibrations of hydroxyl groups and the stretching vibration of N-H of CS [81].

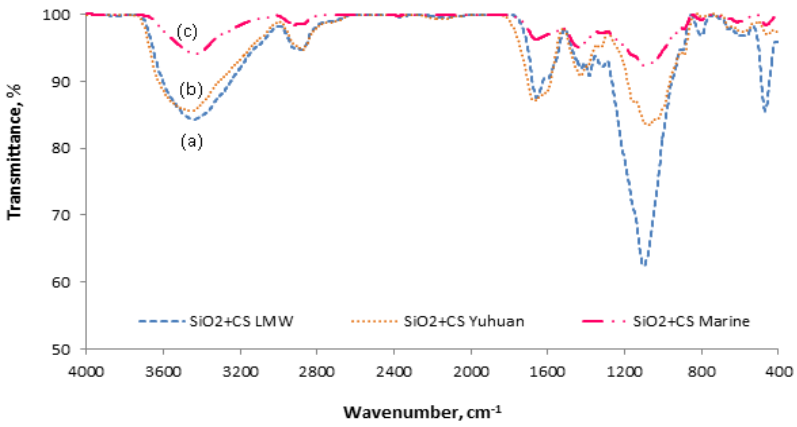

Fig. 71 FT-IR of **SiO_2+CS LMW** (a), **SiO_2+CS Yuhuan** (b), and **SiO_2+CS Marine** (c)

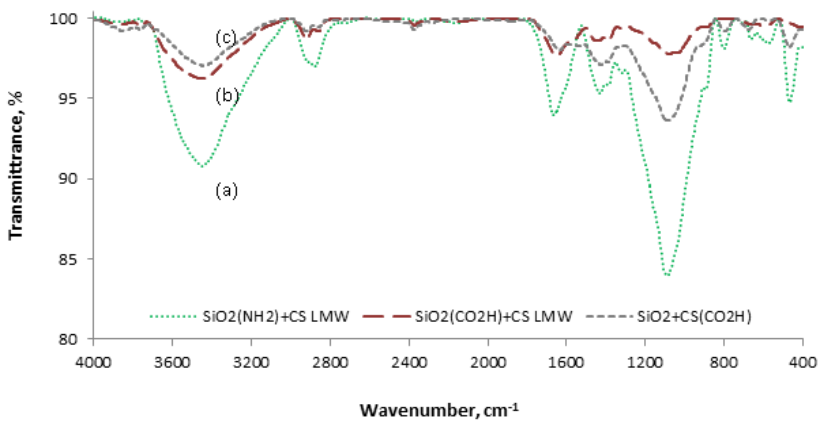

Fig. 72 FT-IR of **$SiO_2(NH_2)$+CS LMW** (a), **$SiO_2(CO_2H)$+CS LMW** (b), and **SiO_2+CS(CO_2H)** (c), respectively

In the case of **$SiO_2(NH_2)$+CS LMW (**Fig. 72**a**) the band at around 3448 cm^{-1} (**SiO_2+CS LMW)** is shifted to 3485 cm^{-1}. This shift may be due to the -NH_2 group grafted onto the surface of silica.

Due to the carboxylic acid moieties present in **$SiO_2(CO_2H)$ (**Fig. 60**b**), an absorption was observed at 1711 cm^{-1}. However, this band did not appear in **$SiO_2(CO_2H)$+CS LMW (**Fig. 72**b**). This absence could be attributed to a relatively small number of CO_2H groups compared to amide moieties in CS and the above discussed interactions between the CS and the CO_2H groups.

For **SiO_2+CS(CO_2H) (**Fig. 72**c**), the band at 1429 cm^{-1} and 1627 cm^{-1} due to COO^- symmetric and asymmetric vibration from **CS(CO_2H)** were shift to 1440 cm^{-1} and 1650 cm^{-1} after the coating of CS(CO_2H) onto the silica surface.

From FT-IR data, a proposed model of the possible interaction between CS and silica is represented in Fig. 73. The CS chains were adsorbed on silica particles via different types of interactions such as an electrostatic attraction [82] and H-bonding [83] as describe on pages 112-113.

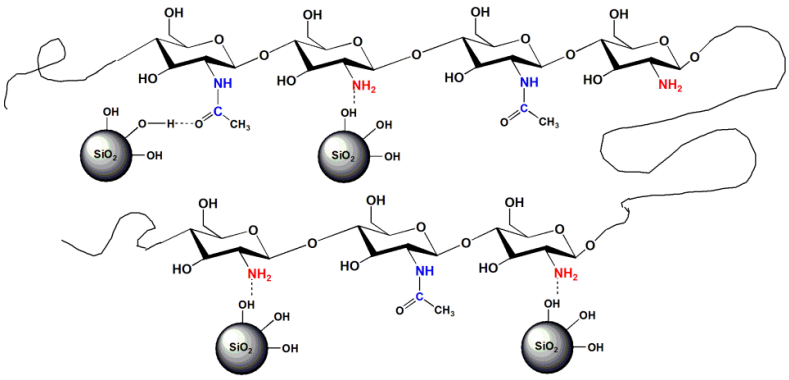

Fig. 73 Schematic possibility of interaction between active sites of CS and silanol groups of silica

3.5.6 Morphology Analysis of the Composite by SEM

The surface morphology of the **CS LMW** polymer was investigated by SEM as shown in Fig. 74**a**. The **CS LMW** image shows a dense and smooth surface texture which was similar to the observation of the surface morphology of CS by E.-J. Lee *et al.* [74]. In contrast, the morphology of the carboxymethyl-CS material (**CS(CO_2H)**) was rough. There were some porous points on the surface of the **CS(CO_2H)** (see Fig. 74**b**). This could favour the accessibility for metal adsorption.

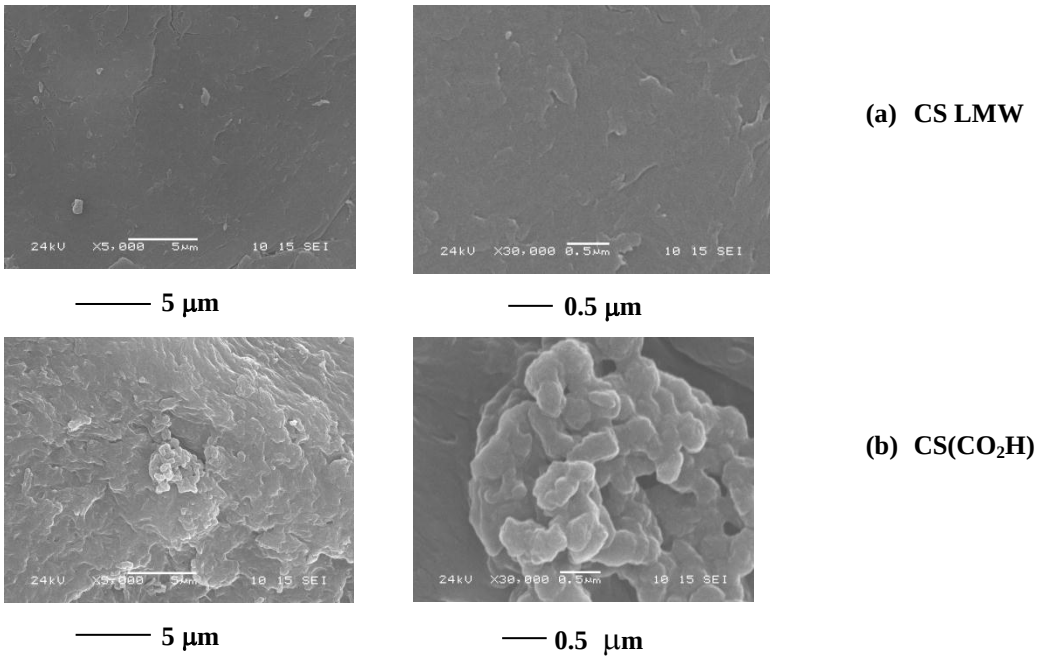

Fig. 74 SEM images of unmodified CS (a) compared to carboxymethyl CS (b)

Next, the morphology of the hybrid materials (**SiO_2+CS LMW**, **SiO_2+CS Marine**, **$SiO_2(NH_2)$+CS LMW**, **$SiO_2(CO_2H)$+CS LMW** and **SiO_2+CS(CO_2H)**) was investigated by SEM. The surface of the silica particles, before coating with CS, was quite rough and irregular as shown in Fig 29**a**. After biopolymer coating, the CS-coated silica hybrid composites (**SiO_2+CS LMW, SiO_2+CS Marine**, **$SiO_2(NH_2)$+CS LMW**, and **$SiO_2(CO_2H)$+CS LMW** showed a rigid texture with small gains of the silica nanoparticles distributed homogeneously in the CS matrix which was due to the high coverage of CS (see Fig. 75**a-d**) [84]. In contrast, the morphology of the carboxymethyl CS-coated silica (**SiO_2+CS(CO_2H)**) showed a heterogeneous texture of the carboxymethyl CS molecules (Fig. 75**e**).

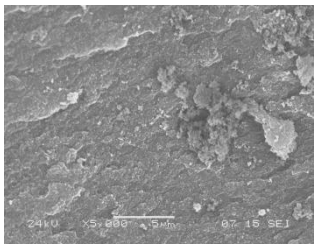

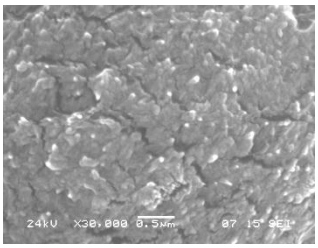

(a) SiO_2+CS LMW

5 µm **0.5 µm**

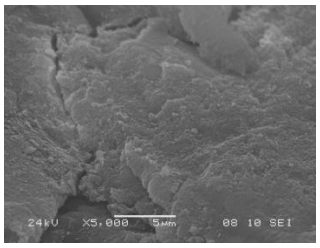

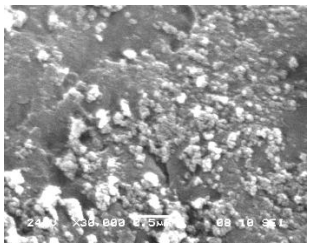

(b) SiO_2+CS Marine

5 µm **0.5 µm**

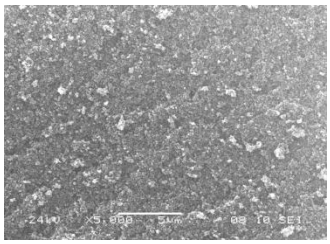

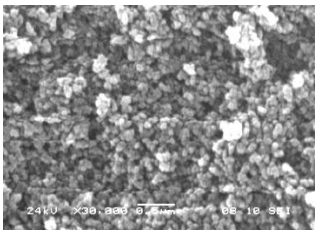

(c) $SiO_2(NH_2)$+CS LMW

5 µm **0.5 µm**

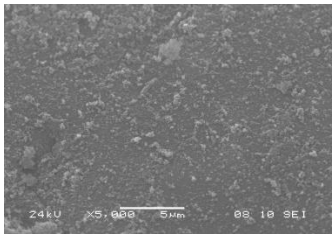

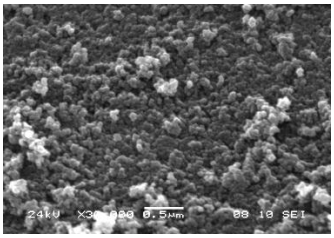

(d) $SiO_2(CO_2H)$+CS LMW

5 µm **0.5 µm**

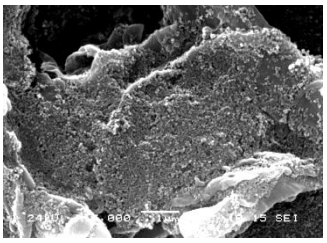

(e) SiO_2+CS(CO_2H)

1 µm

Fig. 75 SEM images of CS-coated silica materials

In particular, Atomic Force Microscopy imaging allows us to observe the surface of **SiO_2** and **SiO_2+CS LMW**. Each colloidal **SiO_2** solution and/or colloidal **SiO_2+CS LMW** solution was deposited onto a thin glass substrate and kept in a desiccator to dry the sample before scanning. The AFM image shown in Fig. 76 was obtained by scanning a 4 µm x 4 µm surface area, revealing the presence of colloidal nodules on the glass substrates, having an average

height of about 50 nm for **SiO_2** (Fig. 76**a**). On the contrary, CS-coated silica displayed a homogeneous coating with the thickness between 300 and 400 nm (Fig. 76**b**).

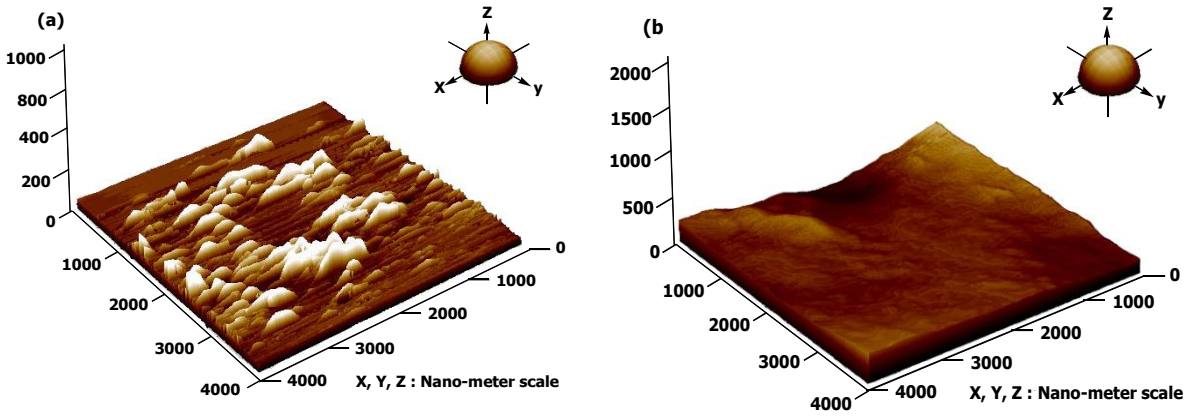

Fig. 76 The surface morphology of **SiO_2** (a), and **SiO_2+CS LMW** (b)

3.5.7 pH and Conductivity Measurement

The behavior of the hybrid composites solution in aqueous solution was studied by measuring the pH and conductivity values in DI water at various times for 72 hours. For the hybrid composites (**SiO_2+CS LMW**, **SiO_2+CS Marine**, **SiO_2+CS Yuhuan**, **$SiO_2(CO_2H)$+CS LMW**, **$SiO_2(NH_2)$+CS LMW** and **SiO_2+CS(CO_2H)**), their pH values reached about 7.6-8.9. The pH of the hybrid materials solution (0.5% w/w) increased when compared to the non-grafted silica solution (0.5% w/w, ~ pH 5.7) or carboxyl-grafted silica solution (0.5% w/w, ~ pH 4.2), due to coating of the particle surface by the CS polymer.

Conductivity values of all modified silica composites, as well as non-grafted silica were also investigated. It was found that the conductivity of all composites remained quite stable after 24 hours. The conductivity of **SiO_2+CS LMW** was found to be in the range 18 - 22 μS/cm after 24 hours. For **SiO_2+CS Marine**, the conductivity was found to be in the range of 26 - 31 μS/cm. The conductivity value of the two bio-hybrid materials was quite close. However, the conductivity of the CS-coated silica materials was superior to those of the carboxyl-grafted silica and **SiO_2**. This could be explained by the influence of CS molecules on the silica surface. The conductivity in the presence of CS increased due to the displacement of the equilibrium dissociation of the acid and progressive dissolution of protonated CS (M. Rinaudo *et al*, 1999) [85].

In the case of **$SiO_2(NH_2)$+CS LMW** and **SiO_2+CS(CO_2H)**, their conductivity values were found around 400 μS/cm and 350 μS/cm, respectively. After silica was surface-coated

with carboxymethyl-CS (**SiO_2+CS(CO_2H)**), its conductivity value was close to that of unmodified CS-coated amine grafted silica (**$SiO_2(NH_2)$+CS LMW**). The conductivity in the presence of modified CS and/or modified silica increased due to the appearing of counter ion on the modified CS (CS-COO^-Na^+) and/or modified silica (SiO_2-$NH_2^+Cl^-$). The Cl^- concentration in the solution of **$SiO_2(NH_2)$+CS LMW** determined by Mohr's method was found to be around 0.02 M. After intensively rinsing with DI water, the conductivity value of **$SiO_2(CO_2H)$+CS LMW** was found to be around 3-6 μS/cm. The pH and conductivity measurements conducted on these hybrid composites imply that these composites are quite stable in aqueous solution at least for 72 hours.

3.5.8 Zeta Potential

In order to study the interfacial properties of the colloidal silica material, the zeta potential of the hybrid composites was determined at 25 ^oC. The results are shown in Fig. 77**a**-**b**. For comparison, the zeta potential values of the unmodified particles were also represented. The point of zero charge (pzc) of the Aerosil 200 silica particles was around pH 3. At pH > 3, the zeta potentials decreased. This induced an increase of the concentration of the negative charges on the silica surface. An unequivocal reversal of the sign of the zeta potential was noticed after coating the two types of silica by CS at an acidic pH. The pzc of the coated silica composite was reached at a pH 6.5. Therefore, the zeta potentials of the hybrid composites were positive at pH < pzc. This could be explained by the protonation of amino groups to give positively charged -NH_3^+ species at acidic pH (in the absence of a salt, the pKa value of CS is 6.5) [86]. The zeta potential turned to negative values at pH higher than pzc. Under alkaline conditions, the amino-groups were deprotonated. Therefore, the zeta potential was negative. Note that the zeta potential values of the five types of CS-coated silica (**SiO_2+CS LMW**, **SiO_2+CS Marine**, **$SiO_2(CO_2H)$+CS LMW**, **$SiO_2(NH_2)$+CS LMW**, and **SiO_2+CS(CO_2H)**) were quite close. This result could be the consequence of a large degree of coating by CS on our silica particles. The results of zeta potentials were consistent with the results reported by T. Witoon and his team. The zeta potentials of the CS-silica hybrid material prepared at low pH (2-3) were positive. At this low pH, amino groups of CS were highly protonated and the zero charge of silica surface was formed. So, the presence of CS macromolecules in the mixtures prevents the aggregation of silica nanoparticles [87].

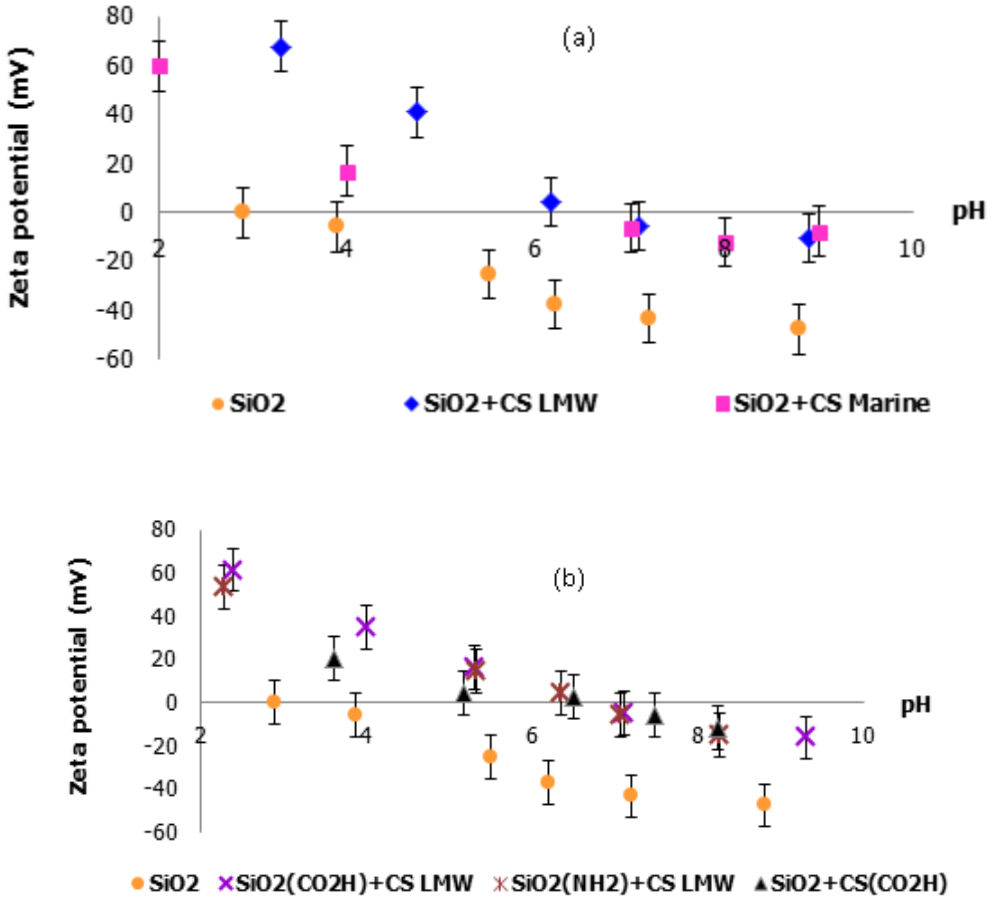

Fig. 77 The zeta potential values of **SiO_2** compared with CS-coated silica (**SiO_2+CS LMW**, and **SiO_2+CS Marine**) (a), and the **SiO_2** compared with CS LMW-coated grafted silica SiO_2 materials (**$SiO_2(CO_2H)$+CS LMW**, **$SiO_2(NH_2)$+CS LMW**, and with carboxymethyl CS-coated silica **SiO_2+CS(CO_2H)** (b)

3.5.9 Hydrodynamic Size Measurement

The hydrodynamic size of the six modified silica materials was also investigated. The dried composites **SiO_2+CS LMW**, **SiO_2+CS Marine**, **SiO_2+CS Yuhuan**, **$SiO_2(CO_2H)$+CS LMW**, **$SiO_2(NH_2)$+CS LMW**, and **SiO_2+CS(CO_2H)** were ultrasonicated for 30 min before measuring their size. The hydrodynamic size of the six hybrid composites is given in Table.3.10. The hydrodynamic size of the six hybrid composites was higher than 1 µm. These values were in accordance with the deposition of CS supported on the silica surface. These results were similar to the results reported by J.-S. Chang and co-workers. The average size of the hybrid material which was measured by light-scattering grew to 9.7 µm due to CS deposition [73].

Table 3.10 Hydrodynamic size of untreated silica, and six hybrid composites

Materials	Average hydrodynamic size
SiO_2	328 ± 25 nm
SiO_2+CS LMW	> 1 µm
SiO_2+CS Marine	> 1 µm
SiO_2+CS Yuhuan	> 1 µm
$SiO_2(CO_2H)$+CS LMW	> 1 µm
$SiO_2(NH_2)$+CS LMW	> 1 µm
SiO_2+CS(CO_2H)	> 1 µm

Conclusion

In this chapter, the biosorbent **CS LMW**, **CS Yuhuan**, and **CS Marine** have been characterized by several methods. The %DD was found to be 73, 75, and 77% for **CS Marine**, **CS Yuhuan**, and **CS LMW**, respectively. The degree of deacetylation of the **CS LMW** was obtained by infrared spectroscopy and elemental analysis. Independently of the method, the %DD of CS LMW was found to be 77%. The results showed that there was no significant difference for the %DD values determined from the two methods. In order to improve the adsorption properties and solubility, **CS LMW** was chemically modified by synthesis of *N*, *O*-carboxymethylchitosan the derivative **CS(CO_2H)**. The composite was characterized using FT-IR spectroscopy confirming the successful introduction of carboxyl groups on the CS scaffold. The surface morphology of a functionalized CS composite was characterized by SEM technique. The morphology of the modified composite of **CS(CO_2H)** showed a rough and porous texture which would enhance its adsorption properties. In the literature, the *N*-carboxymethylchitosan derivatives exhibited an promising efficiency for Cu(II) adsorption [78]. This *N*-carboxymethylchitosan derivatives was also used to bind with Au(III) [38]. In order to overcome the disadvantages of CS (swelling), the CS was deposited on Aerosil 200 as supporting material.

These CS-coated silica (activated and/or functionalized) composites were successfully prepared using reaction mild conditions. The composites were characterized using FT-IR, SEM, AFM, zeta potential, hydrodynamic particles size, and BET specific surface the same as neat CS and modified CS. The behavior of the composites in aqueous solutions was studied by measuring the pH and conductivity values. The hybrid composite showed a stability

property in aqueous solution for at least 72 hours. The carbon amount of CS coated on the silica surface was measured by the Total Organic Carbon (TOC) method. It was found to be 1.67 x 10^{-3} mol/g for **CS LMW**. The amine content was also determined by elemental analysis. It was found to be 4.51 x 10^{-3} mol/g for **SiO_2+CS LMW**. The CS amount determined from the latter method was higher than that determined by the former method. In the former method, the solid sample required the chemical procedure to convert the solid sample to solution (dissolving with acetic acid). Therefore some residue would be lost. The hybrids composites of **SiO_2+CS LMW**, **SiO_2+CS Yuhuan, SiO_2+CS Marine**, **$SiO_2(NH_2)$+CS LMW, $SiO_2(CO_2H)$+CS LMW**, and **SiO_2+CS(CO_2H)** were tested as adsorbent for Cu(II), and Ni(II) ions removal form aqueous solution at optimum pH describing in Chapter 4.

Experimental Part

3.6 Materials and Apparatus

Chloroacetic acid (99.3%) was purchased from Aldrich Chemical Company. Inc., Switzerland. Sodium bicarbonate was purchased from Prolabo, Switzerland. Glacial acetic acid (99.9%) was purchased from Sigma-Aldrich, Germany. All reagents were analytical grade. The amount of CS adsorbed on silica surface was quantified by means of a TOC analyzer instrument (TOC-5050, Shimadzu, Japan).

3.7 Preparation of Carboxymethyl-modified CS

CS LMW was dispersed in 100 ml isopropyl alcohol and stirred for 30 min at ambient temperature. An amount of 10 mol/L sodium hydroxide (15 ml) was added to the CS solution (in six equal portions) and stirred for 45 min. Then, chloroacetic acid (4 g)/ isopropyl alcohol solution was added to the mixture solution in four equal portions. The solution was stirred for 5 h at 50 ^oC. The solid product was filtered off, washed with ethanol (80%, v/v) until a filtrate reached a neutral pH. The product was dried at 50 ^oC to obtained *N,O*-Carboxymethyl chitosan. The schematic preparation is shown in Fig. 66 [61].

3.8 Preparation of Organic-inorganic CS/silica Hybrid Composites

A 0.5% of each colloidal (non-grafted and/or grafted) silica was added to 100 ml of a 2% CS solution (2 g of **CS LMW** or **CS Yuhuan**, or **CS Marine** dissolved with 100 ml of 1% CH_3COOH) while being stirred with a magnetic stirrer for 1 night. The above process led to the formation of silica-CS suspension (see Fig. 78**a**). This suspension was poured into 500 ml of 0.1 M NaOH solution while being stirred to neutralize excess acid. Then the particles were successively washed with DI water. The material was dried in an oven at 100 ^oC for 24 hours, crushed and kept in desiccator until it was used. In the case of carboxymethyl CS, it was first dissolved in 100 ml of DI water for 24 hours before adding colloidal silica into the CS solution (see Fig. 78**b**) [61].

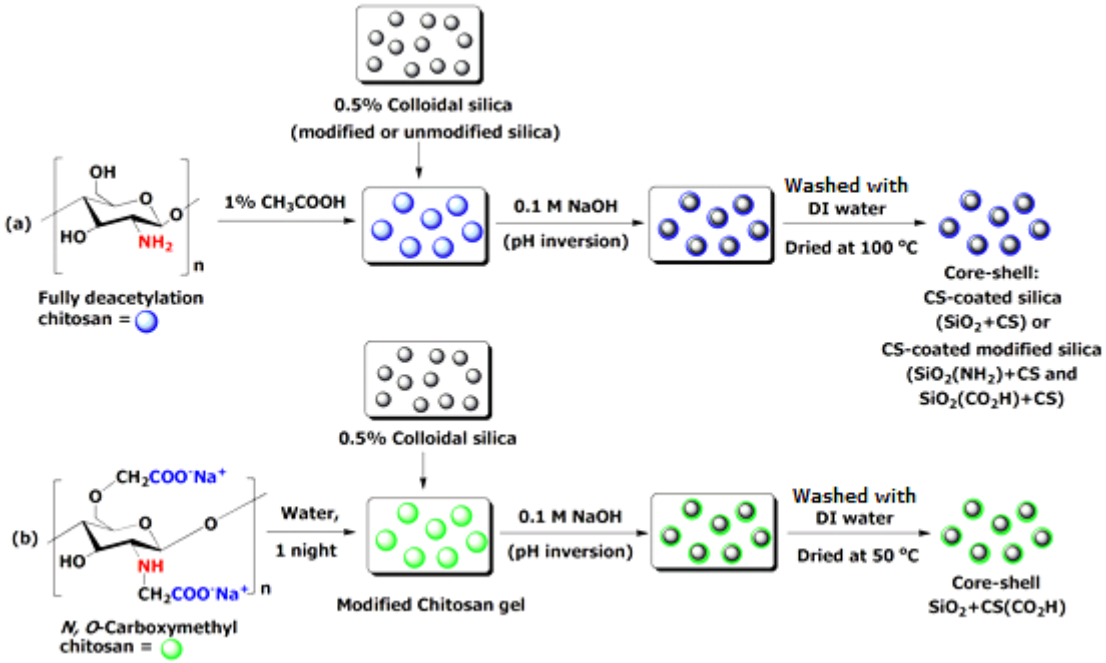

Fig. 78 Schematic preparation of CS-coated Silica hybrid materials:
CS-coated silica (modified or unmodified) (a), Carboxymethyl CS-coated silica (b)

3.9 Determination of Concentration of CS Adsorbed on Silica by Total Organic Carbon (TOC)

The carbon content of CS-grafted untreated silica particle was quantified by TOC analysis (Shimadzu, TOC-5050, Japan). The sample was prepared as follows: an 0.1 g amount of the composite was suspended in 10 ml of 1% CH_3COOH solution leading to dissolution of CS from the composite. The amount of carbon of CS of the initial concentration of CH_3COOH (1%) and the mixed solution between CH_3COOH and CS adsorbed on silica was determined. The concentration of CS was then calculated.

References

1. L. Fuks, D. Filipiuk, and M. Majdan, *Transition metal complexes with alginate biosorbent*, J. Mol. Struct., 792 (2006) 104-109.
2. S. Smitha, P. Shajesh, P. Mukundan, T.D.R. Nair, and K.G.K. Warrier, *Synthesis of biocompatible hydrophobic silica-gelatin nano-hybrid by sol-gel process*, Colloid Surface B, 55 (2007) 38-43.
3. J.B. Xu, D.A. Spittler, J.P. Bartley, and R.A. Johnson, *Alginic acid silica hydrogel coating for the protection of osmotic distillation membrane against wet-out by surface active agents*, J. Membrane Sci., 260 (2005) 19-25.
4. Y.Y. Luo, Y.Q. Wang, J.P. Zhong, C.Z. He, Y.Z. Li, and Z. Peng., *Interaction between fumed-silica and epoxidized natural rubber*, 21 (2011) 777-783.
5. X. Huang, Y. Wang, Q. He, X Liao, and Bi Shi, *Pd(0) Nanoparticle Stabilized by Tannin-grafted SiO_2 Beads and Its Application in Liquid-hydrogenation of Unsaturated Organic Compounds*, Catal Lett., 133 (2009) 192-200.
6. X. Ye, Y. Zhou, Y. Sun, J. Chen, and Z. Wang, *Structure and infrared emissivity of collagen/SiO_2 composite*, Appl. Surface Sci., 254 (2008) 5975-5980.
7. Z. Zarzycki, M. Dorabialska, R. Zarzycki, and A. Wojtasz-Pajak, *The mechanism of sorption of Ag^+ ions on chitosan mecrogranules: IR and NMR studies*, Progress on Chemistry and Application of Chitin and its Derivatives, 14 (2009) 49-64.
8. X.-G. Chen, and H.-J. Park, *Chemical characteristics of O-carboxymethyl chitosans related to the preparation conditions*, Carbohydr, Polym., 53 (2003) 355-359.
9. S.-L. Wang, and S.-H. Chio, *Deproteinization of Shrimp and Crab Shell with the Protease of Pseudomonas Aeruginosa K-187*, Enzyme Microb. Technol., 22 (1998) 629-633.
10. M. Bajaj, J. Winter, and C. Gallert, *Effect of deproteination and deacetylation conditions on viscosity of chitin and chitosan extracted from Crangon shrimp waste,* Biochem. Eng. J. 56 (2011) 51-62.
11. I. Aranaz, M. Mengíbar, R. Harris, I. Paños, B. Miralles, N. Acosta, G. Galed, and Á. Heras, *Functional Characterization of Chitin and Chitosan*, Curr. Chem. Biol., 3 (2009) 203-230.
12. Y. Xu, C. Gallert, and J. Winter, *Chitin purification from shrimp wastes by microbial deproteination and decalcification*, Appl. Microbiol. Biotechnol., 79 (2008) 687-697.
13. D.K. Youn, H.K. No, and W. Prinyawiwatkul, *Physicochemical and functional properties of chitosans affected by sun drying time during decoloration,* LWT - Food Sci. Technol., 42 (2009) 1553-1556.
14. M. Laka, and S. Chernyavskaya, *Preparation of chitosan powder and investigation of its properties*, Proc. Estonian. Acad. Sci. Chem., 55 (2006) 78-84.
15. J. Kumirska, M. Czerwicka, Z. Kaczyński, A. Bychowska, K. Brzozowski, J. Thöming, and P. Stepnowski, *Application of Spectroscopic Methods for Structural Analysis of Chitin and Chitosan*, Mar. Drugs., 8 (2010) 1567-1636.
16. G. Dupuis, and J.-G. LeHoux, *Recovery of chitosan from aqueous acidic solutions by salting-out. Part 2: Use of salts of organic acids,* Carbohydr. Polym., 68 (2007) 287-294.
17. Q.Z. Wang, X.G. Chen, N. Liu, S.X. Wang, C.S. Liu, X.H. Meng, C.G. Liu, *Protonation constants of chitosan with different molecular weight and degree of deacetylation,* Carbohydr. Polym., 65 (2006) 194-201.

18. M. Rinaudo, G. Pavlov, and J. Desbrières, *Influence of acetic acid concentration on the solubilization of chitosan,* Polymer, 40 (1999) 7029-7032.
19. S. Demarger-Andre, and A. Domard, *Chitosan carboxylic acid salts in solution and in the solid state*, Carbohydr., Polym., 23 (1994) 211-219.
20. M. Wang, L. Xu, X. Ju, J. Peng, M. Zhai, J. Li, and G. Wei, *Enhanced radiation crosslinking of carboxymethylated chitosan in the presence of acids or polyfunctional monomers*, Polym. Degrad. Stabil., 93 (2008) 1807-1813.
21. O.A.C. Monteiro Jr., and C. Airoldi, *Some studies of crosslinking chitosan-glutaraldehyde interaction in a homogeneous system*, Int. J. Biol. Macromol., 26 (1999) 119-128.
22. F. Xi, and J. Wu, *Macroporous chitosan layer coated on non-porous silica gel as a support for metal chelate affinity chromatographic adsorbent,* J. Chromatogr. A, 1057 (2004) 41-47.
23. F. Xi, and J. Wu, *Preparation of macroporous chitosan layer coated on silica gel and its application to affinity chromatography for trypsin inhibitor purification,* React. Funct. Polym., 66 (2006) 682-688.
24. X. Pang, T. Casagrande, and I. Zhitomirsky, *Electrophoretic deposition of hydroxyapatite-$CaSiO_3$-chitosan composite coatings,* J. Colloid Interface Sci., 330 (2009) 323-329.
25. X. Pang, and I. Zhitomirsky, *Electrophoretic deposition of composite hydroxyapatite-chitosan coatings,* Mater. Charact., 58 (2007) 339-348.
26. F. Sun, X. Pang, and I. Zhitomirsky, *Electrophoretic deposition of composite hydroxyapatite-chitosan-heparin coatings.* J. Mater. Process. Technol., 209 (2009) 1597-1606.
27. F.Q. Hu, G.F. Ren, H. Yuan, Y.Z. Du, S. Zeng, *Shell cross-linked stearic acid grafted chitosan oligosaccharide self-aggregated micelles for controlled release of paclitaxel*, Colloids Surface B, 50 (2006) 97-103.
28. Y. Liang, L. Deng, C. Chen, J. Zhang, R. Zhou, X. Li, R. Hu, and A. Dong, *Preparation and properties of thermoreversible hydrogels based on methoxy poly(ethylene glycol)-grafted chitosan nanoparticles for drug delivery systems,* Carbohydr. Polym., 83 (2011) 1828-1833.
29. Y. Yang, X. Liu, W. Yu, H. Zhou, X. Li, and Xi. Ma, *Homogeneous synthesis of GRGDY grafted chitosan on hydroxyl groups by photochemical reaction for improved cell adhesion,* Carbohydr. Polym., 80 (2010) 733-739.
30. M. Bertoldo, S. Nazzi, G. Zampano, and F. Ciardelli, *Synthesis and photochromic response of a new precisely functionalized chitosan with "clicked" spiropyran,* Carbohydr. Polym., 85 (2011) 401-407.
31. M. Gümüşderelioğlu, and S. Aday, *Heparin-functionalized chitosan scaffolds for bone tissue engineering,* Carbohydr. Res., 346 (2011) 606-613.
32. L. Hakim, A. Sabarudin, K. Oshita, M. Oshima, and S. Motomizu, *Synthesis of cross-linked chitosan functionalized with threonine moiety and its application to on-line collection/concentration and determination of Mo, V and Cu*, Talanta, 74 (2008) 977-985.
33. F. Sousa, G.M. Guebitz, and V. Kokol, *Antimicrobial and antioxidant properties of chitosan enzymatically functionalized with flavonoids,* Process Biochem., 44 (2009) 749-756.
34. M.R. Gandhi, G.N. Kousalya, N. Viswanathan, and S. Meenakshi, *Sorption behaviour of copper on chemically modified chitosan beads from aqueous solution*, Carbohydr. Polym., 83 (2011) 1082-1087.
35. P. Miretzky, and A.F. Cirelli, *Hg(II) removal from water by chitosan and chitosan derivatives: A review*, J. Hazard. Mater., 167 (2009) 10-23.
36. A.J. Varma, S.V. Deshpande, and J.F. Kennedy, *Metal complexation by chitosan and its derivatives: a review*, Carbohydr. Polym., 55 (2004) 77-93.

37. N.T. An, D.T. Thien, N.T. Dong, and P.L. Dung, Water-soluble N-carbxyethylchitosan derivatives: *Preparation, characteristics and its application, Carbohydr. Polym*., 75 (2009) 489-497.
38. W.S.W. Ngah, and K.H. Liang, *Adsorption of gold(III) ions onto chitosan and N-carboxymethylchitosan: Equilibrium studied*, Ind. Eng. Chem. Res., 38 (1999) 1411-1414.
39. L.S. Molochnikov, A.V. Pestov, E.V. Zabolotskaya, *Solid-state structure of copper complexes of N-(2-carboxyethyl)chitosan*, J. Appl. Spectrosc., 75 (2008) 648-652.
40. G.Z. Kyzas, M. Kostoglou, and N.K. Lazaridis, *Copper and chromium(VI) removal by chitosan derivatives-Equilibrium and kinetic studies*, Chem. Eng. J., 152 (2009) 440-448.
41. R. Qu, C. Sun, C. Ji, C. Wang, H. Chen, Y. Niu, C. Liang, and Q. Song, *Preparation and metal-binding behavior of chitosan functionalized by ester- and amino-terminated hyperbranched polyamidoamine polymers*, Carbohydr. Res., 343 (2008) 267-273.
42. E. Repo, J.K. Warchol, T.A. Kurniawan, and M.E.T. Sillanpaa, Adsorption of Co(II) and Ni(II) by EDTA- and/or DTPA-modified chitosan: Kinetic and equilibrium modeling, Chem. Eng. J., 161 (2010) 73-82.
43. J.O. Marques Neto, C.R. Bellato, J.L. Milagres, K.D. Pessoa and E.S. de Alvarenga, *Preparation and Evaluation of Chitosan Beads Immobilized with Iron(III) for the Removal of As(III) and As(V) from Water*, J. Braz. Chem. Soc., 24 (2013)121-132.
44. V.K. Mourya, and N.N. Inamdar, *Chitosan-modifications and applications: Opportunities galore*, React. Funct. Polym., 68 (2008) 1013-1051.
45. M. Gumusderelioglu, and S. Aday, *Heparin-functionalized chitosan scaffolds for bone tissue engineering*, Carbohydr. Res., 346 (2011) 606-613.
46. S. Mathews, R. Bhonde, P.K. Gupta, and S. Totey, *A novel tripolymer coating demonstrating the synergistic effect of chitosan, collagen type 1 and hyaluronic acid on osteogenic differentiation of human bone marrow derived mesenchymal stem cells*, Biochem. Biophys. Res. Commun., 414 (2011) 270-276.
47. A.D. Martino, M. Sittinger, and M.V. Risbud, *Chitosan: A versatile biopolymer for orthopaedic tissue-engineering*, Biomaterials, 26 (2005) 5983-5990.
48. M.-T. Yen, J.-H. Yang, and J.-L. Mau, *Physicochemical characterization of chitin and chitosan from crab shells*, Carbohydr. Polym., 75 (2009) 15-21.
49. J. Cho, M.-C. Heuzey, A. Bégin, P.J. Carreau, *Viscoelastic properties of chitosan solutions: Effect of concentration and ionic strength*, J. Food Eng., 74 (2006) 500-515.
50. G. Crini, and P Badot, *Application of chitosan, a natural aminopolysaccharide, for dye remmoval from aqueous solutions by adsorption processes using batch studies : A review of recent literature*, Prog. Polym. Sci., 33 (2008) 399-447.
51. A. Webster, M.D. Halling, and D.M. Grant, *Metal complexation of chitosan and its glutaraldehyde cross-linked derivative*, Carbohydr. Res., 342 (2007) 1189-1201
52. R. Signini, J. Desbrieres, and S.P. Campana Filho, *On the stiffness of chitosan hydrochloride in acid-free aqueous solutions*, Carbohydr. Polym., 43 (2000) 351-357.
53. M.-K. Lee, S.-K. Chun, W.-J. Choi, J.-K. Kim, S.-H. Choi, A. Kim, K. Oungbho, J.-S. Park, W.S. Ahn, and C.-K. Kim, *The use of chitosan as a condensing agent to enhance emulsion-mediated gene transfer*, Biomaterials, 26 (2005) 2147-2156.
54. V. Babak, I. Lukina, G. Vikhoreva, J. Desbrières, and M. Rinaudo, Interfacial properties of dynamic association between chitin derivatives and surfactants, Colloidals Surface A, 147 (1999) 139-148.

55. A. Anitha, S. Maya, N. Deepa, K.P. Chennazhi, S.V. Nair, H. Tamura, R. Jayakumar, *Efficient water soluble O-carboxymethyl chitosan nanocarrier for the delivery of curcumin to cancer cells*, Carbohydr, Polym., 83 (2011) 452-461.

56. M.S.B.A. Rasad, A.S. Halim, K. Hashim, A.H.A. Rashid, N. Yusof, S. Shamsuddin, *In vitro evaluation of novel chitosan derivatives sheet and paste cytocompatibility on human dermal fibroblasts*, Carbohydr, Polym., 79 (2010) 1094-1100.

57. A. Zhu, S. Dai, L. Li, and F. Zhao, Salt effect on aggregation of O-carboxymethylchitosan in aqueous solution, Colloids Surface B, 47 (2006) 20-28.

58. X. Liu, Q. Wang, X. Zhuang, B. Wu, F. Yang, and A. Zeng, *Study on antibacterial activity of O-carboxymethyl chitosan sodium salt and spinnability of O-carboxymethyl chitosan sodium salt/cellulose polyblends in N-methylmorpholine-N-oxide system*, Carbohydr. Polym., 89 (2012) 104-110.

59. D. Zhao, J. Huang, S. Hu, J. Mao, and L. Mei, *Biochemical activities of N,O-carboxymethyl chitosan from squid cartilage*, Carbohydr. Polym., 85 (2011) 832-837.

60. R.A.A. Muzzarelli, *Carboxymethylated chitins and chitosans*, Carbohydr. Polym. 8 (1988) 1-21.

61. P. Liang, Y. Zhao, Q. Shen, D. Wang, and D. Xu, The effect of carboxymethyl chitosan on the precipitation of calcium carbonate, J. Cryst. Growth, 261 (2004) 574-576.

62. Q.-H. Shi, Y. Tian, X.-Y. Dong, S. Bai, and Y. Sun, *Chitosan-coated silica beads as immobilized metal affinity supported for protein adsorption*, Biochem. Eng. J., 16 (2003) 317-322.

63. Z. Lei, and S. Bi, *The silica-coated chitosan particle from a layer-by-layer approach for pectinase immobilization*, Enzyme Microb. Tech., 40 (2007) 1442-1447.

64. A.R. Cestari, E.F.S. Vieira, A.A. Pinto, and E.C.N. Lopes, *Multistep adsorption of anionic dyes on silica/chitosan hybrid. 1. Comparative kinetic data from liquid-and solid-phase models*, J. Colloid Interface Sci., 292 (2005) 363-372.

65. A. El Kadib and M. Bousmina, *Chitosan bio-based organic-inorganic hybrid aerogel microspheres*, Chem. Eur. J., 18 (2012) 8264-8277.

66. F. Xi, J. Wu, Z. Jia, and X. Lin, *Preparation and characterization of trypsin immobilized on silica gel supported macroporous chitosan bead*, Process Biochem., 40 (2005) 2833-2840.

67. K. Grandfield, and I Zhitomirsky, *Electrophoretic deposition of composite hydroxyapatite-silica-chitosan coating*, Mater. Charact., 59 (2008) 61-67.

68. H. Queen, *Electrospinning chitosan-based nanofibers for biomedical applications*, 2006.

69. S. Sabin and L.H. Block, *Improved infrared spectroscopic method for the analysis of degree of N-deacetylation of chitosan*, Polym. Bull. 39 (1997) 67-71.

70. K.C. Gupta, and F.H. Jabrail, *Effects of degree of deacetylation and cross-linking on physical characteristics, swelling and release behavior of chitosan microspheres,* Carbohydr. Polym., 66 (2006) 43-54.

71. F.-C. Wu, R.-L. Tseng, and R.-S. Juang, *A review and experimental verification of using chitosan and its derivatives as adsorbents for selected heavy metals*, J. Environ. Manage., 91 (2010) 798-806.

72. B.A. Schumacher, Methods for the determination of total organic carbon (TOC) in soils and sediments, United States Environmental Protection Agency Environmental Sciences Division National Exposure Research Laboratory, (2002).

73. T.V. Kulyk, B.B. Palyanytsya, T.V. Borodavka, and M.V. Borysenko, *Supramolecular structures of chitosan on the surface of fumed silica*, Nanomaterials and Supramolecular Structures, (2010) 259-268.

74. E.-J. Lee, S.-H. Jun, H.-E. Kim, H.-W. Kim, Y.-H. Koh, and J.-H. Jang, *Silica Xerogel-chitosan nano-hybrids for use as drug eluting bone replacement*, J. Mater. Sci.: Mater. Med., 21 (2010) 207-214.

75. X.-M. Zhu, Z.-S. Cai, C.-S. Yang, and S.-B. Shang, *Synthesis of 2-hydroxypropyl dimethylbenzyl ammonium N,O-carboxymethyl chitosan chloride and its antibacterial activity*, J. Chem. Soc. Pak., 31 (2009) 652-659.

76. L. Wang, Q. Li, and A. Wang, *Adsorption of cationic dye on N,O-carboxymethyl chitosan from aqueous solution: equilibrium, kinetics, and adsorption mechanism*, Polym. Bull., 65 (2010) 961-975.

77. G.S. Silva, P.C. Oliverira, D.S. Giordani, and H.F. de Castro, *Chitosan/siloxane hybrid polymer: synthesis, characterization and performance as a support for immobilizing enzyme*, J. Braz. Soc., 22 (2011) 1407-1417.

78. N. Viswanathan, and S. Meenakshi, *Enhanced fluoride sorption using La(III) incorporated carboxylated chitosan beads*, J. Colloid Interface Sci., 322 (2008) 375-383.

79. C. Bartholome, E. Beyou, E. Bourgeat-Lami, P. Chaumont, N. Zydowicz., *Nitroxide-mediated polymerization of styrene initiated from the surface of fumed silica. Comparison of two synthetic routes*, Polymer, 46 (2005) 8502-8510.

80. S.Sh. Rashidova, D.Sh. Shakarova, O.N. Ruzimuradov, D.T. Satubaldieva, S.V. Zalyalieva, O.A. Shpigun, V.P. Varlamov, and B.D. Kabulov, *Bionanocompositional chitosan-silica sorbent for liquid chromatography*, J. Chromatogr. B, 800 (2004) 49-53.

81. J.H. Chen, Q.L. Liu, X.H. Zhang, and Q.G. Zhang, *Pervaporation and characterization of chitosan membranes cross-linked by 3-amiopropyltrimethoxysilane*, J. Membrane Sci., 29 (2007) 125-132.

82. T. Aubry, B. Largenton, and M. Moan, Rheological study of fumed silica suspensions in chitosan solution, Langmuir, 15 (1999) 2380-2383.

83. E. Repo, J.K. Warchoł, A. Bhatnagar, and M. Sillanpää, *Heavy metals adsorption by novel EDTA-modified chitosan-silica hybrid materials*, J. Colloid Interface Sci., 358 (2011) 261-267.

84. L.G. Rebits, D.J. Bennett, P.A. Bhagwat, A. Morin, and R.E. Sievers, *Method for quantifying the sample collected by an Andersen Cascade Impactor using total organic carbon analysis*, J. Aerosol Sci., 38 (2007) 1197-1206.

85. M. Rinaudo, G. Pavlov, and J. Desbrières, *Influence of acetic acid concentration on the solubilization of chitosan*, Polymer, 40 (1999) 7029-7032.

86. W.L. Yan, and R. Bai, *Adsorption of lead and humic acid on chitosan hydrogel beads.* Water Res., 39 (2005) 688-698.

87. T. Witoon, M. Chareonpanich, and J. Limtrakul, *Effect of acidity on the formation of silica-chitosan hybrid materials and thermal conductive property*, J. Sol-Gel Sci. Techn., 51 (2009) 146-152.

Chapter 4

Chitosan-Silica Hybrid Composites as Adsorbents for Water Treatment

Introduction

This chapter describes the application of CS-coated silica hybrid materials as well as amine-modified silica material presented in the preceding chapter for water treatment via adsorption of divalent cations from aqueous solution in a batch experiment. These modified silica-based materials were utilized as adsorbents for removal of Cu(II) and Ni(II) from water. The tests to determine the adsorption efficiency for the binding these metal cations were carried out at room temperature. We used various adsorption isotherms to study the interaction between adsorbates and adsorbents, kinetic isotherms such as pseudo-first-order, pseudo-second-order, intraparticle diffusion, and the Elovich equation (which assumes that the active sites of the sorbent are heterogeneous and exhibit different activation energies for chemisorption) were also investigated to study the adsorption rate. The impact of other adsorption parameters such as initial solution pH, contact time, and initial solution concentration was also investigated.

Adsorption

Since adsorption is an effective method to remove heavy metals from water, this technique has stimulated the interest of many research groups [1,2]. The term "Adsorption" was coined in 1881 by German physicist Heinrich Kayser and can be defined as the adhesion of atoms, ions, or molecules from a gas, liquid, or dissolved solid to a surface [3a]. Another definition describes this term as preferential concentration of one component of a system at an interface where the local (*i.e.*, interface) concentration of one or more components of one or both phases is different from those on the bulk phase [3b]. Adsorption involves two components including adsorbate and adsorbent. The adsorbate is the substance (*i.e.*, metal ion) being adsorbed on the surface of the adsorbent. The adsorbent is a substance (*i.e.* CS-coated silica), on which the adsorption takes place.

For the consideration of the adsorption process, there are two aspects that must be addressed:

(1) Kinetics: the rate at which the adsorption process occurs.

(2) Adsorption isotherms: these are important parameters for describing how the adsorbate interacts with the adsorbent.

On the basis of the types of attraction forces existing between the adsorbate and the adsorbent, adsorption can be classified into two categories: physical adsorption (physisorption), and chemical adsorption (chemisorption).

- The physisorption: the adsorbate molecules are attracted by van der Waals forces with the adsorbent molecules. The physical adsorption can be a monolayer or multilayer adsorption and is an exothermic process characterized by low enthalpy values (around 5-40 kJ/mol).
- In contrast, the chemisorption involves specific interactions between the adsorbent surface and the adsorbate; *i.e.* a chemical reaction between the surface and the adsorbate takes place. Chemisorption is an exothermic process implying high enthalpy values (energy involved can reach several hundreds of kJ/mol) due to chemical adsorption. Characteristic is a much higher heat of adsorption with specific interaction (chemical bonds). Chemisorption by nature is limited to a monolayer process. The chemisorption process necessitates some activation energy, so chemisorption may be much slower than physisorption [3b].

The adsorption process on a porous material takes place in four definable steps shown in Fig. 79. It could be more or less definable in steps, which depends on the characteristic of the adsorbent components such as surface area, porosity, size, etc [4].

(I) *Bulk solution transport*: the movement of the material (metal ions) from the bulk liquid to the boundary layer of a fixed film of liquid surrounding the adsorbent,

(II) *Film diffusion transport*: transport, by diffusion, of the metal ions through the stagnant liquid film,

(III) *Pore transport*: the transport of the metal ions to be adsorbed through the pores by a combination of molecular diffusion through the pore and/or by diffusion along the surface of the adsorbent, and

(IV) *Adsorption*: the attachment of metal ions to adsorbent at an available site.

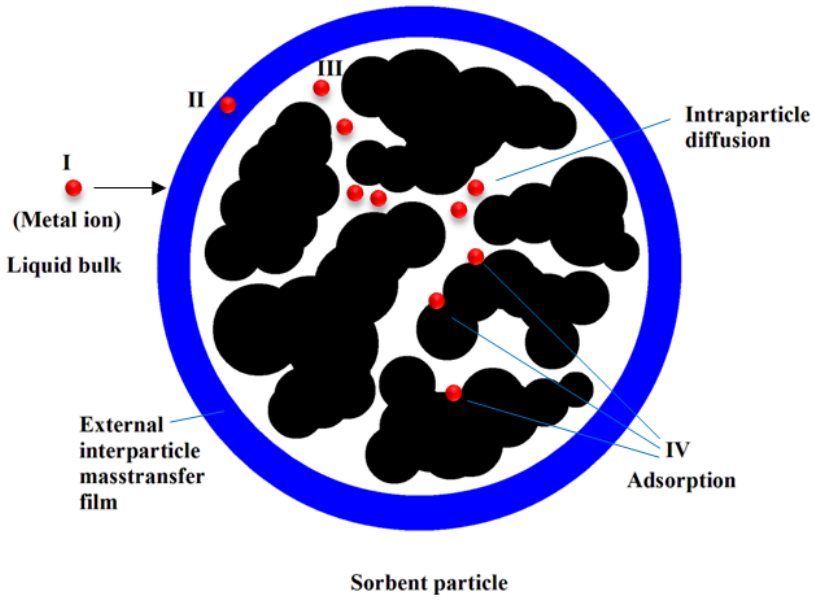

Fig. 79 Schematic illustration of adsorption steps

Adsorption Isotherms in Solid-Liquid Systems

The adsorption from solution at a solid-liquid interface usually involves the measurement of the change of the solute concentration in solution. Based on the form of the isotherm at low concentration, there are four types of isotherm shapes (**L**, **S**, **H**, and **C**-type) as shown in Fig. 80 [5].

- The **L**-type (L refers to Langmuir) isotherm is a common type isotherm. It is identified by its initial region concave to the concentration axis. As the adsorbate concentration increases, the isotherm may reach a plateau (Fig. 80**a**).
- The **S**-type (S refers to Sigmoid) exhibits a low adsorption affinity at low adsorbate concentrations and enhanced adsorption after inflection (Fig. 80**b**).
- The **H**-type (H refers to High affinity) isotherm has a very high initial slope indicating strong adsorption at low adsorbate concentrations. The adsorption at higher concentrations leads to similar changes to those found in both L and S-types. (Fig. 80**c**).
- The last one, **C**-type (C refers to Constant partition) isotherm refers to a system in that the initial concentration ratio between adsorbate and adsorbent is the same. (Fig. 81**d**). This isotherm type provides information about the adsorption mechanism.

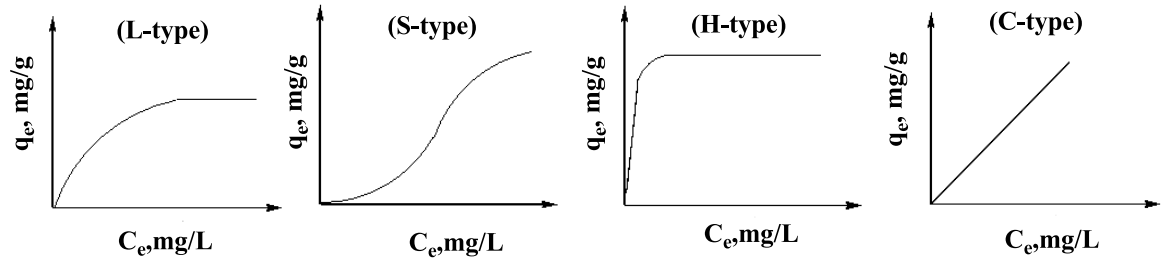

Fig. 80 Shapes of adsorption isotherms in solid-liquid systems

Result and Discussions

This chapter on the adsorption of metal cations is separated into two parts. The first part **A** presents the adsorption of Cu(II) ions by the five novel bio-hybrid silica materials. Some results of the adsorption of Cu(II) onto two types of CS-coated silica materials have been reported in the Journal of Dispersion Science and Technology *"Preparation of Silica-Supported Biosorbents for Copper(II) Removal"* [6]. Complementary, adsorption of Cu(II) at higher concentration (500 mg/L) on the CS-coated silica materials as well as on amine-grafted silica material is presented in this chapter. Moreover, the adsorption of Cu(II) onto CS-coated amine and/or carboxyl grafted silica materials and carboxymethyl CS-coated silica material was also realized. Additional data such as adsorption thermodynamics, adsorption isotherms (*i.e.* Temkin isotherm), adsorption kinetics (*i.e.* intraparticle diffusion, Elovich equation) are presented, furthermore the findings of IR and EDS studies are discussed.

The second part **B** describes the adsorption of Ni(II) ions onto the CS-coated silica (**SiO_2+CS LMW)**, CS-coated carboxyl grafted silica (**$SiO_2(CO_2H)$+CS LMW)** and includes a comparision with carboxymethyl CS-coated silica (**SiO_2+CS(CO_2H)**). The adsorption isotherms have been published in Colloids and Surfaces B: Biointerfaces, *"Adsorption of Ni(II) ions on colloidal hybrid organic-inorganic silica composites"* [7]. In addition, the adsorption kinetics such as pseudo-first-order, pseudo-second-order, and intraparticle diffusion and adsorption parameters at high concentration are discussed in this chapter.

Part A Adsorption of Copper(II) ions on the Composites

In this first part, various silica materials, namely the amino-functionalized silica (**$SiO_2(NH_2)$**), the CS-coated activated silica (**SiO_2+CS LMW**, **SiO_2+CS Marine**, and **SiO_2+CS Yuhuan**), the CS-coated amine-grafted silica (**$SiO_2(NH_2)$+CS LMW**), CS-coated carboxyl grafted silica (**$SiO_2(CO_2H)$+CS LMW**), and the carboxymethyl CS-coated silica (**SiO_2+CS(CO_2H)**) were tested at room temperature as adsorbent for the capture of Cu(II) ions from aqueous solution. The equilibrium isotherms, adsorption kinetics, and adsorption thermodynamics were investigated. The Cu(II)-loaded adsorbents were characterized using FT-IR spectroscopy and Energy Dispersive Spectroscopy (EDS), respectively.

Note: In this present work, the first adsorbent tested as adsorbent for the adsorption of Cu(II) ion was the hybrid silica material **"SiO_2+CS LMW"** (the silica core was coated by a CS shell. To probe whether the adsorption capacity could be further improved, various other types of materials were also investigated. The adsorbents used in this study can be classified into four groups as shown in Table 4.1.

Table 4.1 Classification of the modified silica materials

Group	Material		
(I)	**$SiO_2(NH_2)$**	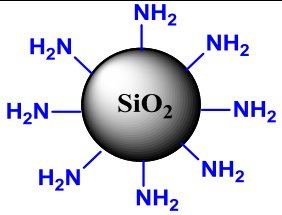 Amine content per gram of silica 0.47 mmol/g	The first group (I): the silica surface was chemically modified by grafting with amine- and/or carboxyl group.
	$SiO_2(CO_2H)$	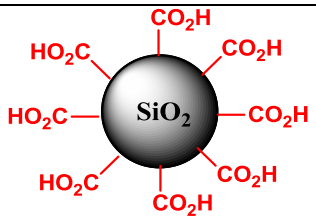 Carbon content on $SiO_2(CO_2H)$ = 0.085 mmol/g	

Table 4.1 Classification of the modified silica materials

Group	Material		
(II)	**SiO_2+CS LMW**, **SiO_2+CS Yuhuan**, and **SiO_2+CS Marine**	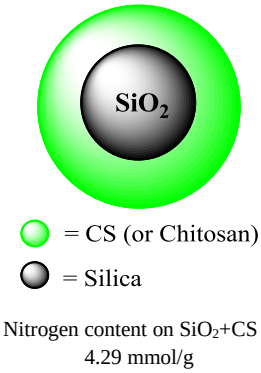 Nitrogen content on SiO_2+CS = 4.29 mmol/g	For the second group (II): the silica surface was coated by different types of CS (CS LMW or CS Yuhuan, and/or CS Marine).
(III)	**$SiO_2(NH_2)$+CS LMW**		Group (III): the silica surface was chemically modified by grafting with amine groups and/or carboxyl groups on its surface. Then it was coated by CS LMW.
	$SiO_2(CO_2H)$+CS LMW	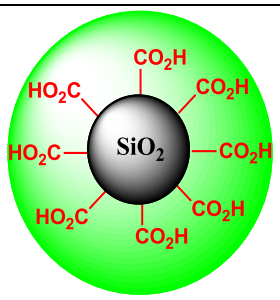	
(IV)	**SiO_2+CS(CO_2H)**	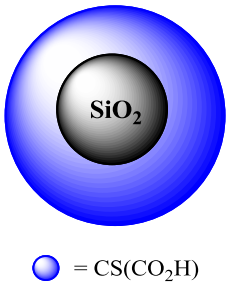	Group (IV): the CS was first chemically modified by functionalization with carboxymethyl groups. Then the carboxymethyl CS was coated on the silica surface.

A1 Effect of Initial Solution pH

The mass of an adsorbent is one of the key parameters influencing the adsorption process. The adsorption capacity for Cu(II) of a polymer-based adsorbent raises when increasing the polymer concentration, since the number of reactive sites responsible for the adsorption process is increased [8]. The amount of copper adsorbed onto the adsorbents (mg/g) was calculated based on the difference of the Cu(II) concentration in aqueous solutions

before and after adsorption, the volume of aqueous solution, and the weight of the modified silica materials according to equation 1

$$\textbf{Adsorption capacity} = \frac{(C_o - C_e)V}{M} \qquad (1)$$

where C_o is the initial metal concentration, mg/L, C_e is the final metal concentration, mg/L, M is the weight (g) of the modified silica material, and V is the volume (L) of the metal solutions.

In this present work, the adsorbent dose was constant at 0.4% (w/w) for all adsorption studies. As previously explained in Chapter 3, the affinity of CS to capture metal ions depends on the pH of the solution. Therefore, the effect of solution pH was investigated. The adsorption at an initial concentration of 500 mg/L Cu(II) was studied on two selected materials, namely **SiO_2+CS LMW** and **$SiO_2(NH_2)$**. Considering that at lower pH ($\leq$ 2) the **SiO_2+CS LMW** is dissolved, this low pH range was not investigated. The adsorption at pH > 6 was not conducted because of the precipitation of $Cu(OH)_2$ from the solution. Therefore, the experiments were carried out in a pH range between 3 and 6.

Fig. 81 shows the effect of pH for the adsorption of Cu(II) on both **$SiO_2(NH_2)$** and **SiO_2+CS LMW**. The pH does not significantly affect the adsorption of Cu(II) on **SiO_2+CS LMW,** while it shows a strong influence for the adsorption of Cu(II) on **$SiO_2(NH_2)$**.

CS in an acidic medium becomes a polyelectrolyte because of the protonation of amino groups. The following equilibrium reaction describes the ionization of CS:

$$\textbf{Chitosan-}NH_2 + H_3O^+ \rightleftharpoons \textbf{Chitosan-}NH_3^+ + H_2O \qquad (2)$$

In the absence of a salt, the pK_a value of CS is found to be equal to 6.5. At pH $\leq$ 6.5, the amino groups on CS are protonated, this reduces the number of binding sites available for the adsorption of Cu(II) ions [9, 10]. In addition, at pH lower than 3 the CS can be dissolved. However, at pH > 6 the precipitation of Cu(II) ions with hydroxide ions to form of $Cu(OH)_2$ occurs. By changing the pH of the metal ions solution, the functional group of adsorbents such as amino groups also changed. Consequently, the surface of the **SiO_2+CS LMW** behaves as a positive charge, reducing the uptake of Cu(II) ion. The adsorption of Cu(II) depends therefore on the solution pH and the binding sites available for adsorption. The optimum pH for the adsorption of Cu(II) onto the modified silica materials was found around pH 5. For this reason, the adsorption isotherms and adsorption kinetics for the adsorption of Cu(II) onto the modified silica materials were studied at pH 5.

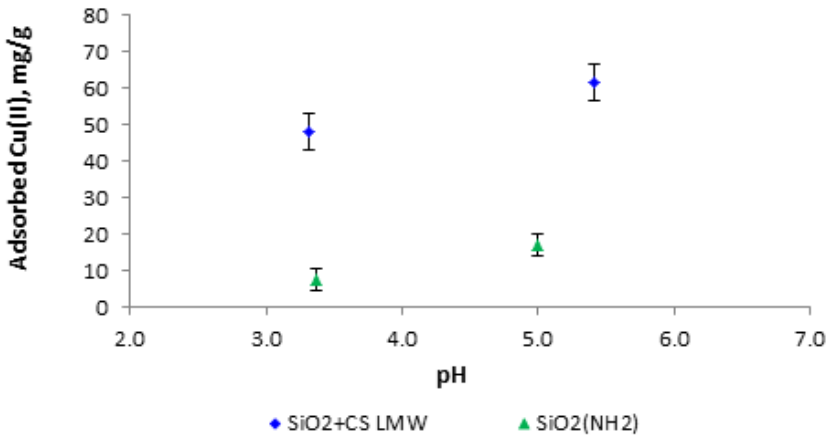

Fig. 81 Effect of the initial pH on the adsorption of Cu(II) ions on amine-grafted silica, and CS LMW-coated silica composites (500 mg/L Cu(II), sorbent = 0.4%)

A2 Effect of the Initial Cu(II) Concentration

The initial concentration of metal ions in solution has a strong effect on the adsorption capacity of pollutants. In general, the adsorption capacity increases when increasing the initial concentration of metals [8].

The effect of the initial concentration of Cu(II) was investigated using various Cu(II) concentrations in the range between 100 and 1.000 mg/L. The adsorption parameters: pH 5, adsorbent dose (0.4%), and the contact time (24 h) were fixed [11]. The adsorbents used in this part were group I (**$SiO_2(NH_2)$**), group II (**SiO_2+CS LMW**), and group IV (**SiO_2+CS(CO_2H)**).

A comparison of the influence of the initial Cu(II) concentration of solution for the adsorption between group I and II is shown in Fig. 82. It was found that an increase of the initial Cu(II) concentration augments the adsorption capacity for all three types of modified silica materials. Fig. 82 shows that **SiO_2+CS LMW** possesses a higher efficiency as a good adsorbent for adsorption of Cu(II) than **$SiO_2(NH_2)$**). This is due to the fact that the former adsorbent (nitrogen content of **SiO_2+CS LMW** = 4.29 mmol/g) owns considerably more -NH_2 binding sites than **$SiO_2(NH_2)$** (0.47 mmol/g). In consequence, the adsorption onto the CS-coated silica materials was found to be higher than the adsorption onto **$SiO_2(NH_2)$**.

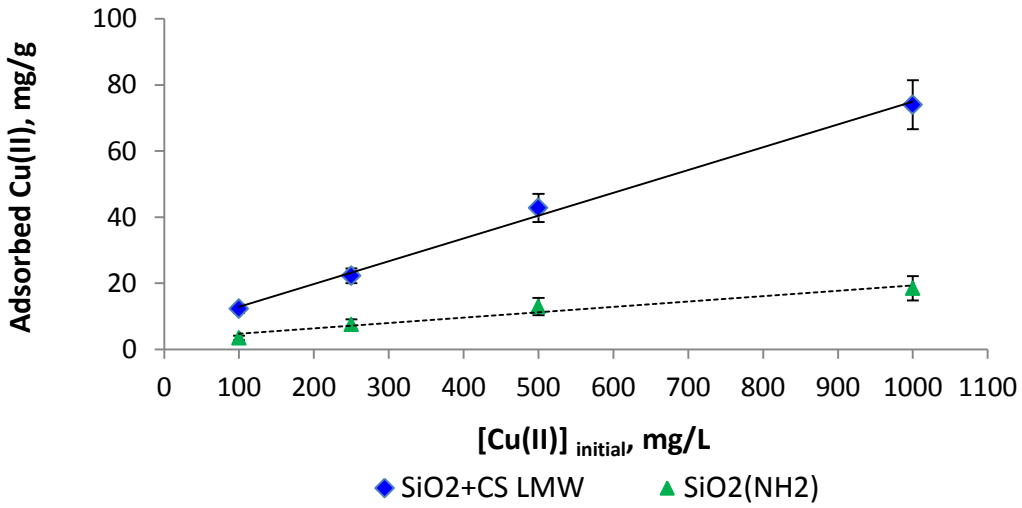

Fig. 82 The effect of initial concentration of Cu(II) ions for adsorption onto **SiO_2+CS LMW** material in comparison with **$SiO_2(NH_2)$**

The comparison between group I (**$SiO_2(NH_2)$**), and group IV (**SiO_2+CS(CO_2H)**), shows in Fig. 83 that an increase of the initial Cu(II) concentration gives rise to the increase of the adsorption capacity for two types of modified silica materials. At the initial Cu(II) concentration of 500 mg/L, the adsorption onto **SiO_2+CS(CO_2H)** was found to be significantly higher than that of **$SiO_2(NH_2)$**. This difference is due to the amount of available active sites (-CO_2H) on CS for the binding of Cu(II) ions. Therefore, the adsorption isotherms were further studied to get a better understanding on the adsorption of Cu(II) onto each selected modified silica materials.

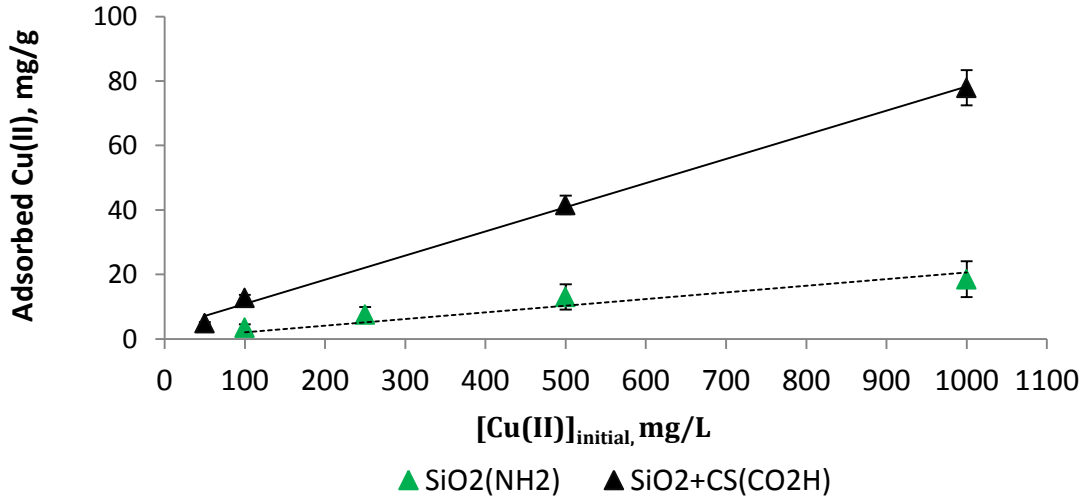

Fig. 83 The effect of initial concentration of Cu(II) ions for adsorption onto **SiO_2+CS(CO_2H)** compared to **$SiO_2(NH_2)$**

A3 Effect of Contact time

The influence of the contact time on the extent of adsorption of Cu(II) was evaluated using three groups of adsorbents: group II (**SiO_2+CS LMW**, and **SiO_2+CS Marine**), group III (**$SiO_2(NH_2)$+CS LMW**, **$SiO_2(CO_2H)$+CS LMW**), and group IV (**SiO_2+CS(CO_2H)**). The contact time was varied in the range 0-1.500 min while the other parameters (initial concentration of Cu(II) solution (500 mg/L), pH 5, and adsorption at room temperature) were fixed.

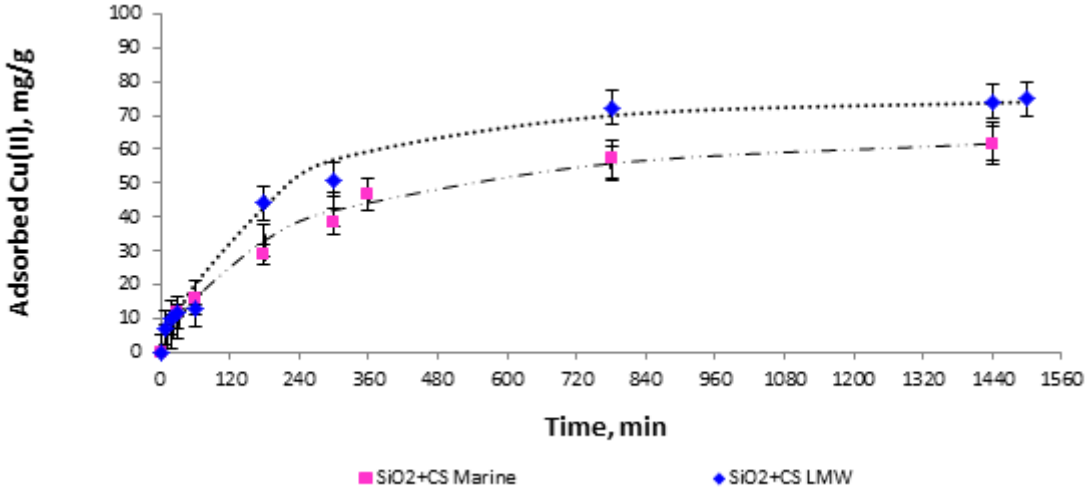

Fig. 84 Effect of contact time for adsorption of 500 mg/L Cu(II) ions onto the hybrid composites (**SiO_2+CS LMW**, and **SiO_2+CS Marine**, at pH 5)

Fig. 84 shows that Cu(II) ions adsorb onto the CS-coated silica materials (**SiO_2+CS LMW**, and **SiO_2+CS Marine)** within the first 10 min. Then the copper was continuously adsorbed onto the adsorbents. The curves show that an extension of the contact time goes in line with an increase of the copper content adsorbed on the composite [10]. The content of Cu(II) adsorbed onto the **SiO_2+CS Marine** and **SiO_2+CS LMW** remains stable after 780 min with an adsorbed amount of 60 mg/g and 74 mg/g for **SiO_2+CS Marine** and **SiO_2+CS LMW**, respectively. These values of adsorbed Cu(II) were determined by Atomic Absorption Spectroscopy (AAS) and calculated using equation 1.

For these types of CS-coated silica materials: **SiO_2+CS LMW**, and **SiO_2+CS Marine**, the adsorption capacity was strongly related to the binding sites, which are only amino groups or both amino and hydroxyl groups cooperating with each other to provide an appropriate special conformation for binding of the Cu(II) ion.

In the case of the silica materials **$SiO_2(NH_2)$+CS LMW** and **$SiO_2(CO_2H)$+CS LMW** as well as for carboxymethyl CS-coated silica **SiO_2+CS(CO_2H)**, the adsorption occured within the first 10 min with an adsorption value of about 80 mg/g. Fig. 85 shows that the content of adsorbed Cu(II) increased only slowly after 10 min. The content of Cu(II) adsorbed onto **$SiO_2(CO_2H)$+CS LMW** remained stable after 960 min with an adsorbed amount of 103 mg/g, while the adsorption of Cu(II) onto **SiO_2+CS(CO_2H)** was quite stable after 1.080 min with an adsorbed amount of 100 mg/g. In contrast, for the **$SiO_2(NH_2)$+CS LMW)** after 1.440 min, no further increase was noticed for the adsorption capacity of Cu(II). The adsorbed amount of Cu(II) onto the **$SiO_2(NH_2)$+CS LMW)** was 79 mg/g. Based on these results, the maximum contact time for the adsorption isotherms study was 1.440 min (24 h).

The content of adsorbed copper on **$SiO_2(NH_2)$+CS LMW** is strongly related to amino binding sites present both on the silica core and the CS shell. The copper concentration adsorbed on **$SiO_2(CO_2H)$+CS LMW** involved both the amino and the carboxyl groups cooperating with each other to provide an appropriate space conformation for binding the Cu(II) ion. In case of **SiO_2+CS(CO_2H)**, the amount of copper adsorbed depends both on carboxyl groups or both carboxyl and hydroxyl groups and as well as residual amino groups. To understand the adsorption system, the adsorption isotherms were further investigated. The FT-IR spectra of the metal loaded adsorbent were also recorded.

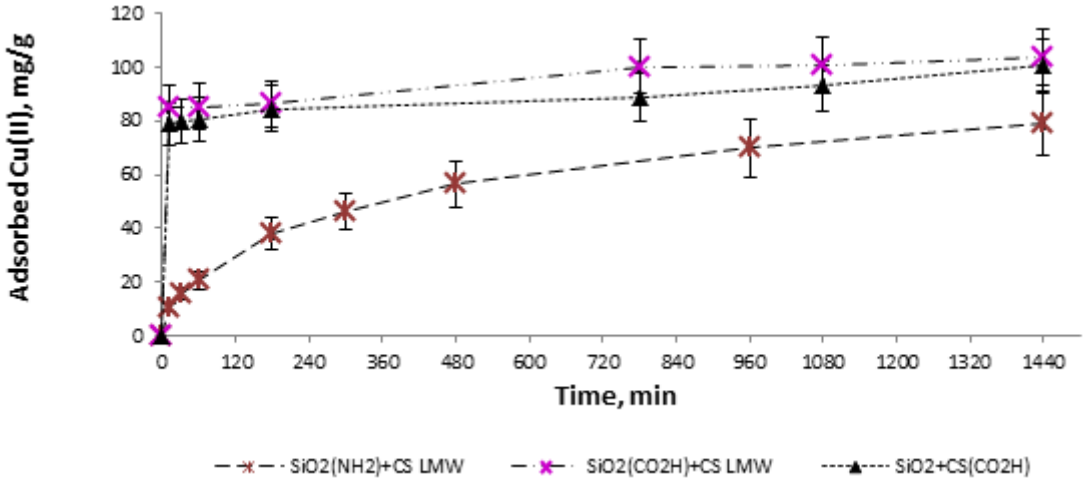

Fig. 85 Effect of contact time for the adsorption of 500 mg/L Cu(II) ions onto the **$SiO_2(NH_2)$+CS LMW**, **$SiO_2(CO_2H)$+CS LMW)**, and **SiO_2+CS(CO_2H)** composites.

A4 Adsorption Isotherms

Isotherm Modeling

Adsorption isotherms represent an important factor for the description of how molecules or ions of adsorbate interact with an adsorbent surface. The isotherms constants are critical in optimizing the usage of adsorbent. Many isotherm models have been reported and used to describe the adsorption of mono solute which could be classified into various classes:

(I) Mono-solute with two parameters (i.e. K_L, n) such as Langmuir, Freundlich, Temkin, and Dubinin-Radushkevich isotherms

(II) Three parameters: Sips (Langmuir-Freundlich), Toth, Redlich-Peterson, Fritz-Schluender, Radke-Prausnitz, etc

(III) Four parameters, for example Fritz-Schluender

The two-parameters Adsorption Isotherms

Equilibrium studies were performed to evaluate various isotherms models to explain the effectiveness of the adsorption process and thereby the adsorption capacity and energy of adsorption. Table 4.2 shows some adsorption isotherms in non-linear form.

Langmuir isotherm

The Langmuir adsorption isotherm (Langmuir, 1918) is widely used for the description the adsorption of a pollutant from an aqueous solution and is based on the following hypotheses:

- the Langmuir isotherm describes an equilibrium adsorption assuming a mono-layer adsorption onto the surface of the sorbent;
- the adsorption takes place at specific homogeneous sites with a finite number of identical sites,
- the adsorption takes place without any interaction between the adsorbed molecules and,
- the energy of the adsorption is constant and there is no transmigration of adsorbate on the surface plane [11, 12].

The Langmuir isotherm can be represented by the following relationship:

$$q_e = \frac{q_m K_L C_e}{1 + K_L C_e} \qquad (3)$$

where q_e and C_e are amount adsorbed (mg/g), and adsorbate concentration in solution (mg/L) at equilibrium. The plot of $1/C_e$ versus $1/q_e$ should give a straight line. The intercept has the value of $1/K_L\, q_m$, where K_L (L/mg) is the Langmuir constant and q_m (mg/g) is the maximum adsorption capacity [13].]. From the highest initial metal concentration C_o (mg/L) and the Langmuir constant K_L (L/mg), can be expressed a dimensionless equilibrium parameter R_L, defined by

$$\mathbf{R_L = \frac{1}{1 + K_L C_o}} \qquad \mathbf{(4)}$$

The value of R_L indicates the type of the isotherm to be either unfavorable ($R_L > 1$), linear ($R_L = 1$), favorable ($0 < R_L < 1$) or irreversible ($R_L = 0$). For example, CS-coated sand (5% chitosan content) has been used to adsorb Cu(II) and the Langmuir isotherms best fits to describe the adsorption of Cu(II) onto the surface [14]. The Langmuir isotherm model also fits well to explain the adsorption of the dyes Acid Red 37 and Acid Blue 25 onto cross-linked Chitosan-ethylene glycol diglycidyl ether beads and showed a better conformity compared to Freundlich and BET isotherms [15].

Freundlich isotherm

The Freundlich constant (Freundlich, 1909) predicts the quantity of metal ion per gram of sorbent at the unit equilibrium concentration [16]. The empirical Freundlich model considers mono-layer adsorption of solute by the adsorbent and assumes that the adsorbent has an energetically heterogeneous surface and different affinity for adsorption and the existence of an interaction between the molecules that adsorbed onto that heterogeneous surface. The Freundlich equation suggests that the adsorption energy exponentially decreases on completion of the adsorptional centres of an adsorbent. The Freundlich adsorption isotherm is given by

$$\mathbf{q_e = K_F C_e^{1/n}} \qquad \mathbf{(5)}$$

where q_e, and C_e are amount adsorbed (mg/g) and the adsorbate concentration at equilibrium in solution (mg/L). Adsorption capacity (K_F) and intensity of adsorption (n) are Freundlich constants, which affect the adsorption process. The constants K_F and n are calculated from the previous equation by plotting log C_e versus log q_e (intercept = log K_F and slope = 1/n). The n value is a measure of the nature and strength of the adsorption process and of the distribution of active sites. If the intensity of adsorption is less than one ($n < 1$), bond energies increase with the surface density. In contrast, if the intensity of adsorption is more than one ($n > 1$),

bond energies decrease with the surface. CS has been used to capture Pb(II) and the adsorption is best explained in this case by the Freundlich isotherm [17]. Freundlich isotherm model provided the best fit for the adsorption of Cu (II) onto chitosan (CS)/sisal fiber (SF)/banana fiber (BF) hybrid composite [18].

Temkin isotherm

The Temkin model (Temkin and Pyzhev, 1940) is used to represent the equilibrium adsorptive behavior between two phases composing the adsorption system considering the effects of some indirect adsorbate/adsorbent interactions on adsorption isotherm. The heat of adsorption of all molecules in the layer would decrease linearly with coverage. The Temkin isotherm is expressed as

$$q_e = \frac{RT}{b_T} \ln (K_T C_e) \qquad (6)$$

where q_e is the amount of metal ions adsorbed per gram of composite (mg/g), C_e is the equilibrium concentration of metal ions in solution (mg/L), $B_T = RT/b_T$, and b_T is a Temkin isotherm constant related to heat of sorption (J/mol), K_T is the equilibrium binding constant (L/mg) corresponding to the maximum binding energy, R is gas constant (8.314 J/mol K), and T is the absolute temperature (K) [14]. The isotherm constant can be obtained from the plot of q_e versus ln C_e. B_T is the adsorption heat linked to the Temkin isotherm constant b_T as equation 7.

$$B_T = \frac{RT}{b_T} \qquad (7)$$

The adsorption of Cr(VI) ions from aqueous solution by ethylenediamine-modified cross-linked magnetic chitosan resin have been explained by the Temkin isotherm [19].

Dubinin-Radushkevich isotherm

Dubinin and Radushkevich (Dubinin, 1960) have reported the characteristic sorption curve which is related to the porous structure of the sorbent [14, 15]. The Dubinin-Radushkevich (D-R) isotherm is postulated within a sorption space close to the sorbent surface to evaluate the sorption free energy. The D-R isotherm, in non-linear form, is generally expressed as follows:

$$q_e = q_m \exp(-\beta\varepsilon^2) \qquad (8.1)$$

where β is the constant related to the adsorption free energy (mol^2/kJ^2), and q_e, q_m, R, and T are explained above, ε is the Polanyi potential which can be calculated by using the following equation:

$$\varepsilon = RT \ln (1+1/C_e) \quad (8.2)$$

E (eq. 9) is the mean free energy of adsorption (kJ/mol) per molecule of metal ion when it is transferred to the surface of the sorbent from infinity in the solution.

$$E = \frac{1}{\sqrt{-2\beta}} \quad (9)$$

E is in the range of 8-16 kJ/mol and refers to an ion-exchange reaction. Dubinin-Radushkevich isotherm has shown good fitting at higher concentration areas for adsorption of Cu(II), Zn(II), and Pb(II) onto Croatian zeolite clinoptilolite [20].

Harkin-Jura isotherm

The Harkin-Jura (Harkin and Jura, 1944) isotherm describes a multilayer adsorption and it can be explained by existence of a heterogeneous pore distribution. The Harkin-Jura can be expressed as shown in equation 10.

$$q_e = \left(\frac{A}{B + \text{Log } C_e}\right)^{1/2} \quad (10)$$

Where A and B are the Harkin-Jura constants, q_e, and C_e have already been mentioned above [21]. The Harkin-Jura isotherm has been used to describe the adsorption of Dyes (Reactive Yellow 2, RY2) onto Cocoa *(Theobroma Cacao)* Shell [22].

Table 4.2 Overlook of some two-parameters adsorption isotherms models

Adsorption isotherm models " Two parameters"				
Isotherms		Plot	Description	Reference
Langmuir	$q_e = \frac{q_m K_L C_e}{1 + K_L C_e}$	$\frac{1}{q_e}$ vs $\frac{1}{C_e}$	This model assumes a mono-layer adsorption onto the surface of the sorbent	[11-15]
Freundlich	$q_e = K_F C_e^{1/n}$	Log qe vs Log Ce	This empirical model considering a mono-layer adsorption of solute by the adsorbent onto heterogeneous surface	[16-18]
Temkin	$q_e = \frac{RT}{b_T} \ln (K_T C_e)$	q_e vs $\ln C_e$	The b_T (a Temkin isotherm constant) related to heat of sorption. The heat of adsorption of all molecules in the layer would decrease linearly with coverage.	[14, 19]
Dubinin-Radushkevich	$\frac{q_e}{q_m} = \exp -\left(\beta\varepsilon^2\right)$	$\ln C_e$ vs $\left(\ln \frac{C_o}{C_e}\right)^2$	This model describes the adsorption on porous structure	[15, 20]
Harkins-Jura	$q_e = \left(\frac{A}{B + \text{Log } C_e}\right)^{1/2}$	$\frac{1}{q_e^2}$ vs Log C_e	This model assumes the presence of multilayer adsorption with the existence of heterogeneous pore distribution	[21,22]

The three-parameters adsorption isotherms

Herein, the adsorption isotherm models represented by three parameters are given in Table 4.3 and some of the adsorption isotherms with three parameters were briefly discussed.

Redlich-Peterson isotherm

The isotherm first proposed by Redlich and Peterson (1959) was modified by Jossens and his co-workers (Jossens, 1978) [13, 23]. It incorporated the features of the Langmuir and Freundlich isotherms into a single equation as follows:

$$q_e = \frac{K_L C_e q_m}{1+K_L(C_e)^n} \qquad (11)$$

where K_L is the Redlich-Peterson isotherm constant (L/mg), and n is the Redlich-Peterson isotherm exponent. The q_e, q_m, and C_e have already been mentioned above. The exponent, n, lies between 0 and 1. There are two limiting behaviours: Langmuir form for n = 1 and Henry's law form for n = 0. Adsorption of copper from wastewater by chestnut shell is well described by the Redlich-Peterson isotherm [24].

Sips isotherm

The Sips (Sips, 1948) model is an empirical model, which is a hybrid of the Langmuir and the Freundlich isotherms.

The Sips model takes the following form for single solute equilibrium data:

$$q_e = \frac{q_m K_S(C_e)^{1/n}}{1+K_S(C_e)^{1/n}} \qquad (12)$$

where K_L is the Sips isotherm constant (L/mg) and n is the Sips model exponent. The q_e, q_m, and C_e have already been mentioned above [23]. At low sorbate concentrations it is effectively reduced to the Freundlich isotherm and thus it does not follow Henry's law. At high sorbate concentrations, it predicts a monolayer adsorption capacity characteristic of the Langmuir isotherm. Chitosan-glutaraldehyde beads have been used to capture Cu(II) and the adsorption was best explained in this case by the Sips isotherm [25].

Toth isotherm

The Toth isotherm (Toth, 1962) is an empirical equation developed to improve Langmuir isotherm fittings (experimental data), and used to describe heterogeneous adsorption systems, which satisfying both low and high-end boundary of the concentration. Its correlation presupposes an asymmetrical quasi-Gaussian energy distribution, with most of its sites having an adsorption energy lower than the peak (maximum) or mean value. The Toth isotherm can be represented by equation 13:

$$q_e = \frac{K_L C_e q_m}{(1+(K_L C_e)^n)^{1/n}} \qquad (13)$$

where K_L is the Toth isotherm constant and n is the Toth isotherm exponent [13, 23]. The q_e, q_m, and C_e have already been mentioned above. For the value of n = 1, this isotherm is

reduced to the Langmuir isotherm. Brazilian kaolinite clay has been used to capture urea and the adsorption could be explained employing the Toth isotherm [26].

Fritz-Schluender isotherm

The Fritz-Schluender isotherm describes the adsorption on heterogeneous surfaces. It can be represented by equation 14 as follows:

$$q_e = \frac{K_L C_e q_m}{1 + q_m (C_e)^n} \qquad (14)$$

where K_L is the Fritz-Schluender isotherm constant and n is the Fritz-Schluender exponent. The q_e, q_m, and C_e have already been mentioned above [27]. *Rhizopus oryzae* (dead fungi) was used as biosorbent to remove *p*-nitrophenol from aqueous phase and it was demonstrated that the Fritz-Schluender isotherm fits to explain the experimental data [28].

Radke-Prausnitz isotherm

The Radke-Prausnitz (Radke and Prausnitz, 1972) isotherm has been derived to make the Langmuir-Freundlich model thermodynamically consistent. It is found to be suitable for weakly adsorbed components. The Radke-Prausnitz isotherm in non-linear form can be represented as seen in equation 15 [23]

$$q_e = \frac{K_L C_e q_m}{1 + K_L (C_e)^n} \qquad (15)$$

where K_L is the Radke-Prausnitz isotherm constant and n is the Radke-Prausnitz isotherm exponent. The q_e, q_m, and C_e have already been mentioned above. According to the literature, the biosorption of Cd(II) onto formaldehyde-treated C*ystoseira indica* (brown marine alga) fits well with the Radke-Prausnitz isotherm [29].

Table 4.3 Some three-parameters adsorption isotherms

Adsorption isotherm models "Three parameters"				
Isotherm		Plot	Description	Reference
Redlich-Peterson	$q_e = \frac{q_m K_L C_e}{1+K_L(C_e)^n}$	$\frac{C_e}{q_e}$ vs $(C_e)^n$	This model involved properties of both Freundlich and Langmuir isotherm. It may be used to represent adsorption equilibrium over a wide concentration range	[23, 24]
Sips (Kobble-Corrigan)	$q_e = \frac{K_L(C_e)^{1/n} q_m}{1+K_L(C_e)^{1/n}}$	$\frac{q_m}{q_e}$ vs $\frac{1}{(C_e)^{1/n}}$	An empirical model, at low ion concentration, this model reduces a Freundlich isotherm and at high ion concentration, it predicts Langmuir isotherm	[23, 25]
Toth	$q_e = \frac{q_m K_L C_e}{(1+(K_L C_e)^n)^{1/n}}$	$\left(\frac{C_e}{q_e}\right)^n$ vs $(C_e)^n$	This model predicts the adsorption on heterogeneous surface. It assumes a quasi-Gaussian energy distribution	[23, 26]
Fritz-Schluender	$q_e = \frac{q_m K_L C_e}{1+q_m(C_e)^n}$	$\frac{C_e}{q_e}$ vs $(C_e)^n$	This model describes the adsorption on heterogeneous surfaces	[27, 28]
Radke-Prausnitz	$\frac{q_e}{q_m} = \frac{K_L C_e}{1+K_L(C_e)^n}$	$\frac{C_e}{q_e}$ vs $(C_e)^n$	This model is suitable for weakly adsorbed materials	[23, 29]

Error Analysis

To evaluate the fit of the different isotherm models to the experimental data, the linear coefficient of determination was examined. The linear coefficient (R^2) represents the percentage of variability in the dependent variable. It has been explained by the regression line. Apart from R^2, other error function (chi-square (X^2) test, it is basically the sum of the squares of the differences between the experimental data and the data which calculate from models, was also calculated to measure the data. The X^2 can be calculated from equation 16 as follows:

$$X^2 = \sum \frac{(q_e - q_{e,m})^2}{q_{e,m}} \qquad (16)$$

where q_e and $q_{e,m}$ are the amount of metal ions adsorbed per gram of composite (mg/g) from experiment and from models, respectively [30a].

Adsorption isotherms: The Case of CS-coated Silica and Amine-Grafted Silica Materials

To investigate the adsorption isotherms at room temperature, a series of Cu(II) solutions at pH 5 in the concentration range between 100 and 1.000 mg/L was prepared, the mass of adsorbent being 0.4%. The contact time was 24 h. The adsorption isotherm of the adsorption of Cu(II) ions by the three types of the CS-coated silica materials (**SiO_2+CS LMW**, **SiO_2+CS Yuhuan**, **SiO_2+CS Marine)** were compared with that of **$SiO_2(NH_2)$**.

The experimental equilibrium data for Cu(II) adsorption onto our materials was calculated from eq. 1. There are various adsorption isotherm models that could be used to interpret our experiment data. In our case, the plot of the solute concentration adsorbed on the solid surface (mg/g) as a function of the solute concentration in the solution at equilibrium (mg/L) could be described by several adsorption models. Langmuir, Freundlich, Temkin, and Sips isotherm models were employed for the experimental data. The representations of the experimental data by four model equations result in a linear curve with the correlation coefficient (R^2) values as tabulated in Table 4.4. Apart from R^2, the chi-square (X^2) was also used to measure the goodness-of-fit. The X^2 values are represented in Table 4.4.

The Temkin isotherm was used for representing the equilibrium adsorptive behavior between two phases composing the adsorption system considering the chemisorption of Cu(II) as adsorbate onto the adsorbent. The R^2 of the Temkin isotherm for the **SiO_2+CS LMW**, **SiO_2+CS Yuhuan**, **SiO_2+CS Marine**, and **$SiO_2(NH_2)$** was in the range between 0.90 and 0.95. The B_T is the Temkin constant, which is related to the heat of adsorption of all the molecules in the layer. It decreases linearly with coverage due to adsorbent-adsorbate interactions. Morever, the adsorption is characterized by a uniform distribution of the binding energies. According to the results of our experiment, the B_T values were 55.37 J/mol, 46.52 J/mol, 31.99 J/mol, and 14.67 J/mol for **SiO_2+CS LMW**, **SiO_2+CS Yuhuan**, **SiO_2+CS Marine**, and **$SiO_2(NH_2)$**, respectively and these results suggest a chemical adsorption.

One of the Freundlich constants is K_F indicating the relative sorption capacity of the system, and the values of K_F were found to be 0.717, 0.914, 1.829, and 0.105 mg/g for **SiO_2+CS LMW**, **SiO_2+CS Yuhuan**, **SiO_2+CS Marine**, and **$SiO_2(NH_2)$**, respectively. The other Freundlich constant n values for the adsorption of Cu(II) indicated the favorability of the adsorption. They were found to be 1.747, 1.545, 1.407, and 1.263 for **SiO_2+CS Marine**, **SiO_2+CS Yuhuan**, **SiO_2+CS LMW**, and **$SiO_2(NH_2)$**, respectively. These n values were >

than 1, indicating that the adsorption of Cu(II) onto the three types of CS-coated silica materials as well as the amine grafted silica material was favorable at high concentration but less at lower concentration [30b].

Table 4.4 Isotherm constants

Isotherm models	Materials	**SiO_2+CS LMW**	**SiO_2+CS Yuhuan**	**SiO_2+CS Marine**	**$SiO_2(NH_2)$**
Temkin	K_T ($x10^{-2}$, L/mg)	0.74	8.13	2.37	1.01
	B_T	55.37	46.52	31.99	14.67
	R^2	0.95	0.92	0.91	0.90
	X^2	6.00	6.80	8.15	6.94
Freundlich	K_F (mg/g)	0.717	0.914	1.829	0.105
	n	1.407	1.545	1.747	1.263
	R^2	0.98	0.97	0.98	0.99
	X^2	2.88	3.12	3.37	1.49
Langmuir	K_L (L/g)	1.68	0.53	0.30	1.79
	q_m (mg/g)	256.4	140.8	109.9	75.8
	R^2	0.99	0.97	0.99	0.99
	X^2	2.73	2.30	2.64	1.36
Sips	K_S	1.45	2.28	0.43	3.58
	n	1.093	0.863	0.929	0.890
	R^2	0.99	0.95	098	0.97
	X^2	3.05	2.35	3.37	1.49

Table 4.5 R_L values based on Langmuir isotherms

$[Cu(II)]_{Initial}$, mg/L	**SiO_2+CS LMW**	**SiO_2+CS Yuhuan**	**SiO_2+CS Marine**	**$SiO_2(NH_2)$**
1000	0.373	0.654	0.769	0.358

In the case of the Langmuir isotherm, the plots yield a straighter line in the range between 0.97-0.99. The maximum adsorption capacity was calculated utilizing Langmuir isotherm given by equation 2. The maximum adsorption capacity for Cu(II) adsorbed on the adsorbents based on Langmuir isotherm model was found to be 256.4, 140.8, and 109.9 mg/g for **SiO_2+CS LMW**, **SiO_2+CS Yuhuan**, and **SiO_2+CS Marine**, respectively. In contrast, the maximum adsorption capacity of the **$SiO_2(NH_2)$** was found to be much lower (75.8 mg/g). In comparison with literature, the adsorption capacity for Cu(II) uptake by amino-functionalized silica gel was found to be 66.7 mg/g [31]. In the case of amine-grafted activated carbon, the adsorption capacity was found to be 54.6 mg/g at pH 5.8 [32]. The maximum adsorption

capacities for Cu(II) adsorbed on the adsorbents were ranked in the following order as shown in Table 4.4:

SiO_2+CS LMW > SiO_2+CS Yuhuan > SiO_2+CS Marine > $SiO_2(NH_2)$

From these findings, it can be deduced that the %DD value of CS influences the adsorption of Cu(II). Fig. 86 shows the comparison of the experimental Cu(II) adsorption curves with theory models of Langmuir, Freundlich, and Sips isotherm plots (plotting between C_e versus q_e).

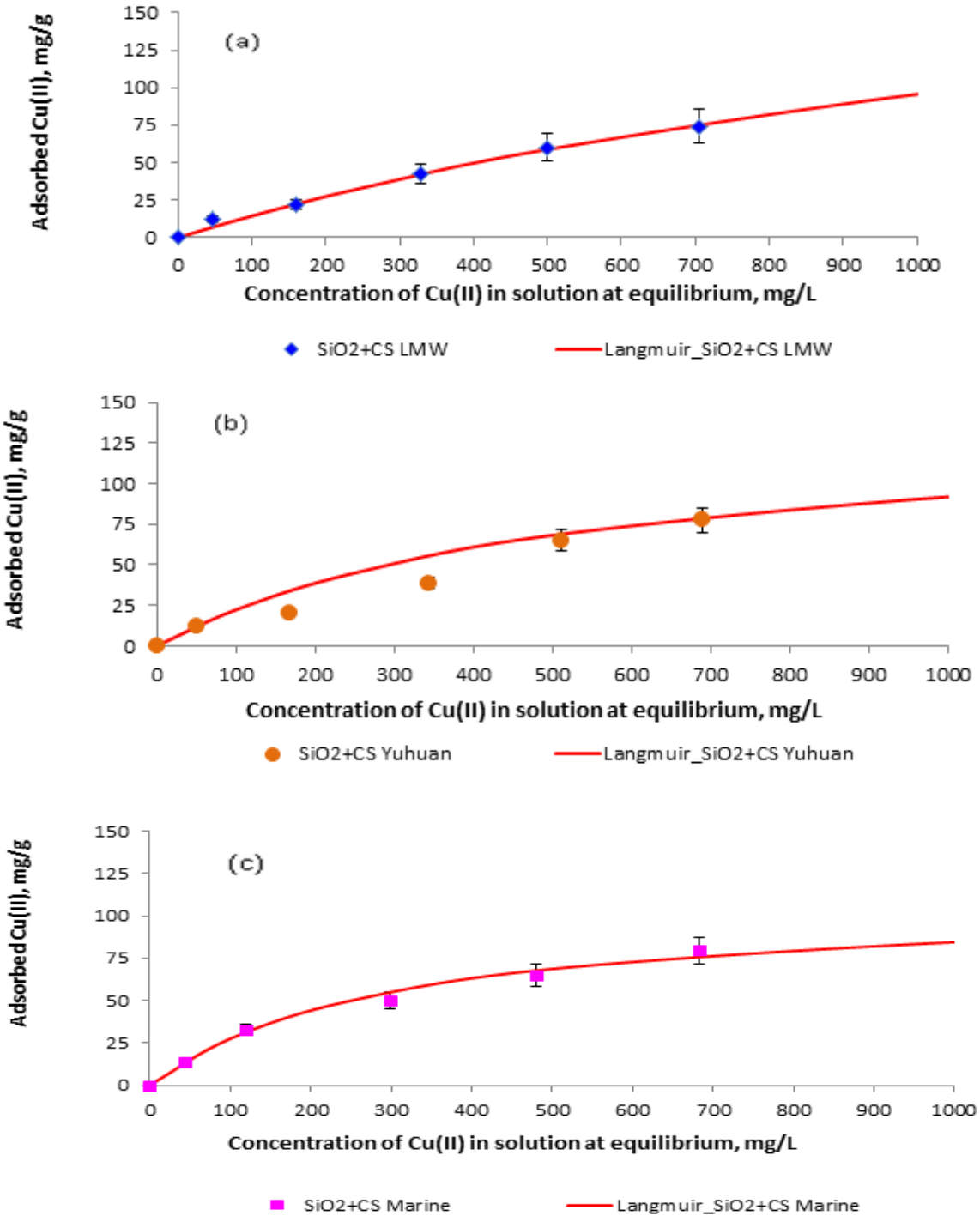

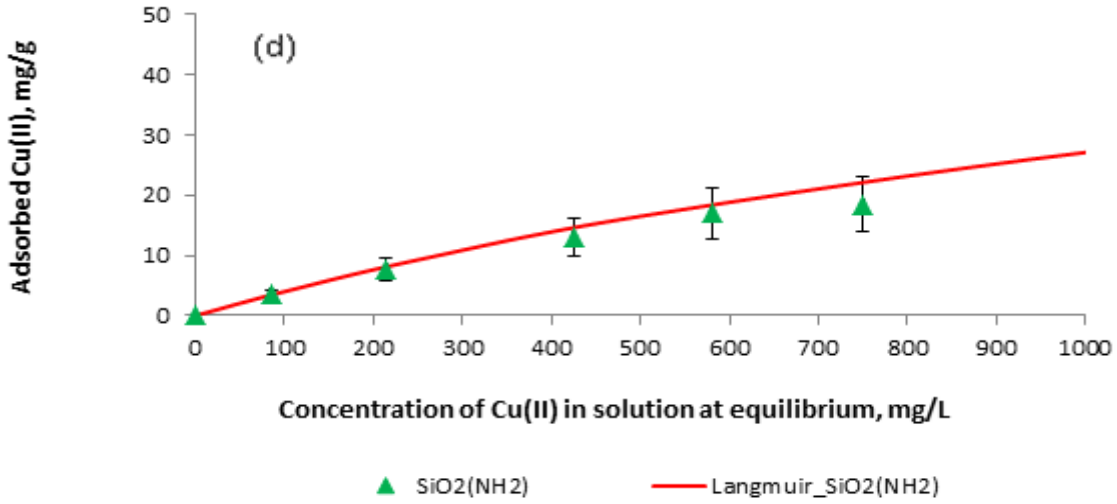

Fig. 86 Comparison of experimental adsorption curves of Cu(II) adsorbed on the modified silica materials with Langmuir isotherm plots:
SiO_2+CS LMW (a), **SiO_2+CS Yuhuan** (b), **SiO_2+CS Marine** (c), and **$SiO_2(NH_2)$** (d)

The Langmuir isotherm can be expressed in terms of a dimensionless constant separation factor or equilibrium parameter (R_L). The values of R_L for initial Cu(II) concentration of 1.000 mg/L are given on Table 4.5. The R_L values are between $0 < R_L < 1$ meaning that the adsorption of Cu(II) onto the adsorbent is favorable. Results show the R_L values as follows: **SiO_2+CS LMW** (R_L = 0.373), **SiO_2+CS Yuhuan** (R_L = 0.654), **SiO_2+CS Marine** (R_L = 0.769), and **$SiO_2(NH_2)$** (R_L = 0.358). Therefore, the adsorption by the three types of CS-coated silica materials (**SiO_2+CS**) as well as for **$SiO_2(NH_2)$** was favorable. The smaller R_L value indicates a highly favorable adsorption. This result was consistent with Freundlich isotherm where the adsorption of Cu(II) was favorable at high concentration.

In the case of Sips isotherm (a combination of the Langmuir and Freundlich isotherms), the Sips isotherm presented the same parameters values of Langmuir isotherm model, since the n Sips exponent value was 1.000 [34a]. At high concentrations, the Sips isotherm reaches a constant value and approaches to Freundlich type at low concentrations. Our results show that the n values are 1.093, 0.863, 0.929 and 0.890 for **SiO_2+CS LMW**, **SiO_2+CS Yuhuan, SiO_2+CS Marine** and **$SiO_2(NH_2)$**, respectively. The n values of the four types of our adsorbents close to the unity predict a homogeneous adsorption.

In this study, the R^2 values of the four models fit in the order as follows: Langmuir > Freundlich > Sips > Temkin for **SiO_2+CS LMW**, **SiO_2+CS Yuhuan** and **SiO_2+CS Marine** as well as for **$SiO_2(NH_2)$**. This result was similar to the result for adsorption of Cu(II) onto the electrospun CS nanofibers where the adsorption was well described by Langmuir isotherm

model [33]. Similarly, the adsorption of Cu(II) onto a cross-linked chitosan-γ-acrylonitrile copolymer was well described by Langmuir isotherm model [34b].

When comparing the values of the error functions, it was found that Langmuir model best fits the Cu(II) adsorption onto three types of CS-coated silica materials as well as amine grafted silica material. The models show high R^2 and low X^2 values. Fig. 86a-d confirms that the adsorption of Cu(II) onto CS-coated silica materials as well as amine grafted silica material matches well with Langmuir isotherm.

Adsorption isotherms: The case of CS-coated Amine and/or Carboxyl Grafted Silica Materials and Carboxymethyl CS-coated Silica

The adsorption experiments of Cu(II) using the chemically modified silica materials (**$SiO_2(CO_2H)$+CS LMW** and **$SiO_2(NH_2)$+CS LMW)** as well as the carboxymethyl CS-coated silica **SiO_2+CS(CO_2H)** were also investigated at room temperature. To determine the equilibrium isotherm, a series of Cu(II) solutions at pH 5 in the range between 50 and 1.000 mg/L was prepared. The calculated constants of the four isotherm equations (Eq. 3, 5, 6, and 12) along with R^2 and RMSE values are presented in Table 4.6.

The Temkin isotherm was used for representing the equilibrium adsorptive behavior between two phases composing the adsorption system considering the chemisorptions of the adsorbate (in our case Cu(II)) onto the adsorbent). The R^2 of the Temkin isotherm for the adsorption of Cu(II) onto the **$SiO_2(NH_2)$+CS LMW**, and **$SiO_2(CO_2H)$+CS LMW** was found between 0.93-0.98 (see Table 4.6). The B_T values were 36.27, and 41.93 for the **$SiO_2(NH_2)$+CS LMW**, and **$SiO_2(CO_2H)$+CS LMW**, respectively. These parameters of heat of adsorption indicate again chemisorption.

The Freundlich parameter "n" indicates the favourableness of the adsorption. The two adsorbents **$SiO_2(NH_2)$+CS LMW** and **$SiO_2(CO_2H)$+CS LMW** showed n values > than 1 as shown in Table 4.6, indicating that the adsorption intensity is favorable at high concentration.

Fig 87(**a-b**) shows a comparison of the experimental data of the Cu(II) adsorption curve on the hybrid materials with theory models of Langmuir isotherm plots (plotting between C_e versus q_e). When comparing the experimental data with theoretical data, it was found that the adsorption of Cu(II) onto **$SiO_2(NH_2)$+CS LMW** and **$SiO_2(CO_2H)$+CS LMW** is close to the prediction of the adsorption by the Langmuir isotherm (Fig 4.8a-b). Based on the Langmuir isotherm, the maximum adsorption capacities for adsorbed Cu(II) was found to

be 270.3 mg/g, and 232.6 mg/g for **$SiO_2(NH_2)$+CS LMW** and **$SiO_2(CO_2H)$+CS LMW**, respectively (see Table 4.6). The maximum adsorption capacities for copper adsorbed can be ranked in the following order: **$SiO_2(NH_2)$+CS LMW > $SiO_2(CO_2H)$+CS LMW**.
The group II adsorbents are better adsorbents than the group I adsorbents. It is assumed that Cu(II) was adsorbed onto the CS-coated modified silica materials by monolayer adsorption.

The Langmuir isotherm can be expressed in terms of a dimensionless constant separation factor or equilibrium parameter (R_L). The values of R_L for initial Cu(II) concentration (1.000 mg/L) were shown in Table 4.7. The R_L values of the **$SiO_2(NH_2)$+CS LMW** was 0.441. For **$SiO_2(CO_2H)$+CS LMW**, the value of R_L was 0.613. This indicated that adsorption of Cu(II) was favorable at high initial concentration of Cu(II).

In the case of the Sips isotherm, the n values are 1.134, 0.873 and 1.156 for **$SiO_2(NH_2)$+CS LMW**, **$SiO_2(CO_2H)$+CS LMW** and **SiO_2+CS(CO_2H)**, respectively. The n values as shown above are close to one. This could suggest a homogeneous adsorption.

According to R^2 and X^2 values (Table 4.6), the adsorption of Cu(II) onto **$SiO_2(NH_2)$+CS LMW** and **$SiO_2(CO_2H)$+CS LMW** matches well with Langmuir isotherms as can be seen in Fig. 87a-b.

Table 4.6 Isotherm constants

Isotherm models	Materials	**$SiO_2(NH_2)$+CS LMW**	**$SiO_2(CO_2H)$+CS LMW**	**SiO_2+CS(CO_2H)**
Temkin	K_T ($x10^{-2}$, L/mg)	19.4	2.84	2.68
	B_T	36.27	41.93	30.51
	R^2	0.93	0.98	0.90
	X^2	6.29	13.69	11.01
Freundlich	K_F (mg/g)	0.884	1.548	0.521
	n	1.469	1.544	1.341
	R^2	0.95	0.88	0.96
	X^2	5.99	6.80	7.92
Langmuir	K_L (L/g)	1.27	0.63	2.08
	q_m (mg/g)	270.3	232.6	333.3
	R^2	0.99	0.98	0.99
	X^2	5.62	5.83	1.85
Sips	K_S	0.71	2.88	0.99
	n	1.134	0.873	1.156
	R^2	0.98	0.99	0.98
	X^2	9.99	25.83	3.03

Table 4.7 R_L values based on Langmuir isotherms

$[Cu(II)]_{Initial}$, mg/L	**$SiO_2(NH_2)$+CS LMW**	**$SiO_2(CO_2H)$+CS LMW**	**SiO_2+CS(CO_2H)**
1000	0.441	0.613	0.325

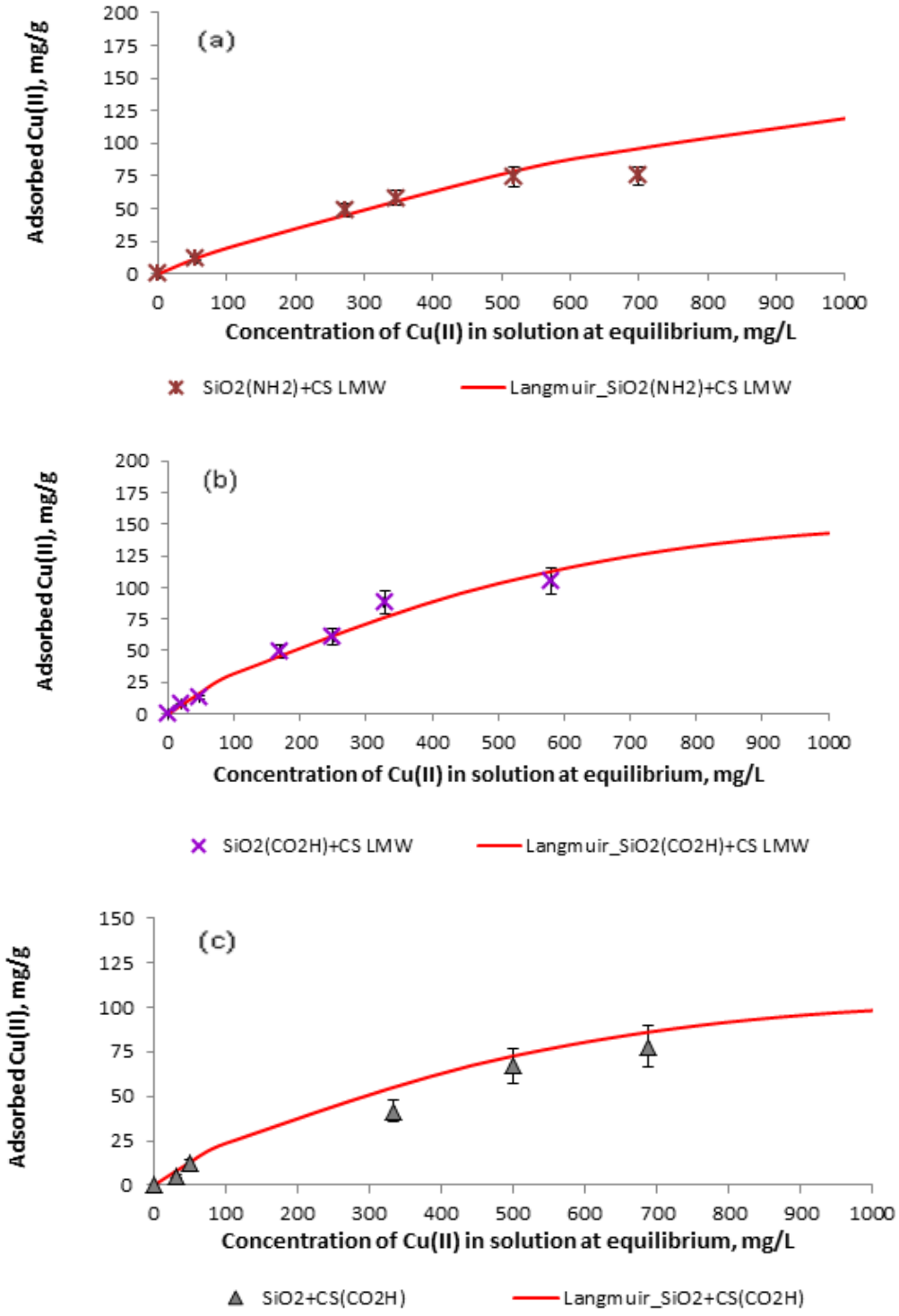

Fig. 87 Comparison of experimental data of adsorption curve of Cu(II) adsorbed on the hybrid materials with Langmuir isotherm plots:

$SiO_2(NH_2)$+CS LMW (a), **$SiO_2(CO_2H)$+CS LMW** (b), and **SiO_2+CS(CO_2H)** (c)

In the case of **SiO_2+CS(CO_2H)**, according the R^2 values, the adsorption of Cu(II) was close to prediction in the following decreasing order:

Langmuir > Sips > Freundlich > Temkin isotherms (Table 4.6).

For the Temkin isotherm, the R^2 was found to be 0.90. The B_T was 30.51 for **SiO_2+CS(CO_2H)** in accordance with a chemisorption. However, the model was not suitable to describe the data compared to the other three models, since R^2 is low and RMSE quite high (see table 4.6).

In case of the Freundlich isotherm, according to the R^2 of 0.96, the value of K_F was calculated and found to be 0.521 mg/g for **SiO_2+CS(CO_2H)**. The other Freundlich constant (n) value for the adsorption of Cu(II) indicated the favorableness for adsorption. It was found to be 1.341 for **SiO_2+CS(CO_2H)**. The n values suggest a favorableness for the adsorption of Cu(II) onto the carboxymethyl CS-coated silica materials at high adsorbate concentration.

According to R^2 and X^2, the adsorption of Cu(II) onto **SiO_2+CS(CO_2H)** matched well with Langmuir isotherms (see Table 4.4). The maximum adsorption capacities for Cu(II) adsorbed on the adsorbents was found to be 333.3 mg/g. This let assume that Cu(II) was adsorbed onto the modified CS-coated silica material (**SiO_2+CS(CO_2H)**) by monolayer adsorption. From the literature, the adsorption of Cu(II) was found to be 318 mg/g for carboxyl-grafted CS derivative at pH 6 [35]. The R_L values of the **SiO_2+CS(CO_2H)** was in the range between 0.325-0.906. This indicates that the adsorption of Cu(II) is favorable at high initial concentration of Cu(II) solution, similar to CS-coated grafted silica materials **(SiO_2+CS)** and non-modified CS-coated grafted silica materials (**SiO_2(NH_2)+CS LMW** and **SiO_2(CO_2H)+CS LMW**). The q_m value of **SiO_2+CS(CO_2H)** was higher than that of **SiO_2+CS LMW**. This could be due to both the functional groups attached on modified CS (-CO_2H) and residual -NH_2 acting as active sites to capture Cu(II) ions.

In the case of Sips isotherm, the n values of all types of our materials are close to the unity as shown in Tables 4.4 and 4.6. Therefore, homogeneous adsorption occurred for the adsorption of Cu(II) onto seven types of materials (**SiO_2+CS LMW**, **SiO_2+CS Yuhuan**, **SiO_2+CS Marine**, **SiO_2(NH_2)**, **SiO_2(NH_2)+CS LMW**, **SiO_2(CO_2H)+CS LMW** and **SiO_2+CS(CO_2H)**).

The results reveal that the adsorption equilibrium data best fit with the Langmuir isotherm. Therefore, the maximum adsorption capacity of Cu(II) onto our novel materials, obtained from the adsorption isotherm study (based on Langmuir isotherm) is represented in Fig 88a. For comparision, the maximum adsorption capacities of three types of CS-coated

silica materials with other adsorbents described in the literatures are shown in Fig. 88b. The other two-parameter isotherm models such as Dubinin-Radushkevich, Harkins-Jura, and the other three-parameters isotherm models (Redlich-Peterson, Toth, Fritz-Schluender, Radke-Prausnitz) have not been used to interpret our data.

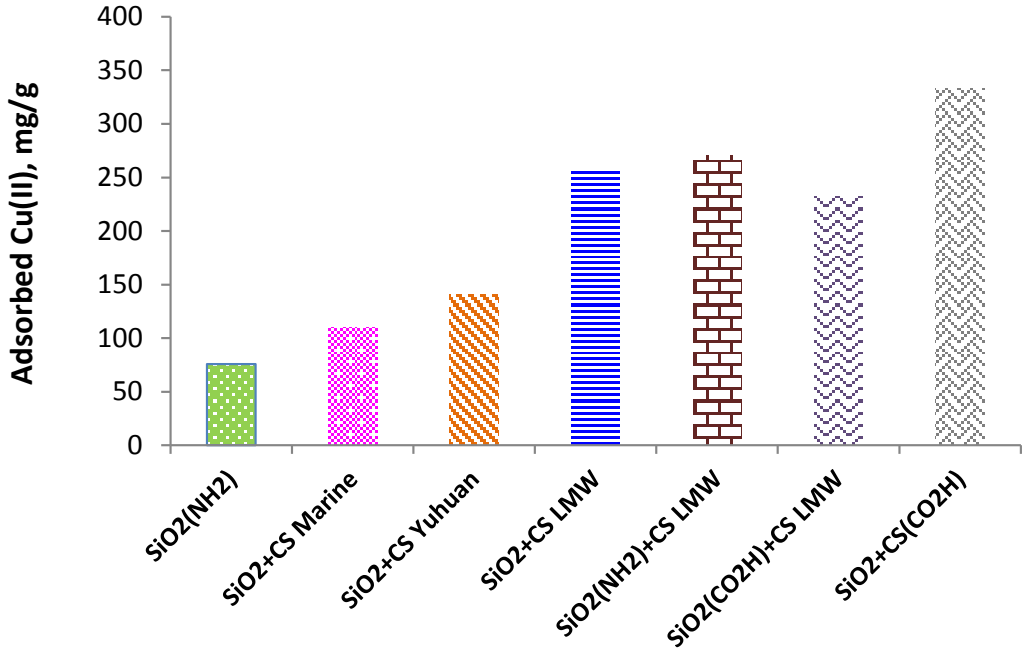

Fig. 88a Maximum Cu(II) adsorption capacities of seven types of CS-coated silica materials and a comparison with amine-grafted silica material

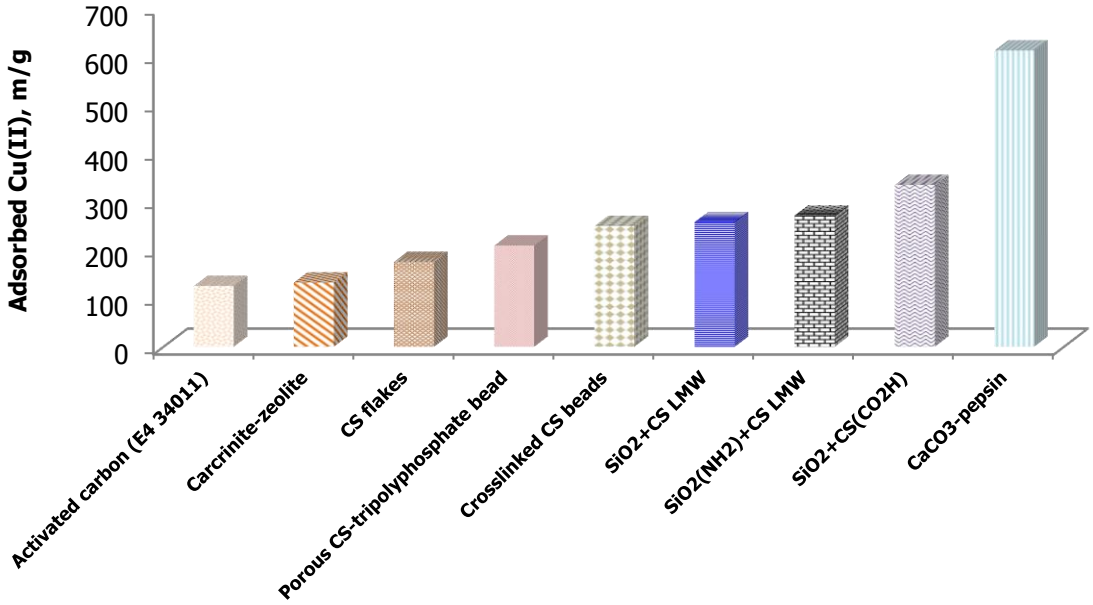

Fig. 88b Comparison of the maximum adsorption capacities of three types of CS-coated silica materials with some other adsorbent described in the literatures

A5 Adsorption Kinetics

The adsorption kinetics represent another important physicochemical parameter to evaluate the qualities of a good sorbent. They describe the adsorbate uptake rate and the rate controling the residence time (average amount of time that a particle spends in a particular system) of adsorbate at the solid-liquid interface.

Removal of Cu(II) by our hybrid sorbents as a function of time is shown in Fig. 90-93. The adsorption curve for Cu(II) ions reveals that the adsorption is initially rapid. To identify the rate-controlling mechanisms during the adsorption of copper, three steps were considered:

- Mass transfer of the metallic ion from the bulk solution to the chitosan surface,
- Adsorption of the metallic ion onto sites,
- Internal diffusion of the metallic ion onto chitosan.

For this purpose, the pseudo-first-order, pseudo-second-order (Ho and McKay, 1998), and intraparticle diffusion were used. The better fit was estimated in terms of the coefficient of determination (R^2).

Pseudo-First Order

The pseudo-first order has been used for the description of a reversible equilibrium between liquid and solid phases [36]. The pseudo-first order equation is expressed as equation 17

$$\ln((q_e - q_t)/ q_e) = - k_1/t \qquad (17)$$

where k_1 (min^{-1}) is the rate constant of pseudo-first order sorption, *t* is time, and q_e (mg/g) and q_t (mg/g) are the sorption capacities at equilibrium and at time *t*, respectively.

Pseudo-Second Order

The pseudo-second order model assumes the rate-limiting step of a chemisorption. The pseudo-second order chemisorption kinetic equation is expressed in equation 18 [37]

$$q_t = \frac{q_e^2 \, k_2 t}{q_e k_2 t + 1} \qquad (18)$$

where k_2 is the rate constant of the pseudo-second order sorption (g/mg/ min), t is time, and q_e (mg/g) and q_t (mg/g) are the sorption capacity at equilibrium and at time t, respectively.

Elovich

The equation defining the the Elovich model is based on a kinetic principle assuming that the adsorption sites increase exponentially with adsorption, which implies a multilayer adsorption. It is expressed as equation 19.

$$q_t = \frac{1}{\beta} \ln \alpha \beta + \frac{1}{\beta} \ln t \qquad (19)$$

Where α is related to the chemisorption rate (mg/g min), β is related to the surface coverage (mg/g min) during any experiment. A slope ($1/\beta$) and an intercept ($1/\beta \ln \alpha\beta$) are obtained from a plot of q_t versus ln t [38].

External mass transfer

The adsorbate can be transferred from the solution phase to the surface of the adsorbent through several steps. The steps may include external diffusion, pore diffusion, surface diffusion and adsorption on the pore surface. The external mass transfer can be written in a mathematical form as follows:

$$\frac{dq_t}{dt} = K_L A_s(C_t - C_S) \qquad (20)$$

where K_L is the liquid-solid external mass transfer coefficient (m/s), A_S is the specific surface area of adsorbent (m^2/Kg), C_t is the liquid phase concentration of sorbate at time (t) in the bulk solution (mM), C_S is the concentration of sorbate at sorbent interface (mM). The K_L can be estimated using the limit theorem: at t = 0, C approaches to C_0 and C_S approaches to zero as

$$K_L = \frac{\lim_{t \to 0} \frac{dq}{dt}}{A_s C_o} = \frac{h}{60 A_s C_o} \qquad (21)$$

$$A_s = \frac{6}{\rho_b d_p} \qquad (22)$$

where ρ_b is the bulk density of the adsorbent (kg m^{-3}), d_p is the mean particle diameter (m), and h is the initial sorption rate (mmol/g/min) [39].

Intraparticle diffusion (Vermeulen)

The intraparticle diffusion has been used in the analysis of a mass transfer mechanism of metal adsorption. The Vermeulen's intraparticle diffusion is expressed as

$$F_t^2 = \left[1 - \exp\left(\frac{-\pi^2 D_e t}{R_a^2}\right)\right] \qquad (23)$$

where F_t^2 is equal to q_t / q_e (fractional at time t), D_e is the effective diffusion coefficient (m^2/s) and t is time (second), R_a(m) is the radius of spherical adsorbent particles. The slope of the plot of ln $[1/(1)F_t^2)]$ versus t gives D_e [40].

Intraparticle diffusion (Weber and Morris)

The intraparticle diffusion model based on the theory proposed by Weber and Morris is expressed as

$$q_t = k_{int}\, t^{1/2} + C \qquad (24)$$

where k_{int} is the intraparticle diffusion rate constant (mg/g $min^{1/2}$), t is the time (min), and C is a intraparticle diffusion constant (or the intercept of the line, mg/g). It is directly proportional to the boundary layer thickness. A value of C close to zero indicates that diffusion is the only controlling step of the adsorption process. The k_{int} can be determined from the straight line plots of q_t against $t^{1/2}$. According to equation (24), if the plots give a straight line and pass through the origin, then the adsorption is controlled solely by the intraparticle diffusion. In contrast, if the plots show multi-linear plots, such plots indicate that two or more steps take place. The first portion is the external surface adsorption or boundary layer diffusion of solute molecule (ions). The second portion is the gradual adsorption stage, where intraparticle diffusion is rate-controlling. The final portion is the equilibrium adsorption stage where intraparticle diffusion starts to slow down due to low adsorbate concentrations [12, 38]. Some adsorption kinetics are shown in Table 4.8

Table 4.8 Some adsorption kinetics

Adsorption kinetics				
Kinetic		Plot	Description	Reference
Pseudo-first order	$\ln((q_e - q_t)/q_e) = -k_1/t$	$\ln(q_e - q_t)$ vs t	This model fits to experimental adsorption kinetic results when physical adsorption is dominant	[34]
Pseudo-second order	$q_t = \frac{q_e^2 k_2 t}{q_e k_2 t + 1}$	$\frac{t}{q_t}$ vs t	This model describes chemical adsorption	[37]
Elovich equation	$q_t = \frac{1}{\beta}\ln\alpha\beta + \frac{1}{\beta}\ln t$	q_t vs ln t	It assumes that the active sites of the sorbent are heterogenous and therefore exhibit different activation energies for chemisorption	[38]

Adsorption kinetics				
Kinetic		Plot	Description	Reference
External mass transfer	$\frac{dq_t}{dt} = K_L A_s(C_t-C_S)$	$\frac{C_t}{C_s}$ vs t	The external mass transfer has been used in the analysis of mass transfer mechanism of metal adsorption	[39]
Intraparticle diffusion (Vermeulen)	$F_t^2=\left[1 - \exp\left(\frac{-\pi^2 D_e t}{R_a^2}\right)\right]$	$\ln\left(\frac{1}{1-F_t^2}\right)$ vs t	It assumes that the adsorption process is controlled by chemical reaction	[40]
Intraparticle diffusion (Weber and Morris)	$q_t = k_{int} t^{1/2} + C$	q_t vs $t^{1/2}$	If the line passes through the origin then adsorption is the rate-controlling step. When the plot do not pass through the origin, it shows that adsorption is not only rate-limiting step	[12, 38]

Adsorption Kinetics: CS-coated Silica Materials and Amine-Grafted Silica

The adsorption kinetics were investigated by adsorption of Cu(II) (500 mg/L) onto two CS-coated silica materials: group II (**SiO_2+CS LMW**, **SiO_2+CS Yuhuan**, and **SiO_2+CS Marine)** and were compared to group IV adsorbent **$SiO_2(NH_2)$**. The amount of adsorbent was constant (0.4%). The adsorption took place at pH 5, and the contact time was in the range between 10 and 1.440 min. The pseudo-first-order, pseudo-second-order, intraparticle diffusion, and Elovich adsorption kinetics were employed to interpret the experimental data.

The adsorption rate of Cu(II) ions at the solid solution interface onto four CS-coated silica materials with an equilibrium established between the two phases was studied using the pseudo-first-order and pseudo-second-order model. The k_1 and k_2 values are the rate constant of pseudo-first order sorption and the rate constant of the pseudo-second order sorption, respectively. The validity of the kinetic models is tested by the magnitude of the correlation coefficients (R^2) shown in Table 4.9, it was found that the both pseudo-first-order and pseudo-second-order models (Fig. 89-92) provided a good fit for the adsorption kinetics of Cu(II) onto **SiO_2+CS LMW**, **SiO_2+CS Yuhuan**, **SiO_2+CS Marine**, and **$SiO_2(NH_2)$**. Based on pseudo-second-order, the k_2 values it can be deduced that Cu(II) is quickly adsorbed onto the adsorbents in the following order:

SiO_2+CS Marine > **SiO_2+CS LMW** > **SiO_2+CS Yuhuan** > **$SiO_2(NH_2)$**.

Table 4.9

Pseudo-first-order, pseudo-second-order, Intraparticle diffusion, and Elovich constants values

Kinetic isotherms		**SiO_2+CS LMW**	**SiO_2+CS Yuhuan**	**SiO_2+CS Marine**	**$SiO_2(NH_2)$**
Pseudo-first-order	k_1 (x 10^{-3} min)	2. 30	2.07	3.22	2.30
	q_e (mg/g)	76.40	24.62	54.60	32.24
	R^2	0.97	0.96	0.98	0.97
Pseudo-second-order	k_2 (x10^{-3} g/mg/ min)	0.04	0.29	0.06	0.01
	q_e (mg/g)	98.04	37.74	70.42	99.01
	R^2	0.97	0.97	0.99	0.97
Intraparticle diffusion	k_{int} (mg/g $min^{1/2}$)	2.42	0.63	1.73	1.24
	C (mg/g)	1.97	9.56	8.48	5.88
	R^2	0.96	0.99	0.89	0.80
Elovich	β (g./mg min)	0.06	0.24	0.07	0.11
	R^2	0.94	0.80	0.97	0.91

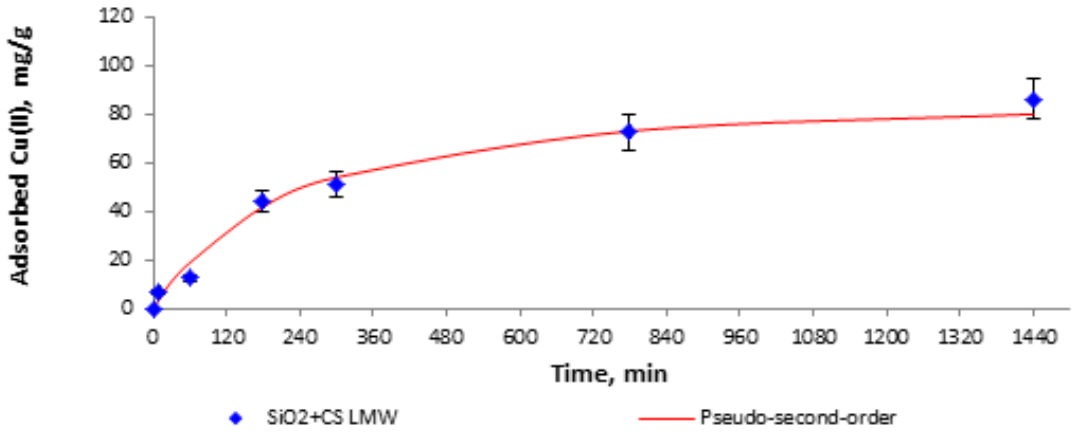

Fig. 89 Pseudo-second-order curve of the Cu(II) adsorption on **SiO_2+CS LMW**

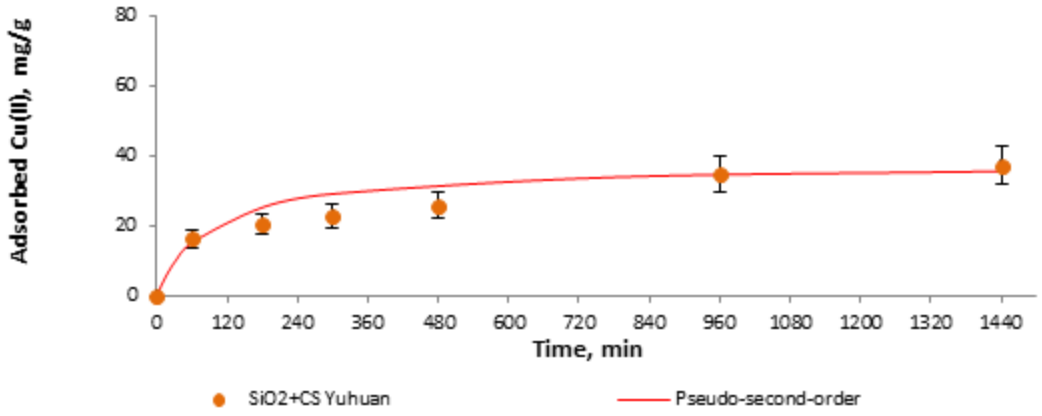

Fig. 90 Pseudo-second-order curve of the Cu(II) adsorption on **SiO_2+CS Yuhuan**

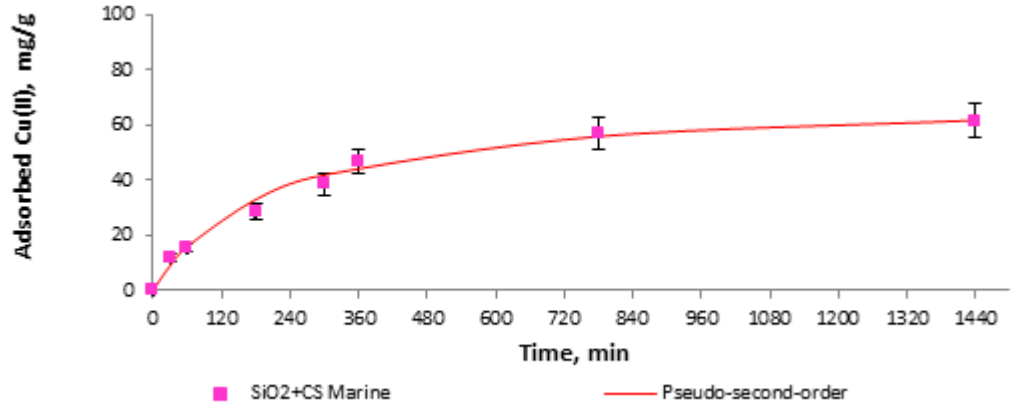

Fig. 91 Pseudo-second-order curve of the Cu(II) adsorption on **SiO_2+CS Marine**

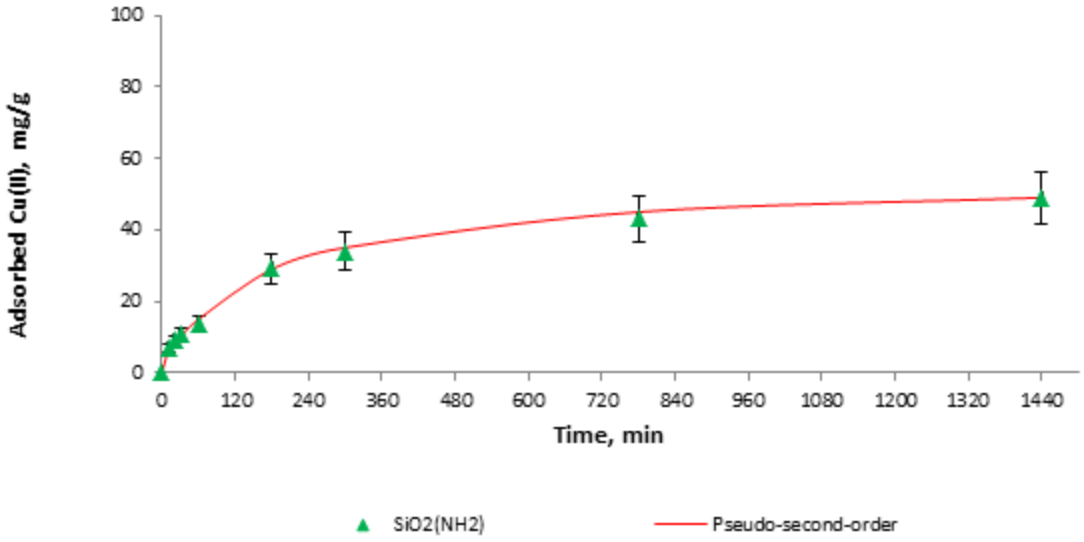

Fig. 92 Pseudo-second-order curve of the Cu(II) adsorption on **$SiO_2(NH_2)$**

Both pseudo-first order and pseudo-second order kinetics did not allow clarifying the diffusion mechanism; therefore the kinetics results were analyzed using the intraparticle diffusion equation. Table 4.9 represents the intraparticle diffusion constants for adsorption of Cu(II) onto **SiO_2+CS LMW**, **SiO_2+CS Yuhuan**, **SiO_2+CS Marine**, and **$SiO_2(NH_2)$**. The plots (R^2 = 0.80-0.99) for all four adsorbents gave rise to a straight line. However, since the lines did not pass the origin for all four adsorbents, one may conclude that the intraparticle diffusion was not the only rate-controlling step involved in the adsorption process. The intraparticle diffusion rate constants (k_{int}) were 2.42 mg/g $min^{1/2}$, 0.63 mg/g $min^{1/2}$, 1.73 mg/g $min^{1/2}$, and 1.24 mg/g $min^{1/2}$, for **SiO_2+CS LMW**, **SiO_2+CS Yuhuan**, **SiO_2+CS Marine**, and **$SiO_2(NH_2)$**, respectively. In addition, the plots showed the C values that give an idea about the thickness of the boundary layer. The C values were for **SiO_2+CS LMW** (C = 1.97), **SiO_2+CS Yuhuan** (C = 9.56), **SiO_2+CS Marine** (C = 8.48), and **$SiO_2(NH_2)$** (C = 5.88),

respectively. In the case of **SiO_2+CS LMW**, the C value close to zero indicates that diffusion is the only controlling step of the adsorption process.

The Elovich equation which assumes that the active sites of the sorbent are heterogeneous was also used to interpret the experimental data. The R^2 values for the Elovich equation plots were in the range between 0.80-0.97, and lower than those of the pseudo-second-order (see Table 4.9). Therefore, in contrast to the other three models, the Elovich model is not appropriate to describe the data.

Adsorption Kinetics: CS-coated Amine and/or Carboxyl-Grafted Silica Materials and Carboxymethyl CS-coated Silica

The adsorption kinetics were furthermore investigated for the adsorption of Cu(II) (500 mg/L) onto the two group III CS-coated silica materials **$SiO_2(NH_2)$+CS LMW**, and **$SiO_2(CO_2H)$+CS LMW)** as well as the group IV adsorbent **SiO_2+CS(CO_2H)**. The amount of adsorbent was constant (0.4%). The adsorption took place at pH 5, and the contact time was in the range between 0 and 1440 min. As adsorption kinetics, pseudo-first-order, pseudo-second-order, intraparticle diffusion, and Elovich were employed to interpret the experimental data.

The adsorption rate of Cu(II) ions at the solid-solution interface onto three CS-coated silica materials with an equilibrium established between the two phase was studied using the pseudo-first-order which is commonly used to the adsorption of liquid-solid system based on adsorbent capacity) and the pseudo-second-order which derived by assuming that two surface sites could be occupied by one divalent adsorbate ion). Table 4.10 and Fig. 93-95 show the adsorption kinetics study for copper adsorption onto these group III and IV adsorbents. It was found that both pseudo-first-order and pseudo-second-order models were the model that provided a good fit for adsorption kinetics of Cu(II) onto **$SiO_2(NH_2)$+CS LMW** and **$SiO_2(CO_2H)$+CS LMW**). When comparing the k_2 values of the group III (**$SiO_2(CO_2H)$+CS LMW**) adsorbent with the group I material (**$SiO_2(NH_2)$**, it can be seen that Cu(II) is adsorbed more rapidly onto the modified group III silica material than onto group I. This is probably due to the fact that **$SiO_2(CO_2H)$+CS LMW** own two functional groups (-NH_2 and -CO_2H) in the CS shell, whereas **$SiO_2(NH_2)$** bears only a -NH_2 monolayer on its surface.

In case of **$SiO_2(NH_2)$+CS LMW**, it was found that both the pseudo-first-order and pseudo-second-order were fit to describe the adsorption mechanism with the correlation

coefficient ($R^2 \geq 0.98$). However, the pseudo-first-order was better fit with the R^2 value of 0.99 than the pseudo-second-order model. According to the pseudo-first-order model, it could be assumed that one adsorbate species (Cu(II) ion) reacts with one active site ($-NH_2$) on the surface of **$SiO_2(NH_2)$+CS LMW**. This result was similarly to the adsorption of Cu(II) onto sodium hydroxide modified waste mycelium of *A. awamori* where the adsorption mechanism followed the pseudo-first-order odel [41a].

In order to gain insight into the mechanisms and rate controlling steps affecting the kinetics of adsorption, the kinetic experimental results were analyzed by the intraparticle diffusion model (Weber and Morris) to elucidate the diffusion mechanism. The k_{int} is the intraparticle diffusion rate constant, mg/g $min^{1/2}$.

Table 4.10 Pseudo-first-order, pseudo-second-order, Intraparticle diffusion, and Elovich constants values

Kinetic isotherms		**$SiO_2(NH_2)$+CS LMW**	**$SiO_2(CO_2H)$+CS LMW**	**SiO_2+CS(CO_2H)**
Pseudo-first-order	k_1 (x 10^{-3} min^{-1})	2.07	2.30	0.46
	q_e (mg/g)	65.01	21.16	23.49
	R^2	0.99	0.97	0.82
Pseudo-second-order	k_2 (x 10^{-3} g/mg/ min)	0.06	0.59	0.44
	q_e (mg/g)	85.47	104.17	99.01
	R^2	0.98	0.99	0.96
Intraparticle diffusion	k_{int} (mg/g $min^{1/2}$)	2.03	0.55	0.60
	C (mg/g)	7.09	76.62	81.35
	R^2	0.98	0.89	0.95
Elovich	α (g./mg min)	0.47	18.52	19.95
	β (g./mg min)	0.07	0.24	0.28
	R^2	0.95	0.83	0.78

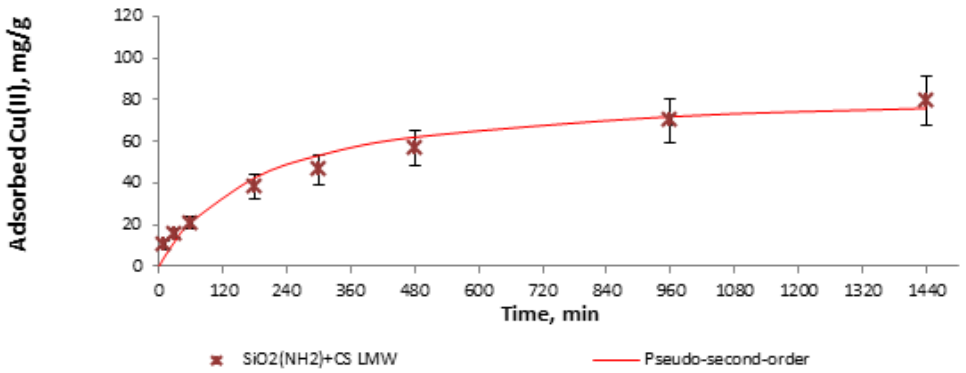

Fig. 93 Pseudo-second-order curve of the Cu(II) adsorption onto **$SiO_2(NH_2)$+CS LMW**

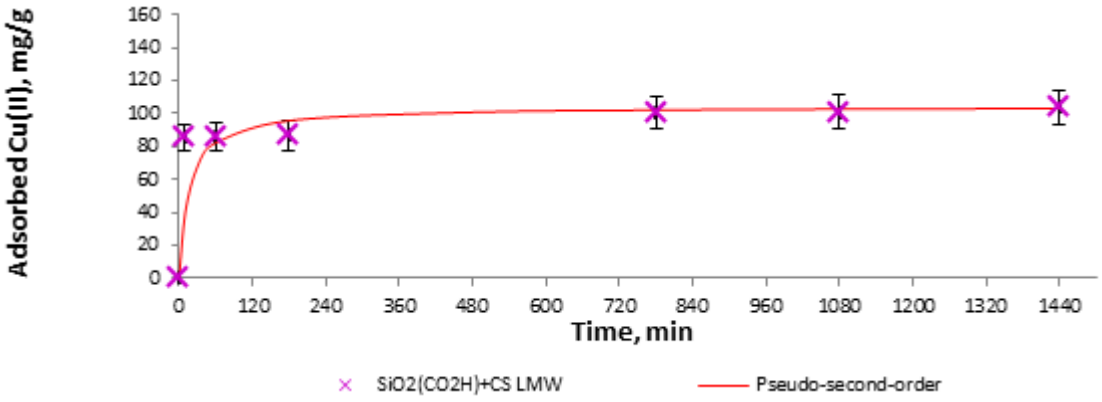

Fig. 94 Pseudo-second-order curve of the Cu(II) adsorption onto **$SiO_2(CO_2H)$+CS LMW**

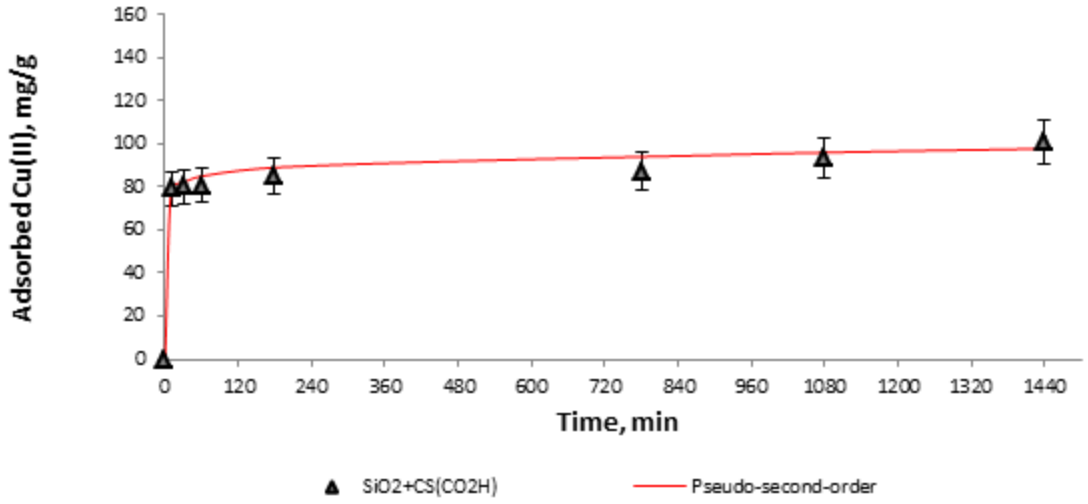

Fig. 95 Pseudo-second curve of the Cu(II) adsorption on **SiO_2+CS(CO_2H)**

Table 4.10 shows the intraparticle diffusion constants for adsorption of Cu(II) on **$SiO_2(NH_2)$+CS LMW**, **$SiO_2(CO_2H)$+CS LMW**, and **SiO_2+CS(CO_2H)**. The plot for all data is shown as a straight line (R^2 = 0.89 to 0.98). Since the lines did not pass the origin for all three adsorbents, intraparticle diffusion can be excluded as only rate-controlling step. Moreover, the plots showed a curvature which was attributed to boundary layer diffusion effect or external mass transfer effect. The rate constants, $k_{int,}$ were 2.03 mg/g $min^{1/2}$, 0.55 mg/g $min^{1/2}$, and 0.60 mg/g $min^{1/2}$, for **$SiO_2(NH_2)$+CS LMW**, **$SiO_2(CO_2H)$+CS LMW**, and **SiO_2+CS(CO_2H)**, respectively. In addition, the k_{int} value for Cu(II) adsorption onto **$SiO_2(CO_2H)$+CS LMW** and **SiO_2+CS(CO_2H)** is close to the k_{int} value (0.2491 mg/g $min^{1/2}$) for the adsorption of Cu(II) on CS-bentonite material [41b]. Moreover, the C value given in Table 4.10 is showing that **SiO_2+CS(CO_2H)** has a higher C value (C = 81.35 mg/g) than

$SiO_2(CO_2H)$+CS LMW. It was consistent with the k_{int} value where **SiO_2+CS(CO_2H)** showed the lower adsorption rate compared to **$SiO_2(CO_2H)$+CS LMW**.

The Elovich equation was also used to interpret the experimental data. In the case of **$SiO_2(NH_2)$+CS LMW**, the R^2 value was found to be 0.95, a value lower than that obtained from the pseudo-first-order model (R^2 = 0.99). Morever, for **$SiO_2(CO_2H)$+CS LMW** and **SiO_2+CS(CO_2H)**, the R^2 values were found to be quite low (R^2 <0.83). Therefore, the Elovich equation is not fit to explain the adsorption of Cu(II) onto **$SiO_2(NH_2)$+CS LMW**, **$SiO_2(CO_2H)$+CS LMW** and **SiO_2+CS(CO_2H)** comparing to the first-order and the second-order model (see Table 4.10).

A6 Characterization of the Cu(II)-loaded Composite

A6.1 The FT-IR Spectrum of the Cu(II)-loaded SiO_2+CS LMW Composite

The FT-IR spectrum of Cu(II) adsorbed on **SiO_2+CS LMW** is shown in Fig. 96**a**. The -OH and -NH stretching vibrations observed at 3447 cm^{-1} in the spectrum of **SiO_2+CS LMW** appear shifted to a higher wave number (3477) cm^{-1} upon adsorption of copper. A band at 1598 cm^{-1} (amide II from CS) of **SiO_2+CS LMW** composite was not found after copper adsorption. The -OH bending and -SiO rocking vibration in the spectrum of **SiO_2+CS LMW** at 1645 cm^{-1} and 486 cm^{-1} were shifted to 1714 cm^{-1} and 497 cm^{-1} after Cu(II) loading onto the **SiO_2+CS LMW** composite. These shifts could be explained by the complexion of Cu(II) by -NH_2, and -OH, leading to changes in IR peak positions [16]. The same trend was observed for **SiO_2+CS Marine** and **SiO_2+CS Yuhuan** materials. In case of Cu(II) loaded onto **SiO_2+CS LMW**, the bands at around 1130 cm^{-1} and 680 cm^{-1} are due to the stretching vibration of sulfate S-O bonds and new weak band in the range of 500-400 cm^{-1} shows that SO_4^{2-} conterions take part in the coordination rather than existing as free ions in the complexes [41b].

Concerning **$SiO_2(NH_2)$**, after loading with Cu(II) the bands at 3460 and 1654 cm^{-1} were shifted to 3489 and 1676 cm^{-1}, respectively. Therefore, the copper ions interact with the -NH_2 group; however an interaction with both the -NH_2 and -OH groups cannot be ruled out.

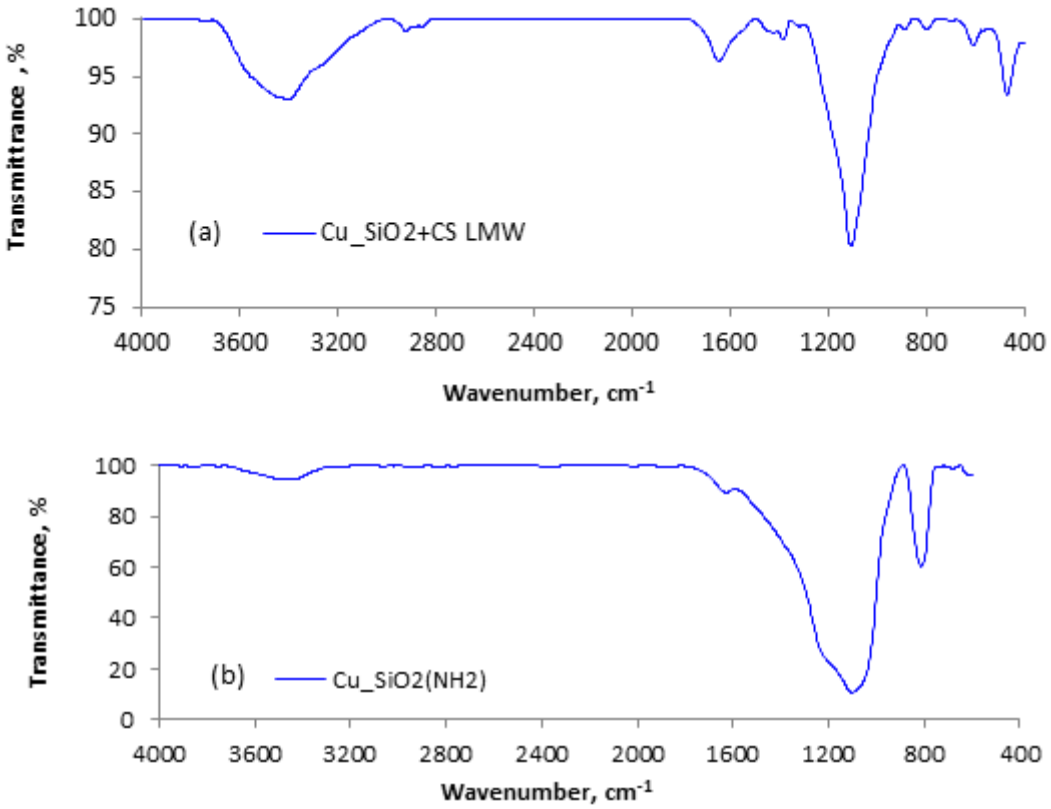

Fig. 96 FT-IR of Cu loaded **SiO_2+CS LMW** (a), and Cu loaded **$SiO_2(NH_2$** (b)

For the **$SiO_2(NH_2)$+CS LMW**, **$SiO_2(CO_2H)$+CS LMW** and **SiO_2+CS(CO_2H)**, the FT-IR spectra of Cu(II) loaded **$SiO_2(NH_2)$+CS LMW** (Fig. 97**a-b**) display also changes concerning position and intensity of the peaks upon Cu(II) binding. The same results were observed for Cu(II) loaded **$SiO_2(CO_2H)$+CS LMW** and Cu(II) loaded **SiO_2+CS(CO_2H)**. From these observations, it can be deduced that the -NH_2, -OH, and -CO_2H groups are involved as binding sites to form complexes with the Cu(II) ion, thus causing the spectral changes.

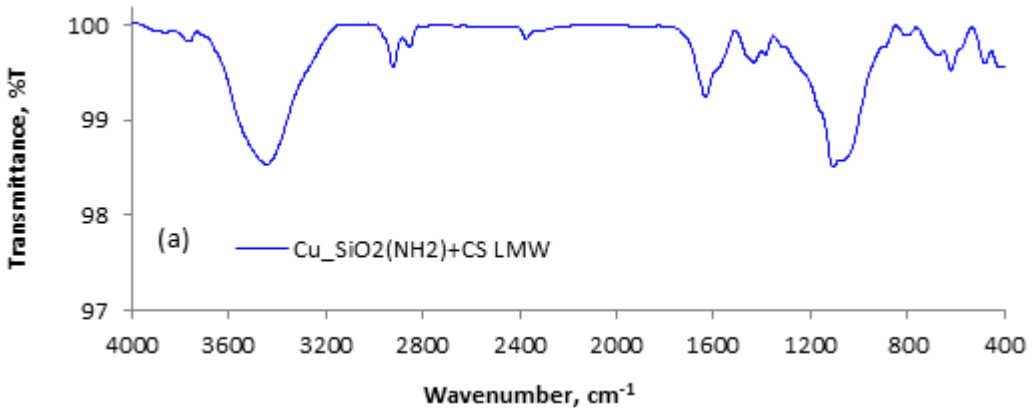

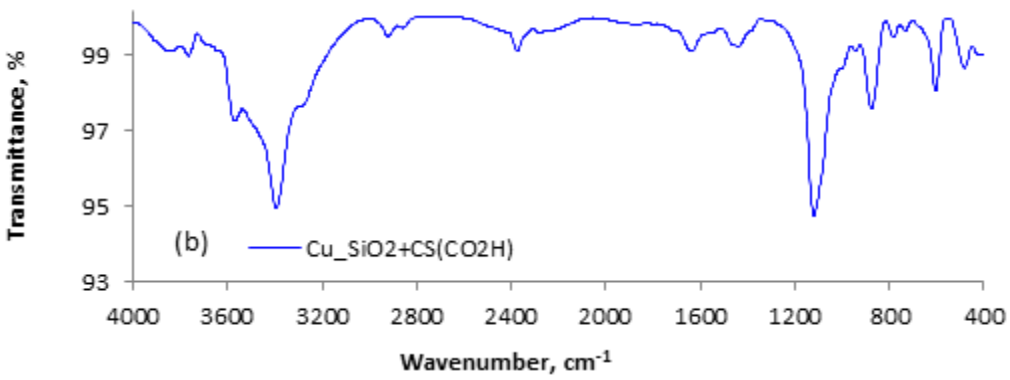

Fig. 97 FT-IR of Cu loaded **$SiO_2(NH_2)$+CS LMW** (a), and Cu loaded **SiO_2+CS(CO_2H)** (b)

A6.2 Energy Dispersive Spectroscopy (EDS)

The EDS spectrometer was utilized for elemental analysis of the copper adsorbed on the CS-silica hybrid materials. Five points on the surface of the copper-loaded modified silica materials were analyzed. Fig. 98**a-b** shows three peaks of sulphur, silica and copper, which were the three major constituents of the composites (**SiO_2+CS LMW** and **SiO_2+CS Marine**). The amount of the copper in percentage is shown in Table 4.11. The average copper amount for **SiO_2+CS LMW** was 20.52 ± 3.4 %, and for **SiO_2+CS Marine** it was 16.53 ± 1.3 %.

The finding indicated that the amount of the copper of both hybrid composites observed from each of the five points, represented as a percentage was close to each other. From the results, it can be assumed that the copper ions were quite homogeneously adsorbed on the CS-coated silica hybrid composites.

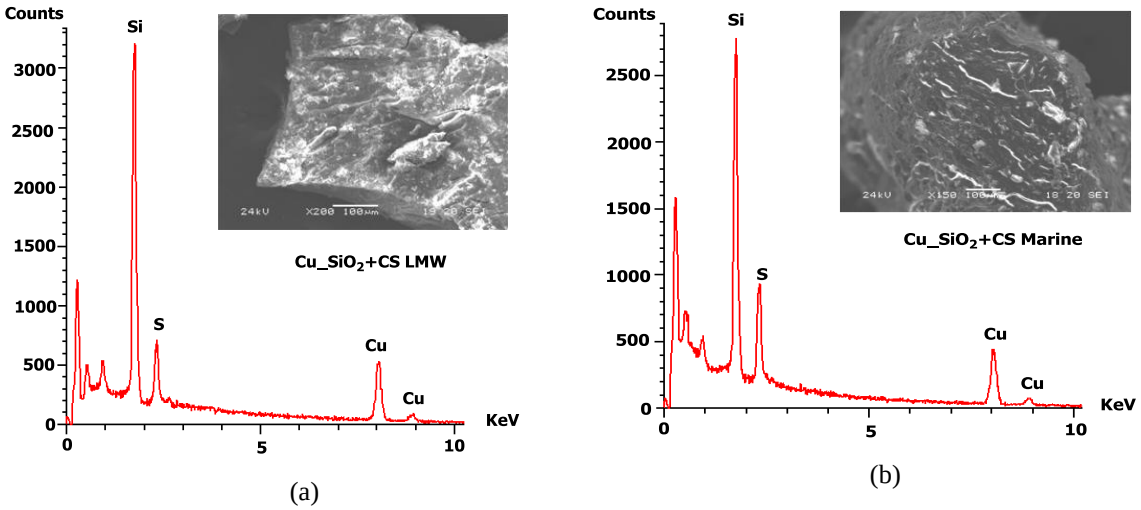

Fig. 98 SEM images and corresponding EDS spectra of Cu-loaded **SiO_2+CS LMW** (a), and Cu loaded **SiO_2+CS Marine** (b), respectively

Table 4.11 The EDS value of five-point measurement on sample surface

Materials	%Atomic					
	1	2	3	4	5	Average
SiO_2+CS LMW	20.1	18.2	21.8	18.9	17.6	20.5±3.4
SiO_2+CS Marine	16.7	16.1	14.6	17.1	18.2	16.5±1.3

A7 Interaction of Copper(II) with CS

The IR results provide the information that the complexation between CS-coated silica and the metal cation may be through the free amino groups on CS structure. Fig. 99**a** shows a metal ion bounded with one amine group as a donor [42]. In a report of Domard and co-workers, the Density Functional Theory (DFT) method was used to study the interaction between Cu(II) and CS. The computing showed as most stable form the pending complex (Fig. 99**a**). This complex consists of only one Cu(II), one amino group and oxygen atoms of the three other ligands involved in the highest occupied molecular orbital (HOMO). The interaction involves the *d* orbitals of the Cu(II) ion and the *p* orbitals of the N atoms [42, 43].

The study of the interaction between Cu(II) and CS by Desbrières *et al.* determined by both potentiometric study and spectroscopic method confirms that at pH ~ 5.3, Cu(II) ions are complexed with one -NH_2 group of CS under the most stable form {$[Cu(\text{-}NH_2)]^{2+}$, $2OH^-$, H_2O, **I**} (Fig. 99**a**). In contrast, when the pH is above 5.8, the complex {$[Cu(\text{-}NH_2)]^{2+}$, $2OH^-$, **II**} ligated by two amino groups is formed (Fig. 99**b**) [44].

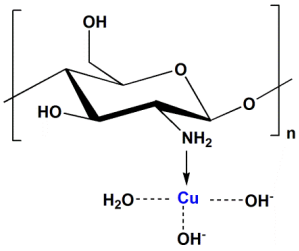

(a) Complex **I**, pH 5.3

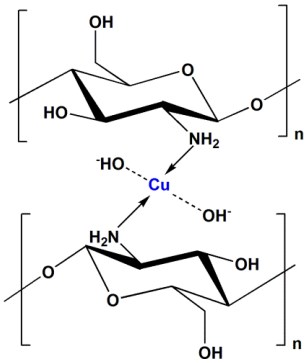

(b) Complex **II**, pH > 5.8

Fig. 99 Complexation between Cu(II) ions and amino groups of CS

The formation of a transition metal complex can be described by means of the Lewis acid-base theory, where an acid is the acceptor of a pair of electrons from a base. CS (**L**) is the Lewis base presenting -OH and -NH_2 basic sites and Cu(II) is the Lewis acid (**M**) [45].

The formation of the complex ML_n from a metal **M** and a ligand **L** can be represented as follows

$$M + L \rightleftharpoons ML;\ ML + L \rightleftharpoons ML_2;\ .....ML_{n-1} + L \rightleftharpoons ML_n$$

$$K = \frac{[ML_n]}{[ML_{n-1}][L]} \qquad (25)$$

where ML_n is the ligated metal complex, and **n** is the maximum co-ordination number.

The stability constant **K** of the complexation of Cu(II)-chitosan was investigated by Desbrières and co-workers by the Bjerrum method. The principle of this method is based on the determination of the different species formed in solution by potentiometric titration (see detail in reference [45]). The complex **I** shows a higher formation constant (log K = 5.47) than the complex **II** (log K = 2.62). It can be assumed that only one amino group has a larger formation constant meaning a larger stability constant and lower dissociation [44].

The complexation of metallic ions depends on the stability constant of the metal-ligand complex, but also on the dissociation constant of the ligand obtained from the equilibrium reaction shown in eq. 29.

$$-NH_3^+ + H_2O \rightleftharpoons -NH_2 + H_3O^+ \qquad (29)$$

$$K_a = \frac{[-NH_2][H_3O^+]}{[-NH_3^+]}$$

The pK_a can be calculated using the Katchalsky equation as shown in equation 30.

$$pK_a = pH + \log \frac{[x]}{[1-x]} \qquad (30)$$

where x is the neutralization degree of amino group. From the report of Desbrières *et al*., the pK_a is constant and equals to 6 [45].

The interaction of CS with metal ions can be described as follows:

$$CS\text{-}NH_2 + H_3O^+ \rightleftharpoons CS\text{-}NH_3^+ + H_2O \qquad (31)$$

$$CS\text{-}NH_2 + M^{n+} \longrightarrow (Complex)^{n+} \qquad (32)$$

$$CS\text{-}NH_3^+ + M^{n+} + H_2O \longrightarrow (Complex)^{n+} + H_3O^+ \qquad (33)$$

Recently, the complex ion equilibria between *N,O*-carboxymethyl chitosan with metal ions such as Cu(II), Ni(II), Co(II), Mn(II) and Zn(II) have been investigated by potentiometric titration [46]. From the results, it was possible to arranged the log *K* values in the order Mn <

Co < Ni > Zn. These thus established stability constants were consistent with the order within the Irving-William series for divalent high-spin metals [47].

According to another recent DFT computing study and geometry optimization of the possible aquo-complexes resulting from complexation between Cu(II) and CS residues, the trend of coordination with paramagnetic Cu(II) is $-NH_2$ > -OH at C3 > H_2O > $NHCOCH_3$ [48]. In this article, the coordination number of the resulting complexes is discussed. In contrast to studies of other research groups, the group of Lü proposes an initial hexacoordination over a tetracoordination. In this work, the pendant model proposed by Domard in ref 45 (Fig. 99) and the bridge model were compared. Whereas Domard is in favor of a pendant model, Lü concludes that the bridge model is superior to the pendant model. In a paper of Y.A. Skorik *et al*., the complexation of *N*-(2-Carboxyethyl)chitosan with Cu(II) ions was investigated in aqueous solution. It was demonstrated by pH-potentiometric and UV-spectrophotometric techniques that the complexation model depends on the degree of substitution (DS) of CS: the $[Cu(Glc\text{-}NR_2)_2]$ (bridge model) complexes are predominant for two lower substituted (DS 0.42 and 0.92) whereas the increase of DS (1.61) leads to formation of $[Cu(Glc\text{-}NR_2)]$ (pendant model) complexes [49a]. To support their findings the authors prepared also an CS-Cu(II) model complex and characterized it by single-crystal X-ray diffraction.

Therefore there is still some controversy on this subject. Since a Cu(II) ion readily coordinates H_2O molecules, the coordination sphere around the metal centre depends surely from its environment. A sample of a CS-Cu(II) adduct obtained from aqueous solution may change the coordination number after drying by loss of water molecules and than even rehydrate partially upon exposure to humidity of air. This may also hamper the interpretation of the IR spectra. Note that gray-white anhydrous $CuSO_4$ becomes bluish after exposure to humid air by reformation of the well-known deep-blue $CuSO_4$ x 5 H_2O complex [49b].

Numerous studies have been conducted using various types of adsorbent for Cu(II) adsorption at optimum pH. Table 4.12 presents a comparison of the adsorption capacity of the results. The adsorption of Cu(II) onto plant biomass was found to be 17.87 - 263.2 mg/g [50-52a], coffee wastes was found to be 70 mg/g [52b], activated carbon (rice husk) was found to be 112.4 mg/g, activated carbon (Tunisian date stones) was found to be 31.2 mg/g, activated carbon number E4 34011 was found to be 125.0 mg/g, fly ash was found to be 69.9 mg/g [53-54], natural sorbent was found to be 187 mg/g [20], sissoo sawdust (*Dalbergia*) was found to be 263.2 mg/g [53], modified silica was found between 11.8 - 126.2 mg/g [55-62], modified CS was found to be 8.7 - 219 mg/g [63-79b], polyacrylonitrile grafted CS was found to be

239.3 mg/g [70a], CS/clay/magnetite composite was found to be 17.2 mg/g [70b], maghnite was found to be 21.78 mg/g [70c], and zeolite was found to be 20.9 - 132.2 mg/g [71-75]. However, under similar adsorption conditions (pH 5), significantly lower q_{max} values in the range of 20.9 - 97.2 mg/g are reported for modified silica, and q_{max} values in the range of 35.5 - 139.3 mg/g are reported for modified CS. In addition, M. Hébrant *et al.* report that the extraction of copper(II) by colloidal dispersions of porous fumed silicas (FS200 and/or FS390) grafted with 5-phenyl-azo-8-hydroxyquinoline found to be 97% for an initial copper concentration of 5×10^{-5} M) [70d]. Considering, the content of 5-phenyl-azo-8-hydroxyquinoline attached to the silica is limited (0.15 mm/g at the maximum).

Table 4.12 Some maximum adsorption capacities of Cu(II) by various adsorbents.

Materials	Cu(II))	pH	Reference
Cinnamomum camphora (Camphor tree)	17.9	4	[50a]
Agricultural waste (Sugar beet pulp)	28.5	4	[50b]
Aspergillus niger	28.7	5	[50c]
Activated carbon (Tunisian date stones)	31.25	5	[51a]
Sawdust (Meranti wood)	37.17	6.6	[51b]
Sodium hydroxide treated Orange peel	50.3	5.3	[52a]
Coffee wastes	70	5	[52b]
Fly ash	69.9	6	[53]
Sissoo sawdust (*Dalbergia*)	263.2	6	[53]
Activated carbon number E4 34011	125.0	6	[53]
Activated carbon (rice husk)	112.43	-	[54]
Natural sorbent	187	6.5	[20]
Resacetophenone loaded 3-aminopropyltriethoxysilane-silica gel	11.80	6.0-7.5	[55a]
N-[3-(trimethoxysilyl)-ethylenediamine grafted silica	16.59	5.5-6	[55b]
Cyanex 272 [bis(2,4,4-trimethylpentyl)phosphinic acid] immobilized silica	20.9	5.3	[56]
4-amino-2-mercaptopyrimidine immobilized silica gel	28.41	5-6	[57]
Modified SBA-15 mesoporous silica with 3-aminopropyl-triethoxysilane or with salicylaldehyde	44	4.8	[58]
Amine-functionalized silica SBA-15	52.7	-	[59]
Aminopropyl functionalized silica gels	97.2	5	[60]
Amino-functionalized Fe_3O_4 nanopartiles	25.77	6	[61]
Melamine-based dendrimers amine-functionalized SBA-15 silica	126.2	4	[62]
CS-GLA	8.7	6	[63a]
Crosslinked CS with epichlorohydrin	35.5	6	[63b]
Modified magnetic CS	35.5	5	[63c]
CS beads	64.6	4.5	[25]

Materials	Cu(II))	pH	Reference
CS-alginate beads	67.7	4.5	[25]
Thiourea-modified magnetic CS	66.7	4-5	[64]
6,6'-piperazine-1,4-diyldimethylenebis (4-methyl-2-foformyl) phenol-CS	82.64	6.5	[65]
Cross-linked magnetic chitosan-2-aminopyriine glyoxal Schiff's base resin	124	5	[66]
Epichlorohydrin (ECH)-CS, Triphosphate (TPP)	130.7	6	[67]
Carboxymethyl chitosan hydrogel bead	139.27	5	[68]
N-carboxymethylchitosan	192	6.5	[69]
Polyacrylonitrile grafted CS	239.3	7	[70a]
CS/clay/magnetite composite	17.2	5	[70b]
Maghnite (Clays)	21.8	-	[70c]
Bentonite	20.9	4	[71]
Natural zeolite	23	5	[72]
Natural bentonite	45.47	7	[73]
CS-coated sand	228	4.2	[14]
Oxide modified bentonite	105.4	6	[74]
Cancrinite- zeolite	132.2	6	[75]
CS-tripolyphosphate beads	26.1	4.5	[76a]
CS-cellulose acetate	48.2	5	[76b]
CS-coated alumina	86.2	4	[77]
CS coated perlite beads	104	4.5	[44]
Saccharomyces cerevisiae - CS coated magnetic nanoparticles	144.9	4.5	[78]
Cottonseed protein-PAA hydrogel composite	219	4.0-5.5	[79a]
Macroporous chitosan membrane	19.9	5	[79b]
Porous chitosan-tripolyphosphate beads	208.3	5	[79c]
Carboxyl functionalized silica gel	163	4	[80a]
Benzene-1,2,4,5-tetrol modified polyacrylamide	18.87	5.4	[80b]
$CaCO_3$-pepsin	611	neutral	[80c]
$SiO_2(NH_2)$	75.8	5	Present work
SiO_2+CS Marine	109.9	5	Present work
SiO_2+CS Yuhuan	140.8	5	Present work
SiO_2+CS LMW	256.4	5	Present work
$SiO_2(CO_2H)$+CS LMW	232.6	5	Present work
$SiO_2(NH_2)$+CS LMW	270.3	5	Present work
SiO_2+CS(CO_2H)	333.3	5	Present work

The maximum adsorption capacity was obtained in the case of aChitosan-coated sand with a value of 228 mg/g. [14]. The adsorption of Cu(II) on CS-coated silica (present work), 109.9 - 333.3 mg/g, was higher than the adsorption of Cu(II) on a CS-coated alumina hybrid

composite (86.2 mg/g) [77]. The adsorption of Cu(II) on our materials (**$SiO_2(NH_2)$+CS LMW** and **$SiO_2(CO_2H)$+CS LMW**) was also higher than that of CS-coated perlite beads (104 mg/g, pH 4.5), and that of the Saccharomyces cerevisiae / CS-coated magnetic nanoparticles (144.9, pH 4.5) [44, 78]. Cottonseed protein-poly (acrylic acid) copolymer hydrogel composite found to be 219 mg/g (pH 4.0-5.5) [79a]. At pH 5, macroporous chitosan membrane found to be 19.87 mg/g [79b] and Porous chitosan-tripolyphosphate beads found to be 208.3 mg/g [79c]. Carboxyl functionalized silica gel (specific surface = 320 m^2/g) found to be 163 mg/g [80a]. The **$SiO_2(NH_2)$+CS LMW**, **$SiO_2(CO_2H)$+CS LMW**, and **SiO_2+CS(CO_2H)** showed a very good sorbent due to the two effective sites: amino groups and carboxyl groups, on the structure of the silica core and CS shell.

Based on the Langmuir isotherm, the adsorption of Cu(II) onto the carboxymethyl CS-coated non-grafted silica material **SiO_2+CS(CO_2H)**) showed still better adsorbent properties compared to CS-coated silica material **SiO_2+CS LMW**. The former types of material exhibit probably a higher adsorption capacity due to the presence of two available groups (-NH_2 and -CO_2H) for the uptake of Cu(II) ions.

A8 Comparision between the Adsorption of Cu(II) onto CS-coated Silica from of Copper Sulphate and Copper Nitrate Solution: Influence of the Counter Ion

Under real world conditions contaminated water contains also several other ions (both cations and anions), affecting the adsorption of a given metal. Consequently, the effect of some commonly occurring counter ions on the adsorption behavior of Cu(II) by our materials was studied. A typical water sample containing chloride ions, and nitrate ions was doped with known quantities of adsorbate metal ions. These samples were used as the water matrix for adsorption. Adsorption of Cu(II) onto CS-coated silica material **SiO_2+CS LMW** from solutions of $Cu(NO_3)_2$ was studied at room temperature. The adsorption took place at pH 5 and contact time was 24 hours. The initial concentration of Cu(II) was in the range between 50 mg/L to 1.000 mg/L. The dose of sorbent was fixed as 0.4% in solution. Similar conditions were also employed to the adsorption of Cu(II) onto **SiO_2+CS LMW** from solutions of $CuSO_4$ to allow a comparison. Fig. 100 shows a more efficient Cu(II) adsorption from solution for $CuSO_4$ compared to $Cu(NO_3)_2$. The adsorption of Cu(II) fitted well with Langmuir isotherms and the q_m values were 256.4 mg/g for the adsorption from $CuSO_4$ solution and 196.1 mg/g for the adsorption from $Cu(NO_3)_2$ solution. This result is consistent

with the work reporting by F. Kopecky and co-workers who found that the maximum adsorption capacities for Cu(II) on CS suspended in aqueous solution were 190 mg/g for $CuSO_4$, 170 mg/g for $Cu(ClO_4)_2$ and 140 mg/g for $Cu(NO_3)_2$ [80d]. When SO_4^{2-} anions are present in the solution, the adsorption of Cu(II) onto **SiO_2+CS LMW** was higher than that in NO_3^- solution. The same finding was also briefly communicated by T. Mitani and co-workers, who investigated the effect of counter ions such as SO_4^{2-} and Cl^- on the adsorption of Cu(II) salts onto CS in swollen CS beads [81]. According to the Freundlich isotherms, it was found that the adsorption of Cu(II) from sulphate solution is higher than that from $CuCl_2$ solution. The sulphate ion had the ability to enhance the adsorption of copper ion onto chitosan beads.

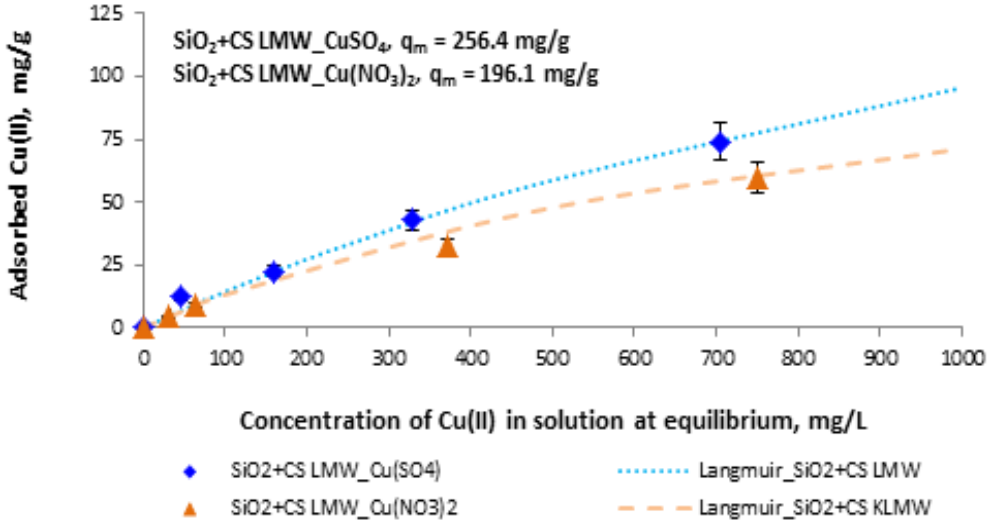

Fig. 100 Comparision of the Cu(II) adsorption onto **SiO_2+CS LMW** from $CuSO_4$ x $5H_2O$ and $CuCl_2$ x $2H_2O$ solutions at pH 5

The result of these three independent studies confirm that the Cu(II) adsorption depends on the nature and charge (monovalent vs divalent) of the counter ions in solution. Of course this preliminary investigation needs to be explored more in depth in future studies. Note, that in contrast to the increasing number theoretical and experimental studies on the interaction of Cu(II) with CS on a molecular level, the coordination and bonding mode (supramolecular, hydrogen bridges, …) of the anion has been neglected and deserves to be taken more in consideration.

Part B Adsorption of Nickel(II) on the Composites

After our thorough study on the various parameters affecting the capture Cu(II) salts on CS-coated silica hybrid materials from aqueous solution, we were intrigued to extend our project on other divalent transition metals. Since the three **SiO_2+CS LMW**, **$SiO_2(CO_2H)$+CS LMW)**, and **SiO_2+CS(CO_2H)** appeared to be promising adsorbents for the uptake of Cu(II) ions, these three materials were selected to probe their propensities for the uptake of Ni(II) ions. The batch adsorption of Ni(II) on the silica composites were also carried out at room temperature. Again, first the effect of contact time and of the initial solution pH for Ni(II) ions adsorption were investigated, then the equilibrium isotherms and adsorption kinetics were studied. The Ni(II)-loaded silicas (functionalized and/or hybrid) were also characterized using FT-IR, furthermore EDS was used to investigate the adsorption behaviour of $NiSO_4$ on these composites.

B1 Effect of the Solution pH

To study the effect of pH on the effective of adsorption of Ni(II), experiments were conducted in the pH range 3-7, using of adsorbent concentration of 0.4% and a Ni(II) concentration 500 mg/L. Fig. 101 displays the effect of pH on the adsorption of Ni(II) onto 0.4% **$SiO_2(CO_2H)$+CS LMW**. The adsorption capacity increases with increasing the pH of the solution going from pH 3 to 7, the maximum uptake of Ni(II) occurring for **$SiO_2(CO_2H)$+CS LMW** at pH 7. A similar result was obtained for adsorption of Ni(II) on **SiO_2+CS LMW**. Remind that at pH 7, amino groups binding sites are not protonated; therefore the non-bonding electron doublets are fully available to interact with metal cations (see eq. 31-33). An example for the adsorption of various heavy metal ions, among them Ni(II) and Cu(II), by resacetophenone loaded 3-aminopropyltriethoxysilane grafted on silica gel at pH 6-7 is reported by A. Goswami [55].

At pH > 8, the adsorption capacity decreases due to the precipitation of Ni(II) with hydroxide forming [$Ni(OH)_2$] [82-84a]. At an acidic pH, the surface charge on the particles became positive due to protonation, thus inhibiting the binding of the metal cation due to a deactivation and an electrostatic repulsion with the protonated amino group.

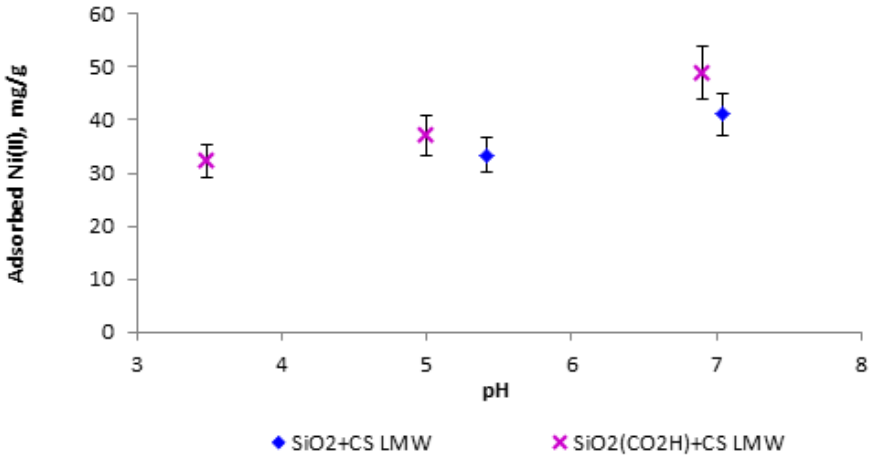

Fig. 101 Effect of initial solution pH for adsorption of Ni(II) (500 mg/L) on 0.4% **SiO_2+CS LMW** and **$SiO_2(CO_2H)$+CS LMW**

B2 Effect of the Initial Concentration of Nickel(II) Solution

The effect of initial concentration of Ni(II) adsorbed onto **SiO_2+CS(CO_2H)** was investigated using various initial concentration of Ni(II) between 50 mg/L and 1.000 mg/L. Fig. 102 shows that the increase of the initial Ni(II) concentration goes in line with an increase of the adsorption capacity of **SiO_2+CS(CO_2H)**. This could be ascribed by the initial concentration providing an important driving force to overcome all mass transfer resistances of Ni(II) ions between the aqueous and solid phase. Therefore, a higher initial Ni(II) concentration could enhance the adsorption process. A similar observation was reported for the adsorption on CS immobilized on bentonite [41a]. At an initial concentration of 50 mg/g and 100 mg/L, the Ni(II) uptake by **SiO_2+CS(CO_2H)** was low (< 5.8 mg/g). Hence, at a higher initial concentration (500 mg/L and 1.000 mg/L), the adsorption capacity of adsorption of Ni(II) on the **SiO_2+CS(CO_2H)** was much higher (81.7 mg/g) than at low Ni(II) concentration. This could be explained as following reasons. Firstly, a higher Ni(II) concentration led to more binding sites on the surface of the **SiO_2+CS(CO_2H)** compared with a lower initial Ni(II) ions concentration for the same adsorbent dosage. Lastly, a higher Ni(II) ions concentration increased driving force to overcome the mass transfer resistance of Ni(II) ions between the aqueous and solid phases [84b]. It could be implied that the **SiO_2+CS(CO_2H)** was favorable to adsorp Ni(II) ions at high concentration.

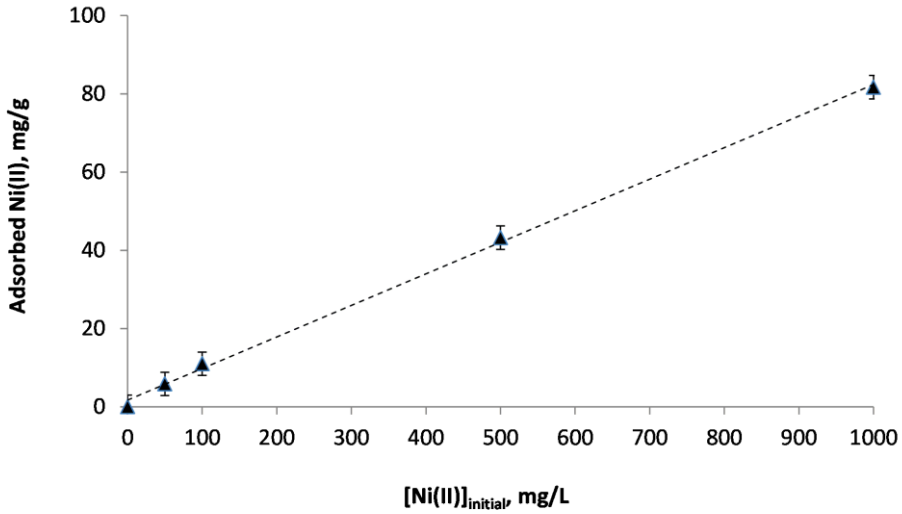

Fig. 102 Effect of the initial Ni(II) concentration on the adsorption onto 0.4% **SiO_2+CS(CO_2H)** (contact time = 24 h, pH 7)

B3 Effect of Contact Time

The effect of contact time on the extent of adsorption was also investigated at room temperature. The adsorption parameters (pH 7, adsorbent dose = 0.4%, and initial concentration of Ni(II), 1.000 mg/L) were fixed. The adsorption of Ni(II) ions by three types of composites was studied in the interval between 0 - 1.440 min.

Fig. 103 shows the influence of the contact time for the Ni(II) adsorption on **SiO_2+CS LMW, SiO_2(CO_2H)+CS LMW** as well as on **SiO_2(CO_2H)**. It is evident that adsorption of Ni(II) ions rapidly occurs onto both **SiO_2+CS LMW** (83.7 mg/g) and **SiO_2(CO_2H)+CS LMW** (87.0 mg/g) as well as on **SiO_2(CO_2H)** (74.5 mg/g) during the first 30 min, then gradually approaches a maximum value and finally attains equilibrium at around 180 min. This result is in accordance with the report of K.A. Krishnan and co-workers where the adsorption of Ni(II) onto activated carbon (sugarcane bagasse pith) attains equilibrium at around 240 min [82]. It was found that the adsorption capacities of Ni(II) onto **SiO_2+CS LMW** and **SiO_2(CO_2H)+CS LMW** materials are quite comparable. However, the content of nickel adsorbed onto **SiO_2+CS LMW** and **SiO_2(CO_2H)+CS LMW** was higher than for **SiO_2(CO_2H)**. The adsorption capacity is strongly related to the binding sites, composed of functional groups such as amino-, hydroxyl- and carboxyl groups cooperating with each other providing an appropriate conformation for chelation of the Ni(II) ion.

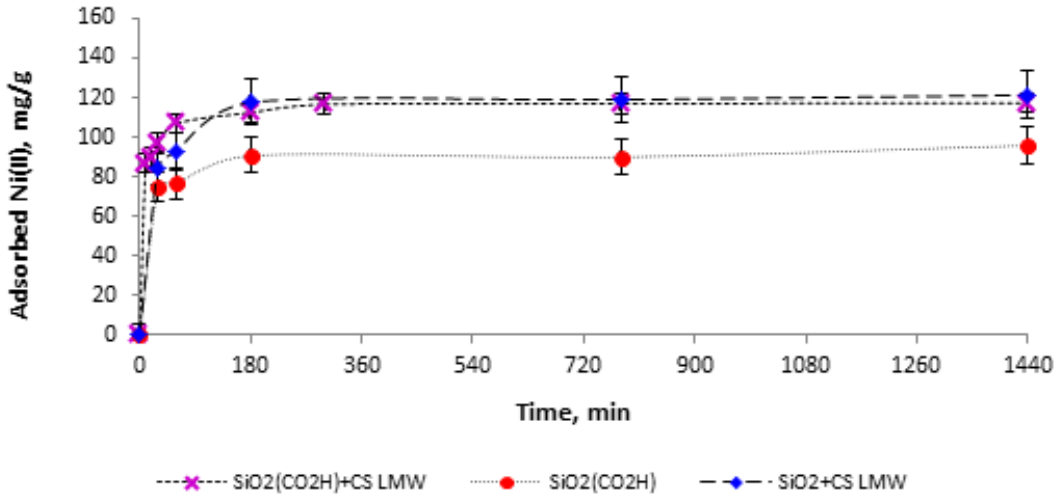

Fig. 103 Effect of contact time for adsorption of Ni(II) (1.000 mg/L) onto **SiO_2+CS LMW**, **$SiO_2(CO_2H)$+CS LMW**, and **$SiO_2(CO_2H)$** at pH 7

B4 Adsorption Isotherm

In order to get a better understanding on the Ni(II) adsorption process, a study of the adsorption equilibrium was undertaken using **SiO_2+CS LMW**, **$SiO_2(CO_2H)$+CS LMW**, and **SiO_2+CS(CO_2H)** as adsorbent, at pH 5 and pH 7 and choosing as 1.440 min as optimum contact time. Four isotherm models (Langmuir, Freundlich, Temkin, and BET) were used in the present study to describe the adsorption data.

It was found that the BET model was not suitable to describe correctly the adsorption of Ni(II) by our materials because all linear regression were lower than 0.8. However, the Langmuir, Freundlich, and Temkin isotherm models provided good fits (see Table 4.16). Fig. 104 - 106 show the isotherm plots between Langmuir isotherms and experimental data for adsorption of Ni(II) onto **SiO_2+CS LMW**, **$SiO_2(CO_2H)$+CS LMW**, and **SiO_2+CS(CO_2H)**, respectively. According to the linear regression (R^2), the plots yield a straighter line in the range between 0.94 - 0.99. Moreover, the chi-square (X^2) values confirm the Langmuir isotherms fitted better to the experimental data than those of the Freundlich isotherms as shown in Table 4.13. The maximum adsorption capacity was calculated utilizing the Langmuir isotherm given in equation 2. The maximum adsorption capacity for Ni(II), based on the Langmuir isotherm model at pH 5, is found to be 104 mg/g, 166 mg/g, and 227 mg/g for **SiO_2+CS LMW**, **$SiO_2(CO_2H)$+CS LMW**, and **SiO_2+CS(CO_2H)**, respectively. However, at pH 7 the adsorption of Ni(II) was superior than at pH 5, where there is a competition between the adsorption of Ni(II) and protonation of amine sites of CS (pKa ~6.3). At pH 7, the maximum adsorption capacity (q_m) for the adsorption of Ni(II) reaches 182 mg/g for

SiO_2+CS LMW, 210 mg/g for **$SiO_2(CO_2H)$+CS LMW**, and 263 mg/g for **SiO_2+$CS(CO_2H)$**. The dimensionless separation factor R_L values for the adsorption of Ni(II) onto our adsorbents at pH 5 and pH 7 are represented in Table 4.14. These R_L values implied that the adsorption of Ni(II) onto the adsorbents was favorable at higher pH.

Table 4.13 Langmuir, Freundlich, and Temkin isotherms for adsorption of Ni(II) onto **SiO_2+CS LMW** and **$SiO_2(CO_2H)$+CS LMW** at pH 5 and pH 7

Isotherm models	Materials	K_L	q_m, mg/g	R^2	X^2
Langmuir	**SiO_2+CS LMW** pH 5	0.4×10^{-3}	104	0.99	1.12
	SiO_2+CS LMW pH 7	3.0×10^{-3}	182	0.96	2.51
	$SiO_2(CO_2H)$+CS LMW pH 5	0.8×10^{-3}	166	0.98	3.07
	$SiO_2(CO_2H)$+CS LMW pH 7	1.1×10^{-3}	210	0.96	5.14
	SiO_2+$CS(CO_2H)$ pH 5	0.7×10^{-3}	227	0.94	2.12
	SiO_2+$CS(CO_2H)$ pH 7	0.5×10^{-3}	263	0.98	2.93
Freundlich	Materials	K_F, mg/g	n	R^2	X^2
	SiO_2+CS LMW pH 5	0.230	1.85	0.99	3.26
	SiO_2+CS LMW pH 7	0.609	3.89	0.99	3.80
Freundlich	Materials	K_F, mg/g	n	R^2	X^2
	$SiO_2(CO_2H)$+CS LMW pH 5	0.493	3.33	0.99	6.99
	$SiO_2(CO_2H)$+CS LMW pH 7	0.452	3.10	0.99	9.32
	SiO_2+$CS(CO_2H)$ pH 5	0.887	1.83	0.96	35.29
	SiO_2+$CS(CO_2H)$ pH 7	0.812	1.80	0.98	35.17
Temkin	Materials	K_T	B_T	R^2	X^2
	SiO_2+CS LMW pH 5	2.57×10^{-3}	243.3	0.99	1.11
	SiO_2+CS LMW pH 7	5.96×10^{-3}	82.9	0.97	1.05
	$SiO_2(CO_2H)$+CS LMW pH 5	2.45×10^{-3}	59.0	0.98	5.22
	$SiO_2(CO_2H)$+CS LMW pH 7	2.79×10^{-3}	91.2	0.99	6.49
	SiO_2+$CS(CO_2H)$ pH 5	3.47×10^{-2}	12.9	0.81	44.64
	SiO_2+$CS(CO_2H)$ pH 7	2.67×10^{-2}	14.1	0.95	42.93

Table 4.14 R_L values based on Langmuir isotherms at 1000 and 3000 mg/L

$[Cu^{2+}]_{Initial}$, mg/L	**SiO_2+CS LMW**		**$SiO_2(CO_2H)$+CS LMW**		**SiO_2+$CS(CO_2H)$**	
	pH 5	pH 7	pH 5	pH 7	pH 5	pH 7
1000	0.714	0.250	0.555	0.476	0.546	0.628
3000	0.454	0.100	0.294	0.232	0.286	0.360

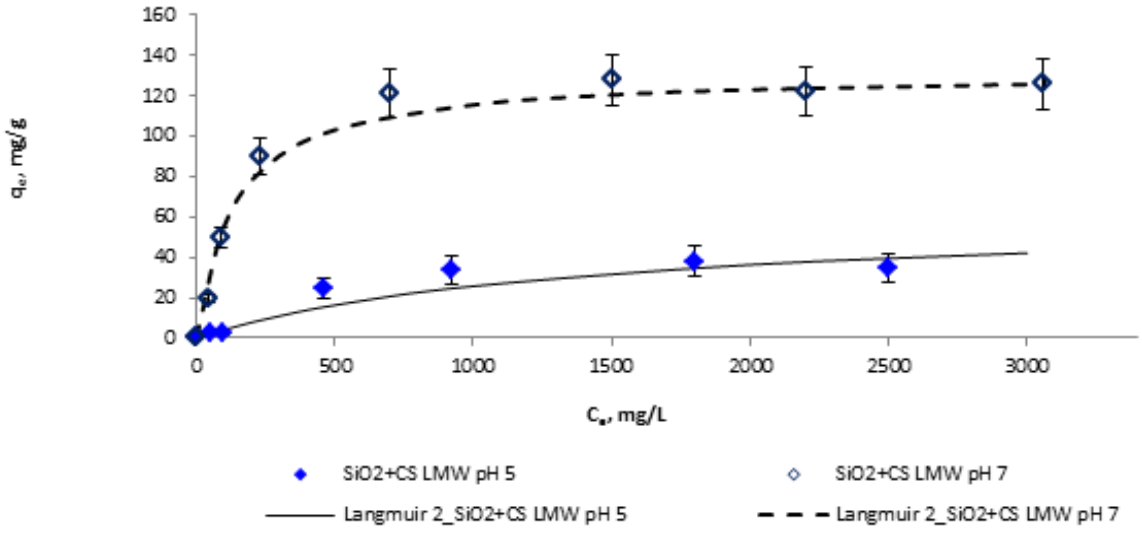

Fig. 104 Comparison between experimental adsorption data and Langmuir isotherms for Ni(II) onto 0.4% **SiO_2+CS LMW** at pH 5 and pH 7

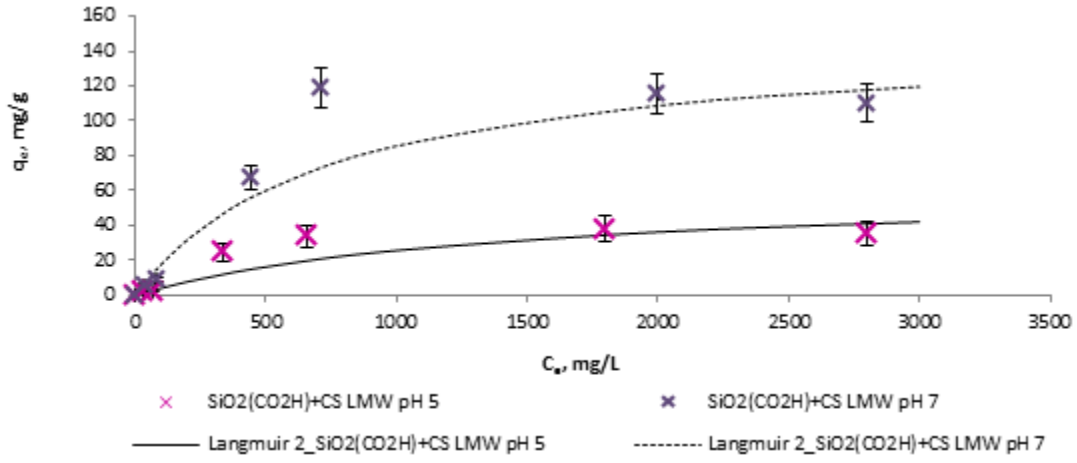

Fig. 105 Comparison between experimental data and Langmuir isotherms for Ni(II) adsorption onto 0.4% **$SiO_2(CO_2H)$+CS LMW**

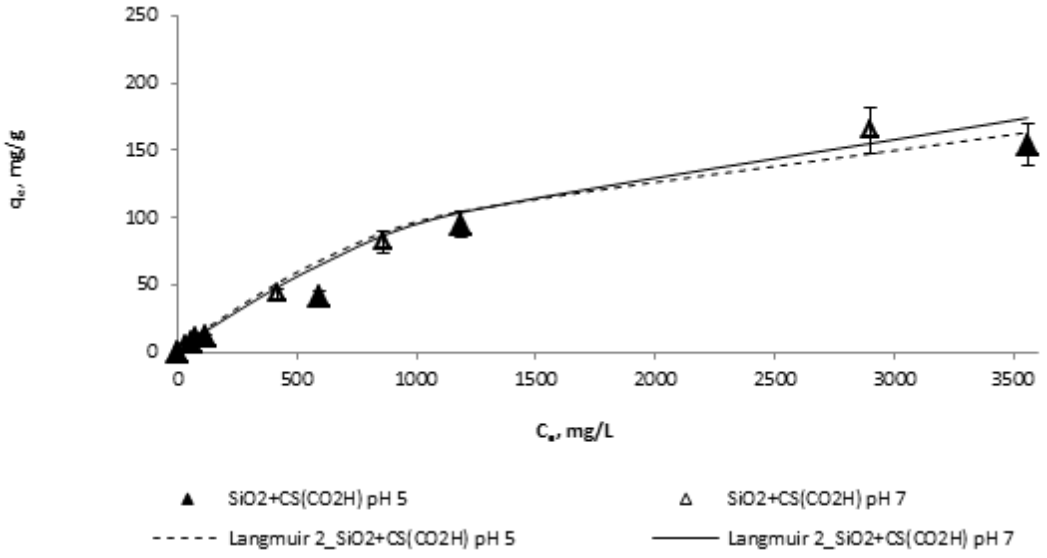

Fig. 106 Comparison between experimental data and Langmuir isotherms for Ni(II) adsorption onto 0.4% **SiO_2+CS(CO_2H)** at pH 5 and pH 7.

According to the Freundlich isotherm model, values of n > 1 represent favourable adsorption conditions. As shown in Table 4.13, the n values for **SiO_2+CS LMW** at pH 7 and both **SiO_2(CO_2H)+CS LMW** types at pH 5 and pH 7 were between 3.10-3.89. It can be implied that adsorption conditions of Ni(II) by **SiO_2+CS LMW** at pH 7 and **SiO_2(CO_2H)** at both pH 5 and pH 7 are more favourable than for **SiO_2+CS LMW** at pH 5 (n = 1.85) and for **SiO_2+CS(CO_2H)** at both pH 5 (n = 1.83) and pH 7 (n = 1.80).

The adsorption of Ni(II) exhibited a good fit with the Temkin isotherm, that describes chemisorption of Ni(II) on the composites. The K_T is the equilibrium binding constant corresponding to the maximum binding energy. The K_T values of the adsorption of Ni(II) onto the adsorbents were between 2.45 x 10^{-3} L/mg and 5.96 x 10^{-3} L/mg. The chemisorption can be represented by the B_T value, which indicates the heat of adsorption. The B_T values for **SiO_2+CS LMW** and **SiO_2(CO_2H)+CS LMW** were in the range between 59.0 J/mol and 243.3 J/mol. In contrast, the B_T value of **SiO_2+CS(CO_2H)** were only 12.9 J/mol at pH 5 and 14.2 J/mol at pH 7, being inferior than that of unmodified CS-coated silica. According to the R^2 values of **SiO_2+CS(CO_2H)** (Table 4.13), the Temkin isotherm does not provides a better fit compared to the Langmuir isotherm.

Moreover, the X^2 value was also used to interpret the adsorption data. For the adsorption of nickel onto **SiO_2+CS LMW**, **SiO_2(CO_2H)+CS LMW** as well as on **SiO_2+CS(CO_2H)**, the adsorption fitted well with the Langmuir isotherm with a low X^2 value of as seen in Table 4.13. Based on the Langmuir isotherm, the maximum adsorption capacity q_m for Ni(II)

adsorbed on the adsorbents at pH 7 was found to be 182 mg/g for **SiO_2+CS LMW**, 210 mg/g for **$SiO_2(CO_2H)$+CS LMW**, and 263 mg/g for **SiO_2+CS (CO_2H)**. The modified silica composites (**SiO_2+CS LMW**, **$SiO_2(CO_2H)$+CS LMW**, and **SiO_2+CS (CO_2H)**) showed an quite satisfying effectiveness to capture of Ni(II) in batch aqueous solution at pH 5 and 7 as seen in Fig. 107a. For comparison, the maximum Ni(II) adsorption capacities of three types of CS-coated silica materials with other adsorbents described in the literature are shown in Fig. 107b.

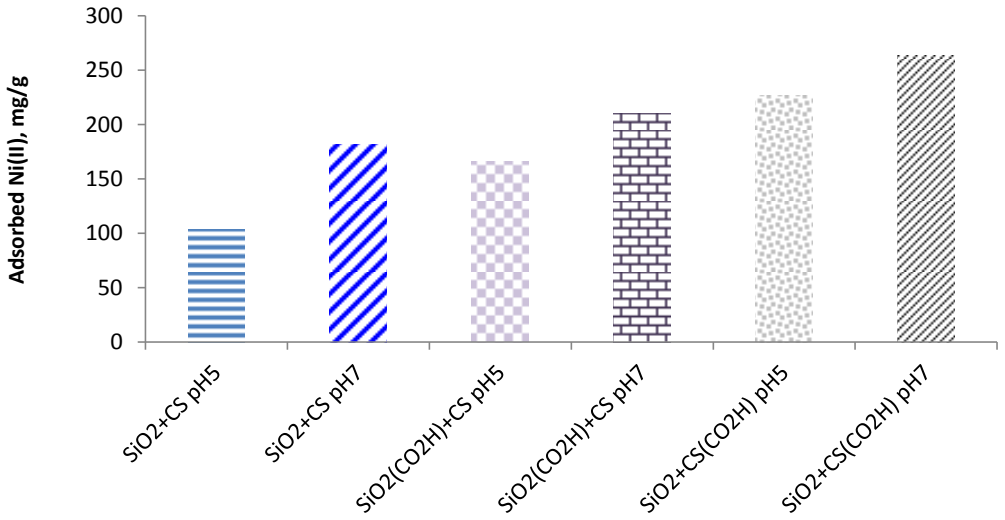

Fig. 107a Maximum Ni(II) adsorption capacities of six types of CS-coated silica materials at pH 5 and pH 7

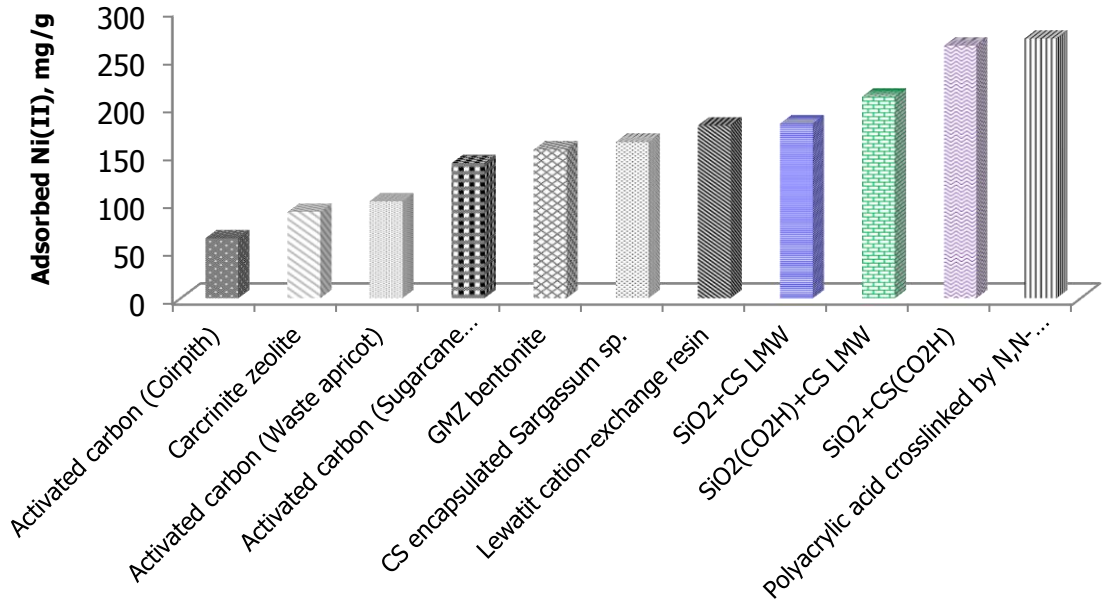

Fig. 107b Comparison of the maximum Ni(II) adsorption capacities of three types of CS-coated silica materials with some other adsorbents described in the literature

B5 Adsorption Kinetics

Experiments were carried out for Ni(II) different concentrations and contact times (min). Each experiment was repeated twice under identical conditions. The pseudo-first-order, pseudo-second-order, intraparticle diffusion, and Elovich constants values are given in Tables 4.15-4.16. The kinetic curve of Ni(II) ions reveals that the adsorption was initially rapid. In order to evaluate the kinetic mechanism controlling the adsorption process, pseudo-second-order kinetics was employed to interpret the experimental data. Fig. 108-110 and Table 4.15 indicate that based on the obtained correlation coefficients (R^2), the pseudo-second-order equation was the model that provided the best fit for the experimental kinetic data. The R^2 values for the pseudo-second-order plot were found to be 0.99 for all the three types of modified silica materials suggesting chemical sorption as the rate-limiting step of the adsorption mechanism and excluding involvement of a mass transfer in solution. Similarly, K.A. Krishnan and co-workers reported that the adsorption of Ni(II) onto activated carbon (sugarcane bagasse pith) best fits for the experimental kinetic data with a k_2 value in the range between 1.6457 $x10^{-3}$ min^{-1} to 9.1386 $x10^{-3}$ min^{-1} [82].

For kinetics, the lower case "k_1 and k_2" are used to study the rate constant and they give definite equilibrium established between the two phases (the adsorption rate of Ni(II) ions at the solid solution interface onto four CS-coated silica materials). Both the pseudo-first and pseudo-second order models could not explain the diffusion mechanism; therefor the kinetic results were interpreted using the intraparticle diffusion equation. The k_{int} is the intraparticle diffusion rate constant (mg/g $min^{1/2}$). Table 4.16 presents the intraparticle diffusion constants for Ni(II) adsorption on **SiO_2+CS LMW**, **$SiO_2(CO_2H)$+CS LMW**, and **SiO_2+CS(CO_2H)**. The plot for the obtained data yielded a straight-line plot. Therefore, we can conclude that the adsorption matches to intraparticle diffusion. The rate constant (Table 4.18), k_{int}, was 35.7 mg/g $min^{1/2}$ and 18.1 mg/g $min^{1/2}$ for **SiO_2+CS LMW** and **$SiO_2(CO_2H)$+CS LMW**, respectively. In addition, the k_{int} of adsorption of Ni(II) on *Thuja orientalis* (cone biomass) found to be 11.55 mg/g $min^{1/2}$ (Initial Ni(II) concentration = 400 mg/L) [85] which closed to that of our material (**$SiO_2(CO_2H)$+CS LMW**, k_{int} = 18.1 mg/g $min^{1/2}$, Initial Ni(II) concentration = 500 mg/L).

Elovich equation is also used to interpret the experimental data. For **SiO_2+CS LMW** and **$SiO_2(CO_2H)$+CS LMW**, the R^2 values for the Elovich equation plot were in the range between 0.93-0.97 suggesting the sorption process fitted to Elovich equation (see Table 4.16). This confirmed that the adsorption of Ni(II) onto **SiO_2+CS LMW** and **$SiO_2(CO_2H)$+CS**

LMW was chemical adsorption. However, for **SiO_2+CS(CO_2H)**, based on the R^2 values which were lower than 0.70 suggesting that both intraparticle diffusion and Elovich were not suitable to describe the adsorption of Ni(II) onto this type of carboxymethyl CS-coated silica material.

Table 4.15 Pseudo-first-order, and pseudo-second-order constant for adsorption of Ni(II)

Materials	Pseudo-first-order			Pseudo-second-order		
	k_1, 1/min	q_e, mg/g	R^2	k_2, g/mg .min	q_e, mg/g	R^2
SiO_2+CS LMW	2.53×10^{-3}	14.92	0.97	1.87×10^{-3}	37.6	0.99
SiO_2(CO_2H)+CS LMW	5.98×10^{-3}	20.12	0.93	0.94×10^{-3}	48.78	0.99
SiO_2+CS(CO_2H)	0.23×10^{-3}	12.95	0.91	2.61×10^{-3}	34.4	0.99

Table 4.16 Intraparticle diffusion and Elovich parameters for the Ni(II) adsorption

Materials	Intraparticle diffusion			Elovich		
	k_{int}, mg/g $min^{1/2}$	C	R^2	α, (mg/g min)	β, mg/g	R^2
SiO_2+CS LMW	35.7	1.55	0.94	0.081	0.03	0.97
SiO_2(CO_2H)+CS LMW	18.1	1.26	1.00	0.177	0.06	0.93
SiO_2+CS(CO_2H)	22.7	1.36	0.65	0.127	0.05	0.64

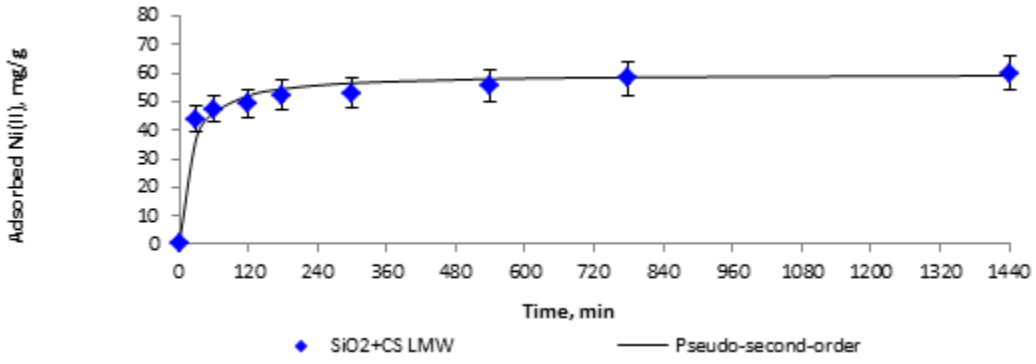

Fig. 108 Pseudo-second-order plot of Ni(II) adsorption onto **SiO_2+CS LMW**

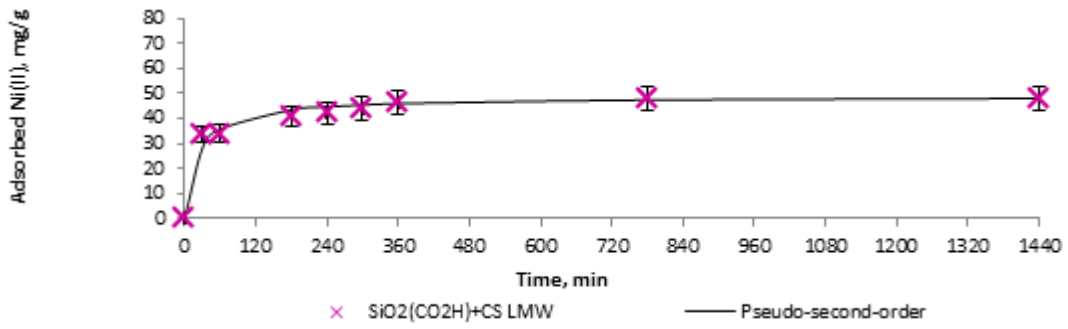

Fig. 109 Pseudo-second-order plot of Ni(II) adsorption onto **SiO_2(CO_2H)+CS LMW**

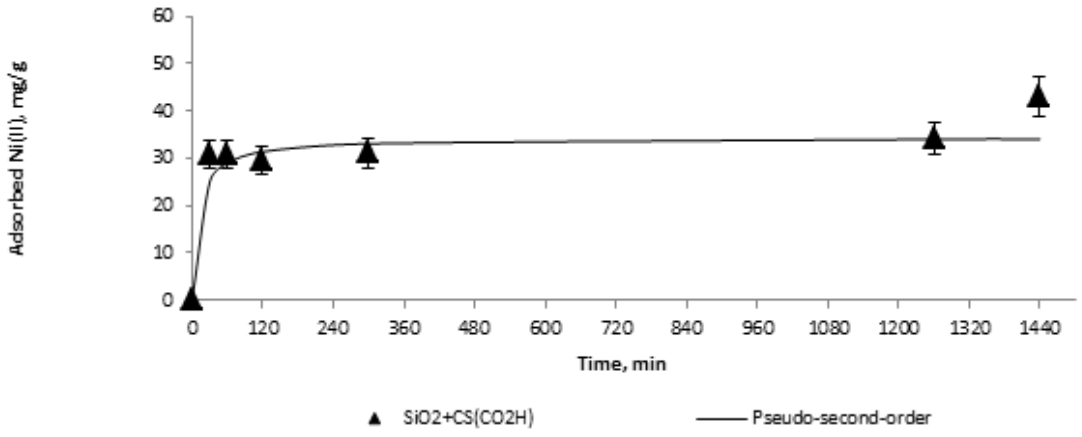

Fig. 110 Pseudo-second-order plot of Ni(II) adsorption onto **SiO_2+CS(CO_2H)**

B6 Characterization of Ni(II)-loaded Composites

B6.1 FT-IR Spectra of Ni(II)-loaded SiO_2+CS LMW and SiO_2(CO_2H)+CS LMW Hybrid Composites

The FT-IR spectra of the Ni(II)-loaded **SiO_2+CS LMW**, **SiO_2(CO_2H)+CS LMW**, and **SiO_2+CS (CO_2H)** composites are illustrated in Fig. 111-113 and Table 4.17. The FT-IR spectrum of Ni(II)-loaded **SiO_2+CS LMW** reveals a shift in intensity and position compared to neat **SiO_2+CS LMW**: the band at 1652 cm^{-1} (C=O stretching vibration for amide I) is shifted to 1660 cm^{-1}. The band at 1565 cm^{-1} (N-H bending of amine group) did not appear [79c]. The band at 3448 cm^{-1} (a characteristic -OH stretching vibration overlaping the -NH stretching vibration for amine groups) is shifted to 3405 cm^{-1} and the –C=O stretching vibration at 1099 cm^{-1} (in -COH) shifts to 1066 cm^{-1}. A similarly result was also observed for Ni(II)-loaded **SiO_2(CO_2H)+CS LMW**. Fig. 112 shows the FT-IR spectrum of Ni(II) loaded **SiO_2(CO_2H)+CS LMW**, revealing a shift of the absorption bands at 3444 cm^{-1} to 3456 cm^{-1} and and a shift of the -C=O stretching vibration (in -COH) from 1080 cm^{-1} to 1024 cm^{-1}.

Fig. 112 shows the FT-IR spectrum of different concentration of Ni(II)-loaded **SiO_2+CS(CO_2H)**. One notes that the absorption bands at 3456 cm^{-1} and 1650 cm^{-1} shift to 3446 cm^{-1} and 1639 cm^{-1}, respectively. The band at 1427 cm^{-1} (CO_2^- symmetric vibration in carboxylic acid) was not detected. The adsorption intensity increased when increasing in Ni(II) concentration (50-1.000 mg/L). The spectral changes are most probably due to the complexation of Ni(II) ion by the -NH_2, -OH, and -SiO sites of **SiO_2+CS LMW**. In the case

of **$SiO_2(CO_2H)$+CS LMW** and **SiO_2+CS(CO_2H)**, -OH, -NH_2 and -CO_2H functions are interacting with the Ni(II) ion.

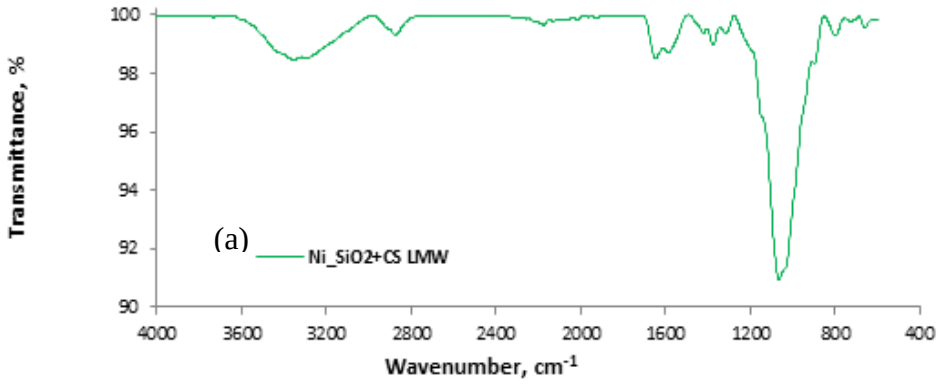

Fig. 111 FT-IR of Ni(II) loaded **SiO_2+CS LMW**

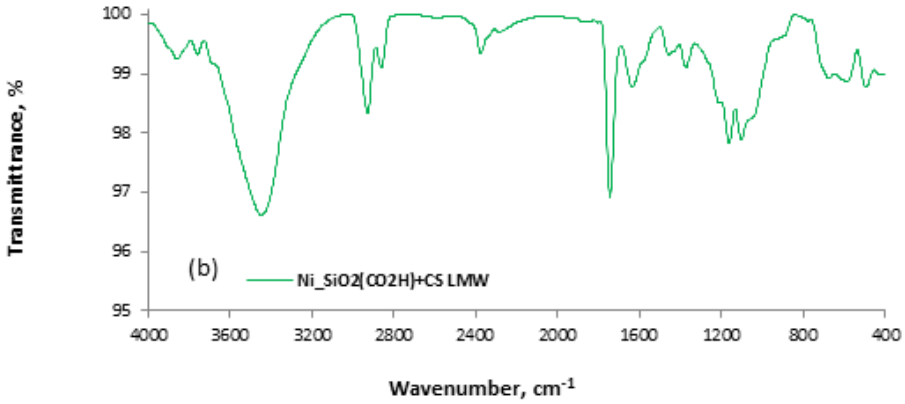

Fig. 112 FT-IR of Ni(II)-loaded **$SiO_2(CO_2H)$+CS LMW**

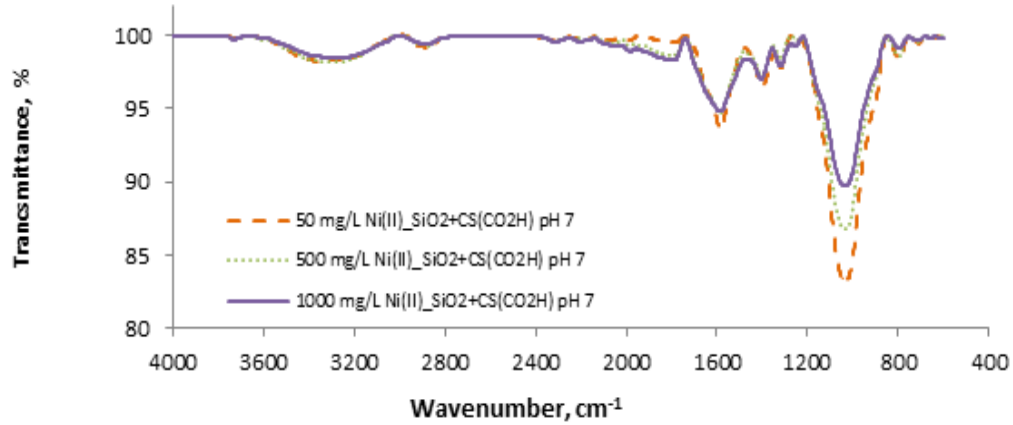

Fig. 113 FT-IR of **SiO_2+CS(CO_2H)** loaded with different Ni(II) concentration at pH 7

Table 4.17 IR analysis of the CS-coated silica hybrid - metal complex

Functional groups	Frequency, cm^{-1}					
	SiO_2 + CS LMW	**SiO_2 + CS LMW - Ni**	**SiO_2 + $CS(CO_2H)$**	**SiO_2 + $CS(CO_2H)$ - Ni**	**$SiO_2(CO_2H)$ + CS LMW**	**$SiO_2(CO_2H)$ + CS LMW - Ni**
Siloxane (from silica)	1099	1066	1083	1101	1080	1024
$-COO^-$ symmetric vibration (carboxylic acid)	-	-	1427	-	1423	1429
$-COO^-$ asymmetric vibration (carboxylic acid)	-	-	1639	1639	1656	1647
Carbonyl (residual amide in CS)	1652	1660	-	-	-	-
-OH (silanols from silica or hydroxyl groups onto CS)	3448	3405	3456	3446	3444	3456

B6.2 Energy Dispersive Spectroscopy

The Ni(II)-loaded modified silica materials were furthermore analyzed by EDS. Fig. 114 displays the EDS spectrum of the nickel-loaded **$SiO_2(CO_2H)$+CS LMW** hybrid composite. The Y-axis shows the counts (number of X-rays received and processed by detector). The X-axis shows the energy level of those counts (KeV and y-exist as counts). Five points on each composite were measured. The averaged value of the nickel content adsorbed on **$SiO_2(CO_2H)$+CS LMW** hybrid composite is given in Table 4.18. It was found that the Ni(II) ion seems to be homogeneously adsorbed on the **$SiO_2(CO_2H)$+CS LMW**.

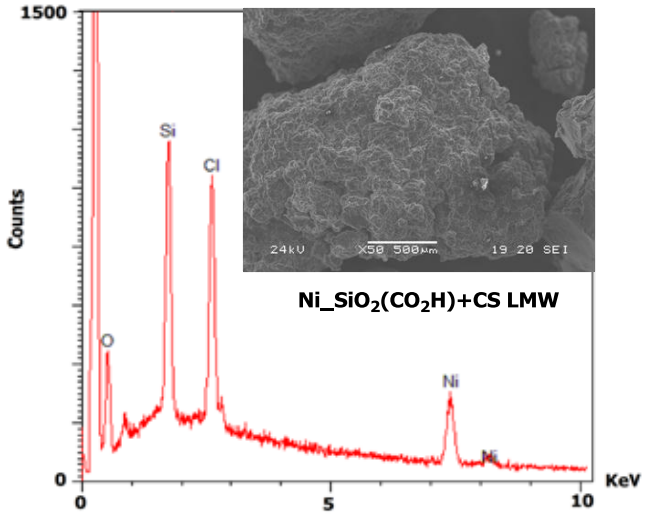

Fig. 114 SEM image and corresponding EDS spectra for the nickel loaded CS-silica hybrid particles : Ni(II) loaded **$SiO_2(CO_2H)$+CS LMW**

Table 4.18 The percentage of nickel content of three points of the hybrid composite

Material	%Nickel					
	1	2	3	4	5	Average
$SiO_2(CO_2H)$+CS LMW	19.6	22.4	24.5	18.8	18.4	20.8±2.6

B7 Interaction of Nickel(II) with CS

From the FT-IR data, an interaction between the biopolymer-coated silica hybrid composites (CS-coated silica) and Ni(II) ions via both -NH_2 and -OH groups was evidenced. The structure of the supposed complex is shown in Fig. 115. The CS chelates the nickel ions by electron-dononation from both oxygen and nitrogen atoms [86]. Note that from a molecular point of view, the interaction between divalent metal ions and the amino residues of CS has been the object of several studies supported by IR, UV-vis, ESR, and XPS techniques and modeling [55, 87-88]. Therefore, it is reasonable to assume that formation of classical surface-bound "Werner-type" coordination complexes, with the high-spin Nickel d^8 ion ligated in an octahedral environment consisting of chelating NH_2 and H_2O molecules, occurs also on the surface of our composites.

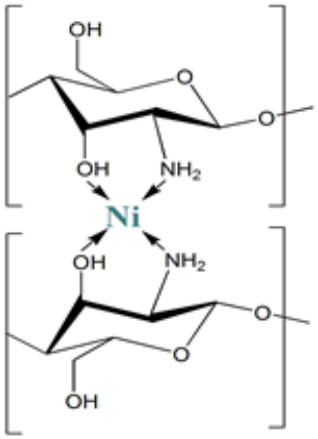

Fig. 115 Complexation between Ni(II) ions and CS-coated silica material [86]

J.W. Bunting, and K.M. Thong reported on the investigation of the stability constant of 1:1 metal-carboxylate complexes determined by potentiometric titration. Stability constant (log *K*) for 1:1 complexes of divalent metal ions and carboxylate anions are shown in Table 4.19 [89]. The concentration of free metal ion [M^{n+}], free carboxylate anion [L^-] and 1:1 metal-ligand complex [ML^+], were calculated from equations for the total concentration of ligand-containing species, electroneutrality and the dissociation constant of the carboxylic acid. The value of stability constant for a 1:1 complex can be calculated using equation 35.

$$K = \frac{[ML^+]}{[M^{2+}][L^-]} \qquad (35)$$

From the log K values, the stabilities of the metal complexes follow the order $Cu^{2+} > Ni^{2+}$, consistent with the Irving-Williams order. The order of log K values for a particular metal ion with the carboxylate anions is the same as the order for the basicities of these anions [89].

Table 4.19 The log K values for 1:1 metal-carboxylate complexes*

Metal ion	Acetic acid	Benzoic acid	Formic acid	Chloroacetic acid
Cu(II)	1.76 ± 0.06	1.51 ± 0.03	1.38 ± 0.03	1.07 ± 0.02
Ni(II)	0.72 ± 0.05	0.55 ± 0.04	0.67 ± 0.02	0.23 ± 0.07

*At 30 ^oC, ionic strength 0.4 mol/L

Table 4.20 Some maximum adsorption capacities of Ni(II) by various adsorbents

Materials	Maximum capacity, mg/g	pH	Reference
Nano crystalline Hydroxyapatite	2.278	6.6	[90a]
Modified oak sawdust	3.29	8	[90b]
Pine bark	6.28	-	[91]
Azadirachtaindica leaf powder	9.1	5.6	[92]
Tamarind (*Tamarindus indica* L.) Bark	15.34	7	[93a]
Askari grape dust	23.923	5	[93b]
Moringa oleifera bark	30.38	6	[94a]
Meranti sawdust	35.971	6	[94b]
Papaya seeds (powder)	40.22	3	[94c]
PEI modified biomass	55	5.5	[95a]
Orange peel	62.89	5	[95b]
Activated carbon (palm shell)	0.130	5	[96a]
Activated Carbon (Algae Marine *Gracilaria*)	2.686	5	[96b]
Activated Carbon (*Cajanus cajan L* Milsp seed shell)	29.60	5	[96c]
Irradiation-grafted activated carbon	55.7	7.7	[96d]
Activated carbon (coirpith)	62.5	5	[96e]
Activated carbon (waste apricot)	101.01	5	[97]
Activated carbon	140.85	6	[85]
Ni(II)-imprinted amino-functionalized silica gel	12.61	8	[98]
Resacetophenone loaded 3-aminopropyltriethoxysilane (APTES)-silica gel	14.89	6-7	[55]
Silica-gel-immobilized *P. vulgaris*	98.01	6.5	[99]

Macroporous CS	5.21	5	[79c]
Materials	Maximum capacity, mg/g	pH	Reference
Thiourea-modified magnetic CS	15.3	4-5	[100]
Modified magnetic CS chelating resin	40.15	7	[101]
Histidine modified CS	55.6	5	[84b]
Cross-linked magnetic chitosan-2-aminopyridine glyoxal Schiff's base	67 ± 2	5	[66]
CS encapsulated *Sargassum* sp.	163	7	[102]
4-amino-3-hydroxy benzoic acid functionalized cross linked Chitosan	96.16	7	[103]
DTPA-modified chitosan	53.1	2.1	[104]
EDTA-modified chitosan	71	2.1	[104]
Hydroxyapatite/CS	8.54	6	[105]
Calcined Bofe bentonite clay	1.91	5.3	[106a]
Zeolite X	52	4.6	[106b]
Carcrinite zeolite	89.9	6	[106c]
CS coated perlite beads	56	5	[107]
CS coated PVC	120	5	[55]
Activated carbon (sugarcane bagasse pith)	140.85	4	[108]
GMZ bentonite	155	5.4	[109]
Non-functionalized activated carbon	44	-	[110]
Polyacrylic acid crosslinked by N,N'-methylenebisacrylamide/montmorillonite	270.3	neutral	[80c]
silica gel immobilized waste biomass	98.01	-	[111]
CS/clinoptiolite	247	5	[112]
Lewatit cation-exchange resin	179.94	6	[113]
SiO_2+CS LMW	104	5	Present work
SiO_2+CS LMW	182	7	Present work
$SiO_2(CO_2H)$+CS LMW	166	5	Present work
$SiO_2(CO_2H)$+CS LMW	210	7	Present work
SiO_2+CS(CO_2H)	227	5	Present work
SiO_2+CS(CO_2H)	263	7	Present work

Numerous studies have been reported on the adsorption of Ni(II) using various types of adsorbents. Table 4.20 presents a comparison of the maximum adsorption capacity for some selected materials. From the literature, the adsorption of Ni(II) was found to be 2.3 mg/g for nano-crystalline hydroxyapatite, 3.3-62.9 mg/g for biomass and/or modified biomass [90a,b-95a,b], 0.13 mg/g for activated carbon (palm shell), 2.7 mg/g for activated carbon (Algae Marine *Gracilaria*), 29.60 mg/g for activated Carbon (*Cajanus cajan L* Milsp seed shell), 55.7 mg/g for irradiation-grafted activated carbon, 62.5 mg/g for activated carbon

(coirpith), 101.01 mg/g for activated carbon (waste apricot), 140.9 mg/g for Activated carbon [82, 84, 96a,b,c,d,e-97], between 12.61-98.01 mg/g for modified silica [55, 98-99], 5.21 mg/g for macroporous CS [79c], 15.3-163 mg/g for modified CS [84b, 100-104], 8.54 mg/g for hydroxyapatite/CS [105], 1.91 mg/g for Calcined Bofe bentonite clay [106a], 52 mg/g for zeolite X [106b], and 89.9 mg/g for Carcrinite zeolite [106c]. Comparison under similar conditions (pH ~5), q_{max} for adsorption of Ni(II) was found to be 56 mg/g for CS coated perlite beads [107], 101.0 mg/g for activated carbon (waste apricot) [97], 120 mg/g for CS coated PVC [55], 140.9 mg/g for activated carbon (sugarcane bagasse pith), 155 mg/g for GMZ bentonite [108-109], and 247 mg/g for CS-clinoptilolite [112]. At pH ~7, the adsorption was found as 163 mg/g on CS-encapsulated *Sargassum* sp [102]. Examples of non-functionalized activated carbon (44.0 mg/g) [110], silica gel immobilized waste biomass (98.01 mg/g) (*Phaseolus vulgaris* L.) [111], and Lewatit cation-exchange resin was found to be 179.9 (pH 6) [113].

When comparing the adsorption of Cu(II) and Ni(II) (500 mg/L) onto **SiO_2+CS LMW** at pH 5, it was found that **SiO_2+CS LMW** binds stronger with Cu(II) (256.4 mg/g) than with Ni(II) (104 mg/g). The same trend was noticed for a cross-linked magnetic chitosan-2-aminopyridine glyoxal Schiff's base resin, which adsorbed Cu(II) (124±1 mg/g) better than Ni(II) (67±2 mg/g) [101]. A similarly observation was reported by A.H. Chen and co-workers who found that the affinity order of glutaraldehyde-crosslinked chitosan is Cu(II) > Ni(II) [114]. In order to find a correlation between the metal ion uptake and metal ion properties, several parameters have to be considered such as the electronegativity of the metal ion, electrostatic attraction due to charge to radius ratio, hydroxo complex formation abilities and preferred adsorption site on the adsorbent are responsible for the preferential adsorption of one metal ion over other [115]. Considering the metal ions electronegativity* of Sanderson as shown in Table 4.21, the adsorption selectivity of metal ions in the present study may tentatively correlated with the latter being Cu(II) (1.98) > Ni(II) (1.94).

*Electronegativity is a chemical property which describes the tendency of an atom or a functional group to attract electrons towards itself.

Table 4.21 Different models for electronegativity values of copper and nickel

Electronegativity	Value in Pauling units	
	Copper	Nickel
Sanderson electronegativity	1.98	1.94
Pauling electronegativity	1.90	1.91

Electronegativity	Value in Pauling units	
	Copper	Nickel
Mulliken electronegativity	1.49	1.75
Allred-Rochow electronegativity	1.75	1.75
Allen electronegativity	1.85	1.88

However, the electronegativity scale developed by Linus Pauling attributes to nickel a value of 1.91 and 1.90 for copper **(**on a scale running from about 0.7 (an estimate for francium) to 2.20 (for hydrogen) to 3.98 for fluorine). Electronegativity has no units but "Pauling units" are often used when indicating values mapped on to the Pauling scale

Therefore, the fixation trend of metal ions on CS-coated silica materials Cu(II) > Ni (II) is not readily explained using solely the electronegativity as argument. However, the well-established Irwing-Williams Series (Mn(II) < Fe(II) < Co(II) < Ni(II) < Cu(II) > Zn(II), [47]) supports the higer affinity for the binding of Cu(II) with respect to Ni(II) ions on our novel materials. Note also that the ionic radii for Cu(II) and Ni(II) ions are 0.71 and 0.72 Å, respectively.

Of course a more detailed analysis on the different binding abilities of divalent transition metal ions with hard nitrogen and oxygen donors would require a more profound discussion of the crystal field theory (the crystal field of Cu(II) is weaker than that of Ni(II), however octahedral Cu(II) complexes are subjected to the Jahn-Teller effect affording an extra stability), Pearson's **H**ard and **S**oft **A**cids and **B**ases (HSAB) concept (http://en.wikipedia.org/wiki/HSAB_theory)* and a Frontier orbital analysis of the interaction between the HOMO of the ligand and the LUMO of the metal center. However, these approaches are beyond the scope of this PhD manuscript and are therefore not further developed.

*According the HSAB concept, Cu(II) and Ni(II) ions are considered as border line cases between hard and soft lewis acids; H_2O, carboylate, ROH and RNH_2 as hard Lewis bases.

Conclusion

In this chapter, the capacity and aptitude of functionalized silica particles of type **$SiO_2(NH_2)$** and in particular those of the chitosan-coated composites **SiO_2+CS LMW**, **SiO_2+CS Marine**, and **SiO_2+CS Yuhuan** for the adsorption of Cu(II) from aqueous solution

has been probed. The adsorption kinetics were evaluated using pseudo-first-order and pseudo-second-order models; it was found that pseudo-second-order kinetics describe the Cu(II) adsorption in a very satisfying manner. Another important finding is the fact that the Langmuir isotherm model fits well with the adsorption studies, suggesting that the adsorbed Cu(II) ions form a monolayer on the adsorbent surface. Based on the Langmuir isotherms, the maximum adsorption capacities were found to be 256.4 mg/g, 140.8 mg/g, 109.9 mg/g, 232.6 mg/g, 270.3 mg/g, and 333.3 mg/g for **SiO_2+CS LMW**, **SiO_2+CS Yuhuan**, **SiO_2+CS Marine**, **$SiO_2(CO_2H)$+CS LMW**, **$SiO_2(NH_2)$+CS LMW**, and **SiO_2+CS(CO_2H)**, respectively. The comparison between different types of CS-coated silica materials, (CS LMW, CS Yuhuan, and CS Marine) reveals that the percentage of adsorbed Cu(II) is correlated with the %DD of CS and increases in the following order:

CS LMW (DD 77 %) > **CS Yuhuan** (DD 75%) > **CS Marine** (DD 73%)

The carboxymethyl CS-coated silica material **SiO_2+CS$(CO_2H$** exhibits a very high adsorption capacity for Cu(II) superior to that of the CS-coated grafted/non-grafted silica materials **$SiO_2(NH_2)$+CS LMW**, **$SiO_2(CO_2H)$+CS LMW**, and **SiO_2+CS LMW**. This observation is tentatively rationalized by the presence of active functional groups ($-CO_2H$ / $-CO_2^-$) on CS, which act as binding sites with a high affinity towards Cu(II) ions [116]. Furthermore, the impact of the nature of the counter ion on the capacity for Cu(II) adsorption onto **SiO_2+CS LMW** was evidenced by a comparative study using $CuSO_4$ and $Cu(NO_3)_2$ solutions. This work shows that under analogous conditions, the adsorption capacity of **SiO_2+CS LMW** for $CuSO_4$ is superior to that $Cu(NO_3)_2$. The Cu(II) adsorption from $Cu(NO_3)_2$ solution also fitted well with the Langmuir isotherm; the maximum adsorption capacity being 196.1 mg/g.

The adsorption of Ni(II was investigated at room temperature using the organo-mineral composites **$SiO_2(CO_2H)$**, **SiO_2+CS LMW**, and **$SiO_2(CO_2H)$+CS LMW**). Again the Langmuir isotherm provided a good fit. Other parameters such as the initial nickel salt concentration, contact time and the pH of the reaction medium have been evaluated. Concerning the pH, the maximum adsorption capacity for Ni(II) on the adsorbent was reached at pH 7 and found to be 189 mg/g for **SiO_2+CS LMW**, 210 mg/g for **$SiO_2(CO_2H)$+CS LMW**, and 263 mg/g for **SiO_2+CS(CO_2H)**, respectively.

Both Cu(II) and Ni(II)-loaded materials were also characterized by IR and EDS spectroscopy as well as by SEM microscopy. A critical comparison with the adsorption capacities of numerous other sorbents described by other research groups reveals that our composites rank among the most efficient materials for this purpose. These “proof of

concept" studies demonstrate the feasibility and promising potential our strategy using chemically modified SiO_2 particles in the domain of wastewater depollution.

Experimental Part

Application of Composites by Retention of Metallic Micropollutants

Chemicals and Apparatus

Analytical grade Copper(II) nitrate and Copper(II) sulphate pentahydrate were purchased from Prolabo, Belgium, analytical grade Nickel(II) chloride was purchased from Merck, Germany. The stock solutions were prepared freshly for each experiment. The pH of the experimental solution was adjusted by adding 0.1 M NaOH or 0.1 M HCl solution. All solutions were prepared using deionized water (DI), 18.2 MΩ.cm, Millipore Milli-Q RO. After equilibrium, the residual aqueous-phase metal solution was analyzed with Atomic Absorption Spectroscopy (AAS, 50B spectra, Varian, USA). Fourier Transform Infrared Spectroscopy (FT-IR spectroscopy, VERTEX 70 Spectrometer equipped with a DTGS detector, BRUKER) was used to characterize the metal-load composites. The Energy Dispersive Spectroscopy analysis of the composites was carried out at the *Centre de Microscopie Electronique*, Université de Franche-Comté.

Adsorption Procedure for Cu(II)

An adsorbate stock solution of 3.000 mg/L of $CuSO_4.5H_2O$ (or $Cu(NO_3)_2.3H_2O$) was prepared in DI water. This stock solution was diluted to the required concentration between 50 mg/L and 1.000 mg/L of Cu(II). Batch adsorption experimental studies were carried out at room temperature with a known initial concentration of Cu(II) ions and an amount of the silica based composites (**$SiO_2(NH_2)$**, **SiO_2+CS Marine**, **SiO_2+CS LMW**, and **SiO_2+CS Yuhuan**) was added. The pH of the suspended aqueous solutions were adjusted with 0.1 M HCl or 0.1 M NaOH. After attaining equilibrium, the adsorbents were centrifuged and the residual aqueous-phase concentration of metal was analyzed by AAS.

To determine the equilibrium isotherm, a series of Cu(II) solutions at pH 5 with initial concentration ranges between 50 - 1.000 mg/L were prepared. The maximum total time of an

experiment was 1.440 minutes. The maximum adsorption capacity was calculated from Langmuir isotherm and Freundlich isotherm plots. The sorption kinetic studies of Cu(II) at pH 5 on the sorbent were evaluated. The concentration of residual Cu(II) in solution at different time intervals in the experiment was analyzed. During the experiment, 1-2 ml of sample solution was taken between 0 to 1.440 minutes, respectively. Samples were analysed by AAS. The results were plotted as adsorbed Cu(II) versus time (min). Each experiment was conducted twice under identical conditions.

Adsorption Procedure of Ni(II)

Batch adsorption experiments were conducted using three types of carboxyl-functionalized silica (**$SiO_2(CO_2H)$**, silica coated with CS LMW (**SiO_2+CS LMW**), and carboxyl-functionalized silica coated with CS LMW (**$SiO_2(CO_2H)$+CS LMW)**), as adsorbent for the uptake of Ni(II) at room temperature. The Ni(II) stock solution was prepared in DI water using $NiCl_2.6H_2O$ and then added to 0.4% of the suspended adsorbents. The pH of the suspending aqueous solution was adjusted with 0.1 M HCl or 0.1 M NaOH.

To determine the equilibrium isotherm, a series of Ni(II) initial concentration solutions ranging between 100 - 1.000 mg/L were prepared. The maximum total time of an experiment was 1440 minutes. The maximum adsorption capacity was calculated using both Langmuir isotherm, Freundlich, Temkin, and BET isotherm models

The adsorption kinetic of Ni(II) on the composites were evaluated at both pH 5, and 7. The concentration of residual Ni(II) in solution at different time intervals in the experiment was analyzed during the experiment. A 1-2 ml of sample solution was taken at 30, 60, 180, 300 and 1440 minutes, respectively. Samples were analysed by AAS.

Calibration curves

To determine the residual concentration of Cu(II) or Ni(II) in the supernatant by AAS using the parameter shown in Table 4.22, an experimental stock solution containing 3.000 mg/L of Cu(II) or Ni(II) was prepared by dissolving Copper(II) sulphate pentahydrate (or Nickel(II) chloride) in DI water. The pH of the metal solution was adjusted to pH 5 by 0.1 M HCl or 0.1 M NaOH. Aliquots of the stock solution were diluted using DI water to get experimental solution of known initial concentrations (2, 4, 6, 8, and 10 mg/L). Batch

adsorption experiments were carried out by adding of 0.4% sorbent into metal solutions. After 24 hours of adsorption process, the supernatant liquids were filtered. The residual Cu(II) concentration in each flask was determined using AAS. For a quantitative estimation of Cu(II) adsorbed onto the surface of modified silica materials, the calibration curve was established by plotting between the absorbance and Cu(II) concentration. This relationship is then used to transform measurements done on test samples in order to quantify the amount of Cu(II) present, as shown in Figure 116. The calibration curve of a Ni(II) standard is shown in Fig. 117.

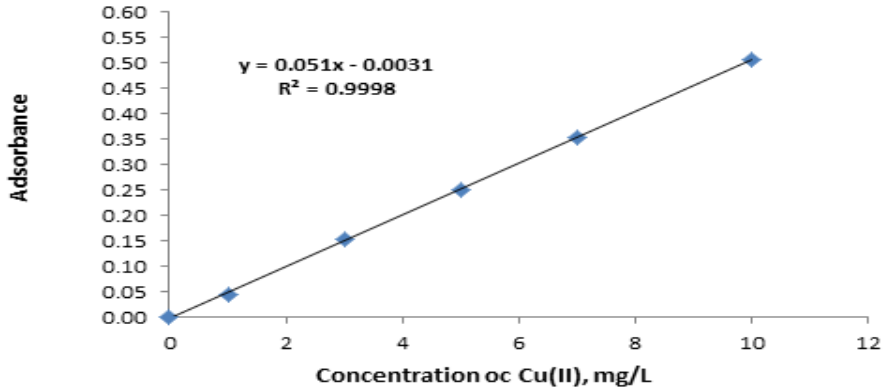

Fig. 116 Calibration curve for Cu(II)

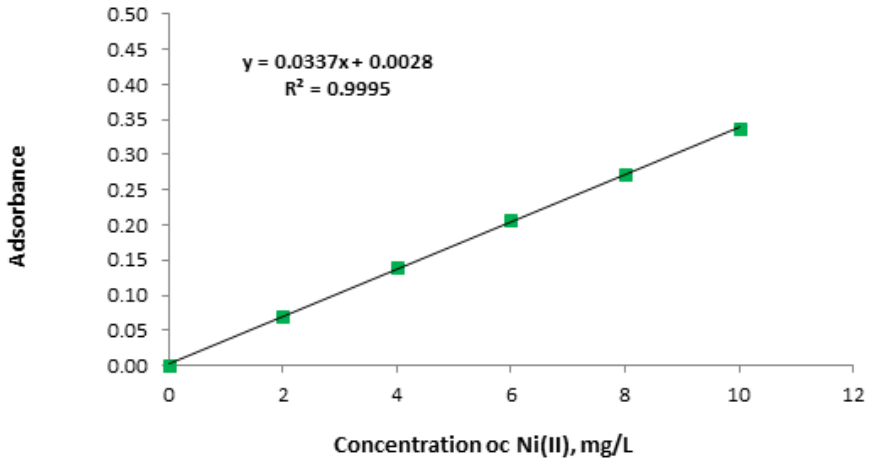

Fig. 117 Calibration curve for Ni(II)

Table 4.22 Operating parameters for metal analysis using AAS

Parameters	**Cu(II)**	**Ni(II)**
Flame Type	Air/acetylene	Air/acetylene
Wavelength	324.7 nm	232.0 nm
Slit Width	0.5 nm	0.5 nm

References

1. S.A. Çetinus, E. Sahin, and D. Saraydin, *Preparation of Cu(II) adsorbed chitosan beads for catalase immobilization*, Food Chem., 114 (2009) 962-969.
2. M. Chiban, A. Soudani, F. Sinan, and M. Persin, *Single, binary and multi-component adsorption of some anions and heavy metals on environmentally friendly Carpobrotus edulis plant*, Colloids Surf., B, 82 (2011) 267-276.
3. (a) H. Kayser, *On the condensation of gases on surfaces in their dependence on pressure and temperature*), Annalen der Physik 248 (1881) 526-537., (b) D. Myers, Surface, interface, and colloids: Principles and applications, 2^{ed}, 1999, 179.
4. S. Kelesoglu, *Comparative adsorption studies of heavy metal ions on chitin and chitosan biopolymers*, Thesis, Graduate School of Engineering and Science of Izmir Institute of Technology, Turkey, 2007.
5. D. Myers, *Surface, interfaces, and colloidals; principles and applications*, John Wiley & Sons, New York, 2^{ed} (1999) p. 203.
6. R. Singhon, J. Husson, M. Knorr, and M. Euvrard, *Preparation of Silica-Supported Biosorbents for Copper(II) Removal*, J. Disper. Sci. Technol., 32 (2011) 1735-1741.
7. R. Singhon, J. Husson, M. Knorr, B. Lakard, and M. Euvrard, *Adsorption of Ni(II) ions on colloidal hybrid organic-inorganic silica composites*, Colloid Surface B, 93 (2012) 1-7.
8. E. Repo, J.K. Warchol, T.A. Kurniawan, and M.E.T. Sillanpää, *Adsorption of Co(II) and Ni(II) by EDTA- and/or DTPA-modified chitosan: Kinetic and equilibrium modeling*, Chem. Eng. J., 161 (2010) 73-82.
9. Y. Xie, S. Li, F. Wang, and G. Liu, *Removal of perchlorate from aqueous solution using protonated cross-linked chitosan*, Chem. Eng. J., 156 (2010) 56-63.
10. S.A. Çetinus, E. Sahin, and D. Saraydin, *Preparation of Cu(II) adsorbed chitosan beads for catalase immobilization*, Food Chem., 114 (2009) 962-969.
11. D. Mohan, C.U. Jr. Pittman, and P.H. Steele, *Single, binary and multi-component adsorption of copper and cadmium from aqueous solutions on Kraft lignin - a biosorbent*, J. Colloid Interface Sci., 297 (2006) 489-504.
12. K.S. Tong, M.J. Kassim, and A. Azraa, Adsorption of copper ion from its aqueous solution by a novel biosorbent Uncaria gambir: Equilibrium, kinetics, and thermodynamic studies, Chem. Eng. J., 170 (2011) 145-153.
13. F. Gimbert, Nadia Morin-Crini, F. Renault, P.-M. Badot, and G. Crini, *Adsorption isotherm models for dye removal by cationized starch-based material in a single component*, J. Hazard. Mater., 157 (2008) 34-46.
14. M.-W. Wan, I.G. Petrisor, H.-T. Lai, D. Kim, and T.F. Yen, *Copper adsorption through chitosan immobilized on sand to demonstrate the feasibility for in situ soil decontamination*, Carbohydr. Polym., 55 (2004) 249-254.
15. K. Azlan, W.N. Wan Saime, and L.L. Ken, *Chitosan and chemically modified chitosan beads for acid dyes sorption*, J. Environ. Sci., 21 (2009) 296-302.

16. (a) S. Liang, X. Guo, N. Feng, and Q. Tian, *Isotherms, kinetics and thermodynamic studies of adsorption of Cu^{2+} from aqueous solutions by Mg^{2+}/K^{+} type orange peel adsorbents*, J. Hazard. Mater., 174 (2010) 756-762. (b) H.M.F. Freundlich, Über die adsorption in Losungen. *Z., Phys. Chem*., 57 (1906) 385-470.

17. J.C.Y. Ng, W.H. Cheung, and G. McKay, *Equilibrium studies for the sorption of lead from effluents using chitosan*, Chemosphere, 52 (2003) 1021-1030.

18. K. Bakiya Lakshmi, and P.N. Sudha, *Adsorption of Copper (II) ion onto chitosan/sisal/banana fiber hybrid composite*, Int. J. Environ. Sci., 3 (2012) 453-470.

19. X.-J Hu, J.-S. Wang, Y.-G. Liu, X. Li, G.-M. Zeng, Z.-L. Bao, X.-X. Zeng, A.-W. Chen, and F. Long, *Adsorption of chromium (VI) by ethylenediamine-modified cross-linked magnetic chitosan resin: Isotherms, kinetics and thermodynamics*, J. Hazard. Mater., 185 (2011) 306-314.

20. J. Peric, M. Trgo, N. Vukojevic Medvidovic, *Removal of zinc, copper and lead bynatural zeolite-a comparison of adsorption isotherms*, Water Res., 38 (2004) 1893-1899.

21. M.R. Samarghandi, M. Hadi, S. Moayedi, F. Barjasteh Askari, *Two-parameter isotherms of methyl orange sorption by pinecone derived activated carbon*, Iran J. Environ. Health. Sci. Eng., 6 (2009) 285-294.

22. M. Shanker, and T. Chinniagounder, Adsorption of Reactive Dye Using Low Cost Adsorbent: Cocoa *(Theobroma Cacao)* Shell, World Journal of Applied Environmental Chemistry, 1 (2012) 22-29.

23. K. Vijayaraghavan, T.V.N. Padmesh, K. Palanivelu, and M. Velan, *Biosorption of nickel(II) ions onto Sargassum wightii: Application of two-parameter and three-parameter isotherm models*, J. Hazard. Mater. B, 133 (2006) 304-308.

24. Z.-Y. Yao, J.-H. Qi, and L.-H. Wang, *Equilibrium, kinetic and thermodynamic studies on the biosorption of Cu(II) onto chestnut shell*, J. Hazard. Mater., 174 (2010) 137-143.

25. W.S. Wan Ngah, and S. Fatinathan, *Adsorption of Cu(II) ions in aqueous solution using chitosan beads,chitosan-GLA beads and chitosan-alginate beads*, Chem. Eng. J., 143 (2008) 62-72.

26. D.L. Guerra, and C. Airoldi, *The performance of urea-intercalated and delaminated kaolinites-adsorption kinetics Involving Copper and Lead*, J. Braz. Chem. Soc., 20 (2009) 19-30.

27. O.M. Akpa, and E.I. Unuabonah, *Small-sample corrected akaike information criterion: An appropriate statistical tool for ranking of adsorption isotherm models*, Desalination, 272 (2011) 20-2

28. Z.L. Yaneva, B.K. Koumanova, and N.V. Georgieva, *Linear and nonlinear regression methods for equilibrium modeling of p-Nitrophenol biosorbent by Rhizopus oryzae: Comparison of error analysis criteria*, J. Chem., 2013, 1-10.

29. S. Chatterjee, D.S. Lee, M.W. Lee, and S.H. Woo, *Enhanced adsorption of congo red from aqueous solutions by chitosan hydrogel beads impregnated with cetyl trimethyl ammonium bromide*, Bioresour. Technol., 100 (2009) 2803-2809.

30. (a) S. Chatterjee, D.S. Lee, M.W. Lee, and S.H. Woo, *Enhanced adsorption of congo red from aqueous solutions by chitosan hydrogel beads impregnated with cetyl trimethyl ammonium bromide*, Bioresour. Technol., 100 (2009) 2803-2809. (b) Y.S. Al-Degs, M.I. El-Barghouthi, A.A. Issa, M.A. Khraisheh, G.M. Walker, *Sorption of Zn(II), Pb(II), and Co(II) using natural sorbents: equilibrium and kinetic studies*, Water Res., 14 (2006) 2645-2658.

31. V. Manu, H.M. Mody, H.C. Bajaj and R.V. Jasra, *Adsorption of Cu^{2+} on amino functionalized silica gel with different loading, Ind. Eng. Chem. Res.*, 48 **(**2009) 8954-8960.

32. W. Yantasee, Y. Lin, G.E. Fryxell, K.L. Alford, B.J. Busche, and C.D. Johnson, *Selective Removal of Copper(II) from Aqueous Solutions Using Fine-Grained Activated Carbon Functionalized with Amine*, Ind. Eng. Chem. Res., 43 (2004) 2759-2764.

33. Z. Cheng, X. Liu, M. Han, and W. Ma, *Adsorption kinetic character of copper ions onto a modified chitosan transparent thin membrane from aqueous solution*, J. Hazard. Mater., 182 (2010) 408-415.

34. (a) L.T. Arenas, E.C. Lima, A.A. dos Santos Jr., J.C.P. Vaghetti, T.M.H. Costa, E.V. Benvenutti, *Use of statistical design of experiments to evaluate the sorption capacity of 1,4-diazoniabicycle[2.2.2]octane/silica chloride for Cr(VI) adsorption*, Colloid Surface A, 297 (2007) 240-248. (b) R. Ramya, P. Sankar, S. Anbalagan, and P.N. Sudha, *Adsorption of Cu(II) and Ni(II) ions from metal using crosslinked chitosan-g-acrylonitrile copolymer*, Int. J. Environ. Sci. 6 (2011) 1323-1338.

35. G.Z. Kyzas, M. Kostoglou, and N.K. Lazaridis, *Copper and chromium(VI) removal by chitosan derivatives-Equilibrium and kinetic studies*, Chem. Eng. J., 152 (2009) 440-448.

36. D.H.K. Reddy, D.K.V. Ramana, K. Seshaiah, and A.V.R. Reddy, *Biosorption of Ni(II) from aqueous phase by Moringa oleifera bark, a low cost biosorbent*, Desalination. 268 (2011) 150-157.

37. A.H. Hawari, and C.N. Mulligan, *Biosorption of lead(II), cadmium(II), copper(II) and nickel(II) by anaerobic granular biomass*, Bioresour.Technol., 97 (2006) 692-700.

38. J.C. Igwe, and A.A. Abia, *Adsorption kinetics and intraparticulate diffusivities for bioremediation of Co(II), Fe(II) and Cu(II) ions from waste water using modified and unmodified maize cob*, Int. J. Phys. Sci., 2 (2007) 119-127.

39. R. Apiratikul, and P. Pacasant, *Batch and column studies of Biosorption of heavy metals by Caulerpa Lentillifera*, Bioresour. Technol., 99 (2008) 2766-2777.

40. N. Saravanan, C. Ahmed Basha, T. Kannadasan, V. Manivasagan, and N.G. Ramesh Babu, *Biosorption of Nickel on Biobeads and Biofilm using Immobilized Escherichia Coli*, Eur. J. Sci. Res., 81 (2012) 231-245.

41. (a) Z. Velkova, M. Stoytcheva, and V. Gochev, *Biosorption of Cu(II) onto chemically modified waste mycelium of Aspergillus awamori: Equilibrium, kinetics and modeling studies*, J. BioSci. Biotech. 1 (2012) 163-169. (b) C.M. Futalan, C.-C. Kan, M.L. Dalida, K.-J. Hsien, C. Pascua, and M.-W. Wan, *Comparative and competitive adsorption of copper, lead, and nickel using chitosan immobilized on bentonite*, Carbohydr. Polym., 83 (2011) 528-536.

42. R. Terreux, M. Domard, C. Viton, and A. Domard, *Interaction study between copper II ion and constitutive elements of chitosan structure by DFT calculation*, Biomacromolecules, 7 (2006) 31-37.

43. R.B. Hernandez, O.R. Yola, and A.L.R. Merce, *Chemical equilibrium in the complexation of first transition series divalent cations Cu^{2+}, Mn^{2+} and Zn^{2+} with chitosan*, J. Braz. Chem. Soc. 18 (2007) 1388-1396.

44. S. Hasan, T.K. Ghosh, D.S. Viswanath, and V.M. Boddu, *Dispersion of chitosan on perlite for enhancement of copper(II) adsorption capacity*, J. Hazard. Mater., 152 (2008) 826-837.

45. M. Rhazi, J. Desbrières, A. Tolaimate, M. Rinaudo, P. Vottero, and A. Alagui**,** *Contribution to the study of the complexation of copper by chitosan and oligomers*, Polymer, 43 (2002) 1267-1276.

46. A.A. Shoukry and W.M. Hosny, *Coordination properties of N,O-carboxymethyl chitosan (NOCC), synthesis and equilibrium studied of some metal ion complexes. Ternary complexes involving Cu(II) with (NOCC) and some biorelevant ligand*, Cent. Eur. J. Chem., 10 (20120 59-70.

47. H. Irving, and R.J.P. Williams, *The stability of transition-metal complexes*, Nature, 162, 746-747.

48. R. Lü, Z. Cao, and G. Shen, *Comparative study on interaction between copper (II) and chitin/chitosan by density functional calculation*, J. Mol. Struct.: THEOCHEM, 860 (2008) 80-85.

49. (a) Y.A. Skorik, C.A.R. *Gomes, N.V. Podberezskaya, G.V. Romanenko, L.F. Pinto, and Y.G. Yatluk, Complexation models of N-(2-Carboxyethyl)chitosans with Copper (II) ions*, Biomacromolecules, 6 (2005) 189-195. (b) http://en.wikipedia.org/wiki/Copper_sulfate.

50. (a) H. Chen, G. Dai, J. Zhao, A. Zhong, J. Wu, and H. Yan, *Removal of copper(II) ions by a biosorbent-Cinnamomum camphora leaves powder*, J. Hazard. Mater., 177 (2010) 228-236. (b) Z. Aksu, and I.A. Isoglu, *Removal of copper(II) ions from aqueous solution by biosorption onto agricultural waste sugar beet pulp*, Process Biochem., 40 (2005) 3031-3044. (c) A.Y. Dursun, *A comparative study on determination of the equilibrium, kinetic and thermodynamic parameters of biosorption of copper(II) and lead(II) ions onto pretreated Aspergillus niger*, Biochem. Eng. J., 28 (2006) 187-195.

51. (a) F. Bouhamed, Z. Elouear, and J. Bouzid, *Adsorptive removal of copper(II) from aqueous solutions on activated carbon prepared from Tunisian date stones: Equilibrium, kinetics and thermodynamics*, J. Taiwan Inst. Chem. Eng., 43 (2012) 741-749. (b) A. Ahmad, M. Rafatullah, O. Sulaiman, M.H. Ibrahim, Yap Yee Chii, and B.M. Siddique, *Removal of Cu(II) and Pb(II) ions from aqueous solutions by adsorption on sawdust of Meranti wood*, Desalination, 250 (2009) 300-310.

52. (a) F. Ning-Chuan, G. Xue-Yi, and L. Sha, *Enhanced Cu(II) adsorption by orange peel modified with sodium hydroxide*, Trans. Nonferrous Met. Soc. China, 20 (2010) 146-152. (b) G.Z. Kyzas, *Commercial coffee wastes as materials for adsorption of heavy metals from aqueous solutions*, Materials, 5 (2012) 1826-1840.

53. M. Raf atullah, O. Sulaiman, R. Hashim, and A. Ahmad, *Adsorption of copper(II) onto different adsorbents*, J. Disper. Sci. Technol., 31 (2010) 918-930.

54. (a) N.K.E.M. Yahaya, M.F.P.M. Latiff, I. Abustan, O.S. Bello, and M.A. Ahmad, *Adsorptive removal of Cu (II) using activated carbon prepared from rice husk by $ZnCl_2$ activation and subsequent gasification with CO_2*, Int. J. Eng. Technol., 11 (2011) 207-211. (b) N. Chiron, R. Guilet, and E. Deydier, Adsorption of Cu(II) and Pb(II) onto a grafted silica: isotherms and kinetic models,Water Res., 37 (2003) 3079-3086.

55. A. Goswami, and A.K. Singh, *Silica gel functionalized with resacetophenone: synthesis of a new chelating matrix and its application as metal ion collector for their flame atomic absorption spectrometric determination*, Anal. Chim. Acta, 454 (2002) 229-240.

56. F. Bari, N. Begum, S.B. Jamaludin, and K. Hussin, *Extraction and separation of Cu(II), Ni(II) and Zn(II) by sol-gel silica immobilized with Cyanex 272*, Hydrometallurgy., 96 (2009) 140-147.

57. A.S. Pereira, G. Ferreira, L. Caetano, M.A. Martines, P.A. Padilha, A. Santos, and G.R. Castro, *Preconcentration and determination of Cu(II) in a fresh water sample using modified silica gel as a solid-phase extraction adsorbent*, J. Hazard. Mater., 175 (2010) 399-403.

58. M. Mureseanu, A. Reiss, I. Stefanescu, E. David, V. Parvulescu, G. Renard, and V. Hulea, *Modified SBA-15 mesoporous silica for heavy metal ions remediation*, Chemosphere, 73 (2008) 1499-1504.

59. J. Aguado, J.M. Arsuaga, A. Arencibia, M. Lindo, and V. Gascón, *Aqueous heavy metals removal by adsorption on amine-functionalized mesoporous silica*, J. Hazard. Mater., 163 (2009) 213-221.

60. V. Manu, H.M. Mody, H.C. Bajaj, and R.V. Jasra, *Effect of Thermal Treatment of Silica Gels on Their Amino Functionalization and Subsequent Adsorption Properties for Cu^{2+} from Aqueous Solution of Copper Sulfate, Ind. Eng. Chem. Res.*, 49 **(**2010) 8184-8191.

61. H. Yong-Mei, C. Man, and H. Zhong-Bo, *Effect removal of Cu(II) ions from aqueous solution by amino-functionalized magnetic nanoparticles*, J. Hazard. Mater., 184 (2010) 392-399.

62. A. Shahbazi, H. Younesi, and A. Badiei, *Functionalized SBA-15 mesoporous silica by melamine-based dendrimer amines for adsorptive characteristics of Pb(II), Cu(II) and Cd(II) heavy metal ions in batch and fixed bed column*, Chem. Eng. J., 168 (2011) 505-518.

63. (a) V. Patrulea, A. Negrulescu, M.M. Mincea, L.D. Pitulice, O.B. Spiridon, and V. Ostafe, *Optimization of the removal of Copper(II) ions from aqueous solution on Chitosan and Crosslinked chitosan beads*, Bioresource., 8 (2013) 1147-1165. (b) A.-H. Chen, S.-. Liu, C.-Y. Chen, and C.-Y. Chen, *Comparative adsorption of Cu(II), Zn(II), and Pb(II) ions in aqueous solution on the crosslinked chitosan with epichlorohydrin*, J. Hazard., 154 (2008) 184-191. (c) C. Yuwei, and W. Jianlong, *Preparation and characterization of magnetic chitosan nanoparticles and its application for Cu(II) removal*, Chem. Eng. J., 168 (2011) 286-292.

64. L. Zhou, Y. Wang, Z. Liu, and Q. Huang**,** *Characteristics of equilibrium, kinetics studies for adsorption of Hg(II), Cu(II), and Ni(II) ions by thiourea-modified magnetic chitosan microspheres.* J. Hazard. Mater., 161 (2009) 995-1002.

65. K.R. Krishnapriya, and M. Kandaswamy, *Synthesis and characterization of a crosslinked chitosan derivative with a complexing agent and its adsorption studies toward metal(II) ions*, Carbohydr. Res., 344 (2009) 1632-1638.

66. M. Monier, D.M. Ayad, and D.A. Abdel-Latif, *Adsorption of Cu(II), Cd(II), and Ni(II) by cross-linked magnetic chitosan-2-aminopyridine glyoxal Schiff's base*, Colloid. Surface B, 94 (2012) 250-258.

67. R. Laus, T.G. Costa, B. Szpoganicz, and V.T. Fávere**,** *Adsorption and desorption of Cu(II), Cd(II) and Pb(II) ions using chitosan crosslinked with epichlorohydrin-triphosphate as the adsorbent*, J. Hazard. 183 (2010) 233-241.

68. H. Yan, J. Dai, Z. Yang, H. Yang, and R. Cheng, *Enhanced and selective adsorption of copper(II) ions on surface carboxymethylated chitosan hydrogel beads*, Chem. Eng. J., 174 (2011) 586-594.

69. N.T. An, D.T. Thien, N.T. Dong, and P.L. Dung, *Water-soluble N-carboxymethylchitosan derivatives: Preparation, characteristics and its application*, Carbohydr. Polym., 75 (2009) 489-497.

70. (a) A. Shanmugapriya, R. Ramya, S. Ramasubramaniam, and P.N. Sudha, *Studies on removal of Cr(IV) and Cu(II) ions using chitosan grafted-polyacrylonitrile*, Arch. Appl. Sci. Res., 3 (2011) 424-435. (b) D.-W. Cho, B.-H. Jeon, C.-M. Chon, Y. Kim, F.W. Schwartz, E.-S. Lee, and H. Song, *A novel chitosan/clay/magnetite composite for adsorption of Cu(II) and As(V)*, Chem. Eng. J., 200-202 (2012) 654-662. (c) M.A. Zenasni, S. Benfarhi, A. Merlin, S. Molina, B. George, and B. Meroufel, *Adsorption of Cu(II) on maghnite from aqueous solution: Effects of pH, initial concentration, interaction time and*

temperature, Nat. Sci.,4 (20120 856-868. (d) M. Hébrant, M. Rose-Hélène, and A. Walcarius, *Metal ion removal by ultrafiltration of colloidal suspensions of organically modified silica*, Colloid Surface A, 417 (2013) 65-72.

71. C.M. Futalan, C.-C. Kan, M.L. Dalida, K.-J. Hsien, C. Pascua, and M.-W. Wan, *Comparative and competitive adsorption of copper, lead, and nickel using chitosan immobilized on bentonite*, Carbohydr. Polym., 83 (2011) 528-536.
72. S. Wang, T. Terdkiatburana, and M.O. Tadé, *Adsorption of Cu(II), Pb(II) and humic acid on natural zeolite tuff in single and binary systems*, Sep. Purif. Technol., 62 (2008) 64-70.
73. S. Kubilay, R. Gürkan, A. Savran, and T. Sahan, *Removal of Cu(II), Zn(II) and Co(II) ions from aqueous solutions by adsorption onto natural bentonite*, Adsorption, 13 (2007) 41-51.
74. E. Eren, *Removal of copper ions by modified Unye clay*, Turkey, J. Hazard. Mater., 159 (2008) 235-244.
75. W. Qiu, and Y. Zheng, *Removal of lead, copper, nickel, cobalt, and zinc from water by a cancrinite-type zeolite synthesized from fly ash*, Chem. Eng. J., 145 (2009) 483-488.
76. (a) W.S. Wan Ngah, and S. Fatinathan, *Adsorption characterization of Pb(II) and Cu(II) ions onto chitosan-tripolyphosphate beads: Kinetic, equilibrium and thermodynamic studies*, J. Environ. Manage., 91 (2010) 958-969. (b) C. Liu, and R. Ba, *Adsorptive removal of copper ions with highly porous chitosan/celluloseacetate blend hollow fiber membrane*, J. Membr. Sci., 284 (2006) 313-322.
77. V.M. Boddu, K. Abburi, A.J. Randolph, and E.D. Smith, *Removal of copper(II) and nickel(II) ions from aqueous solutions by a composite chitosan biosorbent*, Sep. Sci. Technol., 43 (2008) 1365-1381.
78. Q. Peng, Y. Liu, G. Zeng, W. Xu, C. Yang, and J. Zhang, *Biosorption of copper(II) by immobilizing Saccharomyces cerevisiae on the surface of chitosan-coated magnetic nanoparticles from aqueous solution*, J. Hazard. Mater., 177 (2010) 676-682.
79. (a) B. Zhang, Y. Cui, G. Yin and X. Li, *Adsorption of Copper(II) and Lead(II) ions onto Cottonseed Protein-PAA Hydrogel Composite*, Polymer-Plastics Tec. Eng., 51 (2012) 612-619. (b) A. Ghaee, M. Shariaty-Niassar, J. Barzin, and A. Zarghan, *Adsorption of copper and nickel ions on macroporous chitosan membrane: Equilibrium study*, Appl. Surf. Sci., 258 (2012) 7732-7743. (c) S.J. Wu, T.-H. Liou, C.-H. Yeh, F.-L. Mi, and T.-K. Lin, *Preparation and characterization of porous chitosan-triphosphate beads for copper(II) ion adsorption*, J. Appl. Polym. Sci., (2013) 4573-4580.
80. (a) P. Stathi, and Y. Deligiannakis, Humic acid-inspired hybrid materials as heavy metal adsorbents, Colloid Interface Sci., 351 (2010) 239-247. (b) S. Moulay, N. Bensacia, F. Garin, I. Fechete, and A. Boos, *Polyacrylamide-based sorbent sorbent for the removal of hazardous metal*, Adsorpt. Sci. Technol., 31 (2013) 690-709. (c) B. Samiey, C.-H. Cheng, and J. Wu, *Organic-inorganic hybrid polymers as adsorbents for removal of heavy metal ions from solutions: A review*, Materials, 7 (2014) 673-726. (d) F. Kopecky, B. Kopecka, and E. Misikova, *Sorption of Copper(II) on chitosan from solution of copper sulphate, copper perchlorate, and copper nitrate*, Acta Facult. Pharm. Comeninae, 52 (2005) 125-135.
81. T. Mitani, N. Fukumuro, C. Yoshimoto, and H. Ishi, *Effects of counter ions (SO_4^{2-} and Cl^-) on the adsorption of copper and nickel ions by swollen chitosan beads*, Agric. Biol. Chem., 55 (1991) 2419 .

82. K.A. Krishnan, K.G. Sreejalekshmi, and R.S. Baiju, *Nickel(II) adsorption onto biomass based activated carbon obtained from sugarcane bagasse pith*, Bioresource. Technol. 102 (2011) 10239-10247.

83. M. Rafatullah, O. Sulaiman, R. Hashim, and A. Ahmad, *Adsorption of copper(II), chromium(III), nickel(II) and lead(II) ions from aqueous solutions by Meranti sawdust*, J. Hazard. Mater., 170 (2009) 969-977.

84. (a) C.-Y. Chen, C.-Y. Yang, and A.-H. Chen, *Biosorption of Cu(II), Zn(II), Ni(II) and Pb(II) ions by cross-linked metal-imprinted chitosans with epichlorohydrin*, J. Environ. Manage., 92 (2011) 796-802. (b) A. Eser, V.N. Tirtom, T. Aydemir, S. Becerik, and A. Dincer, *Removal of nickel(II) ions by histidine modified chitosan beads*, Chem. Eng. J., 210 (2012) 590-596.

85. E. Malkoc, *Ni(II) removal from aqueous solution using cone biomass of Thuja orients*, J. Hazard. Mater. B, 137 (2006) 899-908.

86. A.G. El Samrani, B.S. Lartiges, and F. Villiéras, *Chemical coagulation of combined sewer overflow: Heavy metal removal and treatment optimization*, Water Res., 42 (2008) 951-960.

87. K.H. Bodek, and A. Kufelnicki, *Interaction of microcrystalline chitosan with Ni(II) and Mn(II) ions in aqueous solution*, J. Appl. Polym. Sci., 98 (2005) 2572-2577.

88. A. Burkhardt, and W. Plass, *Modeling the coordination chemistry of chitosan: Synthesis and characterization of a nickel(II) complex with a 2-aminoglucose Schiff-base ligand*, Inorg. Chem. Commun., 11 (2008) 303-306.

89. J.W. Bunting, and K.M. Thong, *Stability constant for metal 1 : 1 metal-carboxylate complexes*, Can. J. Chem., 48 (1970) 1654-1656.

90. (a) M.E. Argun, S. Dursun, C. Ozdemir, and M. Karatas, *Heavy metal adsorption by modified oak sawdust: Thermodynamics and kinetics*, J. Hazard. Mater., 141 (2007) 77-85. (b) S. Zamani, E. Salahi, and I. Mobasherpour, *Removal of Nickel from Aqueous Solution by Nano Hydroxyapatite Originated from Persian Gulf Corals*, Can. Chem. Trans., 1 (2013) 173-190.

91. S. Al-Asheh, F. Banat, R. Al-Omari, and Z. Duvnjak, *Predictions of binary sorption isotherms for the sorption of heavy metals by pine bark using single isotherm data*, Chemosphere, 41 (2000) 659-665.

92. K.G. Bhattacharyya, J. Sarma, and A. Sarma, *Azadirachtaindica leaf powder as a biosorbent for Ni(II) in aqueous medium*, J. Hazard. Mater., 165 (2009) 271-278.

93. (a) M.A. Abdullah, and A.G. Devi Prasad, *Biosorption of Nickel (II) from Aqueous Solutions and Electroplating Wastewater using Tamarind* (*Tamarindus indica L.) Bark*, Aust. J. Basic Appl. Sci., 4 (2010) 3591-3601. (b) N. Ghasemi, M. Ghasemi , S.R.W. Alwi, Z.A. Manan, *Removal of Nickel (II) from Aqueous Solution by Activated Carbon Prepared from Askari grape dust*, Proceedings of the 6th International Conference on Process Systems Engineering (PSE ASIA), 1047-1052.

94. (a) D. H.K. Reddy, D.K.V. Ramana, K. Seshaiah, and A.V.R. Reddy, *Biosorption of Ni(II) from aqueous phase by Moringa oleifera bark, a low cost biosorbent*, Desalination, 268 (2011) 150-157. (b) M. Rafatullah, O. Sulaiman, R. Hashim, and A. Ahmad, *Adsorption of copper (II), chromium (III), nickel (II) and lead (II) ions from aqueous solutions by meranti sawdust*, J. Hazard. Mater., 170 (2009) 969-977.

(c) R.H. Krishna, and A. Swamy, *Kinetic and isotherm modeling of adsorption of Ni(II) from aqueous solutions onto powder of papaya seeds*, Int. J. Sci. Res. Public., 1 (2011) 1-6.

95. (a) S. Deng, and Y.-P. Ting, *Characterization of PEI-modified biomass and biosorption of Cu(II), Pb(II) and Ni(II)*, Water Res., 39 (2005) 2167-2177. (b) F. Gönen, and D.S. Serin, *Adsorption study on orange peel: Removal of Ni(II) ions from aqueous solution*, Afr. J. Biotechnol., 11 (2012) 1250-1258.

96. (a) Y. B. Onundi, A. A. Mamun, M. F. Al Khatib, Y. M. Ahmed, *Adsorption of copper, nickel and lead ions from synthetic Semiconductor industrial wastewater by palm shell activated carbon*, Int. J. Environ. Sci. Tech., 7 (2010) 751-758. (b) A. Esmaeili, and S. Ghasemi, *Evaluation of the Activated Carbon Prepared of Algae Marine Gracilaria for the Biosorption of Ni (II) from Aqueous Solutions*, World Appl. Sci. J., 6 (2009) 515-518. (c) P. Thamilarasu, P. Sivakumar, and K. Karunakaran, *Removal of Ni(II) from aqueous solutions by adsorption onto Cajanus cajan Milsp seed shell activated carbons*, Indian J. Chem. Tech., 18 (2011) 414-420. (d) A. Ewecharoen, P. Thiravetyan, E. Wendel, and H. Bertagnolli, *Nickel adsorption by sodium polyacrylate-grafted activated carbon*, J. Hazard. Mater., 171 (2009) 335-339 (e) K. Kadirvelu, K. Thamaraiselvi, and C. Namasivayam, *Adsorption of nickel(II) from aqueous solution onto activated carbon prepared from coirpith*, Sep. Purif. Technol., 24 (2001) 497-505.

97. S. Erdogan, Y. Önal, C. Akmil-Basar, S. Bilmez-Erdemoglu, C. Sarıcı-Özdemir, E. Köseoglu, and G. Icduygu, *Optimization of nickel adsorption from aqueous solution by using activated carbon prepared from waste apricot by chemical activation*, Appl. Surf. Sci., 252 (2005) 1324-1331.

98. N. Jiang, X. Chang, H. Zheng, Q. He, and Z. Hu, *Selective solid-phase extraction of nickel(II) using a surface-imprinted silica gel sorbent*, Anal. Chim. Acta, 577 (2006) 225-231.

99. T. Akar, Z. Kaynak, S. Ulusoy, D. Yuvaci, G. Ozsari, and S.T. Akar, *Enhanced biosorption of nickel(II) ions by silica-gel-immobilized waste biomass :Biosorption characteristics in batch and dynamic flow mode*, J. Hazard. Mater., 163 (2009) 1134-1141.

100. L. Zhou, Y. Wang, Z. Liu, and Q. Huang, *Characteristics of equilibrium, kinetics studies for adsorption of Hg(II), Cu(II), and Ni(II) ions by thiourea-modified magnetic chitosan microspheres*, J. Hazard. Mater. 161 (2009) 995-1002.

101. M. Monier, D.M. Ayad, Y. Wei, and A.A. Sarhan, *Adsorption of Cu(II), Co(II), and Ni(II) ions by modified magnetic chitosan chelating resin*, J. Hazard. Mater., 177 (2010) 962-970.

102. F. Yang, H. Liu, J. Qu, and J. P. Chen, *Preparation and characterization of chitosan encapsulated Sargassum sp. biosorbent for nickel ions sorption*, Bioresource Technol., 102 (2011) 2821-2828.

103. K. Seshaiah, Y. Harinath, Y. Suneetha, B. R. Naik, and M.-C. Wang, *Preparation of New sorbent by Functionalization of Cross linked Chitosan with 4-amino-3-hydroxybenzoic acid and its application for solid phase extraction of Ni(II) and Pb(II) from environmental samples and determination by AAS*, Int. J. Appl. Sci. Eng., 10 (2012) 307-317.

104. E. Repo, J.K. Warchol, T.A. Kurniawan, and M.E.T. Sillanpaa, *Adsorption of Co(II) and Ni(II) by EDTA- and/or DTPA-modified chitosan: Kinetic and equilibrium modeling*, Chem. Eng. J., 161 (2010) 73-82.

105. N. Gupta, A.K. Kushwaha, and M.C. Chattopadhyaya, *Adsorptive removal of Pb^{2+}, Co^{2+} and Ni^{2+} by hydroxyapatite/chitosan composite from aqueous solution*, **, J.** Taiwan Inst. Chem. Eng., 43 (2012) 125-131.

106 (a) M.G.A. Vieira, A.F. Almeida Neto, M.L. Gimenes, and M.G.C. da Silva, *Sorption kinetics and equilibrium for the removal of nickel ions from aqueous phase on calcined Bofe bentonite clay*, J. Hazard. Mater., 177 (2010) 362-371. (b) S. Singh, L.K. Verma, S.S. Sambi, and S.K. Sharma, *Adsorption Behaviour of Ni (II) from Water onto Zeolite X: Kinetics and Equilibrium Studies,* WCECS, (2008) 1-6. **(c) W.** Qiu, and Y. Zheng, *Removal of lead, copper, nickel, cobalt, and zinc from water by a carcrinite-type zeolite synthesized from fly as*h, Chem. Eng. J., 145 (2009) 483-488.

107. K. Swayampakula, V.M. Boddu, S.K. Nadavala, and K. Abburi, *Competitive adsorption of Cu (II), Co (II) and Ni (II) from their binary and tertiary aqueous solutions using chitosan-coated perlite beads as biosorbent*, J. Hazard. Mater., 170 (2009) 680-689.

108. K.A. Krishman, K.G. Sreejalekshmi, and R.S. Baiju, *Nickel(II) adsorption onto based activated carbon obtained from sugarcane bagasse pith*, Bioresour. Technol., 102 (2011) 10239-10247.

109. S. Yang, J. Li, Y. Lu, Y. Chen, and X. Wang, *Sorption of Ni(II) on GMZ bentonite effects of pH ionic strength, foreign ions, humic acid temperature*, Appl. Radiat. Isotopes, 67 (2009) 1600-1608.

110. A. Ewecharoen, P. Thiravetyan, E. Wendel, and H. Bertagnolli, *Nickel adsorption by sodium polyacrylate-grafted activated carbon*, J. Hazard. Mater., 171 (2009) 335-339.

111. M.V. Dinu, and E.S. Dragan, *Evaluation of* Cu^{2+}, Co^{2+} *and* Ni^{2+} *ions removal from aqueous solution using a novel chitosan/clinoptiolite composite: Kinetics and isotherms*, Chem. Eng. J., 160 (2010) 157-163.

112. T. Akar, Z. Kaynak, S. Ulusoy, D. Yuvaci, G. Ozsari, and S.T. Akar, *Enhanced biosorption of nickel(II) ions by silica-gel-immobilized waste biomass: Biosorption characteristics in batch and dynamic flow mode*, J. Hazard. Mater., 163 (2009) 1134-1141.

113. N. Dizge, B. Keskinler, and H. Barlas, Sorption of Ni(II) ions from aqueous solution by Lewatit cation-exchange resin, J. Hazard. Mater. 167 (2009) 915-926.

114. A.-H. Chen, C.-Y. Yang, C.-Y.Chen, C.-Y. Chen, and C.-W. Chen, *The chemically crosslinked metal-complexed chitosans for comparative adsorption of Cu(II), Zn(II), Ni(II), and Pb(II) ions in aqueous medium*, J. Hazard (2009) 1068-1075.

115. M. Mohapatra, L. Mohapatra, P. Singh, S. Anand, and B.K. Mishra, *A comparative study on Pb(II), Cd(II), Cu(II), Co(II) adsorption from single and binary aqueous solutions on additive assisted nano-structured goethite*, Int. J. Eng. Sci. Technol.
2 (2010) 89-103.

116. S. Sun, and A. Wang, *Adsorption kinetics of Cu(II) ions using N,O-carboxymethyl-chitosan*, J. Hazard. Mater. B, 131 (2006) 103-111.

General Conclusion and Perspectives

The demand for new green technologies and low-cost production for realizing chemical transformations and material design is becoming a priority. A lot of attention has been devoted to the use of natural polymer for sustainable development and preservation of the environment. In context, we focused our work on the elaboration of functionalized Aerosil 200 particles as efficient absorbents to scavenge divalent metal ions from aqueous solution. The biopolymers chitosan has been chosen to prepare novel organic-inorganic hybrid material. The present work demonstrates that the modified silica materials **($SiO_2(NH_2)$** and **$SiO_2(CO_2H)$**), the modified CS (**$CS(CO_2H)$**), CS-coated silica materials (**SiO_2+CS LMW**, **SiO_2+CS Yuhuan** and **SiO_2+CS Marine**), the CS-coated amine grafted silica material (**$SiO_2(NH_2)$+CS LMW**), the CS-coated carboxyl grafted silica material (**$SiO_2(CO_2H)$+CS LMW**), and the carboxymethyl CS-coated silica material (**SiO_2+$CS(CO_2H)$**) can be developed as adsorbents by the simple procedure.

In Chapter one, neat **SiO_2** was treated with acid to obtain **Activated SiO_2**. The surface of silicas (SiO_2) was protonated after acid treatment causing a decrease in pH values. The pH values of colloidal silica **(Activated SiO_2)** are quite stable during 3 days of analysis (around pH 6). After activation of silica by acidid aqueous solution, the conductivity is quite stable and the average value is ~ 969±8 μS/cm. The **Activated SiO_2** shows a ten times higher conductivity than neat **SiO_2**. This may be due to some residual hydrochloric acid bound on thesurface and surface disturbed by acid molecules. The zeta potential values of the **SiO_2** and **Activated SiO_2** are nearly zero at pH 2. However, at pH > 2, zeta potential values decrease accordingly resulting from an increasing of the concentration of the negative charges on the silica surface.

In Chapter two, the chemical modification of silica is described. The **$SiO_2(NH_2)$** and **$SiO_2(CO_2H)$** materials were synthesis via simple procedure. The surface morphology of the two materials was investigated by SEM and AFM. The surface morphology of **$SiO_2(NH_2)$** and **$SiO_2(CO_2H)$** materials was more uniform and more regular when compared with that of **SiO_2**. The BET value of modified silica materials decreases with an increase of the surface density. The Elemental analysis and BET data allow the calculation of the amino or carboxyl groups grafting density. Therefore, the grafting density of **$SiO_2(NH_2)$** and **$SiO_2(CO_2H)$** are 3.94 μmol m^{-2} and 0.48 μmol m^{-2}, respectively. The behaviour in aqueous solution was investigated by measuring the zeta potential, pH and conductivity. At pH between pH 2 and

pH 8, the zeta potential values of **$SiO_2(NH_2)$** show a positive zeta potential between 41.7 mV to 20.2 mV. In case of **$SiO_2(CO_2H)$**, the zeta potential value of this material changed to a negative zeta potential with the value in the range of -58.8 mV to -61.9 mV (at pH 5-9). The pH value of colloidal amino-, carboxyl grafted silica are quite stable at the period time study with an average pH value of about 9.6 and 4.5 for **$SiO_2(NH_2)$** and **$SiO_2(CO_2H)$**, respectively.

Chapter three deals on the chemical modification of CS. The synthesis of a *N*,*O*-carboxymethylchitosan polymer by reaction of CS with acid in isopropyl alcohol via alkylation reaction provides the carboxymethylchitosan material **$CS(CO_2H)$**. With the aim to prepare novel adsorbent for metal cation removal, the six new silica-based composites (**SiO_2+CS LMW**, **SiO_2+CS Yuhuan**, **SiO_2+CS Marine**, **$SiO_2(NH_2)$+CS LMW**, **$SiO_2(CO_2H)$+CS LMW** and **SiO_2+$CS(CO_2H)$**) have been prepared and the preparative details concerning the synthetic procedure are presented. These hybrid materials were characterized using FT-IR spectroscopy, elemental analysis, and BET specific surface analysis. The elemental analysis allowed the calculation of the number of amine functions (-NH_2). Consequently, the amine function density of **SiO_2+CS LMW** was 4.51×10^{-3} mol per gram. For the other hybrid composite, **$SiO_2(CO_2H)$+CS LMW**, the amine function density was 4.21×10^{-3} mol per gram. In the case of **$SiO_2(NH_2)$+CS LMW**, a somewhat higher nitrogen percentage of 6.05% was obtained consistent with the presence of amino groups both on **$SiO_2(NH_2)$** and **CS LMW**. Consequently, the number of amine functions in **CS LMW** could not be directly calculated. The S_{BET} value of the silica composites containing CS was measured in function of the CS content. The S_{BET} value drops to less than 10 $m^2.g^{-1}$ for the CS-coated silica materials, whereas the neat SiO_2 exhibits a S_{BET} of 182±4 $m^2.g^{-1}$. An increasing of CS molecule affect to a reducing of S_{BET} value. This agrees with the report of E.-J. Lee and co-workers (2010). The neat xerogel exhibits a S_{BET} of 620 $m^2.g^{-1}$, whereas the hybrid containing 30% of CS has a S_{BET} value of 150 $m^2.g^{-1}$. The morphology of five types of the hybrid materials (**SiO_2+CS LMW**, **SiO_2+CS Marine**, **$SiO_2(NH_2)$+CS LMW**, **$SiO_2(CO_2H)$+CS LMW** and **SiO_2+$CS(CO_2H)$**) was also investigated by SEM. The surface of the silica particles, before coating with CS, was quite rough and irregular. However, after biopolymer coating, the CS-coated silica hybrid composites (**SiO_2+CS LMW, SiO_2+CS Marine**, **$SiO_2(NH_2)$+CS LMW**, and **$SiO_2(CO_2H)$+CS LMW** showed a rigid texture with small gains of the silica nanoparticles distributed homogeneously in the CS matrix as current bun (Fig. 1.8, chapter 1) which was due to the high coverage of CS. In contrast, the morphology of the carboxymethyl CS-coated silica (**SiO_2+$CS(CO_2H)$**) showed a heterogeneous texture of the carboxymethyl CS layer. The pH of the hybrid materials (7.6-

8.9) increased when comparing to the non-grafted silica (~ pH 5.7) or carboxyl-grafted silica (~ pH 4.2), due to coating of the particle surface by CS polymer. The conductivity of **SiO_2+CS** was found to be in the range 18 - 31 μS/cm after 24 hours. In case of CS-coated modified silica materials (**$SiO_2(NH_2)$+CS LMW** and **SiO_2+CS(CO_2H)**) their conductivity values were found to be in the range 350 μS/cm and 400 μS/cm. The zeta potential values of the five types of CS-coated silica (**SiO_2+CS LMW**, **SiO_2+CS Marine**, **$SiO_2(CO_2H)$+CS LMW**, **$SiO_2(NH_2)$+CS LMW**, and **SiO_2+CS(CO_2H)**) were quite close with the positive zeta potential value at low pH (2-3). The hydrodynamic size of the six hybrid composites was higher than 1 μm when comparing with SiO_2 (328±25 nm).

In the last chapter, the novel organic-inorganic hybrid composites were revealed as promising adsorbent for efficient removal of Cu(II) and/or Ni(II) from aqueous solutions at room temperature. In case of Cu(II) adsorption onto **$SiO_2(NH_2)$, SiO_2+CS LMW**, **SiO_2+CS Yuhuan**, and **SiO_2+CS Marine** materials, the isotherm of Langmuir fitted well for the adsorption studied. Assuming that the adsorption of Cu(II) is a mono-layer adsorption onto the surface of our sorbents at specific homogeneous sites with a finite number of identical sites and the adsorption takes place without any interaction between the adsorbed molecules. The maximum monolayer adsorption obtained at pH 5 on the adsorbent was found to be 93.3 mg/g for **$SiO_2(NH_2)$** and found to be between 97.0-158.7 mg/g for **SiO_2+CS.** The adsorption capacity of Cu(II) by the CS-coated silica materials acted as a better adsorbent compared to amine grafted silica material. When the silica core was chemically modified with amine and/or carboxyl group before surface coating with CS, the maximum Cu(II) adsorption onto the modified silica materials (**$SiO_2(CO_2H)$+CS LMW** and **$SiO_2(NH_2)$+CS LMW)** was found to be 232.6 mg/g for **$SiO_2(CO_2H)$+CS LMW**, and 243.9 mg/g for **$SiO_2(NH_2)$+CS LMW)**. These two types of the modified silica materials showed the more efficiency for capturing Cu(II) than the CS-coated non-modified silica materials. This was due to the amine or carboxyl groups on the chemically modified silica core. The adsorption rate of Cu(II) ions at the solid solution interface onto four CS-coated silica materials with an equilibrium established between the two phase was studied using the pseudo-first-order, pseudo-second-order. It was found that the pseudo-second-order was the model that provided the better fit for adsorption kinetics of Cu(II) onto six types of CS-coated silica materials (**SiO_2+CS LMW**, **SiO_2+CS Yuhuan**, **SiO_2+CS Marine**, **$SiO_2(NH_2)$+CS LMW**, **$SiO_2(CO_2H)$+CS LMW**, and **SiO_2+CS(CO_2H)**). In order to study the mechanisms and rate controlling steps affecting the kinetics of adsorption, the kinetic experimental results were analyzed by the intraparticle

diffusion model (Weber and Morris). From these results, the straight line did not pass the origin for all the three adsorbents; intraparticle diffusion can be excluded as only rate-controlling step. Moreover, the plots showed a curvature, which was attributed to boundary layer diffusion effect or external mass transfer effect. A comparative study of solutions containing both $CuSO_4$ and $Cu(NO_3)_2$ on the adsorption behavior of Cu(II) by CS-coated silica particles shows that the adsorption of Cu(II) from sulphate solution is higher than that from $Cu(NO_3)_2$ solution in the case of **SiO_2+CS LMW** as sorbent. However, the influence of the counterion on the adsorption process needs to be explored more in depth in future studies and should be extended to other counterions.

In the case of Ni(II) adsorption onto **SiO_2+CS LMW** and **$SiO_2(CO_2H)$+CS LMW**), the isotherm of Langmuir and Freundlich were both fit for the Ni(II) adsorption studied. However, Langmuir best fitted for the adsorption studied. Based on Langmuir isotherm, the maximum adsorption obtained at pH 7 was found to be 189 mg/g for **SiO_2+CS LMW**, and found to be 210 mg/g for **$SiO_2(CO_2H)$+CS LMW**. The effectiveness for adsorption of Cu(II) or Ni(II) by our materials could be due to the carboxyl ($-CO_2H$) or the amine ($-NH_2$) groups on the materials made them possible to offer chelate groups for increasing adsorption capacity. The adsorption kinetics was studied. It was found that the pseudo-second-order was the model that provided the better fit for adsorption kinetics of Ni(II) onto three types of CS-coated silica materials (**SiO_2+CS LMW**, **$SiO_2(CO_2H)$+CS LMW**, and **SiO_2+CS(CO_2H)**). The intraparticle diffusion model (Weber and Morris) was also investigated. The plot for the obtained data showed a straight line plot. Therefore, the adsorption fitted to intraparticle diffusion.

The adsorption kinetics for Cu(II) or Ni(II) adsorption onto the modified silica materials are well described by the pseudo-second-order model, assuming that chemisorption is the rate-controlling mechanism.

There are numerous of advantages of using these novel materials as adsorbents for the treatment of water as follows:

1. The surface of SiO_2-particles can be easily chemically modified to afford novel hybrid materials.

2. They were highly effective for the capture of both Cu(II) and Ni(II) in aqueous solution at room temperature.

3. There is an improved chelation capacity of the metal ions for modified silica particles coated with LMW chitosan.

4. A colloidal system also avoids problems brought about by the viscosity of CS solution, ensuring easy handling.

5. The adsorbents are of low toxicity and friendly to the environment due to the polymeric CS shell coating on the silica nanoparticles (core), since CS is biodegradable.

6. As biosorbent, our materials act as a good candidates for an utilization as adsorbents for water treatment with adsorption capacities superior to numerous other literature- know adsorbents.

To conclude, this thesis, which was the first one started in our research group on the elaboration and use of silica-based composite particle for water treatment, has demonstrated that this strategy is promising and competitive in terms of efficiency and costs compared with other adsorbents studied by other laboratories for this purpose. In this work, the recycling and desorption processes of our composites have been completely neglected due to lack of time. Of course we are aware that the recovery/recycling of an adsorbent is of primordial importance for a potential large-scale use. One possibility for decomplexation of surface-coordinated metal ions could be electrochemical techniques or by decomplexation using a chelating agent having a stronger affinity to bind the metals ions than CS.

Nonetheless, a lot of things concerning synthesis of the composites, their characterisation and their adsorbption capacities could and should certainly be improved:

In order to augment the number of reactive silanol groups on the surface, our Aerosil 200 particles have been activated by acidic treatment with HCl. The conductivy measurements have indicated the presence of some residual HCl despite washing with DI water. Perhaps a better more careful rinsing followed by a prolonged drying at a temperature above 100°C could eliminate residual HCl and chemisorbed water to optimize the degree of silanization.

This study was limited to Aerosil 200 particles with a specific BET surface area of around 200 ± 25 m^2/g. The comparison with other silica particles having smaller and larger particles sizes and specific surface areas such as Aerosil 150 (150 ± 15 m^2/g) and Aerosil 300 (300 ± 30 m^2/g) is desirable to see whether the absorption capacities can be modulated in function of these parameters; e.g. this study will give us more informaton on the effect of silica particles sizes on the adsorption capacity. This project could also be extended to other inorganic oxides such as Al_2O_3 or TiO_2 particles.

In this work, the degree of deacetylation DA of the different CS types was inferior to a DA of 80 %. However, the use of completely deacetylated CS should be investigated to

increase the available amino contents on the CS framework to raise the number of binding site for metal ions, thus optimizing the adsorption capacity. Also the functionalization of CS to carboxymethyl CS could thus be optimized. Also other chemical modifications of CS using the know-how of our group in organic chemistry could constitute an interesting projet for future work.

Morever, to improve the adsorption properties of the sorbents, the coupling of metal ion adsorption with other purification techniques deserves attention. Indeed, some preliminary studies performed in our laboratory indicated that combining the adsorption propensity of the grafted particles with ultrafiltation gives quite encouraging results concerning the retention of Cu(II) ions.

A lot of complementary techniques have been used to characterize the composition, surface structure, particle sizes and adsorption properties of our materials. However, a collaborative work with other laboratories having other facilities absent in our Institut could provide further information on our composites. For example, ^{13}C and ^{29}Si solid-state NMR techniques are more and more employed and could complete the characterization of our composites. Furthermore, the use of X-ray powder diffraction may be an additional tool for the characterisation of our composites.

The present study was limited to the use of Ni(II) and Cu(II) as pollutant. To expand the scale of adsorption by our materials, the adsorption of other metal ions such as Cd(II), Hg(II), Pb(II) and Cr(VI) deserves investigation. An interesting challenge for future studies will also be the exploration of the retention behaviour and selectivity of our materials in the presence of mixtures of different metal ions or couterions. This would represent a next step towards the evaluation and suitableness of our CS-coated silica materials for the removal of pollutants from aqueous solution under real world wastewater conditions.

RESUME DE THESE

Fonctionnalisation de silices colloïdales pour l'adsorption de cations métalliques Cu(II) and Ni(II) Elaboration de composites pour le traitement des eaux

Ce doctorat porte sur la fonctionnalisation de silices colloïdales en vue de la rétention de micropolluants métalliques dans des effluents. Les nanoparticules et microparticules ouvrent des potentialités d'application dans de nombreux secteurs industriels (chimie, environnement, pharmacie...). Ainsi, ces travaux de recherche portent sur la synthèse et la caractérisation de matériaux composites submicroniques : il s'agit de silices colloïdales sur lesquelles sont greffés des silanes ou supportés des polysaccharides. Une des applications de ces travaux de recherche porte sur l'adsorption de métaux de transition sur ces composites en solution aqueuse. Dans le cadre de ce doctorat, les caractéristiques des composites sont définies par leur morphologie de surface, par l'étude des groupements fonctionnels présents, par détermination de leurs surfaces spécifiques ainsi qu'en solution aqueuse par détermination de leurs diamètres hydrodynamiques et de leurs potentiels zéta. Dans un premier temps, la fonctionnalisation de la silice a permis le greffage de groupements carboxyliques et amines dont tes taux de greffage obtenus ont été respectivement de 0,47 µmol/m² et 3,86 µmol/m². En présence de groupements amines, le potentiel ζ des composites est positif jusqu' à pH 9 alors qu'il est négatif dès pH 3 pour des silices non fonctionnalisées. Dans un second temps, la silice est supportée par du chitosane dont le degré de désacétylation est de 77%. Conjointement, l'encapsulation de la silice est réalisées par du chitosane sur lequel des fonctions carboxyliques ont été greffées. La morphologie des particules est alors modifiée, leurs diamètres hydrodynamiques sont plus élevés et leurs potentiels ζ sont positifs jusqu' à pH basique. La rétention d'ions métalliques (Cu(II) et Ni(II)) par ces composites à différents pH est ensuite étudiée. Pour chacun des cations métalliques, les capacités d'adsorption sont déterminées ainsi que les cinétiques d'adsorption. L'application de plusieurs modèles d'isotherme d'équilibre a été réalisée. Dans le cas de Cu(II), à pH 5, les meilleures capacités d'adsorption sont obtenues pour des silices supportées par du chitosane greffé : la capacité de rétention des ions Cu(II) est de 270 mg/g à pH 5. De même, c'est ce composite qui permet la meilleurs rétention des ions Ni(II) à pH 7 avec une capacité d'adsorption de 263 m/g. Concernant la cinétique, le modèle de réaction de surface du pseudo-second ordre s'applique bien aux résultats expérimentaux.

Abstract

This study is focused on the preparation of three types of silica-based composites for the capture of Cu(II) and Ni(II) ions. The first strategy consists in coating chitosan on colloidal fumed silica after acidic treatment yielding the composite **SiO_2+CS**. The second strategy can be separated into two routes: the first one involves surface grafting of silica with aminopropyltriethoxysilane to obtaining silica particles covered by amino groups (**$SiO_2(NH_2)$**). The second one involves in surface condensation of triethoxysilylbutyronitrile, followed by acidic hydrolysis of the surface-bound nitrile groups affording silica particles covered by carboxyl groups (**$SiO_2(CO_2H)$**). In the last step, chitosan has been grafted on the surface bound NH_2 or -CO_2H groups yielding the composites **$SiO_2(NH_2)$+CS** or **$SiO_2(CO_2H)$+CS**. The third strategy involves in the modified CS surface with -CO_2H groups, followed by coating onto the non-modified silica nanoparticles to obtain the composite **SiO_2+CS(CO_2H)**. The novel hybrid materials were characterized by IR spectroscopy, scanning electron microscopy, atomic force microscopy, and zeta potential measurements. Batch experiments were conducted to study the sorption performance of these composites for Cu(II) and Ni(II) removal from aqueous solution at optimum pH at 298 K. The kinetics were evaluated utilizing pseudo-first-order, pseudo-second-order, and intraparticle diffusion models. The adsorption kinetics followed the mechanism of the pseudo-second-order equation for all types of adsorbents. The adsorption isotherms were evaluated utilizing Langmuir, Freundlich, and Temkin models. The best interpretation for equilibrium data was given by Langmuir isotherm model. This study demonstrates that the adsorption capacities for Cu(II) ion is more efficient for the **SiO_2+CS** (256 mg g^{-1}) compared to **$SiO_2(NH_2)$** (75 mg g^{-1}). However, the carboxyl grafted CS-coated silica **(SiO_2+CS(CO_2H)** exhibited an excellent adsorption capacity (333 mg g^{-1}). In case of Ni(II), based on Langmuir isotherm the maximum adsorption capacity found to be 182 mg $g^{-1}$for **SiO_2+CS**, and 210 mg g^{-1} for **$SiO_2(CO_2H)$ + CS**. Using single-metal solutions, these adsorbents were found to have an affinity for metal ions in order as Cu(II) > Ni(II). The adsorption of Cu(II) ion by **SiO_2+CS** was affected by the nature of the respective anion. Application of these composite materials to remove Cu(II) and Ni(II) from aqueous solution was shown to be more efficient than the adsorption capacities of many sorbents probed by other research groups.

Keywords: functionalized silica, chitosan-coated silica, adsorption isotherms, Cu(II), Ni(II)